Structure-Function Relationships of Metal Coordination Complexes for Non-Aqueous Redox Flow Batteries

by

Jonathan Kucharyson

A dissertation submitted in partial fulfillment
of the requirements for the degree of
Doctor of Philosophy
(Chemical Engineering)
in the University of Michigan
2017

Doctoral Committee:

Professor Levi T. Thompson, Chair
Professor Mark Barteau
Professor Melanie Sanford
Professor Johannes Schwank

2017

Dedication

This dissertation is dedicated to the two most important women in my life. While I played with glove boxes and destroyed all of my clothes with acid, my wife worked tirelessly to provide for our family; she supported me during discouraging moments, and placed much of her own ambitions and hobbies on hold. She is an intelligent, caring, beautiful woman and I am blessed beyond measure to call her me wife. The second individual has covered me with vomit, screamed at me countless times, and filled my heart with more love than I ever thought possible. My daughter is the reason I wake up in the morning (literally and figuratively), and to write a dedication to you, Laila, is a dream come true. Finally, I would like to thank my Father, Mother, and brothers for always encouraging me to do everything to the best of my abilities. Your support through all of life's ups and downs means the world to me, and I hope that I have made you proud.

Acknowledgements

Table of Contents

List of Figures

List of Tables

List of Abbreviations

$acac^-$	Acetylacetonate
ACN	Acetonitrile
BE	Bulk electrolysis
BF_4^-	Tetrafluoroborate
bpy	2,2'-bipyridine
C	Concentration
CE	Coulombic efficiency
$Co(acac)_3$	Cobalt(III) acetylacetonate
$Cr(acac)_3$	Chromium(III) acetylacetonate
C/D	Charge-discharge
CV	Cyclic voltammetry
D_O	Diffusion coefficient
E^O	Standard Potential
E_c	Potential at the cathode
E_a	Potential at the anode
E_{pc}	Peak cathodic potential
E_{pa}	Peak anodic potential
EE	Energy efficiency
EXAFS	Extended X-ray fine absorption structure
F	Faraday Constant
$Fe(acac)_3$	Iron(III) acetylacetonate
i_c	Charging current
i_d	Discharging current
i_{pc}	Peak cathodic current
i_{pa}	Peak anodic current
k^0	Kinetic rate constant
LCF	Linear combination fitting
LSV	Linear-sweep voltammetry
MCC	Metal coordination complex

Mn(acac)$_3$	Manganese(III) acetylacetonate
PTFE	Polytetrafluoroethylene
PCM	Polarizable Continuum Model
RFB	Redox flow battery
Ru(acac)$_3$	Ruthenium(III) acetylacetonate
SOC	State of charge
TBA$^+$	Tetrabutylammonium
TEA$^+$	Tetraethylammonium
V(acac)$_3$	Vanadium acetylacetonate
VE	Voltage efficiency
VO(acac)$_2$	Vanadyl acetylacetonate
XAS	X-ray absorption spectroscopy
XANES	X-ray absorption near edge structure
XRD	X-ray diffraction

Abstract

Non-aqueous redox flow batteries could enable the large-scale deployment of variable energy generation technologies, such as wind and solar, as well as decrease the required capacity and increase the efficiency of conventional power plants. Redox flow batteries use liquid electrolytes containing soluble active materials, which allows for the decoupling of power and energy, yielding a battery with a theoretically infinite cycle life. Commercially available redox flow batteries utilize aqueous chemistries, which are limited by the voltage window of water. To overcome this limitation, recent studies have employed non-aqueous electrolytes using redox active polymers, redox active organics, or metal coordination complexes (MCCs) as the active material. The studies described in this dissertation seek to develop structure-function relationships for MCCs; in particular functional group modifications were used to better understand the impact of structure and composition on standard potentials, solubility, and stability. For metal acetylacetonates (acacs), a class of MCCs utilizing redox "innocent" ligands, functional groups consisting of long chain esters were found to significantly increase their solubilities, in some cases achieving up to 1.8M in acetonitrile. Computational analysis suggested that the increased solubilities were primarily due to decreased solvation energies. For the same ligand class, different metals were shown to have a significant effect on the experimentally determined standard potentials, and density functional theory (DFT) calculations were shown to accurately predict these potentials as being a function of the highest occupied or lowest unoccupied molecular orbital energies (HOMO/LUMO). Importantly, the cycle life of

individual half-reactions for a number of MCCs with promising characteristics were quantified using cyclic bulk electrolysis, and the cycle life was shown to correlate to calculated HOMO or LUMO metal density values. For the metal acacs, X-ray absorption spectroscopy was used on two representative MCCs, tracking the charge distribution and structural changes that occur during reduction and oxidation. Significantly different side reactions were observed for each complex, with ligand shedding occurring for vanadium(III) acac during reduction and vanadyl(IV) acac conversion followed by a solvent stabilizing reaction occurring during oxidation. For ruthenium(III) acac, minimal structural changes occurred during reduction, leading to a robust cycle life, while the electrochemical signature dramatically changed during oxidation producing an unknown species with a structure identical to ruthernium(III) acac within 3Å from the Ru atom. Finally, an MCC class with non-innocent ligands, salicylaldimine, was investigated. Ultimately, solubility and stability relationships were used to generate a chromium complex with a solubility of 1.14M which can be reversibly oxidized for ~200 cycles. Combined, these studies provide a foundation for the rational design of next generation active species for non-aqueous RFBs.

Chapter 1

Introduction

1.1 Redox Flow Batteries

In 2015 the United States produced more than 87% of its electricity from non-renewable resources, and of those non-renewable sources, almost 70% were fossil fuels such as coal, natural gas and crude oil [1]. While the consumption of fossil fuels and their anticipated depletion represents a problem, there is also growing concern about greenhouse gas emissions, with the United States releasing almost 5.3 billion tons of carbon dioxide into the atmosphere in 2015. Despite the potential environmental benefits, solar and wind energy generation contributed to less than 6% percent of the United States' electricity portfolio in 2015 [1]. One of the main challenges to wide-scale integration of wind and solar energy into the electrical grid is their high variability [2]. The demonstration of large-scale energy storage technologies would enable load-leveling to smooth variability in wind and solar energy supplies and even allow conventional fuel (e.g. natural gas and/or coal) power plants to operate at higher efficiencies [3].
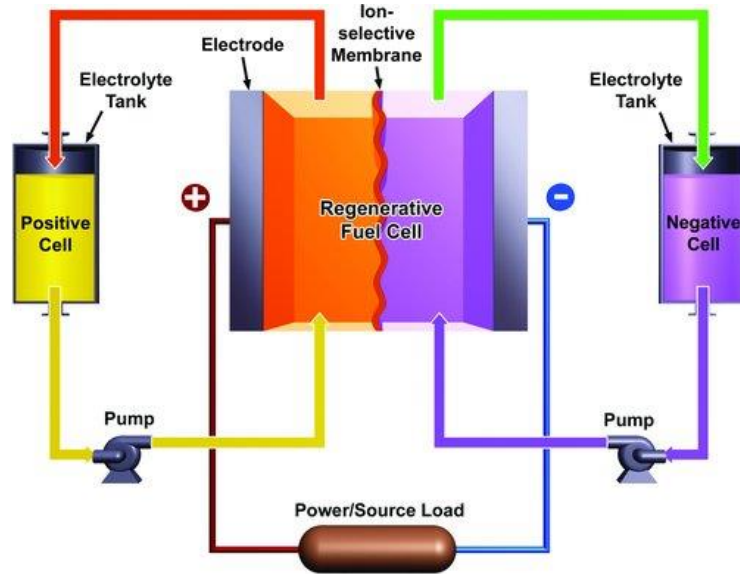
Figure 1.1.1-1 Redox flow battery schematic [4]

Among the energy storage options that have been investigated, redox flow batteries (RFBs) offer a number of features that make them attractive for large-scale energy storage, including their long lifetimes, as a result of power/energy density decoupling [5]. Typical batteries increase energy and power simultaneously by using larger electrodes, which also increases the mass transfer limitations [6]. In contrast, RFBs consist of solvated active species (electrolytes) which are stored in reservoirs to prevent self-discharge (Figure 1.1.1-1) [7]. These electrolytes are pumped past electrodes that are separated by a membrane or separator. The electrodes are typically inert, and only function as a source of or sink for electrons. Therefore, the total energy capacity can be manipulated by the size of the external reservoirs, while the total power can be altered by the size of the electrodes, or the number of stacks. During charging, the catholyte is oxidized and the anolyte is reduced. The reverse occurs during discharge. For the purposes of clarity, the catholyte reaction will be referred to as the oxidation reaction, and the anolyte reaction will be referred to as the reduction reaction. Energy is generated or stored as a consequence of differences between the standard potentials of the two redox

events, and the speed at which the reactions take place. For active materials with ideally reversible redox couples, this theoretically represents an infinite number of cycles [8]. The electrolytes are comprised of an active species, supporting electrolyte, and solvent. The active species influences a number of the properties of the RFB, namely the cell potential, solubility, reversibility, and kinetics. The supporting electrolyte is electrochemically inactive within the voltage window of the RFB and serves to increase the conductivity of the electrolyte. The solvent influences the solubility of the active species and supporting electrolyte and can influence the cell potential as electrolyzing the solvent is undesired.

1.1.1 Aqueous Redox Flow Batteries

The first aqueous redox flow battery was reported by Posner in 1955 where the SnII/SnIV and FeII/FeIII system was investigated [9]. It, and other early flow systems, did not utilize electrochemical charging and instead relied on chemical regeneration of the electrolytes [10]. The first system which allowed for dissolved ions in the charged and discharged state was the CrII/CrIII and FeII/FeIII researched by NASA in the 1970s [11]. A number of chemistries have been proposed since, but the first system to attract significant attention was the aqueous all-vanadium RFB first researched in the 1980s by Skyllas-Kazacos and co-workers [12], [13]. The all vanadium system is a relatively simple flow battery chemistry because it accesses four oxidation states for a common metal [12], [13]. This eliminates a number of problems associated with cross contamination of the two solutions which was a significant problem with previous designs such as the FeII/FeIII and CrII/CrIII flow battery [11]. As a result, the all

3

vanadium RFB can achieve energy efficiencies as high as 85%, and there are more than 20 installations throughout Japan, Europe, and the U.S. [8].

While the vanadium system was a significant step forward in RFB research, it has not been implemented on a mass scale because it suffers from a low energy density (15-25 Wh/L) caused, in large part, by a cell potential that is limited by the stability window of water (1.23V) [5], [6], [8], [14]. Progress has been made to increase the energy density by increasing the solubility of the active material, but with limited success. The use of 2.5M H_2SO_4 and 6M HCl as the supporting electrolyte has been shown to increase the energy density of the vanadium RFB to 25-43 Wh/L [4], and using VBr as the active species in HBr can increase the active species concentrations to 4M, resulting in energy densities of 35-70 Wh/L [15]. However, a number of issues arise associated with the toxic bromine that is generated and the relatively low coulombic efficiencies [16]. Furthermore, the increase in energy density is fairly minor.

A very recent approach to dramatically lower the cost of aqueous RFBs is to use organic active species. Huskinson and co-workers reported the use of a sulfonated anthraquinone (9,10-anthraquinone-2,7-disulfonic acid) as the anolyte active species and when cycled in a flow cell with a Br_2/Br- catholyte achieved 99% capacity retention per cycle [17]. Another report described the use of the same anthraquinone anolyte species with an organic (1,2-benzoquinone-3,5,-disulfonic acid) catholyte. Extended cycling was not reported and 10% of the capacity was lost in the first cycle [18]. While organic active materials have the potential to dramatically lower cost, their use has only recently been implemented, and additional work is required.

With much of the flow battery research focused on increasing the concentration of the active species, or the number of electrons transferred, increasing the cell potential is the logical next step. With overpotentials, some aqueous batteries can have windows of up to 1.6V [10], but this increase is marginal. The best approach to increase the cell potential is to utilize non-aqueous solvents. Darling and coworkers indicate that an active species of sufficiently high solubility and cell potential could enable non-aqueous RFBs that meet the aggressive Department of Energy goal of $100 per kWh [19].

1.1.2 Non-aqueous Redox Flow Batteries

To increase the cell potential, and therefore the energy density, non-aqueous solvents with wider electrochemical windows must be employed. Many non-aqueous solvents, including acetonitrile (ACN), allow for much higher potentials than water, in some cases as high as 5V [20], but the use of non-aqueous solvents introduces a number of complexities. The two most important issues are the solubility and cyclability of the active species. Water has high polarity and is able to dissolve many species at high concentrations (for example 4M VBr), but non-aqueous solvents have lower polarities [21] and the active species concentrations can be orders of magnitude lower than those for aqueous systems [22]. Because of this, active materials in non-aqueous systems generally consist of a redox active metal that is complexed with ligands to increase solubility; these fall under the class of complexes known as metal-coordination complexes (MCCs) [7]. Other classes of active species are also being investigated; recent work has been performed using small organic molecules and redox active polymers, but results are very preliminary [23]–[25]. Because these active materials are far more

complex than electrolytes used for aqueous systems, there is an increase in possible degradation mechanisms during cycling, which would result in capacity fade [10].

Matsuda and co-workers were the first to describe the use of MCCs as active species for non-aqueous RFBs; tris(2,2'-bipyridine)ruthenium(II) tetrafluoroborate $(Ru(Bpy)_3(BF_4)_2)$ and tris(2,2'-bipyridine)iron(II) tetrafluoroborate $(Fe(Bpy)_3(BF_4)_2)$ were used as active species, and ACN was used as the solvent [26]. Bipyridine has been shown to be a redox active (non-innocent) ligand, so multiple redox couples were expected [27]. The authors showed that the solubilities of $Ru(Bpy)_3(BF_4)_2$ and $Fe(Bpy)_3(BF_4)_2$ in ACN were 0.2M and 0.8M respectively. Cyclic voltammograms revealed that the use of $Ru(Bpy)_3(BF_4)_2$ in ACN could increase the cell potential to 2.6V, and that four redox couples were available in that window. While the ligand has been shown to be non-innocent, the four redox couples were not individually assigned to the metal or ligand, and no trends between the different metals were presented. The electrolyte was tested in a flow cell, and significant capacity fade was observed after 5 cycles. Capacity fade was reported to be due to cross-over of the active material through the Neosepta anion exchange membrane [26].

Chakrabarti and co-workers further characterized the $Ru(Bpy)_3(BF_4)_2$ system, and investigated the use of ruthenium(III) acetylacetonate $[Ru(acac)_3]$, tris(2,2'-bipyridine) iron(II) perchlorate, and rubrene in ACN. Based on results from CV, the expected cell potentials ranged from 1.77 to 2.6V, and the authors reported "poor" solubilities for both $Ru(Bpy)_3(BF_4)_2$ and rubrene, while solubilities for $Ru(acac)_3$ and iron(II) perchlorate in ACN were listed as "high" and "moderate", respectively [28]. The solubility of $Ru(Bpy)_3(BF_4)_2$ being "poor" is in contrast to the work by Matsuda and co-workers

which quantified the solubility as 0.2M [26]. If any redox reactions are metal-based, $Ru(acac)_3$ and $Ru(Bpy)_3(BF_4)_2$ should show similarities in their respective CVs, however there were no common standard potentials presented. No explanation for the differences was offered. The authors also cycled $Ru(acac)_3$ and Fe(II) perchlorate in H-cells, but low states of charge were observed for both systems, the experiments were not conducted inside a glove box which could result in contamination, and only one full cycle was presented [28].

Mun and co-workers continued to investigated metal-bipyridine systems, with $Ni(Bpy)_3(BF_4)_2$ and $Fe(Bpy)_3(BF_4)_2$ both reported to have "high" solubilities in propylene carbonate [29]. Propylene carbonate is significantly less polar than ACN, so observations that $Ru(Bpy)_3(BF_4)_2$ has a "poor" solubility in ACN [28] and similar complexes such as $Ni(Bpy)_3(BF_4)_2$ and $Fe(Bpy)_3(BF_4)_2$ have "high" solubilities in propylene carbonate are counterintuitive. Cycling $Ni(Bpy)_3(BF_4)_2$ and $Fe(Bpy)_3(BF_4)_2$ electrolytes in a flow cell revealed significant capacity fade after only 5 cycles. The authors hypothesized that the loss of capacity was due to active species cross-over, but this was not confirmed [29]. Similar to previous work, there were no trends presented for the changes in the electrochemistry of the different metals, and the differences in capacity fade between the complexes were not discussed.

Our work has focused on the use of "innocent" ligands; which were first defined as ligands which do not alter the oxidation state of the metal of the complex [30]. In reality, all ligands will alter the oxidation state of the metal to some extent [30], [31]. The RFB community has come to define "innocent" ligands as those which do not store charge during reduction or oxidation, and are present only to increase solubility of the

redox-active metal [27], [32], [33]. This is a simplification, and the extent of "innocence" has yet to be investigated in the context of flow batteries. The original non-aqueous RFB work by Matsuda and co-workers utilized non-innocent ligands [26], and a number of studies have been performed with the intent of using non-innocent ligands to achieve more electron transfers [27], [32].
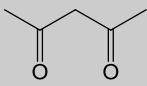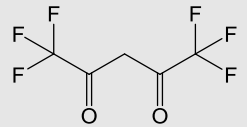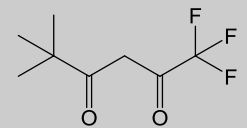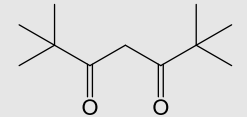
The most studied "innocent" ligand-based RFB system utilizes acetylacetonate-based complexes. Previous work in the Thompson group reported results for three different metal(III) acetylacetonate compounds: Cr, Mn, and V [34]–[39]. The authors showed that Cr(III) acetylacetonate [$Cr(acac)_3$] has a maximum solubility of 0.4M in ACN, four redox couples, and a total cell potential of 4.1V. Work by Saraidaridis and co-workers revealed that thre reduction of $Cr(acac)_3$ results in ligand detachment [40]. While the CVs showed relatively poor reversibility, a cell potential of 4.1V is over three times higher than the potential of water electrolysis. Slow kinetics and possible species cross-over led to a charge-discharge energy efficiency of 21% [38]. $Mn(acac)_3$ was shown to have a maximum solubility of 0.6M, two redox couples, and a cell potential of 1.1V. Despite a low cell potential, the redox reactions were shown to be significantly more reversible than $Cr(acac)_3$, but an unknown side-reaction was observed during H-cell cycling which caused capacity fade [37]. $V(acac)_3$ was shown to have a maximum solubility of 0.6M, two redox couples, and a cell potential of 2.2V. CVs showed quasi-reversibility, and a side reaction generating vanadyl(IV) acetylacetonate [$VO(acac)_2$] due to water and oxygen in solution was reported [34], [36]. By sparging with N_2 during H-cell cycling, coulombic efficiencies of around 70% were achieved, but other reports of experiments in closed systems have also reported $VO(acac)_2$ formation, as well as ligand

detachment [41]–[43]. V(acac)$_3$ has also been tested by Herr et al. in a flow cell. While it is not a direct comparison to other studies because they did not use ACN as the solvent, coulombic efficiencies of 95% and 98% in ACN and tetrahydrofuran solvents, respectively, were reported [42]. For each of these studies the metal was held constant, so no comparisons between the different metals were made. Likewise, while the degradation mechanism of V(acac)$_3$ has been investigated, similar studies have not been conducted on other metal(III) acetylacetonates to determine if similar degradation mechanisms are responsible for their respective capacity fade. This is of particular interest for Cr(acac)$_3$ because it has excellent properties for use as an RFB active material (4.1V, two electron transfers) but has limited reversibility [38], [40].

One other class of MCCs which utilizes an "innocent" ligand are the cyclopentadienyl-based systems, such as ferrocene [44], [45]. Ferrocene is a well-studied complex that undergoes one reversible oxidation reaction and is typically used as a standard for the determination of diffusion coefficients, kinetic rate constants, and standard potentials [20], [44]–[52]. It has recently been used as an active species in the catholyte of RFBs, where the solubility was increased using an ionic functional group. Wei and co-workers were able to cycle the ferrocenium complex (ferrocenylmethyl dimethyl ethyl ammonium bis(trifluoromethanesulfonyl)imide) in a flow cell for 100 cycles with 95% capacity retention at 0.1M. When cycled at 0.8M concentrations, however, significant capacity fade occurred during the first 20 cycles [46]. The same group recently reported reduced capacity fade for the same complex at 1.2M for 500 cycles in a static cell [47]. The cause of the fade has not been investigated and consequently is not well understood.
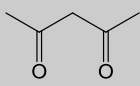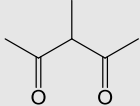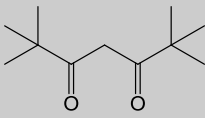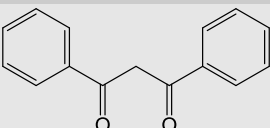
The first experiment to investigate the possibility of increasing the solubility of MCCs via functional groups was conducted by Yamamura et al. in their work using uranium complexes with modified acetylacetonate ligands as the active species [53]. The addition of fluorine functional groups resulted in an increase of the solubility of uranium(II) acetylacetonate from >0.4M to >0.8M in ACN. A subset of the ligands and the resulting uranium MCC solubilities are listed in Table 1.1.2-1. Exact solubilities were not reported for many of the MCCs with high solubility, so it is difficult to elucidate solubility trends, however, it appears that the use of fluorine groups generally increases the solubility of the complex. As far as how the functional groups impact the electrochemistry, the cell potentials were all relatively close to 1.1V with minor shifts in the standard potentials of the two redox couples. No charge-discharge experiments were conducted, however, ligand shedding during the reduction reaction was observed for all complexes by CV.

Table 1.1.2-1 Uranium acetylacetonate functionalization results [53]

Ligand Structure	Solubility (M)
	>0.4
	>0.8
	>0.4
	>0.4

Previous work in the Thompson group has also investigated how ligand functionalization impacts the solubility of acetylacetonate based complexes. Functionalized V(acac)$_3$ complexes were less soluble than V(acac)$_3$, but the solubility was changed by two orders of magnitude (Table 1.1.2-2). Only four functional groups were investigated, and trends were not discussed. None of the complexes were characterized using cycling experiments, so the impact of the functional group on battery performance is unknown. Functionalizing Co(acac)$_3$ has also been investigated, but not to investigate the impact on solubility. Co(acac)$_3$ was functionalized with ethylenediamine by Zhang and co-workers in 2012. In ACN, the resulting complex has three redox couples and a cell potential of 2.0V. Cycling in an H-cell demonstrated coulombic efficiencies of approximately 88% for multiple cycles, but no solubilities were reported [54].

Table 1.1.2-2 Vanadium(III) acetylacetonate functionalization results [55].

Ligand Structure	Solubility (M)
	>0.4
	>0.8
	>0.4
	>0.4

1.1.3   Energy Density Equation

The energy density of non-aqueous RFBs is calculated from the Nernst Equation [20]. The Nernst Equation as well as the energy density is regularly referenced throughout this dissertation, so the theory is discussed here. The following is an example calculation assuming single step reduction and oxidation reactions of species A:

$$\text{Reduction reaction: A} + \text{e}^- \ \text{->} \ \text{A}^{-1} \qquad\qquad \text{Equation 1.1.3-1}$$

$$\text{Oxidation reaction: A -> e}^- + \text{A}^{+1} \qquad\qquad \text{Equation 1.1.3-2}$$

The anodic and cathodic potentials (E_a and E_c, respectively) for the cell are therefore:

$$E_a = E_{Red}^{O} - \frac{RT}{F}\ln(\frac{a_{A^-}}{a_A}) \qquad\qquad \text{Equation 1.1.3-3}$$

$$E_c = E_{Ox}^O + \frac{RT}{F} \ln(\frac{a_{A^+}}{a_A})$$

Equation 1.1.3-4

where E_a is the anodic potential, E_c is the cathodic potential, E^O is the standard potential of the reaction, Red denotes the reduction reaction, and Ox denotes the oxidation reaction, R is the ideal gas constant, T is the temperature, F is Faraday's constant, and "a" is the activity of the given species.

The cell potential (E_{cell}) is defined as the difference between the cathodic and anodic potentials, the activities can be estimated as concentrations of the respective species, and the concentration of each species can be related to the initial concentration of A (C_O) through the use of a parameter defined as the state of charge (SOC). When SOC = unity, the cell is fully charged and the anolyte has been fully reduced, while the catholyte has been fully oxidized. Equation 1.1.3-4 can therefore be converted to:

$$E_{cell} = E^O + \frac{RT}{F} \ln(\frac{C_O \text{SOC}^2}{[C_O(1 - \text{SOC})]^2})$$

Equation 1.1.3-5

where E^O is the difference between the reduction reaction and oxidation reaction standard potentials. The energy density of the cell is therefore:

$$E = 0.5\text{n} \int_0^1 E_{cell} \, dSOC$$

Equation 1.1.3-6

where n is the number of electrons transferred. The integral is multiplied by 0.5 because half of the electrolyte is used for each half-reaction. However, as no parameters in

13

Equation 1.1.3-5 are dependent on the solvent or supporting electrolyte, E_{cell} will be symmetric about E^O and Equation 1.1.3-6 can be simplified to:

$$E = 0.5 \text{n} F E^O C_O$$

Equation 1.1.3-7

This same analysis can be extended to multiple electron transfers at different potentials, by making the assumption that all of the active material will be converted to oxidation states of +1 and -1 before continuing to +2 and -2. The mixtures would still give the same overall E_{cell}. Again, these systems do not involve the solvent or support, so E_{cell} will be symmetric about the E^0 value for each electron transfer. For a multi electron transfer system Equation 1.1.3-7 becomes:

$$E = 0.5 * \text{F} * C_O * (E_1^0 + E_2^0 + etc.)$$

Equation 1.1.3-8

It is important to note that for any chemistry where the supporting electrolyte does participate in the redox reactions, Equation 1.1.3-7 and Equation 1.1.3-8 are not valid because the cell potential will not be symmetric about E^O. Therefore the energy density for such systems must be calculated following Equation 1.1.3-6.

1.2   Research Goal and Approach

My literature review indicates that there has not been a systematic investigation to better understand how different metals, ligands, and functional-groups impact the solubility and electrochemistry of the active species. Work on bipyridine MCCs shows that the metal influences the electrochemistry and, when comparing bipyridine and acetylacetonate complexes, the ligand also plays a significant role in the

14

electrochemistry, but clear trends in the data have not been established. If easily calculated or experimentally determined descriptors for key parameters such as standard potentials, solubility and cycleability could be identified, they would allow for high throughput screening of future complexes.

Solubility data that has been reported in the literature is limited, vague, and in some cases contradictory. The few studies that have been performed to modify the solubility of MCCs with innocent ligands utilized a small number of functional groups, and a complex with a solubility above 1M with multiple redox couples is crucial to the viability of non-aqueous redox flow batteries.

Beyond the fundamental solubility and electrochemical properties of MCCs, this literature review also demonstrates the limited understanding of the stability of MCCs during electrochemical cycling. Most reports hypothesize that capacity fade is due to cross-over of the active species, but the same active species is used as both the anolyte and catholyte, so while cross-over will cause decreased coulombic efficiencies, it will not result in capacity fade. Reactions with the membrane are a known issue [56], and electrode-active species reactions have also been reported [55]. With significant capacity fade observed for most reports presented here, stability remains a significant challenge. Truly innocent ligands also has yet to be experimentally verified, and could be a means of determining the cause of instabilities.

The goal of this work is to develop structure-function relationships of MCCs primarily utilizing innocent ligands, for the purpose of enabling the design of next-generation active materials for non-aqueous RFBs. The following objectives were established to achieve this goal.

1. Investigate the impact of functional groups and metals on the electrochemistry and solubility of metal(III) acetylacetonates. Identify an interesting complex to characterize in a flow cell.

2. Identify and quantify key parameters influencing the electrochemical stability of metal(III) acetylacetonates during reduction and oxidation.

3. Investigate the degree of ligand innocence of representative acetylacetonate complexes using electronic and molecular structure characterization techniques.

4. Explore other ligand systems and establish structure-function relationships that extend across classes of ligands.

To achieve these objectives, several studies were conducted that each relied on a combination of experimental and computational techniques. A brief description of what is presented in each chapter and the subsequent conclusion are provided herein.

Chapter 2: Effect of Functional Group and Metal

This chapter describes the impact of a number of functional groups and metals on the electrochemistry and solubility of metal(III) acetylacetonates. Standard potentials, estimated redox reaction reversibilities, and solubilities for each functional group and metal are presented. The experimental data, in conjunction with DFT calculations are used to determine that changing the metal has a significant impact on the free energy of the reduction and oxidation reactions, and that the functional groups primarily influence the solvation energies of the complexes. Correlations are established for both parameters which can be used to predict the properties of future complexes. To determine how changing the functional group will impact battery performance, a functionalized complex

was tested in both an H-cell and a flow cell. Rapid capacity fade is observed, which provides the motivation for research described in **Error! Reference source not found.**.

Error! Reference source not found.**: Stability Assessment**

This chapter describes an in-depth stability analysis to quantify the shelf life, solubility at each oxidation state, and half-reaction cycle lifes of a representative acetylacetonate-based MCC. The capacity fade described in Chapter 2 was found to be a function of the cycle life of each half-reaction, and not due to limited shelf life or decreasing solubilities. To establish trends for the impact of different metals and functional groups on the quantified cycle lives, the cycle lives of a number of metal(III) acetylacetonate half-reactions are quantified and, when complemented by results from DFT calculations, are used to determine that the cycle life of a half-reaction is dictated by the percent of the molecular orbital density on the metal of the complex estimated using Hirschfield Population Analysis (Section 3.2.2). These values are further used to establish a correlation which can be used to predict the cycle life of other complexes, ultimately facilitating their design for RFBs.

Chapter 4: Structural Changes and Charge-Storage Mechanism

This chapter discusses the structural and electronic changes of two representative acetylacetonate complexes during oxidation and reduction, characterized using X-Ray Absorption Spectroscopy. In both cases, the ligands are found to be non-innocent, and the structural changes are used to determine the mechanism of the side-reactions observed during battery cycling experiments. Evidence is presented to support the theory that during oxidation, vanadium(III) acetylacetonate rapidly forms vanadyl(IV)

acetylacetonate, which is then stabilized by the ACN solvent. The Ru-O bonds in ruthenium(III) acetylacetonate are found to reversibly stretch during reduction, and irreversible oxidation is attributed to partial ligand oxidation.

Chapter 5: Salicylaldimine-Based Metal Coordination Complexes

In this chapter, MCCs incorporating salicylaldimine ligands are characterized and structure-function relationships are established. Functional group locations which impact solubility and stability are identified, and used to synthesize a complex with high solubility and a very stable oxidation reaction. This complex is further characterized using a flow cell. Capacity fade is observed, and discussed. The standard potential correlation established in Chapter 1 is found to accurately predict the standard potentials of reduction and oxidation reactions for salicylaldimine-based MCCs, and confirm ligand non-innocence through primarily ligand-based reactions.

Chapter 6: Conclusions and Future Work

The final chapter provides a brief summary of the key findings, and a discussion regarding trends observed for RFBs as a whole. Based on the results of these studies, recommendations for future studies regarding MCCs for non-aqueous RFBs are provided.

Chapter 2

Effect of Functional Group and Metal on Standard Potential and

Solubility

2.1 Background and Approach

As described in Section 1.1.2, while the use of MCCs as active materials for non-aqueous RFBs allows for wider voltage windows, the realized energy densities have been limited by low solubilities [6]. Modifying the parent complex with functional groups has been shown to moderately increase solubility [53], but solubility data in the literature is typically qualitative, and the few studies that have presented quantitative values did not investigate a wide range of functional groups [53], [55]. Therefore, the structural properties which govern the solubility have not been definitively defined.

While the goal of modifying a type of ligand with functional groups is to increase the solubility of the active species, studies have shown that, while minor, the functional group also has an impact on the standard potentials of the complex [53], [55]. Similar to the effect on solubility, the effect of the functional group on the standard potentials is not well understood, and thus cannot be predicted. If changes in the standard potential of a complex with a fixed ligand type using a functional group could be predicted, then new complexes could be designed to maximize the cell potential of the RFB. Even if the solubility and standard potentials could be predicted, the impact of functional group modifications on battery performance has also never been studied, and cycling

experiments on functionalized complexes to confirm that the reversibility of the redox reactions remain unaltered must be performed.

Beyond ligand modification via functional groups, the effect of the metal and ligand type of MCCs on the solubility, and electrochemistry (standard potentials and reversibility) are not well understood. Bipyridine MCC studies demonstrate that different metals have an impact on the electrochemistry [26]–[29], but there has not been a systematic investigation of the effect of metal on standard potentials. Likewise, RFB studies of acetylacetonate-based complexes have never focused on the role that the metal plays on the electrochemical properties [34], [37], [38], which limit the structure-function relationships that can be established. When comparing bipyridine and acetylacetonate studies, reduction reactions for bipyridine complexes are generally assigned to the ligand, while oxidation reactions are assigned to the metal [27], but the same metals used for acetylacetonate-based MCC studies with "innocent" ligands have different oxidation reaction standard potentials [27], [38]. With this in mind, the electrochemistry of MCCs must be affected by both the metal and ligand, and determining which structural properties dictate the standard potentials is vital to the design of future complexes.

This chapter will focus on "innocent" ligands. Innocent ligands, with regards to RFBs, are ligands which only increase solubility of the redox-active metal, and do not participate in the electrochemistry [27], [32], [33]. In reality, as mentioned eariler, the ligand will play a role in both the solubility and electrochemistry of the MCC regardless of if it is innocent or non-innocent [30], [31], and therefore, for this chapter, the ligand type is held constant, while different functional groups and metals are investigated. Studies regarding a non-innocent ligand class are described in Chapter 5.

Metal(III) acetylacetonate complexes were chosen for this project as they are the most widely studied MCCs with "innocent" ligands for use in non-aqueous RFBs [28], [34]–[43], [53]–[55], [57], [58]. Correlations between the complex structure and solubility for these MCCs have not been reported. Similarly, relationships between functional groups and standard potentials have only been investigated in one study, which demonstrated that the standard reduction potential for a series of functionalized manganese(III) acetylacetonate complexes linearly correlated with DFT-estimated lowest unoccupied molecular orbital (LUMO) energies. The oxidation standard potentials, and how the functional group effect translates to other base metals were not investigated [58].

a)

M = V, R = H (**1**) - V(acac)$_3$
M = Cr, R = H (**2**) - Cr(acac)$_3$
M = Mn, R = H (**3**) - Mn(acac)$_3$
M = Fe, R = H (**4**) - Fe(acac)$_3$
M = Co, R = H (**5**) - Co(acac)$_3$
M = Mo, R = H (**6**) - Mo(acac)$_3$
M = Ru, R = H (**7**) - Ru(acac)$_3$
M = Cr, R = Br (**8**)
M = Cr, R = NO$_2$ (**9**)
M = Cr, R = CH$_2$CN (**10**)
M = Cr, R = CH$_2$NMe$_2$ (**11**)

b)

(**12**) (**13**) (**14**)

c)

M = Cr, R = Et, R' = H (**15**)
M = Cr, R = Et, R' = Me (**16**)
M = Cr, R = 2-CH$_2$(thf), R' = H (**17**)
M = Cr, R = CH$_2$CH$_2$OMe, R' = H (**18**)
M = Cr, R = (CH$_2$CH$_2$O)$_2$Me, R' = H (**19**)
M = V, R = CH$_2$CH$_2$OMe, R' = H (**20**)

d)

(**21**) - VO(acac)$_2$ (**22**) - Ferrocene (FCN)
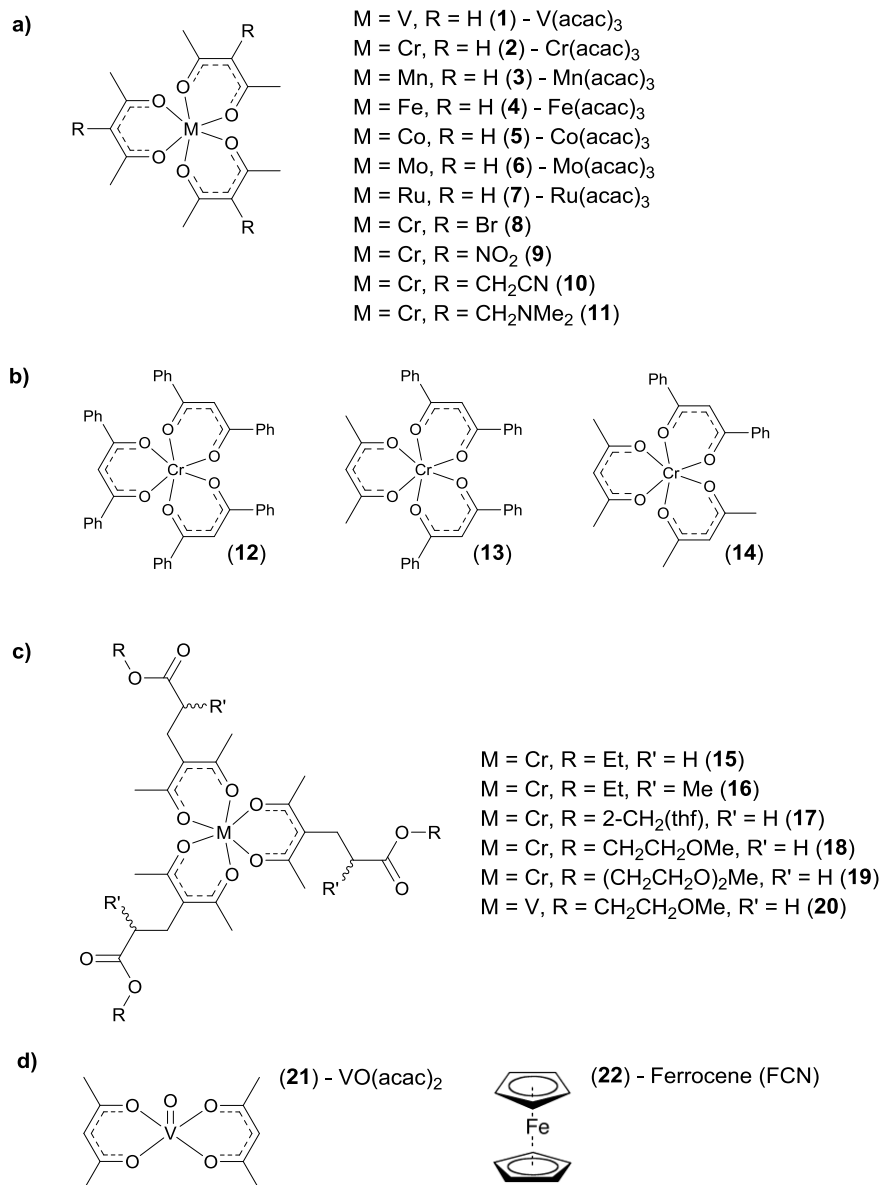
Figure 2.1-1 a) Un-functionalized metal(III) acetylacetonate complexes assessed herein (**1 – 7**), and chromium(III) acetylacetonate complexes with functional groups of varying electronegativity (**8-11**). b) Phenyl-substituted chromium(III) acetylacetonate complexes (**12 - 14**) through ligand disproportionation. c) Ester functionalized chromium(III) and vanadium(III) acetylacetonate complexes (**15 – 20**) d) vanadyl(IV) acetylacetonate (**21**) and ferrocene (**22**).

To elucidate trends with regard to how the metals and functional groups impact the electrochemistry and solubility of metal(III) acetylacetonates, this study utilized a series of metal(III) acetylacetonates of varying metals and functional groups (Figure 2.1-1). First, the standard potentials of each complex were experimentally determined

22

using CV, then compared to calculated values using DFT structure optimizations. Next, solubilities were quantified using a UV-Vis method (Section 2.2.1) and a regression analysis was used to correlate the experimental values to DFT-calculated solvation energies and dipole moments. Finally, as all previous functional group studies did not investigate how the active materials would function under battery cycling conditions [53], [55], two of the most promising candidates were tested using charge-discharge in an H-Cell, and the complex with the best H-cell performance was subsequently tested in a flow cell.

The charge-discharge and most of the cyclic voltammetry and solubility results have been published and can be found in "Metal Acetylacetonate Complexes for High Energy Density Non-Aqueous Redox Flow Batteries," *J. Mater. Chem. A*. **3**, 7929 (2015). The functionalized complexes (**8-20**), and molybdenum(III) acetylacetonate (**6**) were synthesized by Dr. James Suttil and Pablo Cabrera from the Sanford group at the University of Michigan. Details regarding the synthesis procedure and verification of the identities of the functionalized complexes including NMR, XRD, and elemental analysis can be found in the supplementary information of the aforementioned paper, and will not be presented here. Solubility measurements were conducted by both the Sanford group members, and myself. Flow cell studies were conducted by Dr. Ismailia Escalante-Garcia from the Savinell group at Case Western Reserve University. I conducted the cyclic voltammetry, H-cell studies and the density functional theory calculations. Density functional theory calculations were conducted in collaboration with Dr. Lei Cheng from the Curtiss group at Argonne National Lab.

2.2 Experimental Techniques

2.2.1 Solubility Measurements Using UV-Vis Spectrophotometry

Solubilities of each active species were determined using UV-Vis spectrophotometry. The amount of visible and ultraviolet light radiation that a species can absorb scales linearly with concentration according to the Beer-Lambert law:

$$A = \varepsilon C l$$ Equation 2.2.1-1

where A is the absorbance, ε is the molar attenuation coefficient, C is the concentration of the species, and l is the pathlength. Therefore, a series of solutions of known concentrations can be used to determine the molar attenuation coefficient of the species, which can then be used to determine the concentration of a solution with the same species of an unknown concentration.

For these experiments, an Implen P300 UV-Visible Nanophotometer was primarily used, however, several complexes were tested using a Shimadzu UV-1601 UV-Visible spectrophotometer. Solubilities using either device were found to be within error, but far less material is needed for the Nanophotometer. The Nanophotometer functions similarly to a standard UV-Visible Spectrophotometer, but instead of using a cuvette, the pathlength of the sample is controlled using caps which compress a 2μl sample against a sample pedestal (Figure 2.2.1-1). For these studies, a combination of caps resulting in pathlengths of 2, 0.02, and 0.04mm were used. During the measurement, a xenon source is used to scan a wavelength range of 200-950nm and the absorbance is measured using a charge coupled device array with an error of 1%. Furthermore, the Implen P300 Nanophotometer is small enough to be placed inside an argon glove box and samples can be measured without exposure to ambient air.
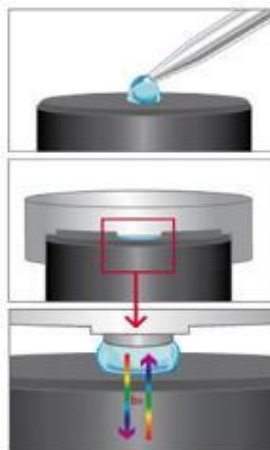
Figure 2.2.1-1 Nanophotometer sample compression

For each complex, a suitable wavelength for absorbance measurements was first determined, and then absorbances of standard solutions were measured at the determined wavelength and used to prepare an absorbance versus concentration calibration curve. Saturated solutions were prepared by portion-wise addition of the desired complex to ACN with stirring until a persistent suspension resulted. The solution was then filtered through cotton wool or centrifuged using an Eppendorf 5415C centrifuge at 8000 rpms for 20 minutes to remove any undissolved material. Finally, three aliquots were diluted in ACN to afford absorbances within the range of the calibration curve. An example set of spectra obtained for the calibration solutions of VO(acac)$_2$ at 301nm can be seen in Figure 2.2.1-2.
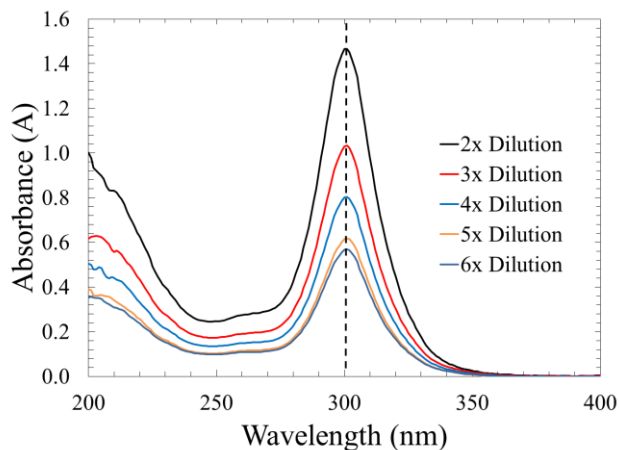
Figure 2.2.1-2 UV-Visible spectra of calibration samples of VO(acac)$_2$ in acetonitrile. Calibration samples were made by diluting 0.040M stock solutions.

For all complexes, the standard deviation was used to estimate the error in solubility, as it resulted in a larger error than the error of the calibration curve assessed by linear regression. The slope of the trendline is equal to the molar attenuation coefficient of the species in units of M^{-1}cm^{-1} (Figure 2.2.1-3).
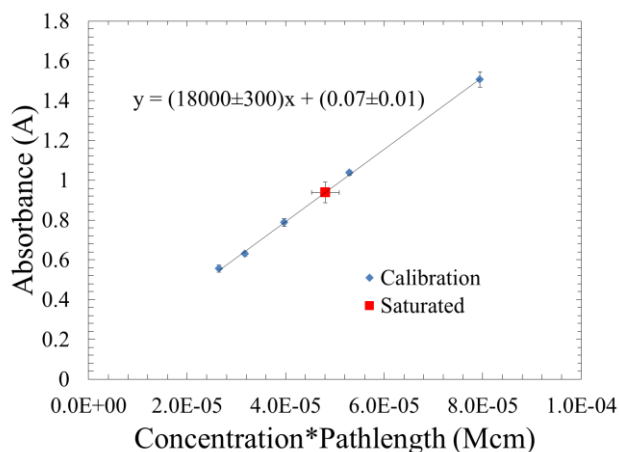
Figure 2.2.1-3 Absorbance vs. concentration and pathlength for calibration curve and saturated samples of VO(acac)$_2$ in ACN at 301nm. Saturated samples were diluted by 4x prior to measurement.

2.2.2   Cyclic Voltammetry [20]
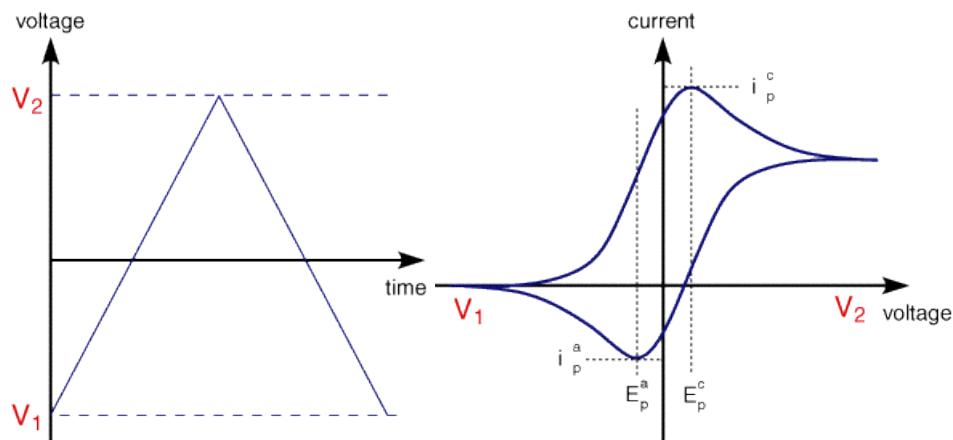
Figure 2.2.2-1 Example Cyclic Voltammogram Input (left) and Output (right) [59].

Cyclic voltammetry (CV) is an electrochemical method which measures the current at an electrode as a function of applied potential with a fixed, linear scan rate, using a potentiostat (Figure 2.2.2-1) [60]. The potential is swept in a cyclic fashion so both oxidative and reductive currents can be seen. CV experiments are conducted using a three electrode system consisting of the working, counter and reference electrodes. These experiments differ from battery cell experiments in that the voltage is measured at a working electrode, and not across a cell. CV also differs for battery cell experiments in that the bulk of the electrolyte is not electrolyzed. The working electrode is the electrode at which the potential is varied; the current is measured between the working and counter electrodes, while the voltage is measured between the working and reference electrodes. The counter electrode has a surface area of at least ten times that of the working electrode to guarantee that the current being generated is a function of the working electrode. Products generated at the counter electrode should not be allowed to diffuse to the working electrode, because the potential at the counter electrode is not controlled and side reactions are likely. Therefore, the counter electrode is typically placed either far

27

from the working electrode or in a fritted chamber (or both). The reference electrode is made of a material that has a stable voltage that does not change with an applied current. Uncompensated resistance, which will cause shifting of the cyclic voltammogram current peaks, is minimized by placing the reference electrode as close as possible to the working electrode. To accomplish this, a Luggin capillary is placed between the working and reference electrodes. Small working electrodes are used so that the bulk of the electrolyte solution is unchanged throughout the measurements, and that any remaining uncompensated resistance has a minimal impact on the applied voltage.

When a macro-electrode is used as the working electrode, mass-transfer limitations cause the current to increase and subsequently decrease to a steady state current, resulting in a peak (see Figure 2.2.2-3). A positive current peak is due to an oxidation reaction, while a negative current peak is due to a reduction reaction. Forward/reverse oxidation and reduction reactions are defined as redox couples.

If an electrochemical reaction does not occur within the tested voltage range, the resulting cyclic voltammogram will not have any peaks, and the current will be entirely due to double-layer capacitance. As seen in Figure 2.2.2-2, a CV of the supporting electrolyte does not reveal any peaks, and the supporting electrolyte will therefore not contribute to the electrochemical signal of the active materials tested. One example of a tested active material can be seen in Figure 2.2.2-3, where the CV shows two primary redox couples and a third couple due to a side reaction. By varying the voltage window and isolating individual couples, the cause of side reactions can be determined. A more detailed analysis for this complex and others is provided in Section 2.3.2.
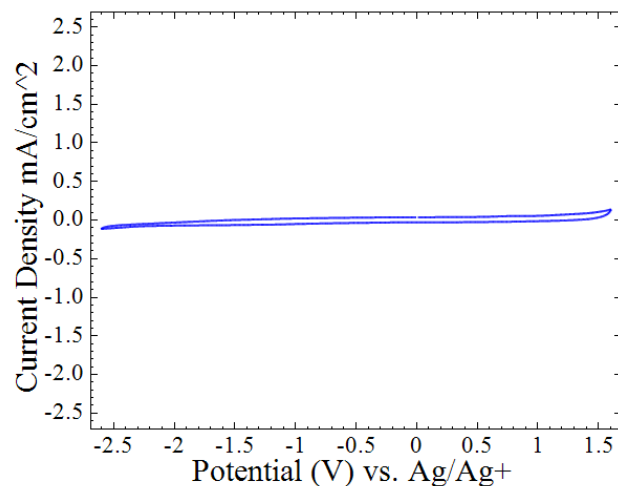
Figure 2.2.2-2 Cyclic voltammogram of 0.1M TBABF$_4$ in acetonitrile
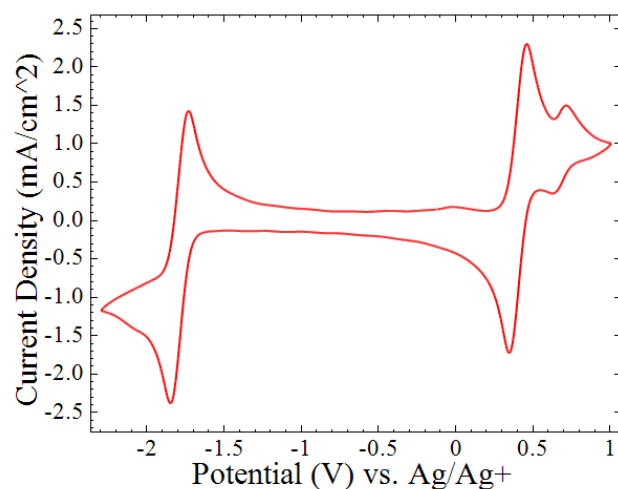
Figure 2.2.2-3 Cyclic voltammogram of 0.01M V(acac)$_3$ with 0.1M TBABF$_4$ in acetonitrile

CVs can be used to gather a number of properties regarding redox couples such as: standard potentials, diffusion coefficients of the active material, and peak height ratios (i_{pc}/i_{pa}) which are used to estimate reversibility. Transfer coefficients and reaction rate constants can also be estimated.

The standard potential (E^O) is defined as the midpoint between the peak potentials, which follows [20]:

$$E^O = \frac{E_{pc} + E_{pa}}{2} \qquad\qquad \text{Equation 2.2.2-1}$$

The diffusion coefficient (D_O) can be determined by conducting CVs at varying scan rates and subsequently using the Randles-Sevcik Equation [20]:

$$i_p = 268{,}600 n^{\frac{3}{2}} A D_O^{\frac{1}{2}} C v^{\frac{1}{2}} \qquad\qquad \text{Equation 2.2.2-2}$$

where i_p is the peak current (A), n is the number of electrons transferred, A is the surface area of the electrode (cm^2), C is the bulk concentration of the active species in solution (mol/cm^3), and v is the scan rate (V/s). Equation 2.2.2-2 is only valid at room temperature, with no mixing, and at scan rates where kinetics are not limiting the peak current [61]. Even for redox couples with relatively fast kinetics (rate constant on the order of 10^3 cm/s) shifting peak potentials will be observed at scan rates >0.1V/s, and will result in inaccurate diffusion coefficients [62].

The peak height ratio of the currents for a measured redox couple are used to estimate the reversibility of the reaction, with an ideal peak height ratio of unity. For this chapter the peak height ratio was used to screen for complexes that were likely to cycle reversibly in charge-discharge (C/D) experiments. The peak height ratio is later shown (**Error! Reference source not found.**) to not be a highly accurate method of predicting he stability or reversibility of a given couple during charge-discharge experiments.

The kinetic rate constant (k^0) can also be estimated using varying scan rate CVs. For a one-step reaction, the peak potential follows [20]:

$$E_P = E^O - \frac{RT}{\alpha F}[0.780 + \ln\left(\frac{D_O^{\frac{1}{2}}}{k^0}\right) + \ln(\frac{\alpha F \upsilon}{RT})^{1/2}] \qquad \text{Equation 2.2.2-3}$$

where R is the ideal gas constant, F is Faraday's constant, and α is the transfer coefficient. Equation 2.2.2-3 can be simplified to:

$$E_P - E^O = -\frac{RT}{2\alpha F}\ln(v) + C \qquad \text{Equation 2.2.2-4}$$

where C is a constant. Plots of E_P-E^O versus $\ln(v)$ can be used to determine α. For an irreversible reaction, Equation 2.2.2-3 can be converted to:

$$i_P = 0.227FACk^0 e^{[-\frac{\alpha F}{RT}(E_P - E^O)]} \qquad \text{Equation 2.2.2-5}$$

where C is the bulk concentration of the active species. The intercept of a plot of $\ln(i_P)$ versus E_P-E^O will be proportional to k^0. For quasireversible reactions, assuming the diffusion coefficients of the oxidized and reduced species are equal, the Nicholson Method can be used to determine the kinetic rate constants, which utilizes a dimensionless parameter defined as [63]:

$$\psi = \frac{k^0 RT}{(\pi D_O F v)^{\frac{1}{2}}} \qquad \text{Equation 2.2.2-6}$$

ψ is found using a correlation curve between ψ and $E_{pc} - E_{pa}$. It is important to note that the Nicholson Method is valid for redox couples with a transfer coefficient between 0.3-0.7 [63].

For these experiments, CV was performed using a PGSTAT302N Autolab Potentiostat and a 600D CH Instruments Potentiostat, with a 10 mL, three electrode

electrochemical cell, fabricated in-house. The three electrodes consisted of a 0.07 cm^2 glassy carbon disk working electrode (BASi), a fritted Ag/Ag+ quasi-reference electrode (BASi) filled with 0.01 M silver tetrafluoroborate in ACN (98%, Sigma Aldrich), and a 23 cm long coiled platinum wire counter electrode (ALS). The working electrode was polished using 9 and 0.3 μm aluminum oxide polishing paper (Fiber Instrument). All tested solutions consisted of 0.01M (or max solubility, if lower than 0.01M) active species with 0.1M tetrabutylammonium tetrafluoroborate (TBABF$_4$) (≥99%, Aldrich) dissolved in anhydrous ACN (Fisher), which were prepared in an Ar-filled MBraun glove box. All commercially available active materials were purchased from Sigma Aldrich and used without further purification, and the remaining complexes were synthesized by the Sanford group at the University of Michigan.

2.2.3 Charge-Discharge Battery Characterization [64]
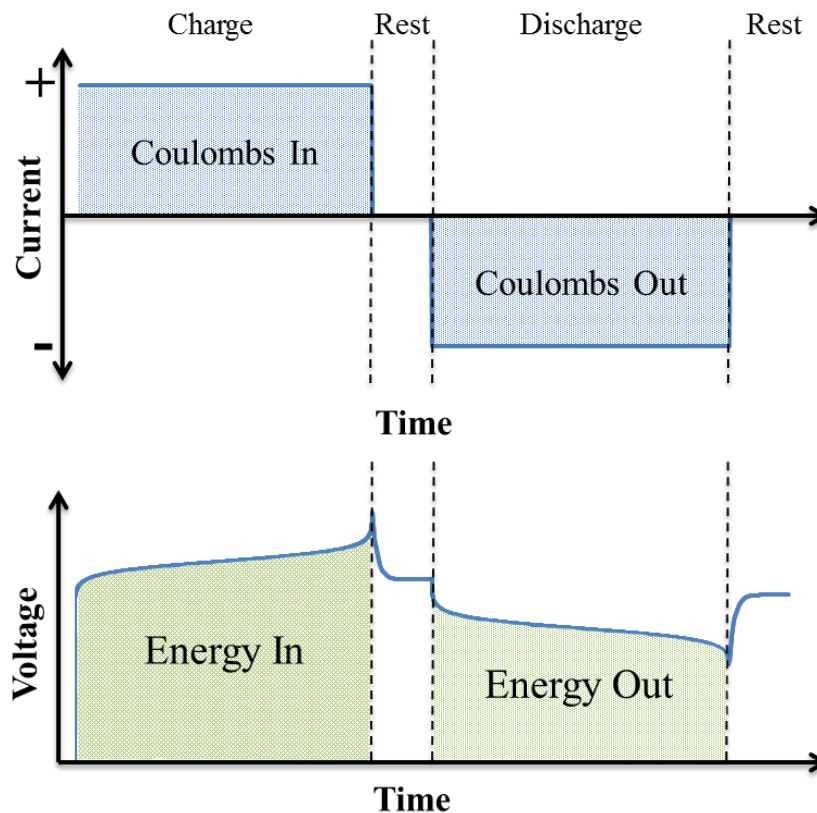
Figure 2.2.3-1 Example Charge-Discharge Input (top) and Discharge (bottom)

Charge-Discharge is an electrochemical method which measures either the current or voltage between two electrodes which is a function of a held potential (chronoamperometry) or current (chronopotentiometry) respectively. The electrodes are much larger than that used in CV, as the bulk electrolyte is meant to be electrolyzed [20]. For this study, charge-discharge experiments were conducted using chronopotentiometry. During charging, energy is inserted into the cell using a positive current, which results in an increasing cell voltage (Figure 2.2.3-1). During discharge, energy is extracted from the cell using a negative current, which results in a decreasing cell voltage. As shown in Figure 2.2.3-1, a brief rest period between charging and discharging is typically employed to allow for the open circuit potential (OCP) to be determined. The OCP is

important because it is the voltage between the two electrodes without an overpotential, and as such can be used to estimate the overpotential of the cell [20]. The number of electrons inserted and subsequently removed from the cell is used to calculate and track the theoretical percent state of charge (SOC). The SOC follows the equation:

$$\text{SOC (\%)} = \frac{it}{nCVF} * 100 \hspace{2cm} \text{Equation 2.2.3-1}$$

where i is the current, t is the time in seconds, and V is the cell voltage. Based on Equation 2.2.3-1, if all of the theoretical electrons have been inserted/extracted from the active material, it would result in a SOC of 100%. Furthermore, the SOC is commonly used as a cut-off to stop charging/discharging the cell. For these experiments, the SOC was monitored, but was not used as a cut-off parameter; instead, cut-off potentials were used to prevent overcharging.

A number of parameters can be determined from charge-discharge experiments including coulombic, voltaic, and energy efficiencies. The coulombic efficiency (CE) is a measure of the percentage of electrons inserted and subsequently extracted and is found using:

$$\text{CE} = \frac{\int_0^{t_d} i_d dt}{\int_0^{t_c} i_c dt} * 100 \hspace{2cm} \text{Equation 2.2.3-2}$$

where c and d denote charging and discharging, respectively. For experimental cells with a large distance between the two electrodes (large overpotential), the CE is the most important parameter as it is not effected by the overpotential. Cross-over, and side reactions, will both result in lower CE values. The voltage efficiency (VE) is a measure of inefficiencies due to overpotentials and is found using:

$$VE = \frac{\int_0^{t_d} V_d dt}{\int_0^{t_c} V_c dt} * 100 \qquad\qquad \text{Equation 2.2.3-3}$$

The energy efficiency (EE) is the CE multiplied by VE and is a measure of the energy loss of the cell, and is the most important parameter for commercial cells.
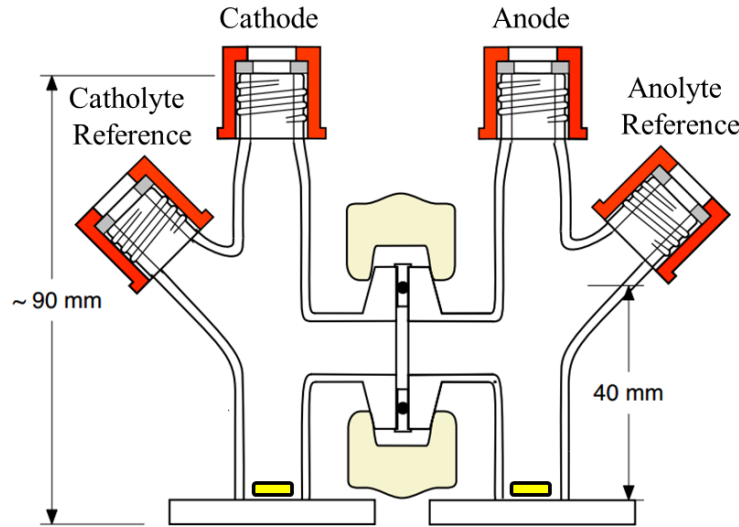
Figure 2.2.3-2 H-cell Schematic [27]

H-cells are commonly used for charge-discharge experiments because they are easily fabricated, set-up, and modified (both the cell itself, and components to be tested). An H-cell differs from a flow cell in that the electrolyte is not pumped but instead mixed using stir bars. This limits the use of high current densities due to mass transfer limitations, and H-cell testing using highly concentrated electrolytes at high current densities is not advised. The electrodes are also much further from each other in an H-cell, to accommodate the clamp used to connect both half cells together. This separation of the electrodes results in large overpotentials and charge-discharge results with low VE and EE are expected.

For this study, chronopotentiometry was first employed in an H-cell (Figure 2.2.3-2) to estimate how an active material would function in an RFB cell while using minimal electrolyte. The constant charging and discharging currents were 0.21 and 0.021mA/cm^2, respectively to match previous studies [34], [38]. The H-cell (Adams & Chittenden) half cells were separated by a Neosepta AHA membrane (Ameridia). These membranes were pre-conditioned in 0.1M tetrabutylammonium tetrafluoroborate ($\geq$99%, Aldrich) in ACN for at least 24hrs. The cell contained two ~6.4cm^2 graphite plate electrodes (McMaster Carr) and two PTFE micro-stir bars (Fisher). The catholyte and anolyte each consisted of 5ml of a solution of 0.05M of the redox active complex with 0.5M tetrabutylammonium tetrafluoroborate dissolved in anhydrous ACN (99.8% over sieves, Fisher). Electrochemical Impedance Spectroscopy (EIS), which is a technique commonly used to estimate the resistance between the electrodes of a flow cell [20], was carried out at frequencies ranging copy (EIS) was carried out at frequencies ranging from 0.1Hz–100kHz at the open cell potential using an AC potential perturbation of 10mV using a PGSTAT302N Autolab Potentiostat. The cell resistance was determined from the intercept of the real part of the impedance at high frequency. The EIS and charge–discharge experiments were performed inside an Ar-filled glove box.

2.2.4 Flow Cell Characterization

Flow cells consist of a cathode and an anode which is separated by a membrane, and the fuel/electrolyte is pumped into the cell from external reservoirs. In the case of fuel cells, the fuel is used to generate electricity, and the process is not reversible [65]. In flow batteries, during charging, the electrolyte is reduced at the anode and oxidized at the cathode, and the resulting electrolyte is pumped back into the external reservoirs. The

opposite reaction occurs during discharge [7]. The electrodes are extremely close to each other to minimize overpotentials due to solution resistance, and thus, energy efficiency values are expected to be much higher than in H-cell experiments [65]. Because flow cells are closed systems, reference electrodes are typically not utilized, and the potential of the cell is monitored rather than the potential of an individual electrode. This makes it difficult to characterize individual half-reactions. Despite limited in situ characterization, flow cells are versatile in that they can be modified to the specific application, and the overall rate of reaction can be controlled by increasing the size of the flow cell, or adding several cells in parallel. This allows for laboratory studies which utilize relatively small flow cells to acquire data which is relevant to commercial-sized systems [65].

After screening two interesting complexes using an H-cell (complexes **18** and **20**), the most promising complex (**20**) was tested in a custom flow cell developed in the Savinell group at Case Western Reserve University (Figure 2.2.4-1). The cell utilized a standard flow-through electrode configuration, with graphite felt SGL GFA 3.0 (3mm thickness, SGL group) electrodes with a geometric area of ~5.65cm^2. Two separators were used, a tetraethylammonium cation (TEA$^+$) exchanged Nafion® 1035 membrane (EW of 1000g/mol, 89μm nominal thickness, Alfa-Aesar), and a Daramic separator (250μm thickness, Daramic LLC). Membrane preparations followed literature methods [41], [66], [67]. TEA$^+$ exchanged Nafion® 1035 was equilibrated in a 0.5MTEABF$_4$ (99%, Fluka) in ACN (99.8%, Aldrich) solution for at least 5 days. Daramic 175 SLI flat sheet microporous separator (250μm thickness, Daramic LLC) was cleaned in methanol, dried in a vacuum oven at 80^OC overnight, then transferred into a N$_2$-filled glove box. Finally, it was soaked in a solution of 0.5M TEABF$_4$ in ACN for at least 5 days. Daramic

175 SLI separator has an average pore size of 0.1μm and a porosity of 58%. After cell assembly, the electrode compression was approximately 20%. Prior to cell assembly, the electrodes were soaked in the test electrolyte for 2hrs. The catholyte and anolyte each consisted of 25ml of a solution of 0.1M active speices with 1M tetraethylammonium tetrafluoroborate (99%, Aldrich) dissolved in anhydrous ACN. The electrolyte was delivered to each cell compartment at 25ml/min by means of a peristaltic pump (Masterflex Mod. 77800, Cole-Parmer®) with two heads. Charge-discharge battery cycles were performed at constant current density of 10mA/cm^2 with cut-off potentials between 1V and 2.3V. EIS was carried out at frequencies ranging from 0.1Hz-250 kHz at the open cell potential bias using an AC potential perturbation of 10mV. Before EIS measurements, the flow cell was resting at the open circuit cell potential for 1.5min. The flow cell resistance value is reported as the intercept of the real part of the impedance at high frequency. A Solartron SI 1287A potentiostat/galvanostat coupled with a Solartron 1260 impedance/gain phase analyzer were employed to conduct the battery cycle testing and EIS measurements. The flow cell was assembled and tested under a N$_2$-controlled atmosphere.
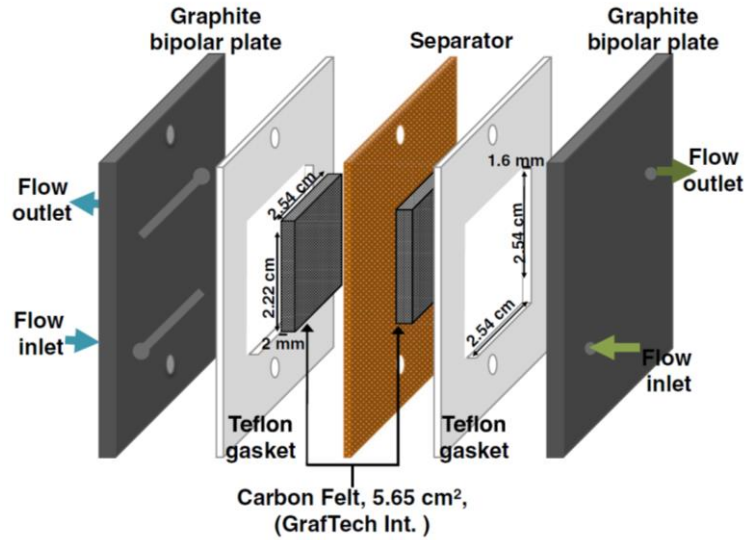
Figure 2.2.4-1 Flow Cell Schematic

2.2.5 Density Functional Theory Calculations

Density functional theory (DFT) is the most widely used method for electronic structure calculations, primarily due to an unparalleled balance between computational expense, and accuracy [68]. DFT, in simple terms, is an approximation of the general Schrödinger equation which follows [69]:

$$H\Psi = E\Psi$$ Equation 2.2.5-1

where H is the Hamiltonian operator, Ψ is the wavefunction, and E is the energy. The wavefunction is generated by the positions of every electron and nuclei in a system. Thus, an electron is described as a wave, and its probable location described by a molecular orbital [69]. For very simple systems (H-atom, 2-D square potential, etc.) an analytical solution to the Schrödinger equation is possible, but for more complex systems, the quantum mechanical wavefunction does not have an analytical solution [68]. Even for just a single oxygen atom, the full wavefunction consists of 10^{24} bytes, or 10^{12} terabytes of data [70]. A number of methods to simplify the Schrödinger equation have been

39

proposed such as the Born-Oppenheimer and Hartree-Fock approximations [71], [72], but the theorem which made the most effective simplification was discovered by Hohenburg and Kohn in 1964, which demonstrated that the electron density, alone, determines the Hamiltonian operator, and therefore the energy of the system [73], [74]. As the energy of the system is a function of the electron density, which is a function of time and space, and as the function of a function is defined as a functional, density functional theory was born [70].

A number of different DFT methods are available because there are numerous approximations for generating molecular orbital shapes (referred to as basis sets) and density functionals (commonly referred to as functionals). Basis sets are comprised of a series of functions typically consisting of gaussian type orbitals (commonly referred to as gaussians) used to describe molecular orbitals, and hundreds are currently available [68]. These range from minimal sets such as STO-nG, where only one basis function comprised of n gaussians is used, to double-zeta basis sets, or even triple-zeta basis sets. Double-zeta basis sets utilize two basis functions and follow the form: X-YZG, where X is the number of core electron gaussians, Y is the number of valence electron gaussians in the first basis function, and Z is the number of valence electron gaussians in the second basis function [68]. For these calculations, the 6-31G(d) double-zeta basis set was primarily utilized, which means that six core electron gaussians, three valence gaussians for the first basis function, and one valence gaussian for the second basis set was used. "(d)" denotes that a polarization function is also being used which accounts for angular momentum in the orbitals, which has been shown to more accurately simulate electron densities in bond sites [75]. The 6-31G(d) basis set is only suitable for elements up to

first row transition metals, so a combination of 6-31G(d) with LANL2DZ (Los Alamos National Laboratory 2-double-z) basis sets were used for DFT calculations involving second row transition metal complexes. LANL2DZ is a double-zeta basis set which is routinely used for second row transition metal calculations, and has been used effectively to optimize various ruthenium based MCCs [76]–[80].

There are also many functionals to choose from, ranging from local density approximation based functionals, which rely purely on DFT approximations, to hybrid functionals which use a combination of DFT and Hartree-Fock wavefunction (H-F) theory. Hybrid functionals are much more accurate in that H-F theory still relies directly on the many-body wavefunction with the electron density approximation of DFT, which obviously increases computational time [81]. For these studies, the B3LYP (Becke, three-parameter, Lee-Yang-Parr) hybrid functional was utilized [82].

2.2.5.1 Standard Potential Calculations

Based on literature results presented herein, for all DFT calculations, the B3LYP functional with 6-31G(d) basis set (and LANL2DZ for Ru complexes) was used to optimize each ground-state structure in a vacuum, followed by single point solvent calculations using a Polarizable Continuum Model (PCM, discussed in Section 2.2.5.3). All structures were confirmed to be minimum energy structures using vibration frequency calculations [68]. The Gaussian 09 software package was used for all DFT calculations [83].

$$\text{MCC(g)} \quad + \quad ne^- \quad \xrightarrow{\Delta G_{red}^{g}(\text{MCC})} \quad \text{MCC}^{n-}(g)$$

$$\Delta G_{solv}(\text{MCC}) \quad \Bigg\downarrow (0) \qquad\qquad \Delta G_{solv}(\text{MCC}^{n-}) \Bigg\downarrow$$

$$\text{MCC(sol)} \quad + \quad ne^- \quad \xrightarrow{\Delta G_{red}^{sol}(\text{MCC})} \quad \text{MCC}^{n-}(sol)$$
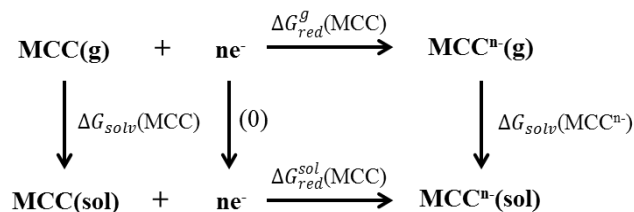
Figure 2.2.5-1 Thermodynamic cycle for calculating the reduction potential of a given MCC, where n is the number of electrons transferred.

$$\text{MCC(g)} \quad \xrightarrow{\Delta G_{ox}^{g}(\text{MCC})} \quad \text{MCC}^{n+}(g) \quad + \quad ne^-$$

$$\Delta G_{solv}(\text{MCC}) \Bigg\downarrow \qquad \Delta G_{solv}(\text{MCC}^{n+}) \Bigg\downarrow \quad \Bigg\downarrow (0)$$

$$\text{MCC(sol)} \quad \xrightarrow{\Delta G_{ox}^{sol}(\text{MCC})} \quad \text{MCC}^{n+}(sol) \quad + \quad ne^-$$
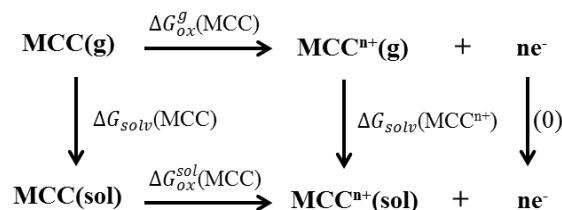
Figure 2.2.5-2 Thermodynamic cycle for calculating the oxidation potential of a given MCC, where n is the number of electrons transferred.

Theoretical standard potentials for reduction and oxidation reactions can be calculated from the thermodynamic cycle using DFT optimized ground-state structures (Figure 2.2.5-1 and Figure 2.2.5-2, respectively) [84], [85]. Ideally, to determine the oxidation/reduction standard potential, the neutral and oxidized/reduced structure would be optimized in a vacuum and in solution, with thermal corrections considered in each optimization. This can be computationally expensive, with frequency calculations required for each structure, and implicit solvent molecules dramatically increasing the number of electrons to consider. Furthermore, literature results using the B3LYP functional with 6-31+G(d) basis set have been shown to be effective at calculating the standard potentials of >1400 organic species using the thermodynamic cycle [84] by assuming minimal entropic differences after reduction/oxidation, and no structural changes from vacuum to solution phases. Computational expense was further reduced by using a Polarizable Continuum Model (PCM, discussed in Section 2.2.5.3) for solvent calculations. The same assumptions were made for similar thermodynamic cycle

calculations for ionic liquids [86], fluorine containing anions [87], nitroaromatic compounds [88], ether-based solvents [89], and functionalized organic benzene complexes [90], all demonstrating good agreement between experimental and theoretical results. Figure 2.2.5-3 shows that the calculated oxidation potentials in the gas phase for a number of benzene-functionalized complexes utilizing a number of different basis sets all closely match the experimental oxidation standard potentials. Results were also presented showing PCM solvation calculations to be highly accurate for the same complexes [90].
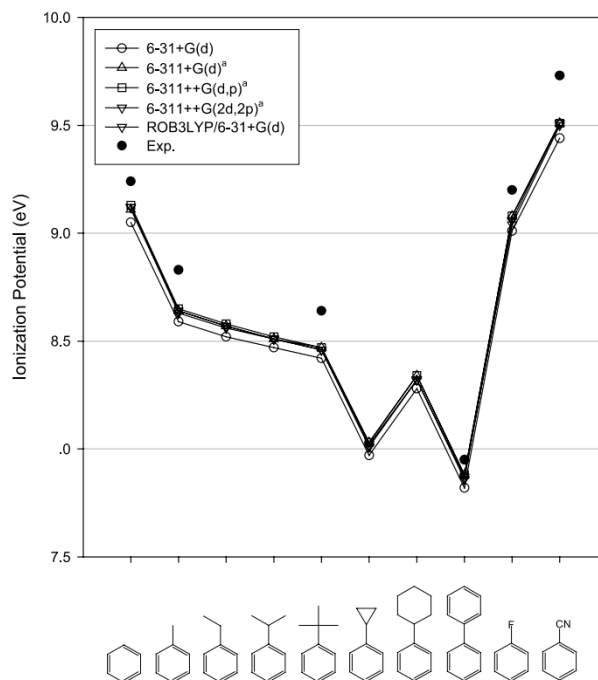
Figure 2.2.5-3 Calculated ionization potentials (ΔG_{ox}^{g}) for functionalized benzene complexes [90].

The standard potentials were calculated following the thermodynamic cycles (Figure 2.2.5-1 and Figure 2.2.5-2) [84], [85]:

$$\text{Reduction: } E^{O} = -\frac{\Delta G_{red}^{sol}}{nF} - 4.7825 \qquad \text{Equation 2.2.5-2}$$

$$\text{Oxidation: } E^O = \frac{\Delta G_{ox}^{sol}}{nF} - 4.7825 \qquad\qquad \text{Equation 2.2.5-3}$$

Where E^O is the standard potential in units of volts vs. Ag/Ag^+, n is the number of electrons, F is faradays constant, -4.7825 is a constant to convert to potential vs. Ag/Ag^+ calibrated using the experimental standard potential of ferrocene, ΔG_{red}^{sol} is the reduction free energy in solution, and ΔG_{ox}^{sol} is the oxidation free energy in solution. The free energies of reduction and oxidation are calculated following Equation 2.2.5-4 and Equation 2.2.5-5, respectively:

$$\Delta G_{red}^{sol}(MCC) = \Delta G_{red}^{gas}(MCC) + \Delta G_{solv}(MCC^{n-}) - \Delta G_{solv}(MCC) \qquad \text{Equation 2.2.5-4}$$

$$\Delta G_{ox}^{sol}(MCC) = \Delta G_{ox}^{gas}(MCC) + \Delta G_{solv}(MCC^{n+}) - \Delta G_{solv}(MCC) \qquad \text{Equation 2.2.5-5}$$

where ΔG_{red}^{gas} and $\Delta G_{ox}^{gas}(MCC)$ are the reduction and oxidation free energy in the gas-phase, respectively, $\Delta G_{solv}(MCC^{n-})$ is the free solvation energy of the reduced complex, $\Delta G_{solv}(MCC)$ is the free solvation energy of the neutral complex, and $\Delta G_{solv}(MCC^{n+})$ is the free solvation energy of the oxidized complex. While calculating the standard potentials using the thermodynamic cycle is faster than experimental determination, it would be advantageous to be able to correlate the standard potentials with the lowest unoccupied and highest occupied molecular orbitals (LUMO/HOMO), as LUMO/HOMO energies can be computed for the neutral complex. These types of correlations have already been demonstrated for quinoxaline based molecules [84]. As seen in Figure 2.2.5-4, strong correlations between the LUMO/HOMO energies and the standard potentials were demonstrated ($R^2 > 0.9$). The possibility of using the same correlation for MCCs has not been tested.
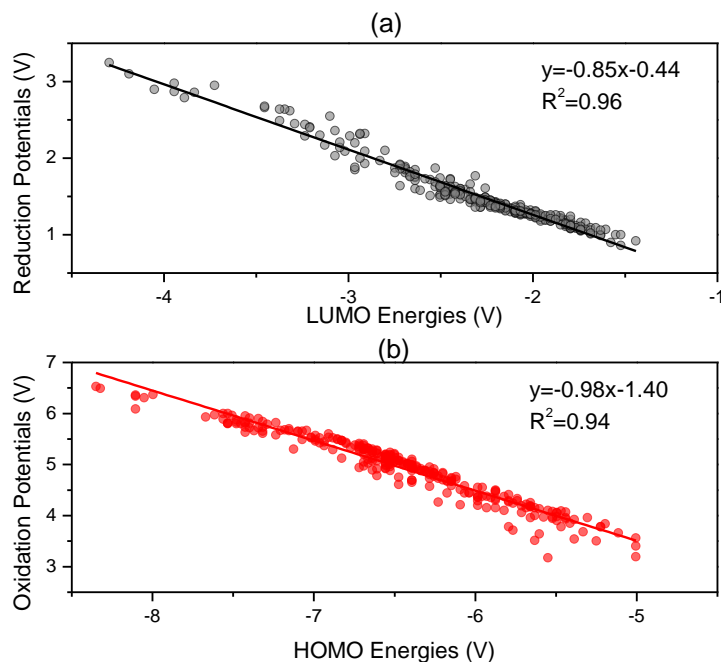
Figure 2.2.5-4 Correlations between reduction potentials and LUMO energies (a) and oxidation potentials and HOMO energies of quinoxaline derivatives [84].

2.2.5.2 Solubility Calculations

Solubilities can be calculated thermodynamically following Figure 2.2.5-5 [91]:

$$\Delta G_{sol} = \Delta G_{sub} + \Delta G_{solv} = -RT ln S_O V_m \qquad \text{Equation 2.2.5-6}$$

where ΔG_{sol} is the free energy for solution, ΔG_{sub} is the sublimation free energy, ΔG_{solv} is the solvation free energy, R is the molar gas constant, T is temperature, S_O is the molar solubility, and V_m is the molar volume of the crystal.

$$\Delta G_{sol} = \Delta G_{sub} + \Delta G_{hydr} = -RT \ln S_o V_m$$
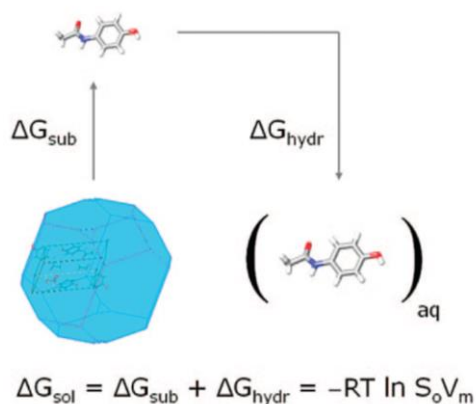
Figure 2.2.5-5 Thermodynamic cycle for solubility calculation of a molecule in water [91].

The solvation free energy can be readily calculated using ground state optimized structures which were used for calculating the standard potentials (solving for ΔG_{solv}(MCC), Figure 2.2.5-1). However, to calculate the molar solubility, a known crystal structure is required, and the sublimation free energy must be calculated. Without synthesizing the complexes, crystal structures are difficult to estimate, and defeat the purpose of predictive correlations. Calculating the sublimation energy is possible, but requires lattice dynamics simulations, which are computationally expensive. Finally, even if the calculations are performed, it has been shown that such calculations can have significant error, and regression models using parameters such as hydrophobicity, and solvation energy were able to yield more accurate predictive correlations for organic molecules in water [91]. For these studies, using the same DFT model system, the solvation energy was calculated for each neutral complex using a PCM for ACN. The solvation energy alone was found to be insufficient to model the solubility of each complex, and so the dipole moment of each complex was also calculated.

For vanadium(III) acetylacetonate, it has been shown that the polarity of the solvent dictates the solubility of the active material [35] governed by Hansen Solubility Parameter effects (like dissolves like, [21]), but similar studies have not been performed with regard to the polarity of the active material. The dipole moment of a complex is a quantifiable measurement of the polarity [92], and can be readily calculated using DFT methods, based on the charge distribution of the complex, and when combined with a PCM (Section 2.2.5.3) the dipole moment of a complex dissolved in a solvent can be estimated. There are a number of quantum mechanical models that can be utilized to estimate dipole moments, but hybrid basis sets were found to give the most reliable estimates of the dipole moments for a number of different organic molecules [93]–[95], and were therefore used in these studies to calculate the dipole moment of the ground-state neutral complexes.

2.2.5.3   Polarizable Continuum Models (PCM)

Polarizable continuum models are commonly used in computational chemistry studies and were designed to make predictions of free energies of solvation, while using substantially less computing power than explicit solvent models [96]–[98]. In continuum solvation models, the solute is placed in a molecular-shaped cavity, while the solvent is estimated as a dielectric continuum with no structure. The cavity is built as a series of connected spheres which are placed at the center of the atoms of the solute being studied (typically generated using van der Waals' radii) [99]. The polarization of the solute is estimated using the Poisson equation [100]. The polarization of the solute, when placed in the dielectric continuum, results in a reaction field (commonly referred to as the Onsager reaction field), which is used to determine the solvation free energy [101]. There

are many PCMs available: those that assume a homogeneous dielectric medium, a nonhomogeneous medium, or an anisotropic solvent medium [102]. For these studies, an integral equation formalism PCM was utilized, which allows for both homogeneous and non-homogeneous media to be studied, and is the standard method utilized in Gaussian 09 [83]. Furthermore it has been shown to be effective at studying charged species [84], [103].

2.3 Effect of Functional Group and Metal on Standard Potentials and Solubility

2.3.1 Approach

To isolate the effect of functional groups and metals on the solubility and electrochemistry of MCCs, the type of ligand was held constant. Acetylacetonate-based complexes were chosen as the acac ligand is considered to be "innocent" and metal acacs are the most widely studied MCCs for use in non-aqueous RFBs [28], [34]–[43], [53]–[55], [57], [58]. While these materials are well studied, no experiments have been performed to elucidate trends between different metals or functional groups and standard potentials and solubilities, and the use of functional groups has yet to produce an active species of comparable solubilities to aqueous electrolytes (e.g. 2M).

A complete list of the complexes investigated in this study can be seen in Figure 2.1-1. The complexes include unfunctionalized metal(III) acetylacetonates using first and second row transition metals (complexes **1-7**), and a series of functionalized chromium(III) and vanadium(III) acetylacetonate complexes (complexes **8-20**). Chromium(III) acetylacetonate is synthetically easier to work with, and was therefore used for most of the functional group investigations. To verify that similar effects are

observed for other metals, a functional group used to generate a highly soluble chromium(III) based complex (**18**) was used to functionalize vanadium(III) acetylacetonate (complex **20**). Vanadyl(IV) acetylacetonate (complex **21**) was also included as it is reported to be a side product during the oxidation of complex **1**. Finally, ferrocene (complex **22**), a well-studied MCC with an "innocent" ligand and highly reversible electrochemistry was used as a standard for diffusion and kinetic constants comparisons [20], [44]–[52].

CV was used to first investigate the effect that the metal and functional group have on the electrochemistry as indicated by differences in standard potentials and reversibility assessed using current peak height ratios. This part of the research follows the procedure described in Section 2.2.2. To quantify the effect on the electrochemistry and generate predictive trends for the design of next-generation materials, DFT structure optimization calculations are also performed. Next, solubilities were quantified using a UV-Vis method (Section 2.2.1) and a regression analysis was used to correlate the experimental values to the DFT-calculated solvation energies and dipole moments.

Another important property for the active species in an RFB is the diffusion coefficient. The diffusion coefficient will impact the power density that can be achieved. Adding substituents to the acetylacetonate ligand is expected to negatively impact the diffusion coefficient, based on the Stokes-Einstein equation [104]. This could result in reduced transport rates and could ultimately limit power densities for the associated RFBs [104]. Therefore, the impact of the metal and functional group on the diffusion coefficient and kinetic rate constant was also evaluated.

2.3.2 Results: Standard Potentials

A widely-used time semi-derivative method was used to deconvolute the CVs, and the reversibility of each couple was estimated using the current peak height ratios (i_c/i_a or i_a/i_c) [105], [106].
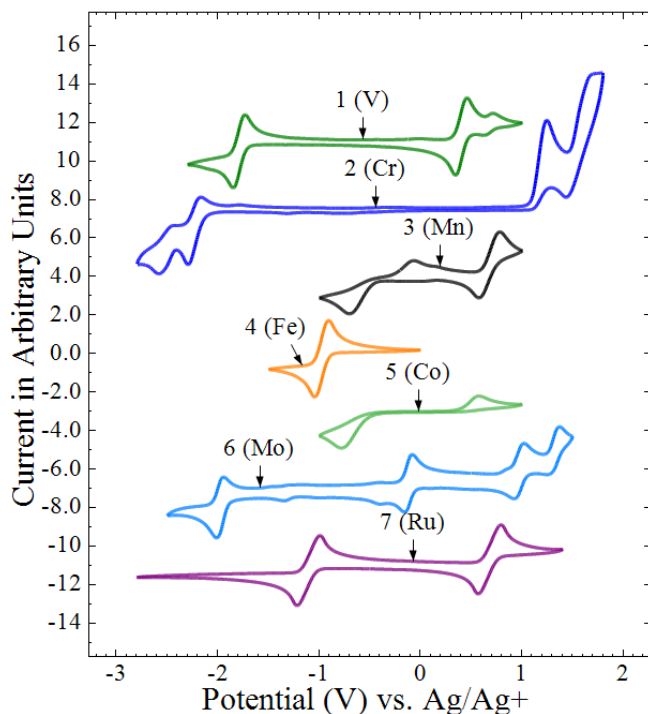
Figure 2.3.2-1 Cyclic voltammograms of parent metal(III) acetylacetonate complexes (**1-7**). Solutions comprised of 0.01M active species with 0.1M TBABF$_4$ in acetonitrile.

Table 2.3.2-1 Electrochemical data for metal(III) acetylacetonate complexes **1-11** and **15-20**. Values in parenthesis are peak height ratios of the respective couple. The peak height ratio is i_c/i_a or i_a/i_c (whichever results in a value less than 1).

Complex	Metal Type	E^1 [V vs. Ag/Ag$^+$]	E^2 [V vs. Ag/Ag$^+$]	E^3 [V vs. Ag/Ag$^+$]	E^4 [V vs. Ag/Ag$^+$]
1	V	-1.79 (0.97)	0.40 (0.98)	-	-
2	Cr	-2.51 (0.45)	-2.24 (0.58)	1.17 (0.25)	1.54 (0.57)
3	Mn	-0.64 (0.19)	0.68 (0.81)	-	-
4	Fe	-0.97 (0.99)	1.26 (0.22)	-	-
5	Co	-0.09 (0.58)			
6	Mo	-1.98 (0.73)	-0.12 (0.83)	0.98 (0.98)	1.33 (0.62)
7	Ru	-1.11 (0.99)	0.68 (0.99)	-	-
8	Cr	-2.17 (0.20)	-1.75 (0.16)	1.28 (0.27)	1.57 (0.32)
9	Cr	-2.44 (0.77)	-	-	-
10	Cr	-2.23 (0.36)	-1.96 (0.32)	1.27 (0.26)	1.61 (0.44)
11	Cr	-2.45 (0.57)	-2.21 (0.59)	-	-
12	Cr	-2.46 (0.79)	-2.13 (0.75)	-1.63 (0.99)	1.23 (0.13)
13	Cr	-2.19 (0.92)	-1.69 (0.93)	1.20 (0.14)	1.61 (0.38)
14	Cr	-2.86 (0.25)	-1.73 (0.85)	1.22 (0.17)	1.68 (0.48)
15	Cr	-2.42 (0.27)	-2.19 (0.34)	0.98 (0.38)	1.39 (0.28)
16	Cr	-2.32 (0.19)	0.97 (0.34)	1.42 (0.25)	-
17	Cr	-2.42 (0.75)	-2.18 (0.45)	0.99 (0.30)	1.35 (0.40)
18	Cr	-2.41 (0.46)	-2.19 (0.30)	0.97 (0.38)	1.34 (0.26)
19	Cr	-2.43 (0.75)	-2.19 (0.42)	0.99 (0.34)	1.38 (0.38)
20	V	-1.88 (0.99)	0.23 (0.99)	-	-
21	V	-1.98(0.18)	0.68(0.79)		
22	Fe	0.11(0.99)	-		

The CV results for all tested complexes are summarized in Table 2.3.2-1. CVs of the parent complexes (**1-7**) are shown in Figure 2.3.2-1; the results indicate that changing the metal for these complexes has a significant impact on the electrochemistry, not only in terms of the standard potentials, but also the reversibility of the reactions (Table 2.3.2-1). Complex **1** (V) has two quasi-reversible couples separated by ~2.2V, with a minor couple at ~0.7V vs. Ag/Ag$^+$ as a result of VO(acac)$_2$ formation. This complex has been widely studied and results reported in this dissertation are similar to those results in the literature [34], [36], [39]–[42], [57]. Complex **2** (Cr) has four couples with limited

51

reversibility (peak height ratios range from 0.25 to 0.58), with the most negative and most positive couples separated by ~4V, which agrees with similar studies in the literature [38], [40]. Complex **3** (Mn) has two quasi-reversible couples separated by ~1.3V both with slow kinetics (peak separations greater than 200mV). Complex **3** (Mn) has been previously tested, with some reports showing increased kinetics for the reduction reaction [37], [107], and another showing similar results to those presented here [58]. Complex **4** (Fe) has one quasi-reversible couple at -1V vs. Ag/Ag$^+$ with relatively fast kinetics and a peak height ratio of 0.99; both agree with other studies [107], [108]. Complex **4** (Fe) also undergoes an irreversible oxidation at 1.26V. Complex **5** (Co) has one couple with a peak separation of over 1V and thus has very slow kinetics. Similar electrochemical results have been reported before, they were attributed to the slow kinetics for ligand shedding during reduction [107], [108]. Complex **6** (Mn) has four redox couples with reasonable current peak height ratios ranging from 0.62 to 0.98 with the most negative and most positive couples being separated by ~3.3V. As seen in Figure 2.3.2-1, a number of peaks due to side reactions are also present, making **6** (Mn) a non-ideal candidate for RFB applications. Complex 7 (Ru) has two quasi-reversible couples separated by ~1.8V with relatively fast kinetics and high reversibility. In previous studies, **7** (Ru) was shown to have two couples separated by ~2V, with peak height ratios of close to unity [104], [107].
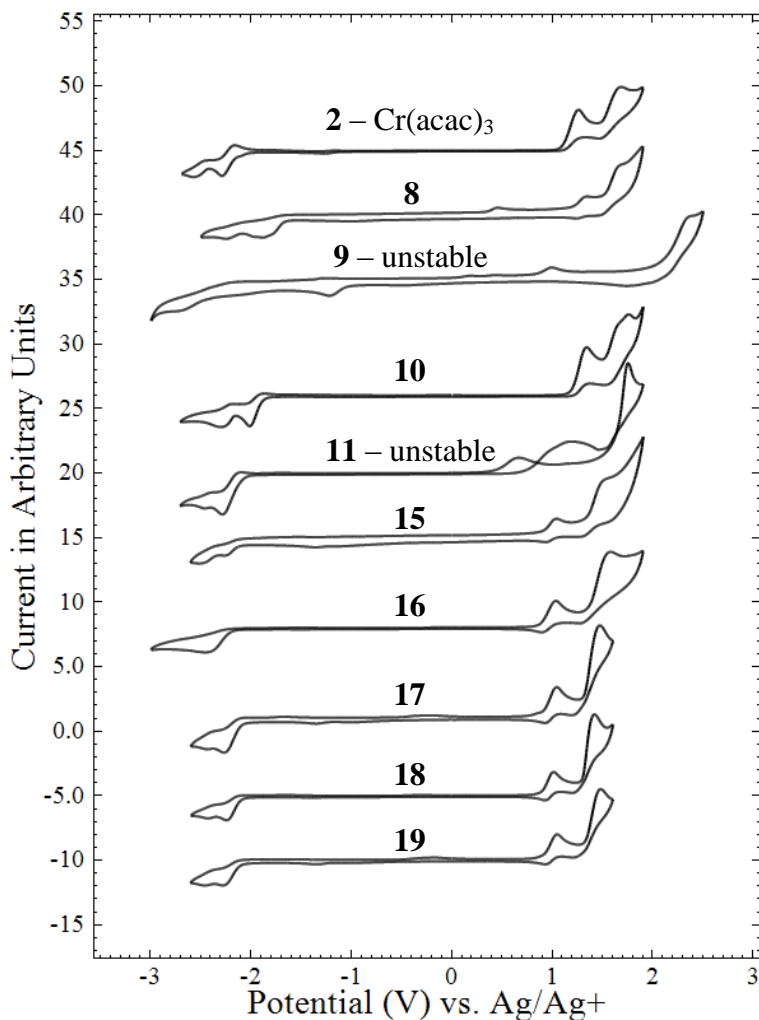
Figure 2.3.2-2 Cyclic voltammograms of functionalized chromium(III) acetylacetonate complexes. Solutions comprised of 0.1M TBABF$_4$ in acetonitrile with varying concentrations of active species based on solubility and availability. Concentrations of active species are as follows: **2**-0.01M, **8**-0.001M, **9**-0.001M, **10**-0.01M, **11**-0.01M, **15**-0.001M, **16**-0.01M, **17**-0.01M, **18**-0.01M, and **19**-0.01 M.

As seen in Table 2.3.2-1 and Figure 2.3.2-2 (complexes **2, 8-11, 15-19**), varying the substituent on the acac ligand has a minor impact on the electrochemistry as long as the resulting complex is stable. Electrochemical characterization of complex **9** shows no redox couples at positive potentials, while only one negative couple is apparent, with slow kinetics (~300 mV peak separation). A previous report of the electrochemical behavior of complex **9** made no mention of slow kinetics; furthermore, an additional

redox couple was mentioned in the prior report but was not observed in the current experiments [109]. Complex **11** shows similar electrochemical behaviour to complex **2** at negative potentials, but there is evidence of side reactions at positive potentials. The other Cr(III) complexes (**8, 10, 15-19**) show electrochemical properties very similar to those of the parent complex **2**, with small shifts in the potentials from complex to complex.

Figure 2.3.2-3 Cyclic voltammograms of vanadium complexes **1** (top) and **20** (bottom). Solutions comprised of 0.01M active species with 0.1M TBABF$_4$ in acetonitrile.

As seen in Figure 2.3.2-3, similar results are observed when complex **1** (V) was functionalized; the redox couples for the resulting complex **20** are shifted to more negative potentials by ~260 mV relative to those of **1**, but the available electrochemical windows (i.e., possible battery cell potentials) for **1** and **20** are nearly identical, at 2.19 and 2.11 V, respectively, and the current peak height ratios are all >0.97.
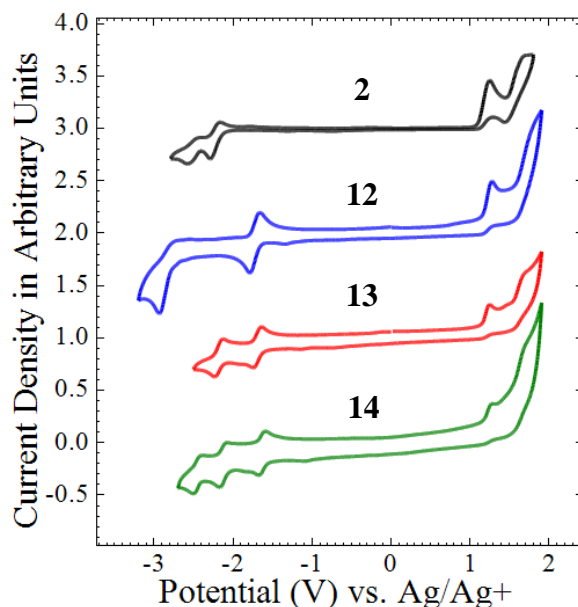
Figure 2.3.2-4 Cyclic voltammograms of 0.01M **2** (black), 0.00014M **14** (green), 0.001M **13** (red) and 0.001M **12** (blue) with 0.1M TBABF$_4$ in acetonitrile.

A previous study of **12** using polarography showed that this complex displays additional redox couples relative to **2**, which we hypothesize are due to redox active functional groups [109]. The heteroleptic complexes **13** and **14** allowed us to assess the extent of this effect. The cyclic voltammetry (Table 2.3.2-1, Figure 2.3.2-4), shows a direct correlation between the number of diphenyl functional groups in the metal complex and the number of additional redox events. Furthermore, these additional redox couples appear to be much more reversible (i_c/i_a closer to unity) than the couples of the parent complex (**2**) and could provide a pathway toward increasing the reversibility of complexes with wide voltage windows, but limited reversibility. However, the incorporation of each redox active phenyl-moiety has an incremental deleterious effect on complex solubility (Section 2.3.3), with complex **12** exhibiting the lowest solubility reported herein. Nevertheless, redox-active functional groups provide a potentially

attractive method for increasing RFB energy density if more soluble ligand motifs can be identified.
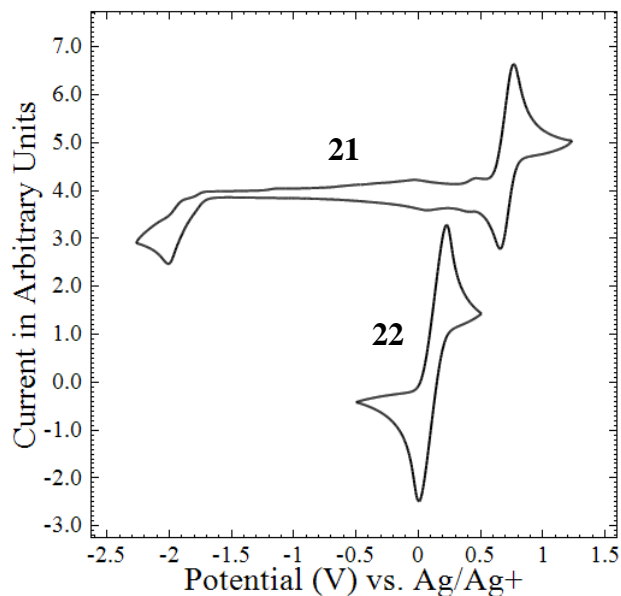
Figure 2.3.2-5 Cyclic voltammograms of complexes **21** (top) and **22** (bottom). Solutions comprised of 0.01M active species with 0.1M TBABF$_4$ in acetonitrile.

As previously described, complex **21** (VO) is a known side product of the oxidation of Complex **1**, so the electrochemistry was also characterized by CV. As seen in Figure 2.3.2-5, **21** has one couple with limited reversibility (peak height ratio = 0.79) at ~0.7V vs Ag/Ag$^+$, and irreversibly reduces at -2.0V vs. Ag/Ag$^+$, which matches data in the literature [36]. Ferrocene and functionalized ferrocene complexes have been shown to have one highly reversible couple, which yields high cycle lives in non-aqueous solvents, and the diffusion and kinetic constants of native ferrocene are well known [20], [46]–[52]. For this study, **22** was found to have one redox couple with high reversibility, at ~0.1V vs. Ag/Ag$^+$.

After experimentally measuring the standard potentials, theoretical standard potentials for complexes **1-4, 7, 18, 20-22** were determined using DFT structure

optimization calculations following the thermodynamic cycle. Complexes **5, 6,** were excluded due to their extremely slow redox kinetics. The functionalized Cr(acac)$_3$ complexes (**8-17,19**) were also excluded from the calculations as the standard potentials are very similar and calculations at each charge state are computationally expensive. All of the optimized structures can be found in Appendix A. The free energy of reaction for each complex can be seen in Table 2.3.2-2. The free energy of reaction values were then converted to standard reduction and oxidation potentials following Equation 2.2.5-2 and Equation 2.2.5-3, respectively (Table 2.3.2-3).

Table 2.3.2-2 Theoretical free energy of reactions from DFT optimized structures.

Complex	Metal Type	ΔG_{red2}^{sol} [kcal/mol]	ΔG_{red}^{sol} [kcal/mol]	ΔG_{ox}^{sol} [kcal/mol]	ΔG_{ox2}^{sol} [kcal/mol]
1	V	-	-65.7	111.1	-
2	Cr	-68.1	-51.1	133.3	279.3
3	Mn	-	-88.9	114.5	-
4	Fe	-	-83.7	134.0	-
7	Ru	-	-83.7	121.3	-
18	Cr	-62.1	-44.4	126.7	266.5
20	V	-	-61.6	106.0	-
21	V	-	-54.3	125.7	-
22	Fe	-	-	115.7	-

Table 2.3.2-3 Theoretical standard potentials from DFT optimized structures.

Complex	Metal Type	E^1 [V vs. Ag/Ag$^+$]	E^2 [V vs. Ag/Ag$^+$]	E^3 [V vs. Ag/Ag$^+$]	E^4 [V vs. Ag/Ag$^+$]
1	V	0.03	-1.94		
2	Cr	1.00	-2.57	1.55	-3.31
3	Mn	0.18	-0.93		
4	Fe	1.03	-1.15		
7	Ru	0.48	-1.16		
18	Cr	0.71	-2.86	1.28	-3.44
20	V	-0.19	-2.11		
21	V	0.66	-2.43		
22	Fe	0.23			

A parity plot of the calculated standard potentials versus the experimental values can be seen in Figure 2.3.2-6. There is good agreement between the theoretical and experimental values (R^2=0.92), with a slight negative deviation at more negative potentials. This is mainly due to a small error for the first reduction of complexes **1** and **18** which is compounded when calculating the second reduction standard potential. The strong R^2 value indicates that the free energy of the reduction or oxidation reaction is what dictates the standard potential values for these complexes, and by changing the metal, the free energy changes significantly, while changing the functional group has a minimal impact. The strong correlation also indicates that this method is very accurate and could be used to determine the voltage window of an unknown acetylacetonate complex. This would allow for screening of theoretical complexes without the need to synthesize the complexes, thereby reducing the cost and required time.
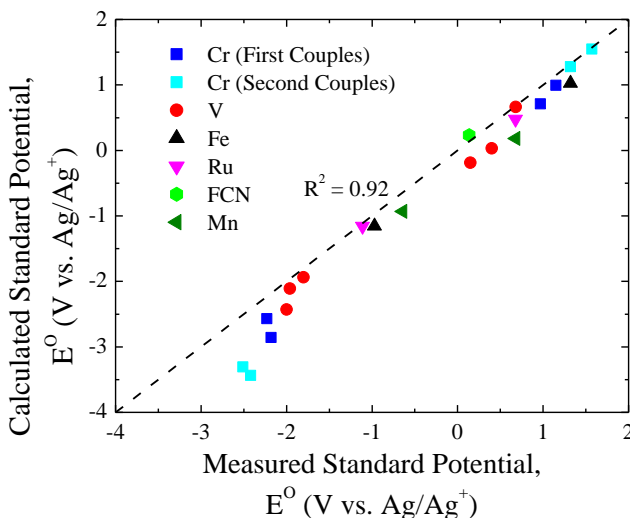
Figure 2.3.2-6 Standard potential prediction by the thermodynamic cycle

As previously discussed in Section 2.2.5.1, correlations have been developed between the LUMO/HOMO and standard potentials for a number of organic species [84].

Therefore, LUMO and HOMO energies were quantified for all of the complexes in Figure 2.1-1 with the exception of complexes **5**, **6**, **9**, and **11-14**. These complexes were not included due to a combination of instabilities, slow kinetics, or minimal solubilities. Complex **6** was not included as the structure could not be successfully optimized using DFT. The individual molecular orbital values can be seen in Table 2.3.2-4.

Table 2.3.2-4 Theoretical molecular orbital energies from DFT optimized structures.

Complex	Metal Type	LUMO of MCC^{-1}(sol) [Hartrees]	LUMO of MCC(sol) [Hartrees]	HOMO of MCC(sol) [Hartrees]	HOMO of MCC^{+1}(sol) [Hartrees]
1	V		-0.0854	-0.2007	
2	Cr	-0.0359	-0.0729	-0.2253	-0.2518
3	Mn		-0.0999	-0.2154	
4	Fe		-0.1159	-0.2312	
7	Ru		-0.1188	-0.2077	
8	Cr		-0.0858	-0.2256	
10	Cr		-0.0763	-0.2261	
15	Cr		-0.0683	-0.2122	
16	Cr		-0.0693	-0.2134	
17	Cr		-0.0687	-0.2115	
18	Cr	-0.0299	-0.0693	-0.2135	-0.2336
19	Cr		-0.0691	-0.2131	
20	V		-0.0491	-0.2123	
21	V		-0.0756	-0.2338	
22	Fe		-0.0107	-0.2000	

As seen in Figure 2.3.2-7, the LUMO and HOMO energies have a strong correlation to the experimentally determined standard potentials (R^2=0.97). This is true even for complexes with multiple reductions and oxidations. The strong correlation also indicates that these calculations are suitable for a number of different functional groups. By using this correlation, the first reduction and first oxidation potentials can be calculated by optimizing just the neutral species. This dramatically decreases the computational expense as the oxidized or reduced structures are not required, and can

also increase the accuracy of the calculations for reduced/oxidized complexes with significantly different entropies. Complex **22** (ferrocene), the only non-acetylacetonate based complex, also fits the correlation curve well. Our original hypothesis was that such a correlation would have minimal error for complexes with similar structures, but these results indicate that the correlation may be suitable for other types of MCCs. This is further investigated in Chapter 5.
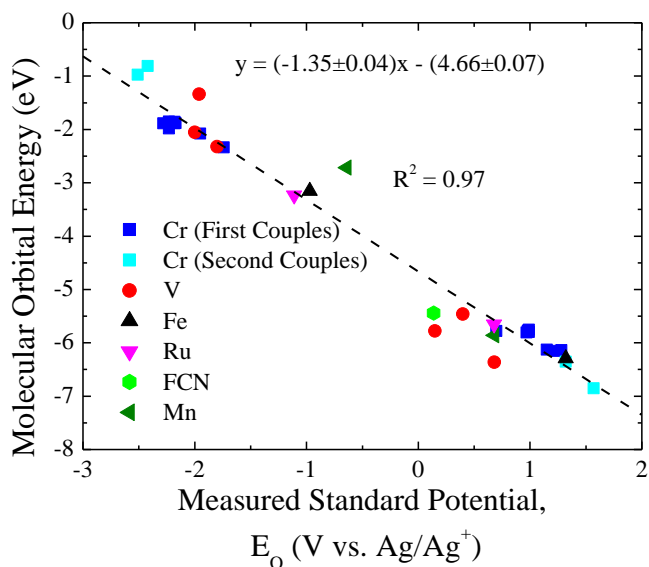
Figure 2.3.2-7 Correlation between orbital energy and standard potential

Based on these results, the standard potentials are therefore dictated primarily by the metal, with the metal directly impacting the LUMO and HOMO energies. For the screening of future complexes, high energy LUMOs and low energy HOMOs would maximize the cell potential.

2.3.3 Results: Solubilities
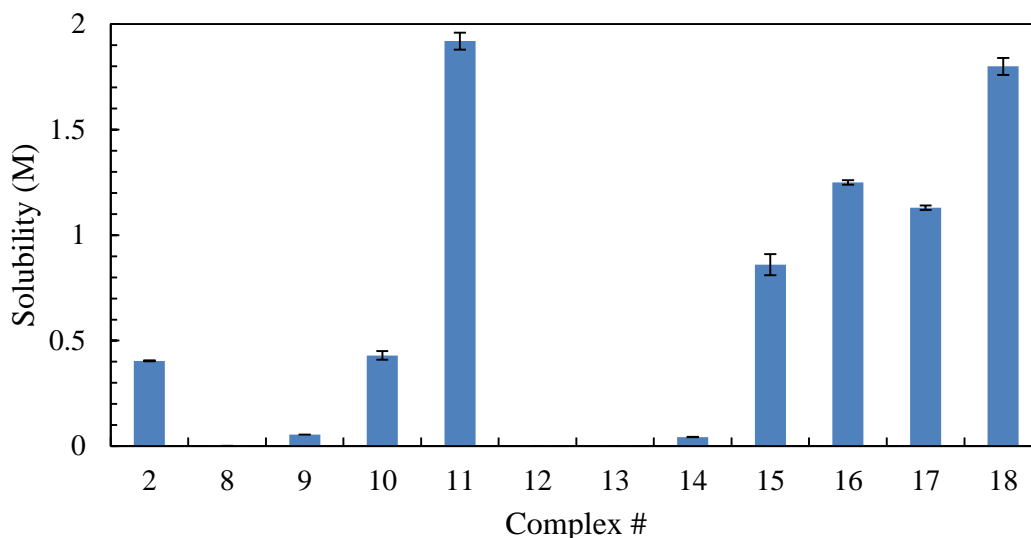
Figure 2.3.3-1 Solubilities of chromium(III) acetylacetonate based complexes (**2**, **8-18**) in acetonitrile.

To elucidate solubility trends, the results for all chromium based complexes (**2, 8-19**) were compared, and can be seen in Figure 2.3.3-1. The parent $Cr(acac)_3$ (**2**) has a solubility of 0.40M, which is consistent with what has been reported in the literature [38]. The incorporation of Br, NO_2, or phenyl substituents on the acetylacetonate ligand has a deleterious effect on the solubility of the corresponding Cr complexes (**8**, **9**, and **12-14**). The addition of a $-CH_2NMe_2$ group at the 3-position (**10**) dramatically enhances the solubility (to 1.92M) [110]; however, this ligand renders the complex unstable (Section 2.3.2). Finally, complexes bearing ester-substituted ligands (**15-18**) show significant enhancements in solubility relative to the parent complex (**2**). The improvements in solubility can be attributed to both the reduction in crystallinity of **15-18**, as they exist at room temperature as highly viscous tars or oils, and the increased incorporation of polar functional groups, such as esters and ethers, which are more miscible with polar solvents such as ACN. DFT results will be used to rationalize the experimental results. Most

dramatically, the complex bearing the 2-methoxyethyl-substituted ester (**18**) is a highly viscous oil with a solubility of 1.8M in ACN. This solubility is ~4-fold higher than that of the parent complex (**2**).

Overall, these studies show that systematic substitution of the acac ligands leads to complexes with solubilities in ACN ranging over four orders of magnitude (5.7×10^{-5} to 1.92 M). Furthermore, these investigations provide insights into the influence of various functional groups on solubility. We anticipate that this latter information will be more broadly applicable to the development of novel redox active molecules for non-aqueous RFBs.

The high solubility and viscous nature of complex **18** led us to hypothesize that further extension of the ether chain would result in a metal complex that is a liquid at room temperature. Indeed, the 2-(2-methoxyethoxy)ethyl-substituted ester complex **19** is a high-viscosity liquid, and the addition of ACN merely serves to dilute this complex. As such, a solubility determination is not meaningful. This molecule (and derivatives thereof) holds promise for the development of high energy density, solvent-free chemistries for RFBs. It is important to note that these solubility measurements are for the neutral complexes. Solubilities for the complexes at different oxidation states will be further discussed in **Error! Reference source not found.**.

To verify that solubility trends hold true for different metals, complex **1** (V) was functionalized with the same 2-methoxyethyl-substituted ester functional group used to increase the solubility of complex **2**. The parent complex (**1**) was found to have a solubility of 0.65M in ACN, which closely matches literature values [34]. When

functionalized, the resulting complex (**20**) was found to have a solubility of 1.32M, a substantial increase from the parent complex (**1**).

Furthermore, the solubilities for complexes with varying metals (complexes **1-7**) are similar and while the metal does have a small impact on the solubility, the functional group has a much larger effect (Figure 2.3.3-2). Without functionalization, complex **4** had the highest solubility in ACN (0.88M), but even when compared to the least soluble parent complex (**6**, 0.22M) they are both within the same order of magnitude.
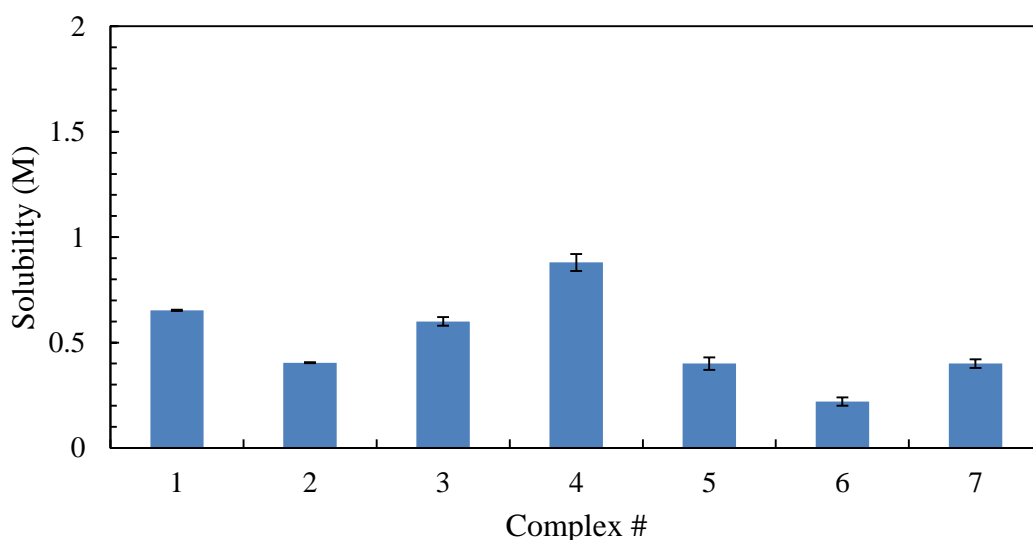
Figure 2.3.3-2 Solubilities of parent metal(III) acetylacetonate complexes (**1-7**) in acetonitrile.

Finally, the solubilities of complexes **21** and **22** were found to be 0.048±0.002M and 0.10±0.01M in ACN, respectively. The solubility of **21** closely matches previously reported values in the literature (0.06M) [55] and is significantly lower than V(acac)$_3$ (complex **1**). Likewise, the solubility of **22** closely matches reported values (~0.14M) [111].

After experimentally determining the solubility of each complex, theoretical solubilities were calculated using the solvation energies and dipole moments (following the procedure in Section 2.2.5.2). Solvation energies were calculated as the difference between the energies of the neutral complexes in a vacuum and those in ACN, using a PCM model [$\Delta G_{sol}(MCC)$] from Figure 2.2.5-1 and Figure 2.2.5-2. The reported values are only for neutral species and values were not obtained for charged species. The dipole moment of each neutral complex in ACN was obtained from single point PCM calculations.

Table 2.3.3-1 Calculated solvation energy, dipole moment and solubility from DFT optimized structures.

Complex	Metal Type	ΔG_{solv} (kcal/mol)	Dipole Moment (μ)	Calculated Solubility (M)
1	V	-16.36	1.21	0.33
2	Cr	-16.38	0.01	0.33
3	Mn	-16.90	1.20	0.35
4	Fe	-16.56	0.06	0.34
7	Ru	-16.95	1.16	0.35
8	Cr	-15.06	0.01	0.29
10	Cr	-32.05	7.83	0.69
15	Cr	-33.92	3.43	1.19
16	Cr	-44.09	9.94	1.20
17	Cr	-32.53	3.04	1.12
18	Cr	-38.13	6.04	1.31
19	Cr	-44.77	3.39	2.01
20	V	-36.92	3.38	1.40
21	V	-13.93	4.56	0.14
22	Fe	-8.58	0.00	0.11

A list of calculated solvation energies, dipole moments, and solubilities can be found in Table 2.3.3-1. Results for complexes **5**, **6**, **9** and **11-14** were not included for the same reasons that they were not included in the standard potential calculations (a combination of instability, slow kinetics, minimal solubility, or unable to optimize the

64

structure). A non-linear, least squares, regression analysis was performed using Minitab, resulting in the following fitting equation:

$$S_O = (\Delta G_{solv}(MCC)A)^B - (\mu C)^D \qquad \text{Equation 2.3.3-1}$$

where μ is the dipole moment, A=-0.033, B=1.80, C=0.092, and D=2.50, $\Delta G_{solv}(MCC)$ is in units of kcal/mol, and S_O is in units of mol/L.
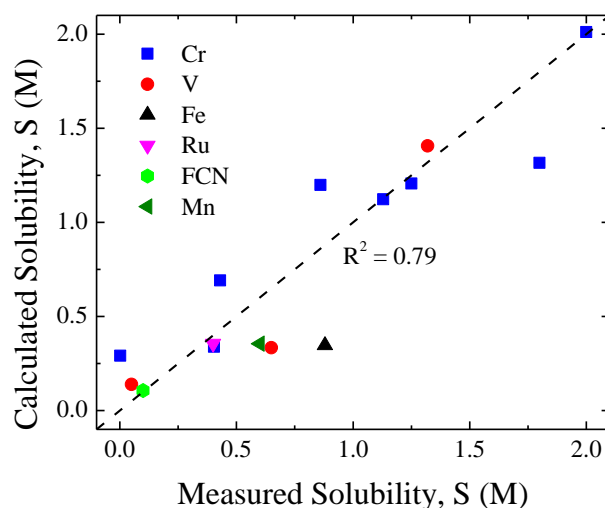
Figure 2.3.3-3 Solubility predictions using Equation 2.3.3-1 versus experimentally measured solubilities.

As seen in Figure 2.3.3-3, the solubility calculated using Equation 2.3.3-1 correlates reasonably well to the experimental values (R^2=0.79). Error in the fit is likely due to not incluuding the sublimation energy, or any parameter that is associated with the sublimation energy (V_m, crystal lattice energy, etc.). Regardless, Equation 2.3.3-1 is useful as an initial screening tool for theoretical complexes, and the solubility of interesting candidates could then be experimentally determined. Similar to the LUMO/HOMO standard potential correlation, Equation 2.3.3-1 accurately predicts the solubility of complex **22** (ferrocene), and could potentially be used for other MCC

systems. The solubility of acetylacetonate-based complexes is therefore primarily influenced by the chosen functional group, with the functional group having the largest impact on the solvation energy and dipole moment of the complex. For screening future complexes, high solvation energies are desireable.

2.3.4 Results: Diffusion Coefficients and Kinetic Rate Constants
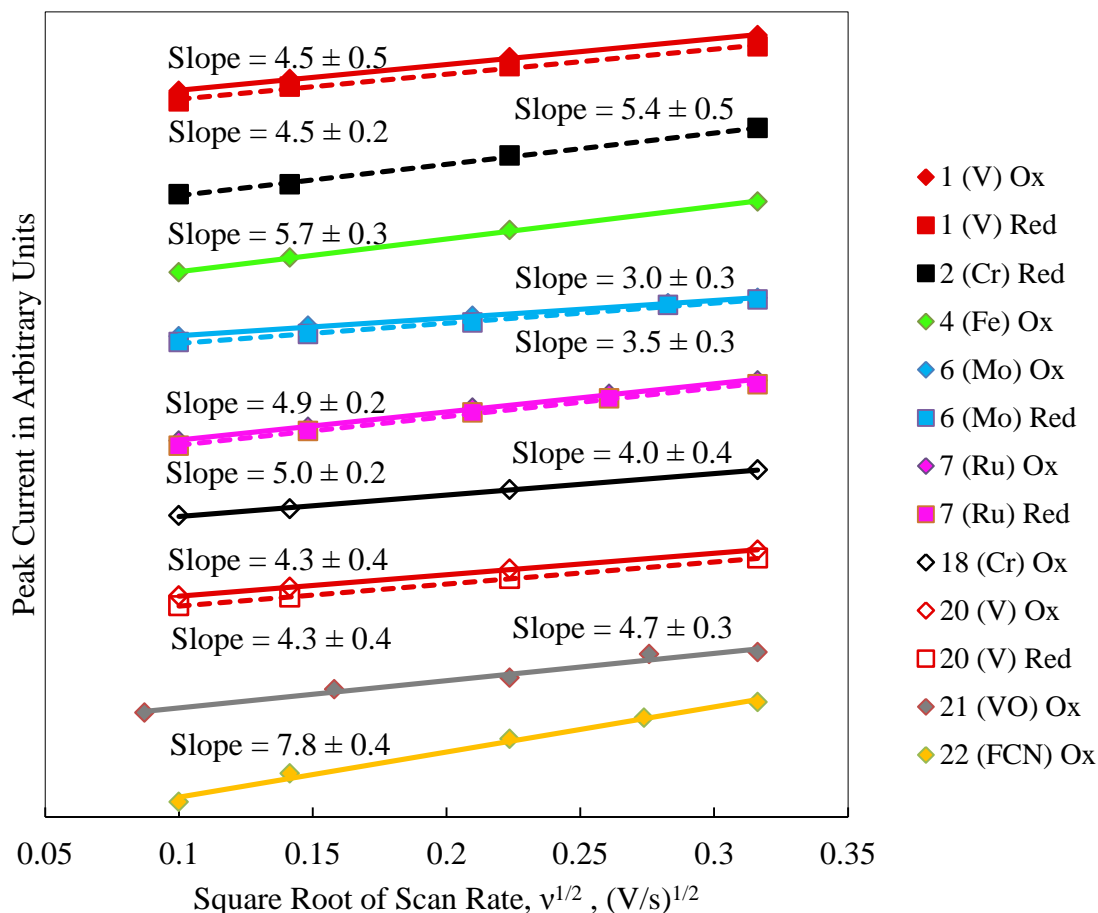
Figure 2.3.4-1 Peak current vs. square root of scan rate plots from CV data

Diffusion coefficients for complexes **1, 2, 4, 6, 7, 18,** and **20-22** in ACN were obtained from cyclic voltammograms at varying scan rates (Figure 2.3.4-1) and the results can be seen in Table 2.3.4-1. The data were fit to the Randles-Sevcik Equation (Equation 2.2.2-2). Effects due to slow kinetics (i_p vs. $v^{1/2}$ non-linearity) were observed

when varying scan rates for complexes **3** (Mn) and **5** (Co), even at 5mV/s, and obtaining accurate diffusion coefficients was not possible. For all other complexes tested, i_p vs. $v^{1/2}$ plots were linear, which indicates a diffusion-controlled redox process (Figure 2.3.4-1). The diffusion coefficients for the parent acetylacetonate complexes (**1, 2, 4, 6, 7, and 21**) are almost all within error, as expected based on their similar structures. The diffusion coefficients for the ether functionalized complexes **20** and **18** are lower than those for **1** and **2**, respectively. This is expected based on the larger substituents on the ligands of **20** and **18** compared to **1** and **2** [104]. However, all of the values for acetylacetonate based complexes are within the same order of magnitude and are expected to be adequate for RFB applications [6]. **22** (ferrocene) is a significantly smaller complex than the acetylacetonate complexes, and has a higher diffusion coefficient. The results obtained for **22** are in good agreement with literature values obtained using both macro and micro electrodes [20], [48]–[50].

Table 2.3.4-1 Diffusion coefficients of parent metal(III) acetylacetonate complexes (**1-7**), highly soluble chromium(III) and vanadium(III) complexes (**18, 20**), vanadyl(IV) acetylacetonate (**21**), and ferrocene (**22**).

Complex	Metal Type	D_O [10^6 cm^2 s^{-1}]	E^1 α_c, α_a	E^1 k^0 [x10^3 cm/s]	E^2 α_c, α_a	E^2 k^0 [x10^3 cm/s]
1	V	5.7±0.5	0.54±0.04 0.53±0.06	1.3±0.1	0.51±0.04 0.56±0.04	1.3±0.1
2	Cr	7.5±0.7	-	-	-	-
3	Mn	-	-	-	-	-
4	Fe	8.1±0.8	0.68±0.06 0.76±0.09	2.6±0.3		
5	Co	-	-	-	-	-
6	Mo	3.2±0.3	0.64±0.03 0.68±0.06	2.4±0.1	0.68±0.03 0.64±0.06	1.9±0.1
7	Ru	6.1±0.8	0.53±0.06 0.41±0.07	1.1±0.1	0.36±0.03 0.44±0.04	1.1±0.1
18	Cr	4.0±0.4	-	-	-	-
20	V	4.3±0.4	0.64±0.08 0.58±0.05	2.5±0.3	0.61±0.05 0.64±0.08	2.5±0.3
21	VO	6.3±0.6	0.46±0.09 0.7±0.1	3.8±0.4	-	-
22	Ferrocene	17±2	0.56±0.04 0.51±0.04	2.9±0.3	-	-

The kinetic rate constants will dictate the kinetic overpotentials of an RFB, and thus will determine the energy efficiency. Literature results have shown kinetic rate constants of MCCs to typically be an order of magnitude greater than those for aqueous active materials [7], so the kinetic overpotential is expected to be low and inconsequential when compared to the overpotential caused by solution resistance. Therefore, as long as the kinetic rate constants for all complexes in this study are an order of magnitude higher than aqueous active species, they will have a minimal impact on the RFB performance. Kinetic rate constants were estimated following the procedure in Section 2.2.2. The number of electrons transferred for all complexes is assumed to be equal to one, which is later proven to be accurate in **Error! Reference source not found.**. Reactions with very low kinetics or irreversible reactions are outside the limits of the fitting curve used by the

Nicholson method [63], and quantifying the kinetic rate constants was not possible. Therefore, rate constants for complexes **2**, **3**, and **5** are not available. The results can be seen in Table 2.3.4-1. The kinetic rate constants for each redox reaction were found to be within the same order of magnitude and are an order of magnitude higher than aqueous systems [7]. These values are used for comparative purposes and rotating disk electrodes (RDEs) or micro-electrodes should be used to obtain the transfer coefficients and rate constants with greater accuracy. However, the kinetic rate constant for **22** (ferrocene) closely matches those in the literature for macro electrode and RDE experiments in similar electrolytes [51], [52].

2.4 Charge-Discharge Performance of Functionalized Chromium(III) and Vanadium(III) Acetylacetonate

2.4.1 Approach

Functionalized Cr complex **18** and functionalized V complex **20** were tested using charge-discharge in an H-cell. **18** and **20** were chosen as they displayed the most attractive combination of solubility and electrochemical properties in ACN. In each experiment, the same complex was used as both the catholyte and anolyte to limit the deleterious effects of cross-over.

The performance of vanadium complex **20** was further investigated in a laboratory-scale flow-through electrode configuration RFB cell. Once again, complex **20** was used as both the catholyte and the anolyte.

2.4.2   Results: H-Cell Performance
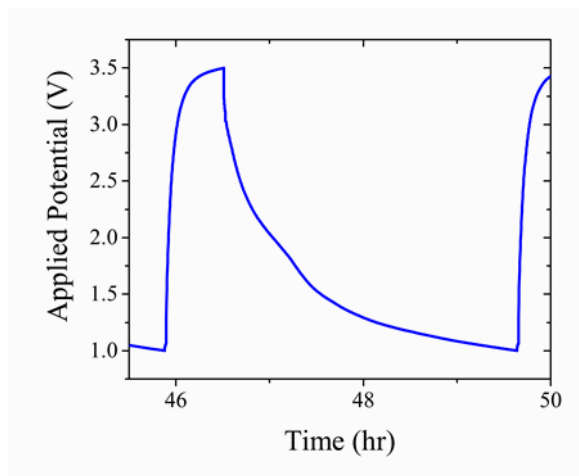
Figure 2.4.2-1 H-cell charge-discharge curve of 0.05 M chromium complex **18** (cycle 7) with 0.5M TBABF$_4$ in acetonitrile. The first stable cycle is shown.

Figure 2.4.2-1 shows charge-discharge results for a 0.05 M ACN solution of complex **18** with 0.5 M of TBABF$_4$ added as the supporting electrolyte. Figure 2.4.2-3 shows the charge-discharge results for **20** under similar conditions. Constant current densities of 0.21 mA/cm^2 and 0.021 mA/cm^2 were used for charging and discharging, respectively. A lower discharging current was used to limit overpotentials and ensure the cell was completely discharged. Cut-off charging potentials of 3.5 V and 2.4 V were used for complex **18** and complex **20**, respectively, with a discharging potential of 1.0 V for both complexes. The charging potentials were selected based on the measured cell resistance of 206 Ω (Figure 2.4.2-2), which would result in a 0.1 V overpotential. This overpotential is primarily due to the large separation between the two electrodes, with contributions from membrane and solution resistances.
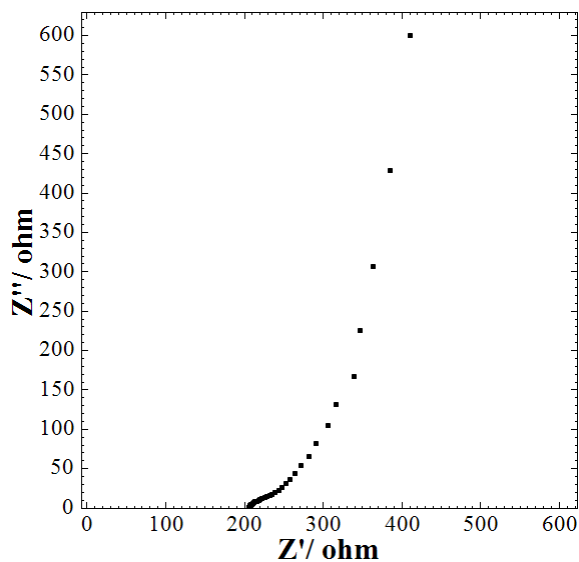
Figure 2.4.2-2 EIS Nyquist plot of H-cell with 0.5M TBABF$_4$ from 0.01-1x10^6 Hz at open circuit potential. R$_S$ = 206Ω.

Solutions containing chromium complex **18** were cycled more than 20 times. In a typical cycle, this complex lacks a discernible voltage plateau during discharge (Figure 2.4.2-1), which is indicative of the poor reversibility of the complex. The coulombic and energy efficiencies for the cell we ~55% and ~25%, respectively. These values are similar to those reported previously for Cr(acac)$_3$ (**2**) in an H-cell (53-58%, and 21-22%, respectively) [38], and are consistent with the similar electrochemical behavior of complexes **2** and **18**, as assessed by CV.
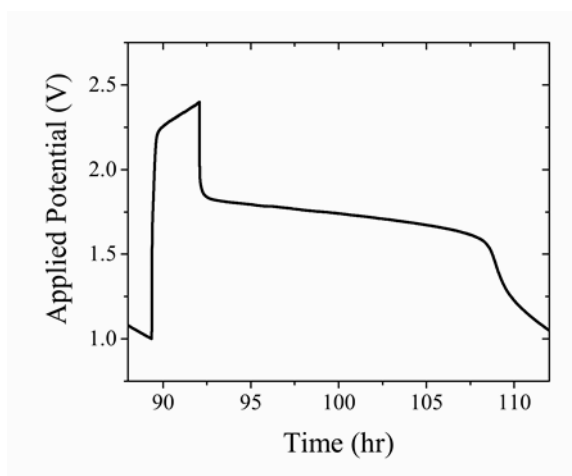
Figure 2.4.2-3 H-cell charge-discharge curve of 0.05 M vanadium complex **20** (cycle 4) with 0.5M TBABF$_4$ in acetonitrile. The first stable cycle is shown.

Figure 2.4.2-3 shows that vanadium complex **20**, in contrast to complex **18**, has a discharge plateau at ~1.8 V, which again correlates to the potential separation of the redox couples determined from the CV when overpotentials are taken into account. The cell averaged coulombic and energy efficiencies of ~76% and ~52%, respectively. These results are similar to those obtained with the parent V(acac)$_3$ (**1**), which was reported to have coulombic efficiencies of 70-73% and an energy efficiency of 34% [34], [36]. The performance of cells containing vanadium complexes is superior to those containing chromium complexes due to the increased reversibility of the redox couples.

2.4.3   Results: Flow Cell Performance

A 0.1M solution of complex **20** with 1M tetraethylammonium tetrafluoroborate (TEABF$_4$) in ACN was evaluated in a laboratory-scale flow cell described in Section 2.2.4. TEABF$_4$ was used due to the increased conductivity compared to TBABF$_4$ [35]. TEABF$_4$ is also inert within the electrochemical window, and will have no impact on the results [20]. Two separators (TEA$^+$ exchanged Nafion® 1035, and Daramic) were used, to test if capacity fade is due to the active species reacting with the membrane. Daramic

72

is a microporous separator that is made out of polypropylene and polyethylene. It is stable in ACN and should be inert to the active material. Likewise, TEA$^+$ exchanged Nafion® 1035 has been shown to be stable in ACN and was previously used to successfully cycle V(acac)$_3$ based electrolytes [41]. Both non-aqueous vanadium RFB cells were initially charged to 75% of the theoretical state of charge (SOC) at 10mA/cm^2. The open circuit cell potential (OCP) and electrochemical impedance was measured at the end of the first charge for both cells. The RFB cell resistance were ~1.75Ω·cm^2 with the TEA$^+$ exchanged Nafion® membrane, and ~1.84 Ω·cm^2 with Daramic, both of which were much lower than that measured for the H-type cell. Thus, higher charge-discharge current densities were employed than were possible with the H-cell. Charge-discharge cycles were performed at 10mA/cm^2, with cut-off charging and discharging potentials of 2.3V and 1.5V, respectively.
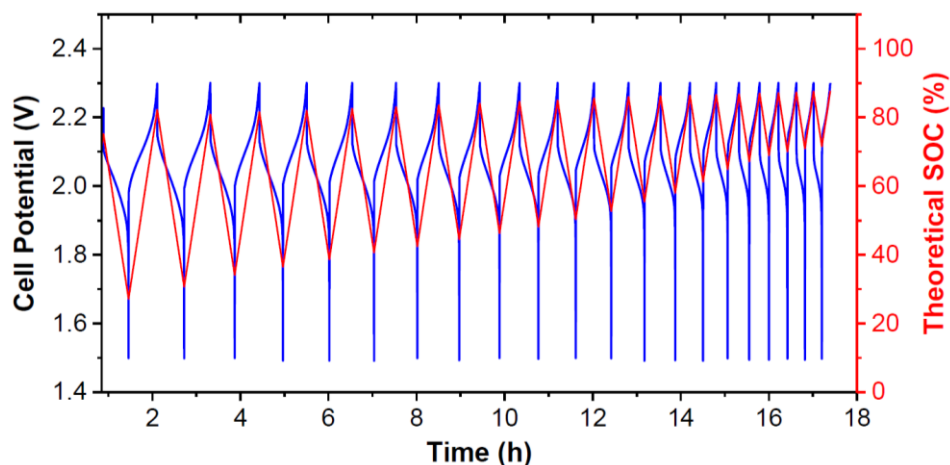
Figure 2.4.3-1 Flow battery charge-discharge cycles of 0.1M vanadium complex **20** with 1M TEABF$_4$ in acetonitrile at 10mA/cm^2 in a RFB cell with a TEA$^+$ exchanged Nafion® membrane. Flow rate: 25ml/min. Room temperature.
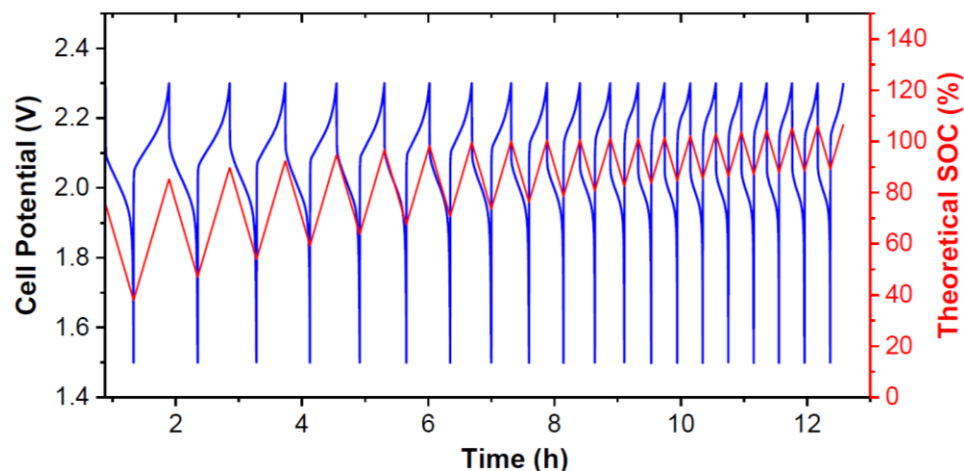
Figure 2.4.3-2 Flow battery charge-discharge cycles of 0.1M vanadium complex **20** with 1M TEABF$_4$ in acetonitrile at 10 mA/cm^2 in a RFB cell with a Daramic separator. Flow rate: 25ml/min. Room temperature.

Both vanadium RFB cells exhibited a single charging potential curve starting at ~2.0V and a discharging potential curve at ~2.1V, as shown in Figure 2.4.3-1 and Figure 2.4.3-2. These results are in good agreement with the potential window predicted for **20** from the CV experiments (2.1V, Table 2.3.2-1). The OCP of both cells was 2.17V at the end of the first charge. As described in Section 1.1.3, a cell potential of 2.1V would correspond to 50% SOC. These cells were charged to 75% SOC, so an elevated OCP of 2.17V makes sense. In both cells, the charging curves increase in potential from cycle to cycle indicating an increasing resistance. Discoloration was observed in both separators after charge-discharge, thus pore blocking is likely the cause. This illustrates the limitations of flow cell studies, and the need for characterization of these active materials in an inert cell, where the half-reactions can be isolated.
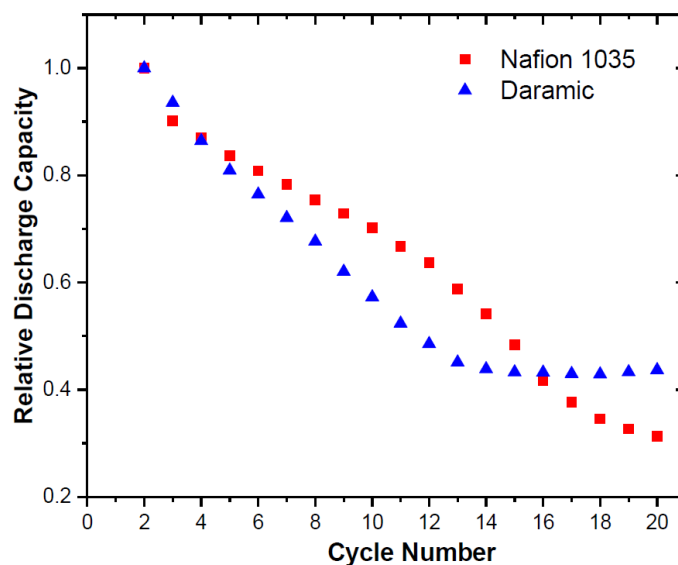
Figure 2.4.3-3 Capacity fade curves for RFB cells with a TEA$^+$ exchanged Nafion®
membrane (red) and a Daramic separator (blue).

The average coulombic and energy efficiencies for the vanadium RFB cells were
~92% and ~87%, respectively. The performance of complex **20** is comparable with that
reported for V(acac)$_3$, using a similar flow cell design [41]. The reported coulombic and
energy efficiencies for 0.1M V(acac)$_3$ were ~90% and ~83%, respectively, at 10mA/cm^2
[41]. However, Figure 2.4.3-3 shows that both cells exhibit rapid capacity fade, and 20%
of the initial capacity is lost after only ~5 cycles. This is an unexpected result, as the CV
of vanadium complex **20** reveals minimal side reactions and, thus, is expected to be quite
stable. As previously mentioned, degradation of V(acac)$_3$ to VO(acac)$_2$ is a known issue
[36], [42] and similar side reactions may be occurring in these experiments. To
investigate this possibility, CVs were obtained of the catholyte and anolyte after cycling
both cells.
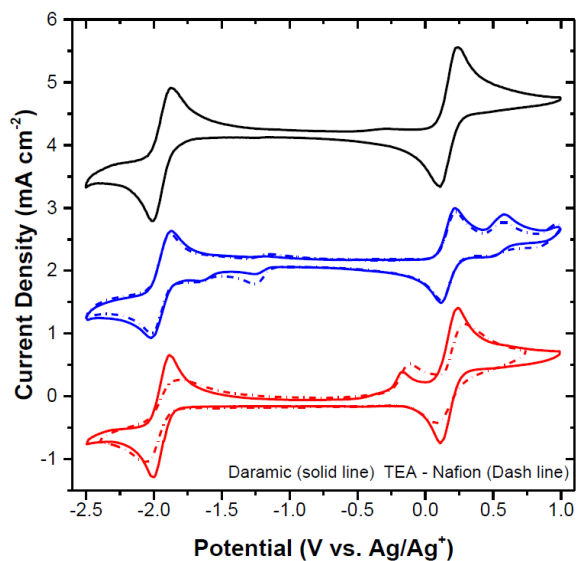
Figure 2.4.3-4 Cyclic voltammograms of 0.01M vanadium complex **20** with 0.1M TBABF$_4$ in acetonitrile (black), 10x diluted flow cell catholyte solutions (blue) and 10x diluted flow cell anolyte solutions (red). Solid lines denote solutions from the RFB cell with a Daramic separator, and dashed lines denote electrolytes from the RFB cell with a TEA$^+$ exchanged Nafion® membrane.

Figure 2.4.3-4 shows that the catholyte solutions for both RFB cells contain a side product with a redox couple at ~0.5V. The redox couple has similar features to that of VO(acac)$_2$, and this product could be a functionalized version of VO(acac)$_2$. Both anolyte solutions contain a side product with an oxidation peak at ~-0.2V. This was confirmed to be due to free ligand by obtaining a CV of the functionalized ligand, which shows an oxidation peak at -0.2V (Figure 2.4.3-5).
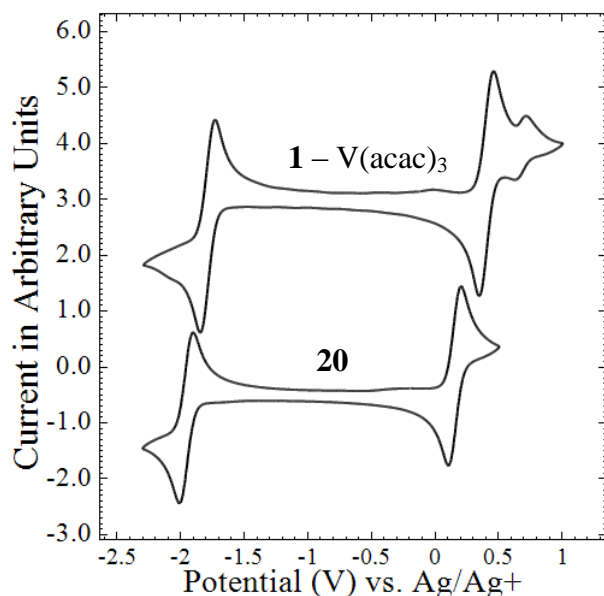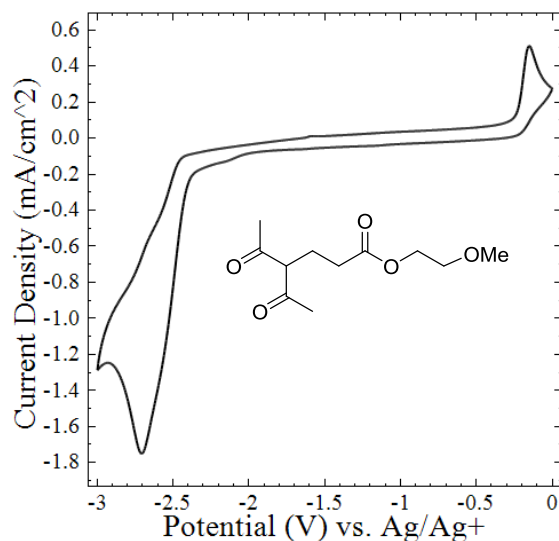
Figure 2.4.3-5 Cyclic voltammogram of complexes **18** and **20** free ligand. Solution comprised of 0.01M active species with 0.1M TBABF$_4$ in acetonitrile.

These side reactions are analogous to those observed during V(acac)$_3$ cycling experiments; however, like literature reported for V(acac)$_3$ cycling experiments [41], the redox couples of the active material appear to be the dominant signal for both anolytes and catholytes, despite the capacity of both cells being less than 50% of the initial capacity (Figure 2.4.3-3). Instead of investigating these half-reactions simultaneously in a flow cell, it would be advantageous to control the potential at one electrode and isolate either the anolyte or catholyte. This is the subject of **Error! Reference source not ound.**.

2.5 Conclusions

This chapter described the design of a series of metal(III) acetylacetonate complexes, and a detailed assessment of their solubilities, electrochemistries, and charge-discharge behavior as a function of metal and functional group structure. We demonstrated that the solubility of these complexes in ACN can be varied by more than four orders of magnitude by tuning the ligand structures through the use of functional

groups. In particular, complexes bearing ligands with ester substituents (**18** and **20**) show high solubilities in ACN, primarily due to influencing the solvation energy and dipole moment of the complex. DFT was used to establish a correlation between the experimentally determined solubilities and the calculated solvation energies and dipole moments. This information could be used for high-throughput screening of future active materials. The solubilities of **18** and **20** in ACN represent 450% and 200% enhancements over $Cr(acac)_3$ and $V(acac)_3$, respectively. Furthermore, it was demonstrated that by changing the metal in these complexes, the electrochemistry is altered. A key descriptor is the free energy of the reduction or oxidation reaction. DFT was used to calculate the free energy of these reactions, and both the calculated reaction energies, and the LUMO/HOMO energies strongly correlate with the experimentally determined standard potentials.

The results from electrochemical and charge-discharge studies show that **18** and **20** have electrochemical properties that are similar to the parent species. In static H-cell charge-discharge experiments, coulombic efficiencies of ~55% were achieved for **18** with 0.5 M $TBABF_4$ in ACN, while coulombic efficiencies of ~76% were achieved for **20** under the same conditions. In initial tests of laboratory scale prototype flow batteries with 0.1 M of **20**, we demonstrated coulombic and energy efficiencies of 92% and 87%, respectively, with operating current densities of 10 mA/cm^2; however, rapid capacity fade was observed, as well as evidence of a species similar to $VO(acac)_2$ in the catholyte and ligand detachment in the anolyte. Furthermore, concentrations of the active species as assessed by CV do not match the experimental capacities, and additional cycling should be possible. Consequently, the stability of these complexes is a concern, and fully

characterizing the capacity fade of each half-reaction, as well as understanding the cause of capacity fade is a critical next step. Regardless, the studies described herein provide a foundation for the rational design of novel active species with predictive correlations for standard potentials and solubilities, with minimal computational effort, that should provide needed support for next generation MCCs for non-aqueous RFB technologies.

Chapter 3

Understanding the Stabilities of Metal(III) Acetylacetonate Complexes

3.1 Background and Approach

The results from Chapter 2 indicate that even for MCCs that are subject to minimal side reactions during cyclic voltammetry (CV), rapid capacity fade occurs during charge-discharge experiments where substantial amounts of materials are oxidized and reduced. Additionally, evidence was presented indicating that functionalized V(acac)$_3$ (complex **20**) can react with the membrane, resulting in increasing high frequency resistance, and active species losses during cycling. These are not the only causes of degradation, as CVs after cycling showed evidence of a species similar to vanadyl(IV) acetylacetonate [VO(acac)$_2$] in the catholyte, and free ligand in the anolyte. Interestingly, the capacity fades more than the concentration of active material remaining in solution (as assessed by CV). Similar membrane interactions, side reaction products, and capacity fade/concentration mismatches have been presented in the literature for vanadium(III) acetylacetonate [36], [40], [41].

Capacity fade could be caused by a number of factors including: solubility changes at different charge states, limited electrolyte shelf-life, the active species reacting with the membrane or electrodes [55], or the electrolyte being electrochemically unstable. The goal of this chapter is to quantify the electrochemical stability of individual half-

reactions. DFT will be used to determine which electronic parameters primarily influence stability.

3.1.1 Current Literature Approach

Often in the literature for non-aqueous RFB active species, the fundamental electrochemical properties of an active species are initially characterized using CV, then subsequently evaluated in charge-discharge H-cell experiments, and finally tested in a flow cell. The problem with this approach is that there are significant differences in the cell materials between CV experiments and H-cell experiments. Furthermore, charge-discharge experiments require cycling of both half-reactions simultaneously, which makes evaluating the stability of the individual half reactions difficult. There are several significant differences between fundamental electrochemistry characterization techniques (CV) and charge-discharge characterization techniques (H-cell or flow cell). These differences include the electrode material, the presence of a membrane, and bulk concentration changes. This section will describe these differences in detail, and illustrate the need for a technique which can characterize electrolytes undergoing bulk reduction/oxidation cyclically to quantify the cycle life of half-reactions.

For RFBs, the electrode should not participate in the electrochemistry [112], [113], and therefore, accurate characterization of the active species depends on the electrode being inert. CVs for non-aqueous RFB electrolytes, are typically conducted using inert electrodes such as glassy carbon or platinum [27], [28], [32], [34], [37], [38], [42], [46], [53]. These working electrode surface areas are also small ($<0.07 cm^2$), so any surface contaminants, such as oxygen functional groups that could react with the active material, will not be in high enough concentrations to change the bulk electrolyte.

Polishing working electrodes prior to CV experiments, and conducting multiple CVs until a consistent signal is observed, are common practices to further control the surface chemistry of the working electrode [20].

In contrast, the most commonly used electrodes in non-aqueous RFB H-cell charge-discharge experiments are graphite plates [34], [37], [38], [53]. Characterization data for the electrodes are typically not presented, and manufacturing techniques vary from company to company resulting in electrodes with different bulk properties and surface chemistries [114], [115]. Graphite plates are not considered to be inert, and have been shown to have a variety of surface oxygen groups (Figure 3.1.1-1) [113], [115]. One study presented evidence of vanadium(III) acetylacetonate reacting with graphite plate electrodes forming unknown products [55]. The electrodes are required to be much larger than those used in CV cells, and therefore the total oxygen available is significantly higher by using graphite plate electrodes. Larger electrodes are required because the bulk of the electrolyte is being reduced/oxidized in charge-discharge experiments. Flow cells also use different electrode materials as even higher surface areas are required. Carbon felts are the most commonly used electrodes, and again, flow cell data is typically not accompanied with characterization data of the electrodes. A number of studies have shown that the surface functional groups can vary significantly depending the on treatment conditionss and the manufacturer [113], [115], [116].
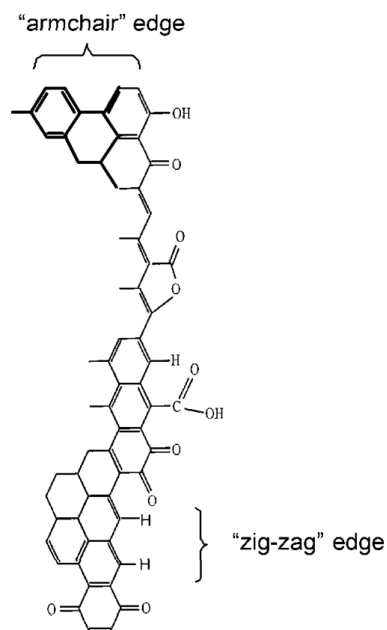
Figure 3.1.1-1 Typical surface oxides that occur at different edge planes of graphite materials [115].

While conducting charge-discharge experiments using working electrodes such as graphite plates or carbon felts may be more representative of how an active species would behave in a flow cell, using an inert electrode would allow for the quantification of the stability of an active material without interactions between the electrode and the active species. Components could then be modified to achieve maximum cycle life of an RFB containing this active species.

In order to bridge the gap between what is learned from CV and learnings from charge-discharge experiments, high surface area glassy carbon was utilized for all of the experiments. Glassy carbon produced in a foam form is referred to as Reticulated Vitreous Carbon (RVC). The electrode material was developed by Chemotronics International in the 1970s [117], and is produced by polymerizing resins such as polyurethane and subsequently carbonizing at $700\text{-}1100^O C$ [118]. The resulting material is amorphous, and has an open pore structure (Figure 3.1.1-2) resulting in high void

volumes (90-97%), and high surface areas [117]. Furthermore, it has very similar surface

chemistries to glassy carbon, and is considered to be electrochemically inert [118].
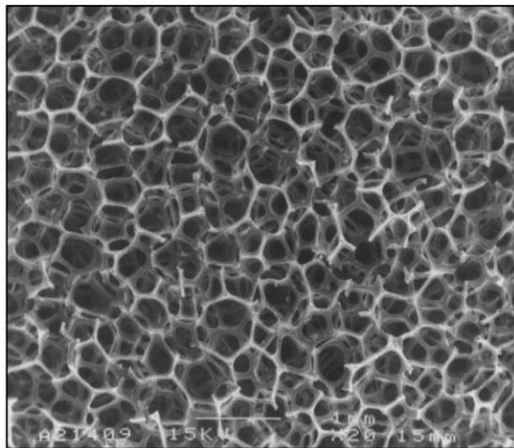
(d) 1 mm ————
Figure 3.1.1-2 SEM micrograph of 100 ppi (pores per inch) RVC [118].

Another difference between charge-discharge and CV experiments, is that CV

cells do not have a membrane, so interactions between the active species and membrane

will not be observed. In charge-discharge experiments, Neosepta AHA is commonly used

(Figure 3.1.1-3) [22]. Neosepta is an anion exchange membrane which is stored in

aqueous solutions with chlorine anions. Removal of these chlorine anions for non-

aqueous applications has been shown to be extremely difficult [55], and the remaining

chlorine anions have been shown to react with $V(acac)_3$ active species [55]. Interactions

between other active materials and Neosepta in other literature studies have not been

reported, and therefore the electrochemical stability of just the active species is difficult

to assess [28], [34], [37], [38], [42]. In an effort to avoid reactions with membranes,

several recent RFB studies have utilized porous separators, such as Daramic or Celgard

[7], [41], [56]. However, previous flow cell results shown in Section 2.4.3 indicate that

acetylacetonate-based electrolytes interact with both ion exchange membranes and

porous separators. To characterize half-cell reactions without conducting extensive research to develop an inert membrane, removing the membrane altogether is the best option.
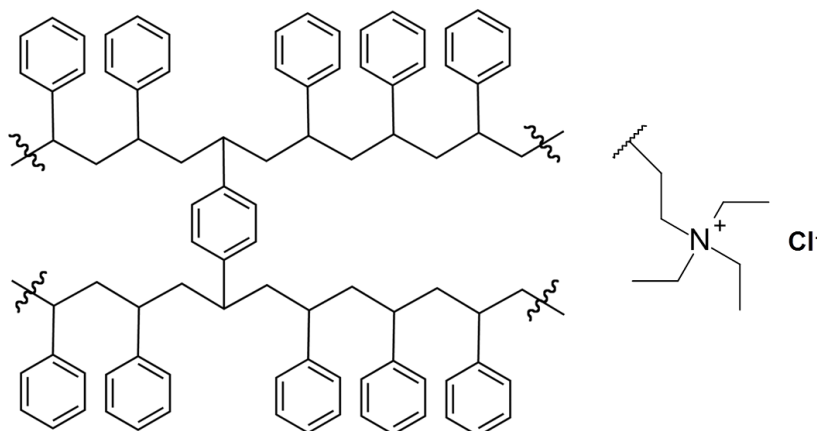
Figure 3.1.1-3 Neosepta AHA molecular structure [119].

Glass frits are widely used in electrochemistry experiments to isolate electrolyte solutions [20]. These frits are typically much thicker than separators or membranes, and therefore are not used in battery testing experiments due to high resistance and compression issues (cracking). Nevertheless, glass is an inert material, and was therefore used as the "membrane" in these studies. Furthermore, for half-reaction characterization experiments, the overpotential between the working and counter electrodes are irrelevant and as long as the voltage is within the limits of the potentiostat, it will not impact the current generated at the working electrode.

The last major difference between CV and charge-discharge experiments is that the bulk concentration is not altered in CV experiments as only a small amount of material near the electrode is subject to redox reactions, but the bulk concentration is changed significantly in charge-discharge experiments. If a minor side reaction is observed during CV, it will be observed to a greater extent in charge-discharge studies,

and thus characterization of an electrolyte where the bulk concentration is cyclically changed, is required.

3.1.2 Approach

Electrode-MCC and membrane-MCC interactions, solubility changes at different charge states, limited electrolyte shelf life, and electrochemical degradation could all cause the capacity fade for acetylacetonate-based electrolytes reported in the literature and in Chapter 2 [36], [40], [41]. Determining the causes of capacity fade requires experimental methods that can modify the bulk electrolyte oxidation state while minimizing or eliminating electrode and membrane interactions. Cyclic Bulk Electrolysis (BE) when using the appropriate electrode and membrane materials can fulfill these requirements. As described in Section 3.1.1, for these studies RVC inert electrodes with ultrafine glass frits as "membranes" were used to minimize electrode interactions and prevent any membrane interactions. The resulting custom bulk electrolysis (BE) cell was developed in our lab and is described in Section 3.2.1.

By avoiding electrode and membrane influences on the stability of an active material, the remaining potential causes for capacity fade are: solubility changes at different charge states, electrolyte shelf life, and electrochemical degradation. The solubilities of RFB active materials at various oxidation states have been shown to change [27], and if the solubility of an active material decreases at different oxidation states, this could result in precipitation and subsequent capacity loss during cycling. Without quantifying the solubility, precipitation could be mistaken for the degradation of the active species.

The changes in solubility at different charge states were quantified for a representative MCC [V(acac)$_3$] by using BE to first electrochemically generate [V(acac)$_3$]$^{-1}$ and [V(acac)$_3$]$^{+1}$ and then quantifying their solubilities using UV-Vis spectroscopy. UV-Vis spectroscopy was used instead of CV due to the high concentrations of active material in the electrolyte solutions. The electrolytes could have been diluted and tested by CV, but the supporting electrolyte concentrations used to determine diffusion coefficients would need to be roughly constant, which is not possible with serial dilutions. The solubility was found to be approximately constant, and as metal(III) acetylacetonates start as a neutral species and are charged upon reduction and oxidation, the solubilities of the reduced and oxidized versions of the complexes presented in Figure 2.1-1 were assumed to be at least equal to that for the neutral species.

Likewise, intermolecular interactions limiting the shelf life (time spent in solution before reaching 80% of the initial concentration) of charged non-aqueous RFB active materials has never been tested, and would cause a loss of capacity. The shelf life of the reduced, neutral, and oxidized version of both V(acac)$_3$ (Figure 3.1.2-1, complex **1**) and highly soluble functionalized V(acac)$_3$ (Figure 3.1.2-1, complex **20**) were quantified by generating the materials using BE, and monitoring their concentrations over time using CV. The shelf life of species at all oxidation states were found to be longer than that required for the charge-discharge studies. By determining the shelf life of both a parent metal(III) acetylacetonate complex, and a highly soluble, functionalized metal(III) acetylacetonate complex, it was assumed that the shelf lives of the other active materials presented in Figure 2.1-1 are not the primary cause of capacity fade.
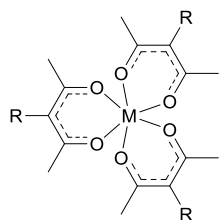
M = V, R = H (**1**) - V(acac)$_3$
M = Cr, R = H (**2**) - Cr(acac)$_3$
M = Mn, R = H (**3**) - Mn(acac)$_3$
M = Fe, R = H (**4**) - Fe(acac)$_3$
M = Ru, R = H (**7**) - Ru(acac)$_3$

(**20**) – Functionalized V(acac)$_3$

(**21**) – VO(acac)$_2$

(**22**) – Ferrocene (FCN)
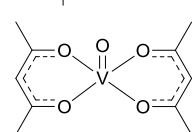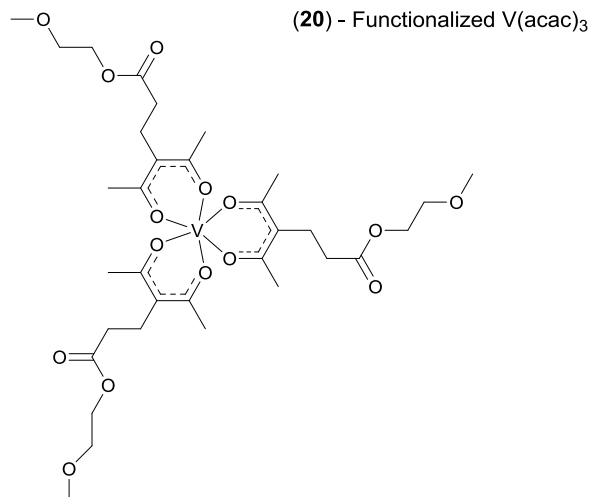
Figure 3.1.2-1 List of complexes tested using cyclic BE.

Next, after ruling out solubility changes and shelf life as primary causes of capacity fade, the cycle life of a number of metal(III) acetylacetonate half-reactions, which appear to be reversible by CV (peak height ratio greater than 0.8, see Table 2.3.2-1), was assessed. To quantify the electrochemical stability of a half-reaction, the cycle life was determined. For these studies, we define the cycle life of a half-reaction as the number of BE cycles to reach 80% of the initial capacity. Crossover within this system is minimized by the ultrafine frit, but small amounts are unavoidable, and will result in capacity fade (see Section 3.2.1). Likewise, RVC electrodes will still contain some surface oxygen functional groups, and some electrode-active species interactions

88

will still take place. Therefore, the quantified cycle life values are for comparative purposes, and could likely be increased with ideal electrodes, and improved membranes.

Finally, DFT calculations were used to establish trends in the data and generate a correlation curve useful for predictive screening of future complexes. A list of the complexes tested is in Figure 3.1.2-1. For consistency with Chapter 2, the same complex numbers will be used.

Complex **20** was synthesized by Dr. James Suttil and Pablo Cabrera from the Sanford group at the University of Michigan. Details regarding the synthesis procedure and verification of the complex including NMR, XRD, and elemental analysis can be found in the supplementary material of "Metal Acetylacetonate Complexes for High Energy Density Non-Aqueous Redox Flow Batteries," *J. Mater. Chem. A*. **3**, 7929 (2015). All other active materials were purchased from commercial sources and used as received. I conducted all of the electrochemical and solubility experiments, as well as the density functional theory calculations. The DFT calculations were conducted in collaboration with Dr. Lei Cheng from the Curtiss group at Argonne National Laboratory.

3.2 Experimental Techniques

3.2.1 Bulk Electrolysis
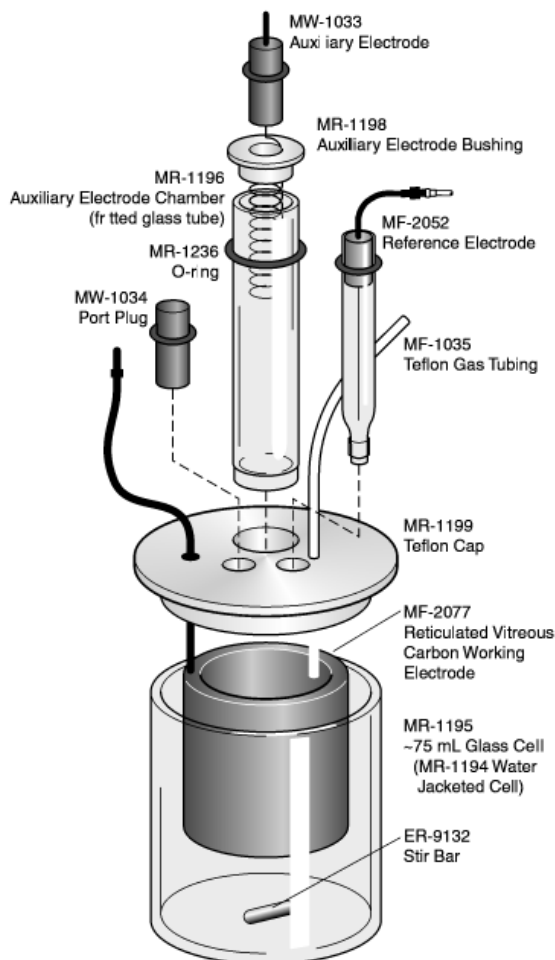
Figure 3.2.1-1 Commercial bulk electrolysis cell [120]

Bulk electrolysis is an electrochemical technique where the oxidation state of the bulk of an electrolyte is altered using a three electrode cell with a mixed working chamber [20]. The oxidation state of the bulk electrolyte is altered by either applying a constant current between the counter and working electrodes and monitoring the potential at the working electrode (chronopotentiometry), or by applying a constant potential at the working electrode and monitoring the current between the working and counter electrodes (chronoamperometry). The working electrode is the electrode being

investigated, the counter electrodes serves as a source of electrons, and the reference electrode is made of a material that has a stable voltage that does not change significantly with an applied current. As the working chamber electrolyte is reduced or oxidized, the opposing reaction occurs in the counter chamber, so a glass frit is used to separate the two chambers to limit cross-contamination. Commercially available BE cells are designed to change the oxidation state of the solution one time, at low concentrations (Figure 3.2.1-1), and are not fit for cyclic BE because the counter chamber is significantly smaller than the working chamber. This causes the counter electrolyte to experience extreme potentials, allowing for deleterious side reactions to occur. Because the bulk of the electrolyte undergoes reduction or oxidation, the state of charge (SOC) and coulombic efficiency described in Section 2.2.3 can be determined and controlled.
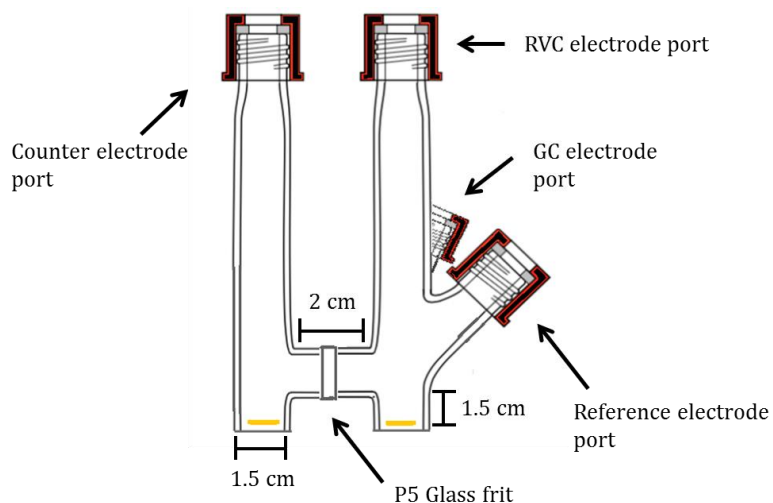
Figure 3.2.1-2 Custom bulk electrolysis cell used for this work

Figure 3.2.1-2 shows the custom cell that was used for the cyclic BE experiments. When compared to the commercially available BE cell (Figure 3.2.1-1) the major difference is the use of equal volume working and counter chambers. The use of equal volume electrolyte chambers, and the same active species in the working and counter

91

chambers, allows the technique to be conducted cyclically. The chambers are separated by a class P5 (1.0-1.6 μm pore size) ultrafine glass frit (Adams & Chittenden). The working electrodes are made from RVC sheets with 60 pores per inch (ERG Aerospace) that are cut into rectangular strips (~1x1x5 cm). Since the bulk electrolyte is being reduced or oxidized, a high surface area working electrode is required, so the reaction can progress faster than crossover through the frit. Crossover is unavoidable, and therefore even for a half-reaction with perfect reversibility, any degradation that occurs in the counter chamber will eventually decrease the capacity of the working electrolyte. Therefore the quantified cycle life values are for comparative purposes. With that said, coulombic efficiencies for stable complexes in this study are >98%, indicating very little crossover. Additionally, similar cells have been utilized to characterize the half-reactions of organic active materials for RFB applications, with one report by Huang and co-workers showing data for 100 cycles with minimal crossover effects [23], [24].

For this study, BE was performed using a PGSTAT100 Autolab Potentiostat with a chronoamperometric method to electrolyze the material as fast as possible to avoid crossover, and to minimize any side reactions due to potentials exceeding the active species voltage window. Holding potentials were chosen to isolate individual redox couples but avoid expected side reactions. The electrolyte was held at a constant potential until the current approached 0.001A and no limit was placed on the SOC. By holding a potential and allowing the current to approach zero, the overpotential also approaches zero, and therefore SOC values are typically >95%.

For shelf life studies, BE was conducted to completely reduce or oxidize electrolytes consisting of 0.1M active species with 0.5M TBABF$_4$ in ACN. The reduced

or oxidized working chamber electrolytes were then placed into a sealed, glass container and allowed to rest in the glovebox. Aliquots of electrolyte were periodically removed and diluted (10 times dilution) and CVs were conducted to quantify the amount of remaining active material using the measured diffusion coefficient and the Randles-Sevcik Equation (see Section 2.2.2).

For the solubility studies, BE was conducted on electrolytes saturated with $V(acac)_3$ to generate $[V(acac)_3]^{+1}$ and $[V(acac)_3]^{-1}$. The electrolytes consisted of 0.5M active species with 0.5M $TBABF_4$. After the electrolytes were completely reduced or oxidized, the concentrations were quantified using the UV-Vis method described in Section 2.2.1. The electrolyte solutions generated for the shelf life studies were used to determine the molar absorption coefficients of the respective active species.

For cycle life studies, all complexes were tested in an electrolyte solution consisting of 0.01M active species with 0.5M $TBABF_4$ in ACN. For a reduction half reaction, the electrolyte was reduced by holding the potential at least 200mV negative of the standard potential for the reaction determined using CV. Subsequently the electrolyte was oxidized by holding a potential at least 200mV positive of the standard potential. For an oxidation half-reaction, the electrolyte was oxidized by holding a potential at least 200mV positive of the standard potential for the reaction determined using CV. Subsequently the electrolyte was reduced by holding a potential at least 200mV negative of the standard potential. This was true for all of the half-reactions tested except for the oxidation half-reactions of complex **1** [$V(acac)_3$] and complex **20** [functionalized $V(acac)_3$] where the electrolyte was oxidized at a potential 100mV positive of the standard potential to avoid the oxidation of $VO(acac)_2$. Based on the Nernst Equation

[20], 99% of the active species will be reduced/oxidized at a potential of 200mV beyond the standard potential, and 90% of the active species will be reduced/oxidized at a potential of 100mV beyond the standard potential. CVs before and after cycling were taken in the same cell shown in Figure 3.2.1-2 by switching from the RVC working electrode, to a 0.07 cm^2 glassy carbon disk working electrode (BASi), and using the same procedure described in Section 2.2.2. Stirring was stopped while obtaining CVs.

3.2.2   DFT LUMO/HOMO Density Quantification

Orbital Composition Analysis allows for the determination of atomic contributions to each orbital of a complex. This is achieved through Population Analysis methods. There are a number of methods available in DFT software packages. The most common is the Mulliken Population Analysis (MPA), which was developed in the 1950s [121]. Other popular methods include the Natural Population Analysis (NPA) [122], the Quantum Theory of Atoms in Molecules (AIM) [123], and/or the Hirshfeld Population Analysis (HPA) [124]. At their core, population analysis methods sum all of the basis functions within an individual orbital shell, and then sum all of the shells that are attributed to an individual atom to get the density of the orbital for each atom. Each method makes assumptions that limit their use for specific systems.

For this study the HPA method was used to determine the density of the LUMO and HOMO for each atom of the neutral complexes in Figure 3.1.2-1. The HPA method has been shown to be extremely robust with various basis sets and has been shown to be significantly more accurate than the MPA, and is suitable for large MCCs [125]. AIM was not used as the atomic density cannot be directly translated to orbital densities [123]. The Multiwfn software package [126] was used for all orbital composition analysis

calculations and structures were optimized using Gaussian 09 [83]. The optimized geometries and details regarding the method can be found in Appendix A and Section 2.2.5, respectively.

3.3 Solubility Studies

3.3.1 Results: V(acac)$_3$, [V(acac)$_3$]$^{-1}$, and [V(acac)$_3$]$^{+1}$

Solubilities of the reduced and oxidized species were determined by completely reducing or oxidizing solutions of 0.5M V(acac)$_3$ (saturated) with 0.5M TBABF$_4$ in ACN as described earlier (Section 3.2.1). The calibration curves can be seen in Figure 3.3.1-1, Figure 3.3.1-2 and Figure 3.3.1-3 and the full spectra for the reduced, neutral, and oxidized complexes can be seen in Figure 3.3.1-4.
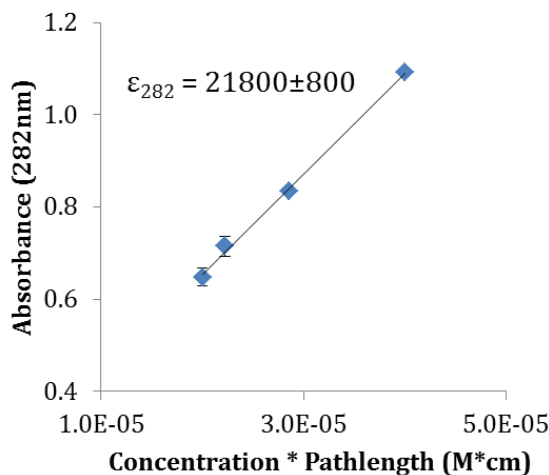
Figure 3.3.1-1 UV-Vis calibration curve of [V(acac)$_3$]$^{-1}$ in acetonitrile at 282nm. Slope equals the molar absorption coefficients in units of M^{-1}cm^{-1}.
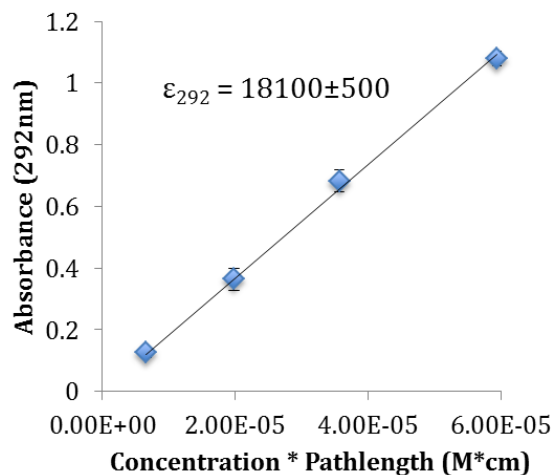
Figure 3.3.1-2 UV-Vis calibration curve of V(acac)$_3$ in acetonitrile at 292nm. Slope equals the molar absorption coefficients in units of M^{-1}cm^{-1}.
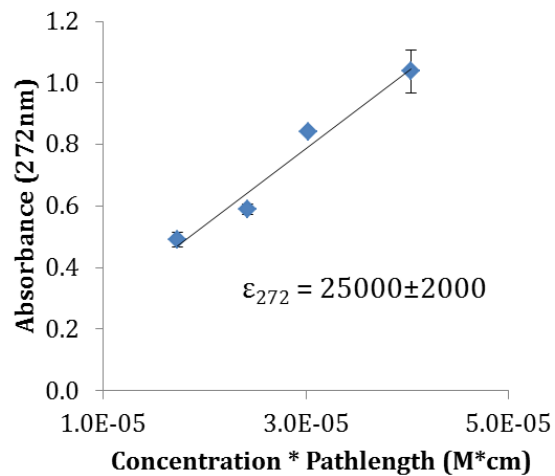
Figure 3.3.1-3 UV-Vis calibration curve of [V(acac)$_3$]$^{+1}$ in acetonitrile at 272nm. Slope equals the molar absorption coefficients in units of M^{-1}cm^{-1}.
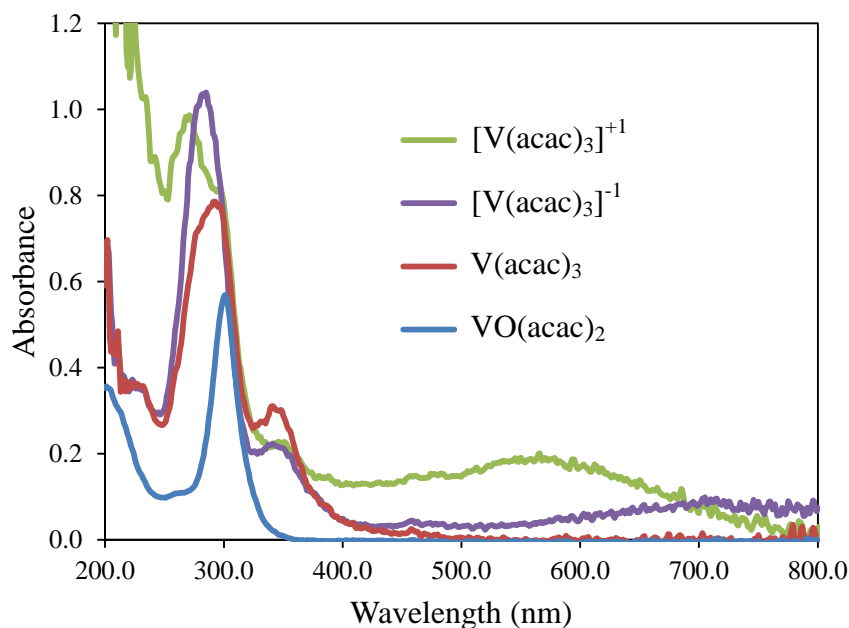
Figure 3.3.1-4 UV-Vis spectra of complex **1** at different oxidation states and complex **21** in acetonitrile.

As seen in Figure 3.3.1-4 the major peaks in the UV-Vis spectra for $V(acac)_3$, $[V(acac)_3]^{-1}$, and $[V(acac)_3]^{+1}$ and $VO(acac)_2$ are within 30nm. This limits the use of UV-Vis to quantify side products, and therefore UV-Vis was only used for solubility measurements. Qualitatively, a small amount of $VO(acac)_2$ appears to be present in the $[V(acac)_3]^{+1}$ spectrum, while the $VO(acac)_2$ peak at 300nm does not appear in the spectrum for $[V(acac)_3]^{-1}$. These results agree with the CV results presented in the shelf life results in Section 3.4.1.

Using this method, the concentration of the reduced or oxidized species could not exceed 0.5M. Note that the actual solubility could be higher, but for RFB applications, it is only important that the solubility does not decrease when oxidized or reduced. As seen in Table 3.3.1-1, there is no decrease in solubility for $[V(acac)_3]^{-1}$. Results for the $[V(acac)_3]^{+1}$ solution suggest that its solubility is ~25% lower than that of the neutral species, based on the CV results, however, as observed in Figure 3.3.1-4 and the shelf life

97

studies, the oxidation of $V(acac)_3$ is accompanied by partial conversion to $VO(acac)_2$, a species with very low solubility in ACN (0.05 ± 0.02M; see Section 2.3.3). Due to the high concentrations of both the active material and supporting electrolyte, generation of a relatively small amount of $VO(acac)_2$ could form particulates. Given this, it was not possible to determine the true solubility of $[V(acac)_3]^{+1}$. Regardless, even if the solubility is 25% lower, it would only limit the capacity for a saturated $V(acac)_3$ with 0.5M $TBABF_4$ in ACN electrolyte by ~25%, and the concentrations used for charge-discharge experiments in the literature are significantly lower (0.1M [41] and 0.05M [36]). For solutions with <0.32 ± 0.03M $V(acac)_3$, there would be no loss in capacity due to solubility limits for $[V(acac)_3]^{+1}$.

Table 3.3.1-1 Solubility of neutral, reduced, and oxidized complex **1** [$V(acac)_3$]. Solubilities determined in acetonitrile with 0.5M $TBABF_4$.

Complex	Solubility (M)
$V(acac)_3$	0.44 ± 0.04
$[V(acac)_3]^{-1}$	$\geq 0.49\pm0.04$
$[V(acac)_3]^{+1}$	$\geq 0.32\pm0.03^{a}$

a $VO(acac)_2$ particulates observed.

As the reduced and oxidized species are charged, and the solvent is polar, the true solubilities are likely higher than neutral $V(acac)_3$. To test this, theoretical solvation energies for $[V(acac)_3]^{-1}$ and $[V(acac)_3]^{+1}$ in ACN were calculated using DFT following the procedure described in Section 2.2.5.2. For both $[V(acac)_3]^{-1}$ and $[V(acac)_3]^{+1}$ the solvation energies were estimated to be ~three times higher than that for neutral $V(acac)_3$ (ΔG_{solv}: neutral = -16.4kcal/mol; oxidized = -47.2kcal/mol; reduced = -55.5kcal/mol). Additional experiments involving solvent evaporation could be used to quantify the true solubility values.

Similar solubility analyses were attempted with saturated solutions of complex **20**, however, as shown later in Section 3.5.2, complex **20** is significantly less electrochemically stable than complex **1** [V(acac)$_3$], and while it was stable enough to quantify shelf life values at modest concentrations, rapid degradation was observed during BE at concentrations of 1.3M in ACN. Likewise, viscosities of the electrolyte solutions increased significantly at high concentrations and therefore mass transport limitations prevented complete reduction or oxidation. Increasing temperatures of the electrolyte solutions would improve mass transfer and quantifying solubilities at different charge states could be possible, however increased temperatures would likely change a number of other properties such as the rate of side reactions, ligand exchange kinetics, etc., and was therefore not attempted.

3.4   Shelf Life Studies

3.4.1   Results: V(acac)$_3$

Shelf lives of the electrolytes were determined by using bulk electrolysis (BE) to completely oxidize or reduce solutions of 0.1M V(acac)$_3$ with 0.5M TBABF$_4$ at 0.5V and -2.1V, respectively, then storing the electrolyte and over time, acquiring aliquots and diluting with ACN by 10 times to characterizing them using CV. The neutral complex shelf life was determined without BE. As seen in Figure 3.4.1-1, the theoretical states of charge during reduction and oxidation of V(acac)$_3$ reached 94 and 96% respectively.
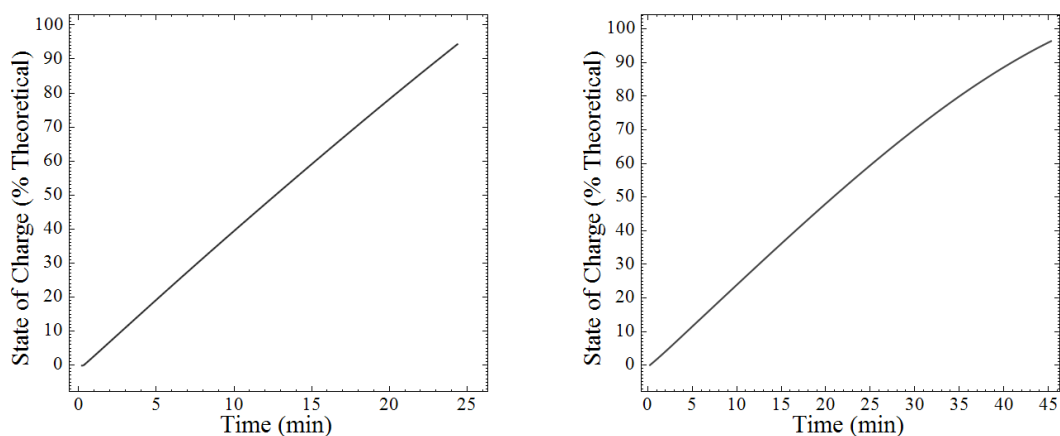
Figure 3.4.1-1 Bulk reduction at -2.1V vs Ag/Ag$^+$ (left) and oxidation at 0.5V vs. Ag/Ag$^+$ (right) of V(acac)$_3$. Solution comprised of 0.1M active species and 0.5M TBABF$_4$ in acetonitrile.

For each electrolyte, CV peak heights were used to quantify concentrations using the Randles-Sevcik equation and known diffusion coefficients associated with V(acac)$_3$ (Table 2.3.4-1). The diffusion coefficient for the reduced and oxidized species were assumed to be the same as the neutral complex based on the Stokes-Einstein equation, and their similar structures [104]. The shelf life is quantified as the length of time before reaching 80% of the initial concentration. The quantified results can be seen in Table 3.4.1-1, and the concentrations over time can be seen in Figure 3.4.1-2.

Table 3.4.1-1 Concentration of V(acac)$_3$ during shelf life studies obtained from cyclic voltammograms. Concentrations calculated using the Randles-Sevcik equation from the experimentally determined diffusion coefficient of V(acac)$_3$.

Complex	Day 0 Concentration (M)	Day 12 Concentration (M)	% Retained	Shelf Life (Days)
V(acac)$_3$	0.0100±0.0004	0.0108±0.0004	108±8	>12
[V(acac)$_3$]$^{-1}$	0.0101±0.0004	0.0106±0.0004	106±8	>12
[V(acac)$_3$]$^{+1}$	0.0097±0.0004	0.0078±0.0003	78±6	>12
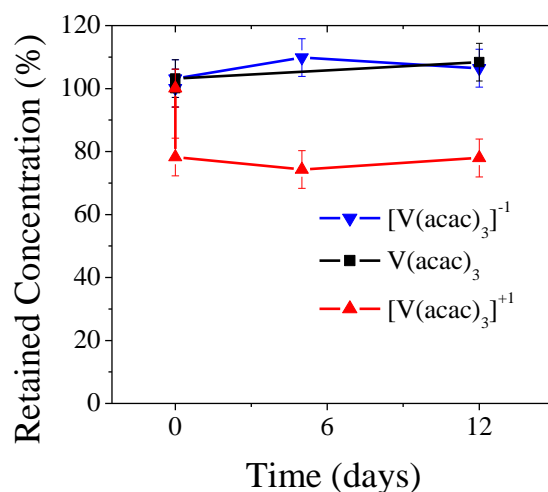
Figure 3.4.1-2 Retained concentrations of electrolyte solutions to determine shelf life. Solutions comprised of 10x diluted shelf life electrolytes (0.1M $V(acac)_3$ with 0.5M $TBABF_4$ in acetonitrile).

Figure 3.4.1-2 shows that all of the solutions had shelf lives of at least 12 days, the length of the experiments. As seen in Figure 3.4.1-3 and Figure 3.4.1-4 there are minimal changes in the CV signature for $V(acac)_3$ and $[V(acac)_3]^{-1}$ solutions after 12 days, and therefore there is no chemical degradation over time. The CVs of $[V(acac)_3]^{-1}$ reveal a very minor couple at ~0V which could be due to a small amount of ligand. There is no change in the peak heights of the couple at ~0V from day 0 to day 12, and is therefore the result of electrochemical degradation. The specifics of this electrochemical degradation will be further investigated in Chapter 4.
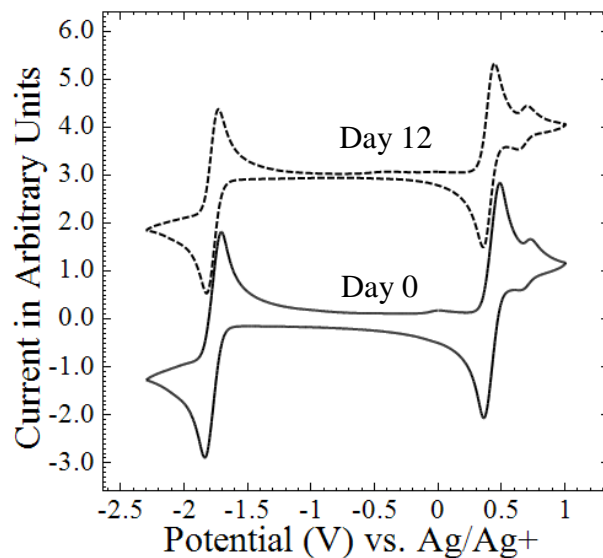
Figure 3.4.1-3 CVs of V(acac)$_3$ to determine shelf life of neutral species . Solution comprised of 0.01M active species and 0.5M TBABF$_4$ in acetonitrile.
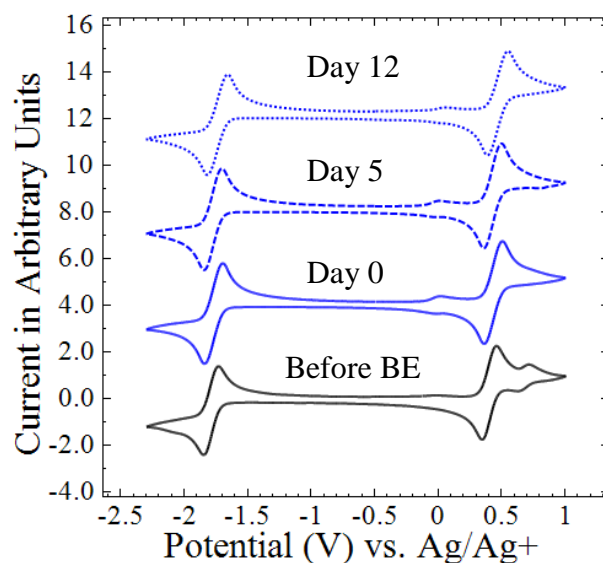
Figure 3.4.1-4 CVs of V(acac)$_3$ after reduction to determine shelf life of [V(acac)$_3$]$^{-1}$. Solution comprised of 0.01M active species and 0.5M TBABF$_4$ in acetonitrile.

CVs for the oxidized species at time intervals can be seen in Figure 3.4.1-5. A comparison of the CVs before BE and immediately following BE (Day 0) reveals three differing features: an increase in the peak heights of the couples at -2.1V and 0.65V, and one new couple at ~-1.1V. As seen in Figure 2.3.2-5, the couples at -2.1V and 0.65V correspond with VO(acac)$_2$ formation, which is expected based on literature results [36],

[41] and the flow cell studies described in Section 2.4.3. Quantification reveals that 22±6% of the active material is converted to VO(acac)$_2$ during oxidation. This observation will be further discussed in Section 3.5.3. Because there are minimal changes in the CV signature from Day 0 to Day 12, we concluded that the loss was due to an electrochemical degradation process; in other words it is not due to chemical degradation over time. Therefore, the shelf life of [V(acac)$_3$]$^{+1}$ appears to be at least 12 days.
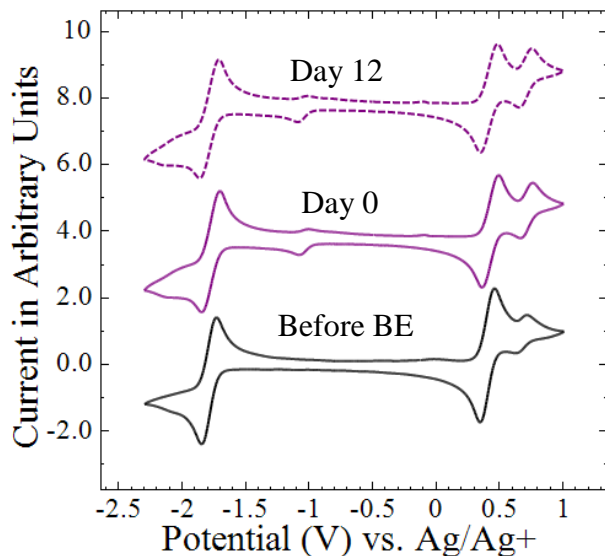
Figure 3.4.1-5 CVs of V(acac)$_3$ after oxidation to determine shelf life of [V(acac)$_3$]$^{+1}$. Solution comprised of 0.01M active species and 0.5M TBABF$_4$ in acetonitrile.

3.4.2 Results: Shelf Life of functionalized V(acac)$_3$ (Complex 20)

The same experiments to determine the shelf lives of V(acac)$_3$ at different oxidation states were conducted for functionalized V(acac)$_3$ (complex **20**). The electrolytes were oxidized or reduced at 0.3V and -2.1V vs Ag/Ag$^+$, respectively. The resulting electrolyte solutions were then characterized over time using CV by acquiring aliquots and diluting them with ACN by 10 times. The neutral complex shelf life was determined without BE. As seen in Figure 3.4.2-1, the theoretical states of charge during reduction and oxidation reached 98 and 91% respectively.
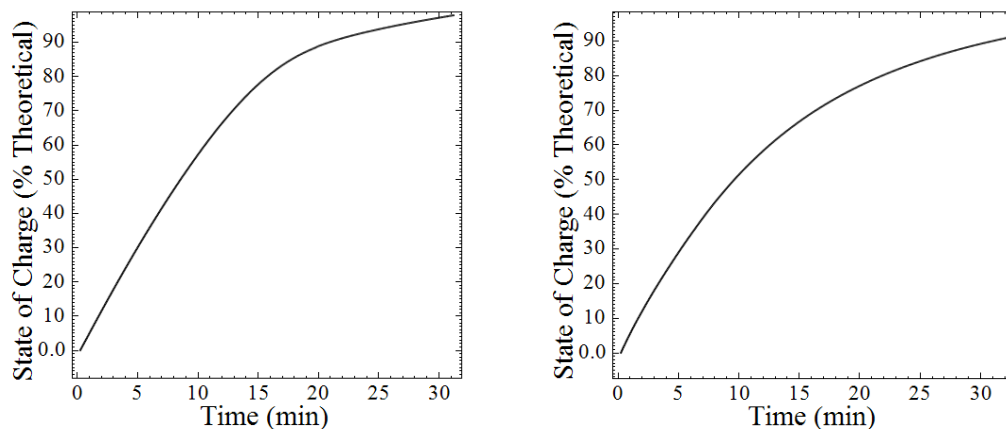
Figure 3.4.2-1 Bulk reduction at -2.2V vs Ag/Ag$^+$ (left) and oxidation at 0.3V vs. Ag/Ag$^+$ (right) of functionalized V(acac)$_3$ complex **20**. Solutions comprised of 0.1M active species and 0.5M TBABF4 in acetonitrile.

The quantified concentration results can be seen in Table 3.4.2-1, and the concentrations over time can be seen in Figure 3.4.2-2.

Table 3.4.2-1 Concentration of **20** during shelf life studies obtained from cyclic voltammograms. Concentrations calculated using the Randles-Sevcik equation from the experimentally determined diffusion coefficient of complex **20**.

Complex	Day 0 Concentration (M)	Day 14 Concentration (M)	% Retained	Shelf Life (Days)
20 - Neutral	0.0095±0.0004	0.0086±0.0004	91±6	>14
[**20**]$^{-1}$	0.0087±0.0004	0.0074±0.0004	78±6	>14
[**20**]$^{+1}$	0.0099±0.0004	0.0053±0.0004	60±6	~3
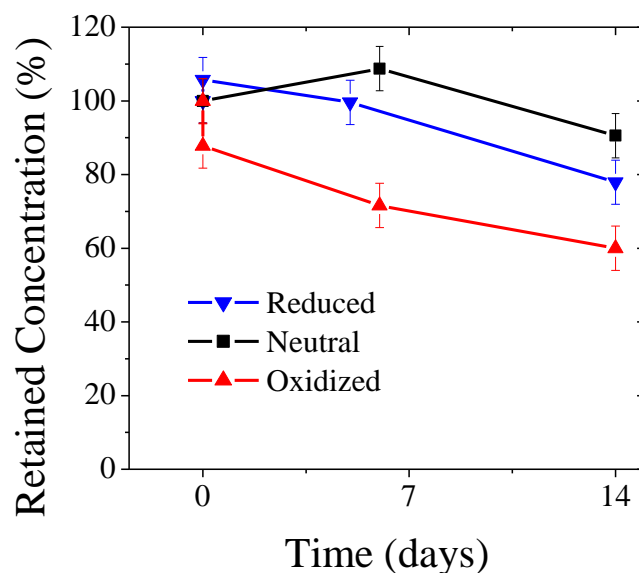
Figure 3.4.2-2 Retained concentrations of electrolyte solutions to determine shelf life. Solutions comprised of 10x diluted shelf life electrolytes (0.1M complex **20** with 0.5M TBABF$_4$ in acetonitrile).

Figure 3.4.2-2 shows that all of the solutions had shelf lives of at least 3 days. Over 14 days, minimal loss of active material was observed for the neutral complex, and CVs of the electrolyte over time (Figure 3.4.2-3) do not reveal any additional features.
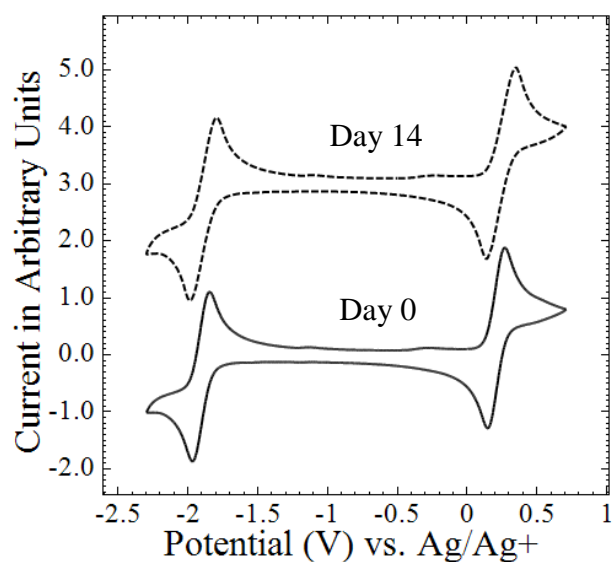
Figure 3.4.2-3 CVs of functionalized V(acac)$_3$ complex **20** to determine shelf life of neutral species . Solution comprised of 0.01M active species and 0.5M TBABF$_4$ in acetonitrile.

While 80% of the initial active species was still available after 14 days for the reduced version of complex **20**, Figure 3.4.2-4 shows that the CV signature of the reduced species does change over time. From the CVs at Day 0 to Day 14, the peak associated with ligand continually increases, and concentrations of the active material consequently decrease. Similar results were observed in the flow cell studies (Section 2.4.3). Therefore, chemical degradation does occur over time, and the shelf life of the reduced version of complex **20** is lower than that for the reduced version of complex **1**. Extended shelf life studies would need to be conducted to quantify exact shelf life values. Regardless, 80% of the reduced electrolyte is still available after 14 days, and the shelf life is not the primary cause for capacity fade.
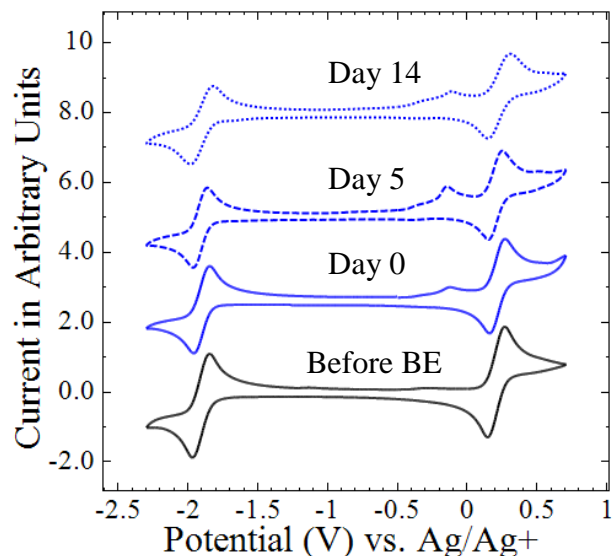
Figure 3.4.2-4 CVs of functionalized V(acac)$_3$ complex **20** to determine shelf life of reduced species . Solution comprised of 0.01M active species and 0.5M TBABF$_4$ in acetonitrile.

Figure 3.4.2-2 shows that the concentration of the oxidized version of complex **20** reached 80% of the initial concentration after three days, and Figure 3.4.2-5 shows that the CV signatures change over time. A couple at ~0.5V, and the height for the reduction

peak at ~-1.5V continually increases over time. Both features were observed in the flow cell studies, but to a lesser extent. Because both features increase over time, they are likely the result of chemical degradation, and the shelf life is therefore lower than that of the oxidized version of complex **1**. There are a number of other minor peaks that do not appear to increase over time and are due to electrochemical processes. Therefore the cycle life is not dictated by the shelf life of the oxidized species. Electrochemical stabilities for the oxidized **20** will be discussed in Section 3.5.3.
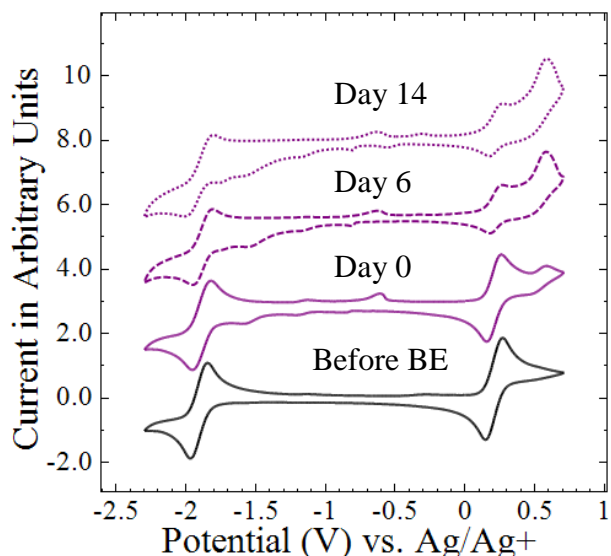
Figure 3.4.2-5 CVs of functionalized V(acac)$_3$ complex **20** to determine shelf life of oxidized species. Solution comprised of 0.01M active species and 0.5M TBABF$_4$ in acetonitrile.

3.5   Electrochemical Stability Assessment

3.5.1   Background and Approach

Based on the shelf life and solubility results, it was assumed that, like complexes **1** and **20**, the remaining complexes stabilities are primarily influenced by electrochemical degradation, and not due to shelf lives or solubilities in the reduced/oxidized state. Obviously the shelf life will play a role for long term experiments, but as shown herein,

even the most stable complexes reach 80% initial capacity within 100 cycles, which takes less than 24 hours.

Cyclic BE was conducted to characterize each half-reaction with a CV determined peak height ratio >0.8 (Table 2.3.2-1) for the complexes listed in Figure 3.1.2-1. The first reduction and oxidation half-reactions (E^2 and E^3, respectively) for complex **2** [Cr(acac)$_3$] do not have peak height ratios >0.8, but were included to confirm that low peak height ratios translate to limited cycle life. The oxidation half-reaction (E^1) of complex **21** [VO(acac)$_2$] was also investigated as the peak height ratio is very close to 0.8 (0.79, Table 2.3.2-1). Finally, the oxidation half-reaction (E^1) of complex **22** (Ferrocene) was also tested as a standard reversible reaction. All complexes were tested in an electrolyte solution consisting of 0.01M active species with 0.5M TBABF$_4$ in ACN. The cycle life of each half-reaction was taken as the number of BE cycles required to reach 80% of the initial capacity. In all cases, 80% initial capacity is reached within 100 cycles and therefore, a shelf life of three days for complex **20** (Section 3.4.2) is of no consequence. CVs were obtained after the BE experiments were completed to assess electrochemical changes that occurred during cycling.

As experimentally determining the stability of MCCs is a time consuming process, correlations between the experimentally quantified cycle life values and a number of both experimentally and computationally determined parameters were attempted. Peak height ratios have already been shown to not correlate well with cycle life values in a flow cell. Likewise, reaction rate constants for the complexes tested in Section 2.3.4 were found to be within the same order of magnitude and therefore are not expected to correlate with cycle lives either. However, considering that results presented

in Section 2.3.2 indicate that the calculated LUMO/HOMO energies strongly correlate to the standard potentials, examining the atomic density of said orbitals could provide insights regarding where the electron is likely to be stored/extracted during reduction/oxidation [68]. Therefore, the atomic density of the LUMO and HOMO that coincides with each half-reaction tested using cyclic BE was determined using the DFT optimized structures listed in Appendix A and the methods outlined in Section 3.2.2.

DFT was also used to investigate the changes that occur during oxidation or reduction. For example, theoretical structural changes during the reduction half-reaction of complex **1** were investigated by optimizing the neutral and reduced versions of complex **1**; changes in the bond lengths were quantified. Ligand shedding has been previously reported to occur during cycling experiments of complex **1** [V(acac)$_3$], [36], [41], [42], [127] and is a known issue not only for other metal-acetylacetonates [53], but for MCCs as a whole [92], [128], [129]. For metal-acetylacetonates, ligand detachment must result in the breaking of the M-O bond. Thus, the M-O bond lengths for the optimized structures coinciding with the respective couples were quantified. Similar stability estimates from theoretical bond length changes have been conducted before, with one study for organic complexes estimating that a bond length increase of 0.1Å would result in a bond rupture [84]. These structures are not transition-states, and bond length changes could be minimized as a result of each complex being at ground state [103].

3.5.2   Results: Bulk Electrolysis Cycle Life Quantification

The stability of all half-reactions with peak height ratios >0.8 quantified using CV were assessed using cyclic BE, and the cycle life was taken as the number of cycles

before reaching 80% initial capacity. The potentials that were cycled during BE to investigate the given half-reaction, and the number of electrons per molecule for the first charge (all ≥ 0.9) can be found in Table 3.5.2-1.

Table 3.5.2-1 Bulk electrolysis cycling parameters and quantified cycle lives. Solutions characterized using bulk electrolysis consisted of 0.01M active species with 0.5M TBABF$_4$ in acetonitrile.

Complex (Redox Couple)	Charging Potential [V vs. Ag/Ag$^+$]	Discharging Potential [V vs. Ag/Ag$^+$]	First Charge e$^-$ /molecule	Average Coulombic Efficiency	Cycle Life [Cycles to 80% Capacity]
1 (E^1)	-2.1	-1.4	0.97	98.0%	35
1 (E^2)	0.5	0.0	1.00	71.2%	20
2 (E^2)	-2.3	-1.7	1.00	4.6%	0
2 (E^3)	1.4	0.2	1.01	0.0%	0
3 (E^2)	1.2	0.2	1.02	1.0%	0
4 (E^1)	-1.4	-0.5	1.01	98.7%	97
7 (E^1)	-1.5	-0.7	0.95	98.3%	43
7 (E^2)	0.8	0.3	0.90	4.9%	0
20 (E^1)	-2.2	-1.6	0.95	97.0%	35
20 (E^2)	0.3	-0.1	0.90	48.8%	0
21 (E^2)	1.0	-0.5	1.00	95.3%	63
22 (E^1)	0.4	-0.5	0.92	99.3%	100

Figure 3.5.4-2 shows the capacity versus cycle number data for a subset of the tested oxidation half-reactions, and Figure 3.5.2-2 shows similar data for the tested reduction half-reactions. Capacity data is not shown for complex **3** [Mn(acac)$_3$] and E^2 of complex **7** [Ru(acac)$_3$] as each reaction was very irreversible and would overlap with the capacity curve of complex **2** [Cr(acac)$_3$]. This can be seen in the limited coulombic efficiencies for the oxidation half-reactions of complexes **3** and **7** (1.0% and 4.9% respectively) in Table 3.5.2-1. The capacity is presented as a percentage of the first cycle charging capacity for comparative purposes, but the first cycle charging capacity for all

complexes tested is very close to a theoretical 1 e⁻/molecule (validating the CV data analysis discussed in Section 2.3.4).
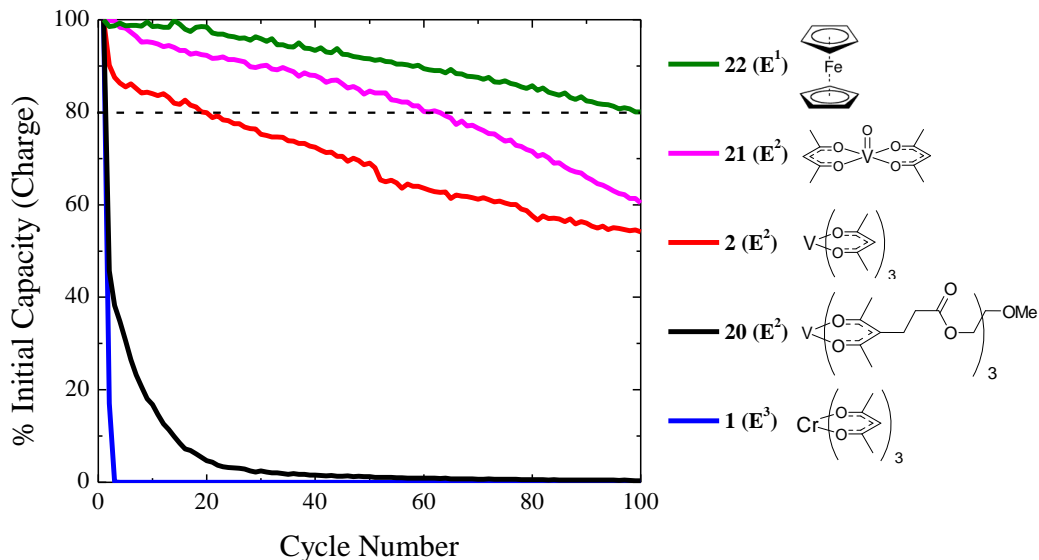
Figure 3.5.2-1 Capacity versus cycle number assessed by BE for positive (oxidation) half-reactions. All electrolytes consisted of 0.01M active species with 0.5M TBABF$_4$ in acetonitrile. Dashed line indicates cycle life cut-off.
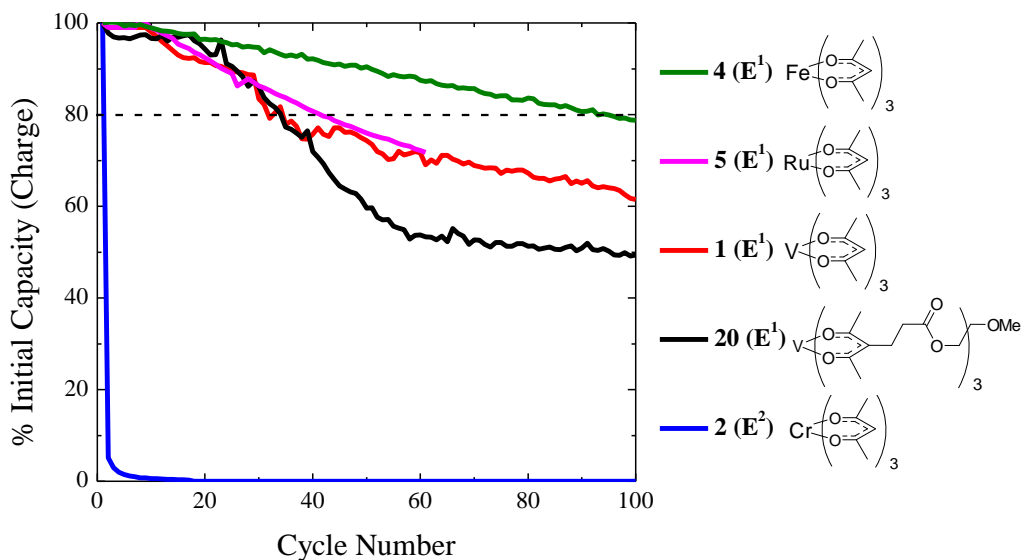
Figure 3.5.2-2 Capacity versus cycle number assessed by BE for negative (reduction) half-reactions. All electrolytes consisted of 0.01M active species with 0.5M TBABF$_4$ in acetonitrile. Dashed line indicates cycle life cut-off.

As previously mentioned in Section 3.2.1, some of the capacity loss is due to unavoidable crossover through the glass frit which will limit the observable cycle life values, and therefore values reported here are for comparative purposes. Complex **22** (ferrocene) was found to have the most stable oxidation half-reaction yielding 100 cycles before reaching 80% initial capacity. While 100 cycles is the highest cycle life of these complexes, based on literature results, ferrocene is expected to surpass 100 cycles [46]. For acetylacetonate-based complexes, complex **21** [VO(acac)$_2$] was found to have the most stable oxidation half-reaction, with a cycle life of 63. Complex **21** is the primary side product during oxidation of complex **1** [V(acac)$_3$] and based on CV peak height ratio (0.79, Table 2.3.2-1) was not expected to be stable. This illustrates the importance of not relying solely on CV experiments, as **21** would be deemed unsuitable as an RFB active material. It also demonstrates the importance of this type of half-reaction characterization, as complex **21** does not have a reduction couple and would not be able to be tested in a full H-cell or flow cell with the same material in both half-cells. Complex **4** [Fe(acac)$_3$] was found to have the most stable reduction half-reaction with a cycle life of 97. This is approximately equal to the cycle life of the oxidation half-reaction of complex **22** (ferrocene) and could be an interesting complex to functionalize to increase solubility. A flow cell with complex **4** in the anolyte and complex **22** in the catholyte would be entirely iron-based and have relatively high stability. Even without functionalization, complex **4** has the highest solubility of all of the parent acetylacetonate complexes with a solubility of 0.88M (Figure 2.3.3-2).

As hypothesized, the instability of both half-reactions for complex **2** [Cr(acac)$_3$] prevents a single BE cycle. The stability of complex **1** was found to be limited by the

cycle life of the oxidation half-reaction with a cycle life of 20, while the stability of the functionalized version (complex **20**) was limited by the oxidation half-reaction which was not able to cycle once. Recall in Figure 2.3.2-3 that CVs of complexes **1** and **20** were virtually identical and therefore the stability is expected to be very similar. The method of estimating stability of a half-reaction using CV peak height ratios is further discredited by the stability of complex **7** [Ru(acac)$_3$], which is limited by the cycle life of the oxidation half-reaction which was not able to cycle once, while possessing a peak height ratio of 0.99 (Table 2.3.2-1).

3.5.3 Results: Electrochemical Changes

For each BE experiment presented in the previous section, CVs of the spent electrolyte solutions were obtained to determine changes in the electrochemical signature. Many of the CVs were obtained after more than 300 cycles, and a significant amount of crossover is expected. Therefore, minor peaks in the CVs of the spent electrolytes will likely be due to degradation products from the counter chamber, and only major products will be discussed. A more detailed analysis of the electrochemical and structural changes that occur during cycling is provided in Chapter 4.
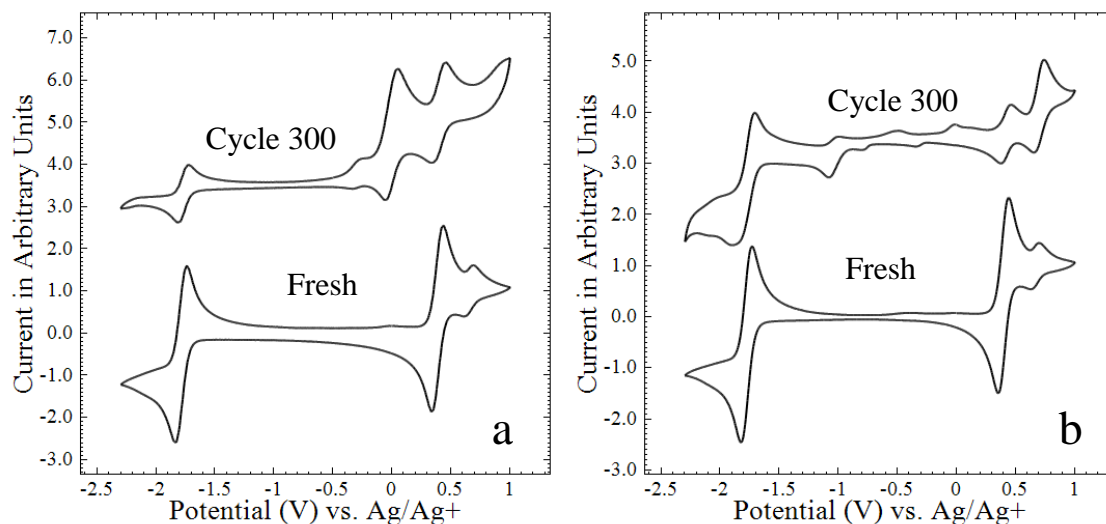
Figure 3.5.3-1 Cyclic voltammograms of 0.01M complex **1** with 0.5M TBABF$_4$ in acetonitrile before and after cyclic BE of the a) reduction reaction (E^1) and b) oxidation reaction (E^2).

In Figure 3.5.3-1a, the CV after cyclic reduction of complex **1** shows a new couple at ~0V and significantly decreased peak heights of the redox couples associated with the fresh material. The peak associated with complex **21** also appears to have decreased which is surprising as complex **21** is a reported irreversible side product during the oxidation of **1**. The couple at 0V could be due to the ligand, but free ligand is reported to have an irreversible oxidation peak and should not have an associated reduction peak. Figure 3.5.3-1b shows that after cyclic oxidation of complex **1** there are numerous peaks due to side reaction products. The predominant couple is at 0.65V which is reported to be due to the formation of complex **21**. There is an additional couple at -1.1V and several minor peaks ranging from -1.0V to 0V. The couple at -1.1V was also observed during shelf life experiments, and has been reported to be due to trace oxygen [36]. A similar couple is observed in CVs of spent complex **20** and is not observed in any of the CVs taken after cyclic BE of the other complexes. This indicates that the couple at -1.1V is not due to trace oxygen and is instead a side product specific to V(acac)$_3$ based complexes.

114

The complexity of these reactions as well as their similarities to the reactions of complex **20** prompted a detailed investigation which can be found in Chapter 4.
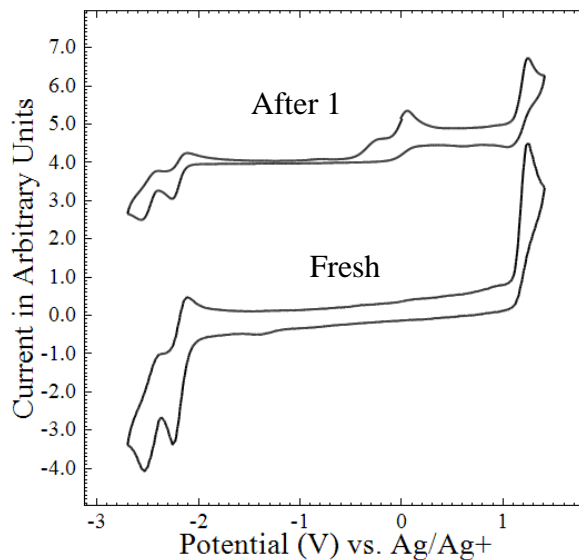
Figure 3.5.3-2 Cyclic voltammograms of 0.01M complex **2** with 0.5M TBABF$_4$ in acetonitrile before and after cyclic BE of the reduction reaction (E^2).

Figure 3.5.3-2 shows that after cyclic reduction, the CV of complex **2** includes an additional peak at 0V. This is likely due to free ligand as the reaction is irreversible and ligand detachment has been shown to occur during the reduction of complex **2** via *in situ* spectroelectrochemical experiments [40].
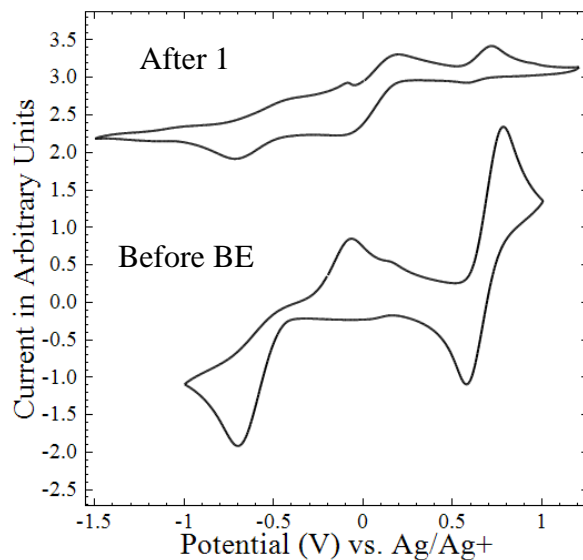
Figure 3.5.3-3 Cyclic voltammograms of 0.01M complex **3** with 0.5M TBABF$_4$ in acetonitrile before and after cyclic BE of the oxidation reaction (E^2).

The CV after cyclic oxidation of complex **3** shows that the couples associated with fresh **3** are significantly decreased after just one cycle. As the oxidation couple is almost completely eliminated from the CV, rapid capacity fade makes sense, and correlates well with the cycle life value of 0 (Table 2.3.4-1). There does not appear to be a significant peak due to side products, indicating that the primary side products are not electrochemically active within the potential window.
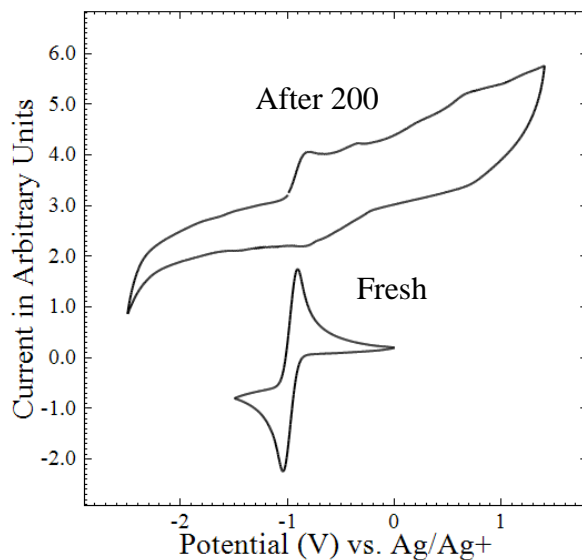
Figure 3.5.3-4 Cyclic voltammograms of 0.01M complex **4** with 0.5M TBABF$_4$ in acetonitrile before and after cyclic BE of the reduction reaction (E^1).

A CV was obtained after cyclic BE of complex **4**, which shows significant degradation of the fresh material, with the redox couple at -1V nearly depleted (Figure 3.5.3-4). There are no major peaks present in the CV after cyclic BE indicating that the primary side product is not electrochemically active within the voltage window. There is also no peak at 0V indicating no ligand shedding occurred.
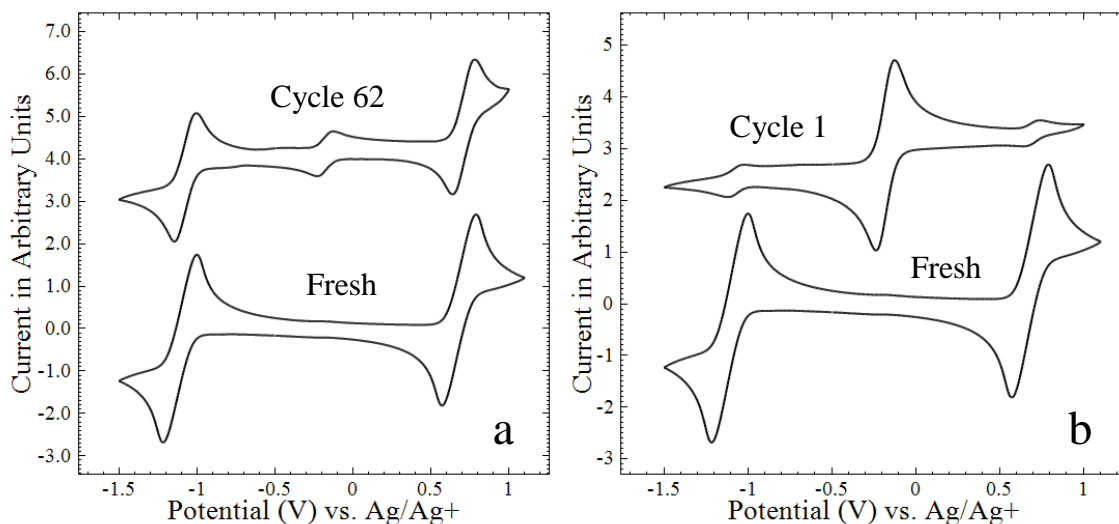
Figure 3.5.3-5 Cyclic voltammograms of 0.01M complex **7** with 0.5M TBABF$_4$ in acetonitrile before and after cyclic BE of the a) reduction reaction (E^1) and b) oxidation reaction (E^2).

A CV of complex **7** after cyclic reduction shows a minor couple at -0.2V due to an unknown side product (Figure 3.5.3-5a). It is not due to free ligand as the couple appears to be fairly reversible and is not at the correct potential. The couple is not the dominant signal after 62 cycles indicating the reduction reaction is fairly stable which is consistent with the cycle life value (43, Table 2.3.4-1). A CV of the electrolyte after cyclic oxidation also reveals a redox couple at -0.2V but in this case it is the dominant signal after just one cycle of the oxidation reaction. This makes sense as the capacity decreased to less than 80% of the initial value within the first cycle (Table 2.3.4-1). Both reactions will be further investigated in Chapter 4.
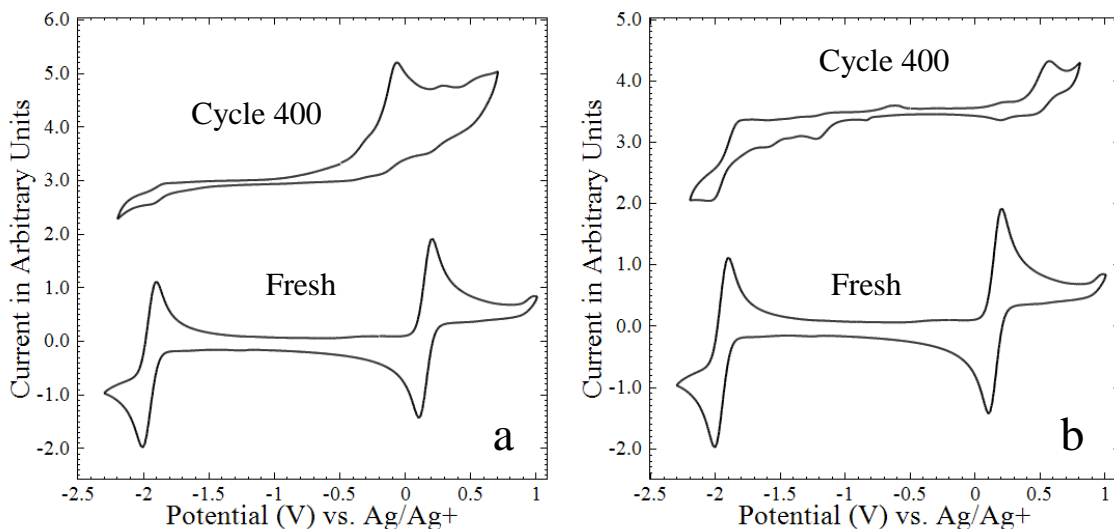
Figure 3.5.3-6 Cyclic voltammograms of 0.01M complex **20** with 0.5M TBABF$_4$ in acetonitrile before and after cyclic BE of the a) reduction reaction (E^1) and b) oxidation reaction (E^2).

In Figure 3.5.3-6a, the CV after cyclic reduction of complex **20** shows similar features that were observed for complex **1**. In particular there is a new couple at ~0V and signals for the redox couples associated with the fresh material are decreased. The couple at 0V was previously shown to be due to ligand detachment in Section 2.4.3. Figure 3.5.3-6b shows that after cyclic oxidation of complex **20** the resulting CV is very similar to the comparable CV of complex **1**. A number of peaks due to side reaction products are visible, and the dominant signal is a couple at 0.5V. This is similar to what was observed during flow cell studies and based on the results for complex **1**, this couple is likely due to a VO(acac)$_2$-like complex. Also in agreement with the results for complex **1**, is the presence of an additional couple at -1.1V. As previously mentioned, these similarities appear to contradict the hypothesis that the couple at -1.1V is due to trace oxygen, and is likely the result of an unknown vanadium species.
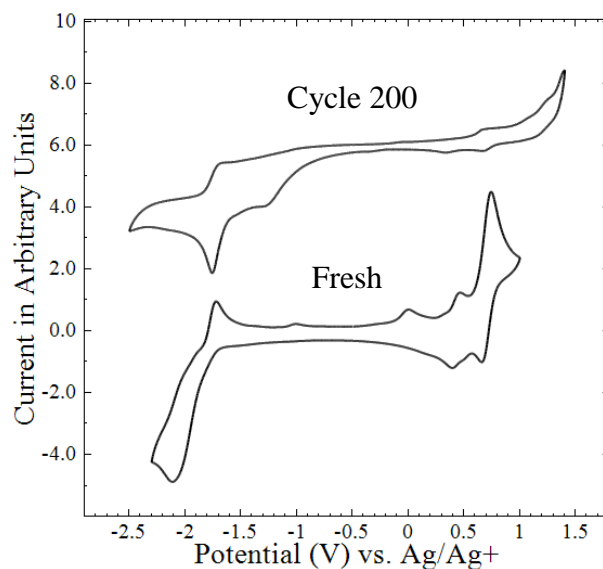
Figure 3.5.3-7 Cyclic voltammograms of 0.01M complex **21** with 0.5M TBABF$_4$ in acetonitrile before and after cyclic BE of the oxidation reaction (E^2).

Figure 3.5.3-7 shows that after long-term cyclic oxidation of complex **21**, very little initial active material remains in solution. The CV of the electrolyte after 200 cycles reveals a new couple at -1.7V which is caused by an unknown side product, and the couple at 0.65V associated with the fresh material is barely visible.
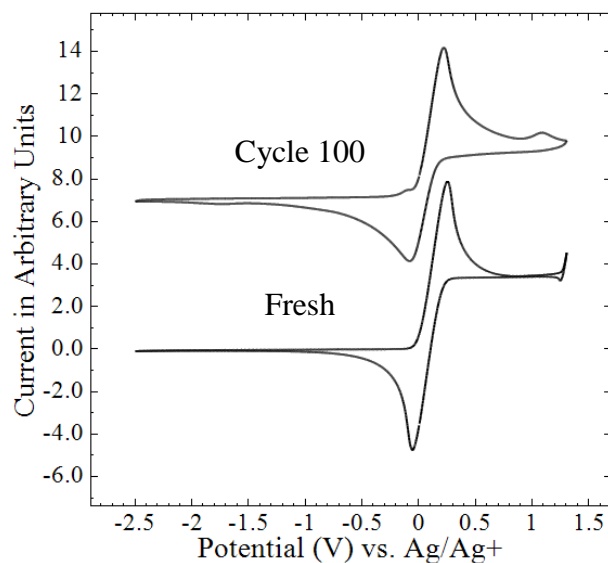
Figure 3.5.3-8 Cyclic voltammograms of 0.01M complex **22** with 0.5M TBABF$_4$ in acetonitrile before and after cyclic BE of the oxidation reaction (E^2).

Figure 3.5.3-8 shows that after 100 cycles of the oxidation reaction of complex **22**, the CV only slightly changes from that of the fresh material. This makes sense as Figure 3.5.2-1 shows that for complex **22**, 80% of the initial capacity is still available after 100 cycles. The peaks heights for the redox couples at 0.1V have decreased slightly indicating that the concentration of the active material has decreased, and the peak height ratio is no longer approximately unity. This could be caused by additional peaks due to side products at potentials near 0.1V, but this has not been confirmed. Regardless, the CV of the cycled material closely matches the capacity fade and the oxidation reaction of complex **22** is significantly more stable than the other acetylacetonate-based oxidation reactions.

3.5.4   Results: Correlations

Structural and electronic parameters were calculated for each complex tested by BE using DFT to understand the cause of electrochemical degradation. Of particular interest was the M-O bond length changes after reduction or oxidation, and the density of the LUMO/HOMO on the metal. The results can be seen in Table 3.5.4-1. Multi-term linear and non-linear regression analyses were performed using Minitab [130] to identify relationships linking the experimentally determined cycle lifes and the DFT parameters as well as the parameters previously assessed using CV (standard potentials, peak height ratios, kinetic rate constants, and diffusion coefficients). Linear, combination and exponential variables were all evaluated. The values of the CV assessed parameters were presented in Chapter 2, and can be found in Table 2.3.2-1 and Table 2.3.4-1. The resulting p-values from the linear regression analysis can be seen in Table 3.5.4-2.

Table 3.5.4-1 DFT calculated bond length changes and LUMO/HOMO densities of complexes tested by BE.

Complex (Redox Couple)	Average M-O Bond Length Change [Å]	LUMO/HOMO Density on Metal [%]
1 (E^1)	0.081	66
1 (E^2)	-0.079	57
2 (E^2)	0.008	23
2 (E^3)	-0.033	21
3 (E^2)	-0.120	34
4 (E^1)	0.104	75
7 (E^1)	0.044	67
7 (E^2)	-0.041	53
20 (E^1)	0.071	63
20 (E^2)	-0.073	55
21 (E^2)	-0.100	77
22 (E^1)	-	78

Table 3.5.4-2 p-values from linear regression analysis.

Parameter	p-Value
E^O	0.529
i_c/i_a or i_a/i_c	0.749
k^0	0.178
D_O	0.222
M-O bond change	0.524
MO metal density	0.014

All combination terms resulted in variance inflation factors (VIF) greater than 5, indicating a high degree of correlation between the variables, and were therefore removed as possible terms. As expected, the standard potentials, peak height ratios kinetic rate constants, and diffusion coefficients do not correlate with the experimentally determined cycle life values (p-values > 0.05). Chapter 2 established that the kinetic rate constants and diffusion coefficients were all within the same order of magnitude, and were therefore not likely to correlate the cycle life. Likewise, the peak height ratios are all above 0.8, but the complexes have a wide range of cycle lifes.

The calculated bond length changes do follow expected trends where the M-O bond decreases during reduction, and increases during oxidation. The acetylacetonate ligand is negatively charged, so a decreasing M-O bond during reduction indicates that a portion of the transferred charge is being stored on the metal. Likewise, an increasing bond during oxidation would indicate that some of the charge is coming from the metal. These trends hold true for all of the complexes analyzed. No bond length increased more than 0.1Å except for two M-O bonds for complex **1**, which could be why previous studies have reported ligand shedding for complex **1**. This will be further discussed in Chapter 4. While the overall M-O bond trends make sense, Table 3.5.4-2 shows that the degree of bond length change does not correlate to the experimentally determined cycle lives, and while ligand detachment could impact stability, it is probably not the primary degradation mechanism.
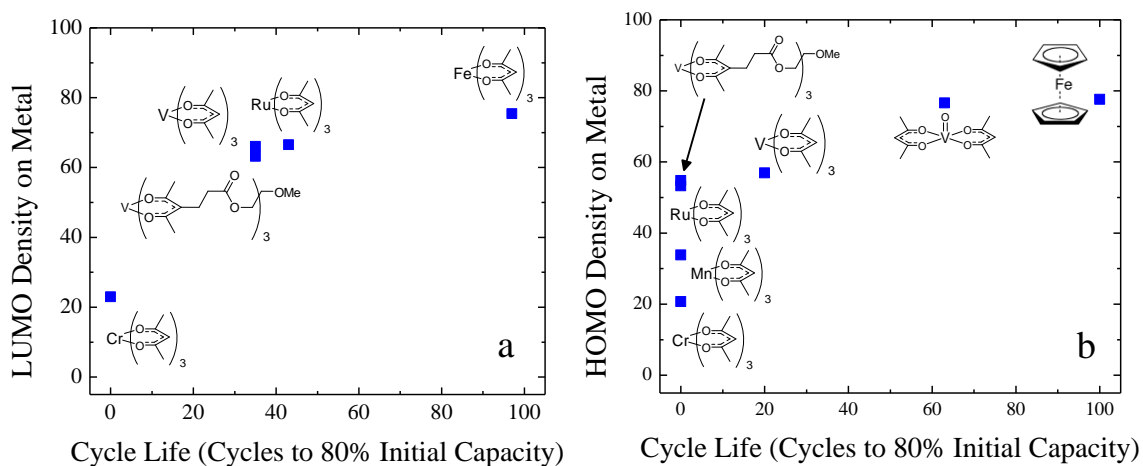
Figure 3.5.4-1 Percent density of LUMO for reduction reaction (a) and HOMO for oxidation reaction (b) on the metal versus cycle life as assessed by bulk electrolysis

The p-value for the molecular orbital density on the metal is less than 0.05, and therefore has a statistically meaningful impact on the cycle life. Figure 3.5.4-1 shows that

increasing the LUMO/HOMO density on the metal resulted in an increased cycle life for both the reduction and oxidation half-reactions. While the stability of **21** [VO(acac)$_2$] did not correlate with CV peak height ratios, it was found to have a much higher orbital density on the metal than the other acetylacetonate complexes. In this case, DFT assesses the reversibility of the reaction better than CV. For reduction half-reactions, Complex **4** was found to be the most stable, and also has the highest orbital density on the metal. These results indicate that the stability of acetylacetonate half-reactions is primarily a function of the orbital density on the metal, and any charge stored on the ligand increases the potential for side degradation reactions.

The aforementioned regression analysis resulted in a predictive equation following the form:

$$CycleLife = 365.7 * MO_{Density} - 196.5$$

<div align="right">Equation 3.5.4-1</div>

where MO$_{Density}$ is the molecular orbital density on the metal as a fraction of unity. A correlation was only possible for reactions with a metal orbital density greater than 50%. The predicted cycle lifes versus the experimentally determined cycle lifes can be seen in Figure 3.5.4-2, which results in an R^2 value of 0.90. This curve could be used to estimate the cycle life of a reduction and oxidation reaction of a given complex by using DFT calculations to optimize just the neutral species of a complex and obtaining the percent of the LUMO and HOMO, respectively, on the metal.
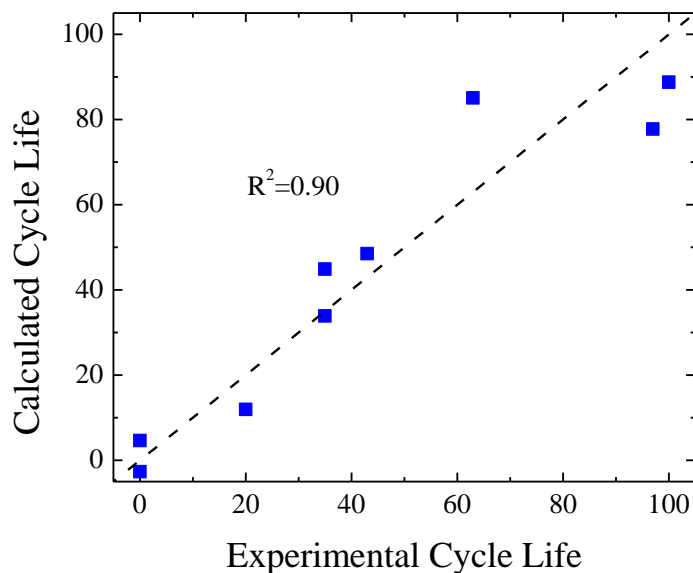
Figure 3.5.4-2 Calculated cycle life versus experimental cycle life for reactions with over 50% orbital density on the metal.

The cycle life of a half-reaction is therefore a function of both the metal and functional group, which influence the charge stored on or extracted from the metal during reduction or oxidation respectively. This makes sense based on the acetylacetonate ligand not possessing any reversible redox couples assessed by CV (Figure 2.4.3-5) [36]. If a metal is not capable of storing or supplying the required electron, the ligand is also not able to store or supply the charge, which will result in active species degradation. For screening of future complexes, complexes maximizing the molecular orbital density on the metal are desired.

3.6   Conclusions

Based on the solubility and shelf life studies, the primary cause for the observed capacity fade of metal(III) acetylacetonate-based electrolytes is electrochemical degradation. Shelf life studies revealed minimal changes in the CV signatures over time,

indicating minimal chemical degradation and adequate shelf lives within the timeframe required for cyclic bulk electrolysis experiments.

Bulk electrolysis was used to determine the cycle life of each half-reaction of various acetylacetonate-based MCCs with a CV current peak height ratio greater than 0.8. Various changes associated with electrochemical side reactions were observed in CVs of the spent electrolytes with ligand detachment commonly occurring during reduction, and oxidation side reactions appearing to be dependent on the metal type. $V(acac)_3$ based active materials appeared to form a $VO(acac)_2$ species upon oxidation, while $Ru(acac)_3$ formed a species with a fairly reversible couple, and $Mn(acac)_3$ and $Fe(acac)_3$ electrolytes formed species which were not electrochemically active within the potential window.

The quantified cycle life values were found to correlate linearly with the DFT calculated percentage of the LUMO/HOMO on the metal center. A calibration curve was generated for LUMO/HOMOs with greater than 50% density on the metal versus cycle life of the respective redox couple, which ccould be used to determine the expected cycle lives of redox couples of theoretical complexes to allow for high-throughput screening. This indicates that the stability of metal(III) acetylacetonate MCCs are primarily influenced by the degree of charge stored/extracted from the metal during reduction/oxidation which is contrary to the categorization of acetylacetonate ligands being innocent and charge transfer occurring entirely on the metal.

Chapter 4

Charge Storage Mechanism and Structural Changes

4.1 Background and Approach

Results presented in **Error! Reference source not found.** indicate that the cycle ifes for acetylacetonate-based MCCs correlate with LUMO and HOMO orbital density on the metal determined using DFT calculations. This suggests a correlation between the cycle life and oxidation state of the metal. This chapter described efforts to experimentally quantify the metal oxidation state. This enabled the degree of ligand innocence to be evaluated.

MCC ligands are defined as either innocent or non-innocent [27], [32], [33], which is a simplification. For metal(III) acetylacetonate complexes, charge transfer is assumed to occur only at the metal center [33]. That is the ligands are innocent. This chapter will experimentally test this assumption and determine if the degree of innocence impacts the cycle life.

Beyond the charge-storage mechanism, understanding the side reactions that occur during these electrochemical processes is important for establishing structure-function relationships. If bond length changes correlate to particular degradation mechanisms, then synthetic methods could be devised to increase the strength of these bonds. Furthermore, CV and UV-Vis are the only techniques that have been used to characterize electrolytes after cycling experiments. CVs of cycled electrolytes were

presented in Section 3.5.3, indicating that ligand detachment occurs during reduction for several acetylacetonate-based active materials, but the products of oxidation side reactions were more difficult to identify, and CV has already been shown to be insufficient for characterizing bulk oxidation state changes. Both techniques also do not allow for the determination of unknown species beyond obtaining CVs or UV-Vis spectra for suspected side products and verifying that peaks occur in approximately the same locations.

X-Ray Absorption Spectroscopy (XAS), can be used to define detailed structural information such as bond lengths, bond angles, and oxidation states of metals, and can be conducted *in situ* during electrochemical reduction or oxidation. With this technique, the degree of ligand innocence, as well as structural changes during electrochemical reduction and oxidation reactions can be quantified. If a side product is at high enough concentrations, XAS could also be used to identify the unknown species.

There are very few reports of the use of XAS to characterize RFB electrolytes. Xie and co-workers reported results for a high-concentration aqueous vanadyl sulfate ($VOSO_4$) (1.5M, with 2.0 M H_2SO_4) solution, indicating the transition from vanadium(III) (V^{3+}) to vanadium(II) (V^{2+}) during anode-side charging and the transition from VO^{2+} to VO_2^+ during cathode-side charging [131]. These results are consistent with the currently understood model for charge storage in aqueous vanadium RFB systems [12], [13]. Prior work in Fe-based ionic liquid RFBs demonstrated that oxidation and reduction resulted in a slight increase and decrease in Fe-O bond length of the active species $[Fe[(OHCH_2CH_2)_2NH]_6-(CF_3SO_3)_3]$. The Fe oxidation state was also found to increase or decrease, with formal charge inferred by X-ray absorption near edge structure

128

(XANES) being less than expected for full charge or discharge. However, actual XANES-derived Fe formal charge values, and correlation of Fe oxidation state to the ionic liquid state of charge, were not determined because of mixing issues within the cell [132]. To the best of our knowledge, this is the only report of the use of XAS to characterize a non-aqueous RFB electrolyte.

For this chapter, two representative metal(III) acetylacetonates [$V(acac)_3$ (complex **1**) and $Ru(acac)_3$ (complex **7**)] previously presented in Chapter 2 and **Error! eference source not found.** were characterized using XAS during reduction and oxidation to quantify oxidation states and examine structural changes. Cyclic BE was used to reduce of oxidize the electrolytes, and *in situ* CV was used to compare with the XAS results.

4.2   Experimental Techniques

4.2.1   X-Ray Absorption Spectroscopy [133], [134]

XAS is a technique which probes the electronic properties and local geometry of specific elements by employing high intensity X-rays to excite core electrons to unoccupied electron states. Each element has a characteristic edge energy required to excite electrons through specific transitions, resulting in a sharp increase in absorption called an "edge." The absorption (difference in photon flux before and after excitation) is monitored over an energy range which is consists of two regions. The energy region ±30 eV of the edge energy is referred to as the X-ray absorption near edge structure (XANES). In this energy range, the electron may be excited into the valence band, which can be used to obtain information regarding geometry (tetrahedral, octahedral, etc.), and oxidation state of the element. The energy range ~40-1000 eV beyond the edge energy is

known as the extended X-ray fine absorption structure (EXAFS). In this energy range, the electron has sufficient energy to be fully ejected from the absorber atom, resulting in constructive and destructive interference of spectral waves caused by the ejected photoelectrons interacting with nearby atoms. This region can be used to quantify bond distances, coordination numbers, and identify the neighboring elements.

4.2.2 Vanadium(III) Acetylacetonate

The characterization of non-aqueous vanadium chemistries using XAS is particularly challenging. These challenges include the necessarily low concentration of the vanadium species (<0.1 M) in typical organic solvents such as ACN, the high concentration of support (0.5M), and the rapid degradation of these species upon exposure of ppm levels of H_2O. Measurements are further compounded by the low energy (5 keV) photons needed to characterize V, which are readily attenuated by ACN. For these reasons, in situ XAS was not possible, and instead XAS was performed on aliquots of the electrolyte taken during BE experiments.

BE experiments were carried out following the same procedure described in Section 3.2.1 with *in situ* CVs taken at intervals during the experiment. For the reduction reaction, the potential was held at -2.1V vs. Ag/Ag^+ to first reduce the material, and subsequently held at -1.4V vs. Ag/Ag^+ to re-oxidize the material. For the oxidation reaction, the potential was held at 0.5V vs. Ag/Ag^+ to oxidize the material, and subsequently held at 0V vs. Ag/Ag^+ to reduce the material back to the neutral state. A current cut-off of 0.1mA was used. For XAS experiments, one BE cycle was performed and aliquots were obtained at steps during the cycle. While aliquots were obtained, BE was stopped, and CV scans were conducted to monitor the change in the electrochemical

130

signature. By stopping the BE process during the CV scans, the length of the experiment results in high cross-over.

The XAS experiments were completed at beamline 10-BM (MR-CAT) of the Advanced Photon Source, Argonne National Laboratory. The beam size was set at 0.5 x 0.5 mm. A 1 mm polyimide capillary tube filled with sample was aligned in the beam with a silicon drift detector (Hitachi Vortex) at a 90° angle to the beam path. All samples were aligned to the metal reference prior to analysis. Data analysis was done using the Demeter software package [135]. XANES analysis consisted of observing shift in edge energy as well as transitions from one species to another as calculated by linear combination fitting (LCF) to known standards.

Measurements were taken in fluorescence mode for the $V(acac)_3$ electrolyte which had previously undergone BE cycling, as well as vanadium standards of V metal, VO_2, V_2O_3, $VO(acac)_2$, and VCl_3. Samples of previously cycled $V(acac)_3$ electrolyte were stored in Kapton capillary tubes in three layers of oxygen-free containers. X-ray collection was taken from 200 eV below the edge of V metal (V E_0 = 5565 eV) to approximately 1200 eV above the edge (~18 $Å^{-1}$) with each measurement taken over the course of 30 minutes. Particular care was taken to capture the edge shape and pre-edge feature, if any. EXAFS data were generated with an AUTOBK function with a spline range from 0 to 18 $Å^{-1}$, Rbkg=1.0 and a normalization order of 2.

Due to the low concentration of $V(acac)_3$ in the samples (0.01 M) and high attenuation of x-rays of this energy in ACN (C_2H_3N, 0.786 g cm^{-3}, absorption length 760 μm at V E_0=5565 eV) useful EXAFS could only be collected in the range 2<k<6 $Å^{-1}$ regardless of collection time. Fourier transform of this $χ(k)$ yields EXAFS spectra useful

for qualitative comparison but with insufficient independent data points for detailed data analysis.

4.2.3 Ruthenium(III) Acetylacetonate Experiments

For Ru(acac)$_3$, constant voltage BE was performed following the procedure described in Section 3.2.1 at a concentration of 0.1M active species with 0.5M TBABF$_4$ in ACN. To characterize the oxidation reaction, the electrolytes were evaluated following BE at 0.8 and 0.4 V versus Ag/Ag+. To characterize the reduction reaction, the electrolytes were evaluated following BE at -1.5 and -0.7 V versus Ag/Ag+. Samples before and after BE were diluted to 0.01M active species with 0.1M TBABF$_4$ in ACN and CVs were collected.

A custom Teflon cell (Figure 4.2.3-1) was built for the *in situ* X-ray absorption experiments run at Argonne National Lab, constructed in the Physics machine shop at the University of Michigan. The cell consisted of three parts: a working electrode chamber, a counter electrode chamber, and a block used to seal a P5 glass frit (Adams & Chittenden) between the two electrode chambers. The dimensions of the counter and working electrode cavities were designed to ensure that the liquid heights were equal when using 5mL of solution in both chambers. The counter electrode chamber (shown on the left side of all explosion diagrams in Figure 4.2.3-1) consists of a 2" long cavity of 0.625" diameter. At the top of the cavity was threading for a 1/2" NPT fitting, where a Pt wire counter electrode was secured using a ¼" Swagelok ultra-torr fitting. A 0.9cm diameter hole was cut into the cavity with an expanded diameter (to 1cm diameter) at the edge to house a #12 Viton o-ring. In the middle connecting block a 1cm diameter groove is cut 8mm into the 1cm slab, with the last 2mm consisting of a reduced hole of 0.9cm diameter

to house a #12 viton o-ring. The working electrode chamber (Figure 4.2.3-2) consisted of a large rectangular cavity to house the working and reference electrodes, and a 1cm x 1cm x 1cm cavity, which acted as the viewing area for X-rays. 7.5mm diameter holes were cut into the sides of the 1x1x1cm cavity, leaving ~250μm thick walls of Teflon to act as "windows" for the X-rays while maintaining an air-tight seal. The working electrode chamber was sealed against the connecting block using a #26 Viton o-ring, housed in an o-ring cut-out. The working electrode, a 1x1x5cm^3 strip of 60 pore per inch reticulated vitreous carbon (ERG Aerospace) attached to a wire using silver epoxy and a 7mm glass tube, was secured in the top of the working electrode chamber using a 1/4" Swagelok ultra-torr fitting with an 1/8" NPT outlet. The reference electrode (Ag/Ag$^+$) was similarly secured using a 1/4" Ultra-Torr to 1/8" NPT Swagelok fitting at a 30° angle to the bottom face, aimed at contacting the top of the liquid in the cell.
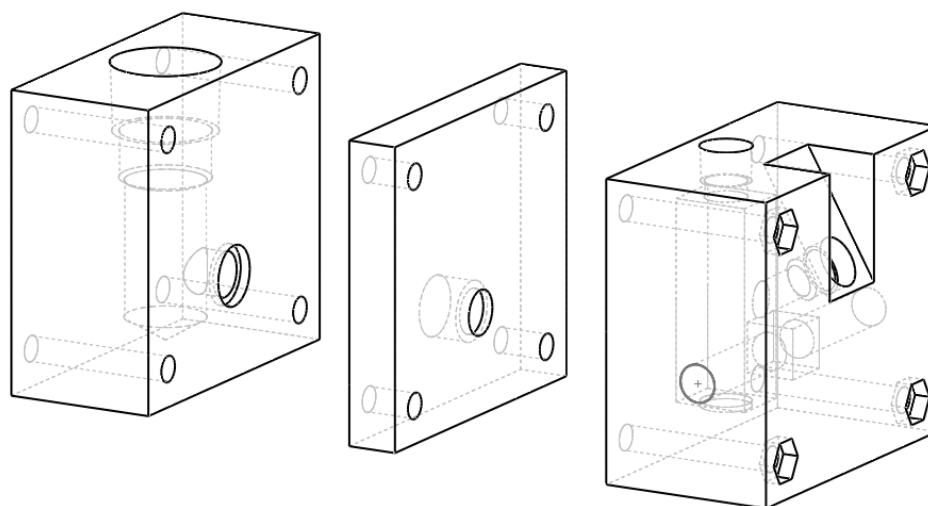
Figure 4.2.3-1 Exploded view diagrams of the bulk electrolysis cell used in the in situ X-ray absorption experiments. From left to right: Counter electrode block, connecting block, working electrode block.
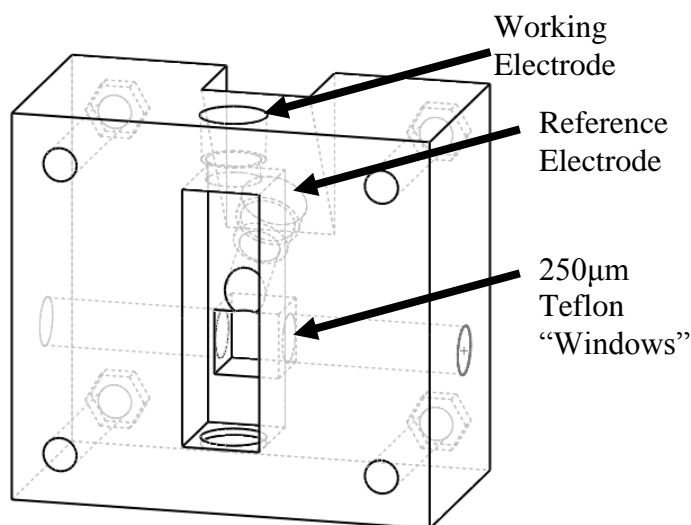
Figure 4.2.3-2 Schematic of working electrode chamber.

Figure 4.2.3-3 Assembled Bulk Electrolysis cell.

Prior to the experiments at Argonne National Lab, the cell was validated at the UM by performing BE of the reduction reaction and oxidation reaction of 0.1M $Ru(acac)_3$ with 0.5M $TBABF_4$ in ACN. The resulting charge-discharge curves were found to closely match the results observed using a conventional glass electrochemical cell (see Section 4.4.2) and correlate to the cycle life values reported in Table 3.5.2-1.

These results are for validation purposes, and the specifics of the reactions will be discussed in Section 4.4.2.
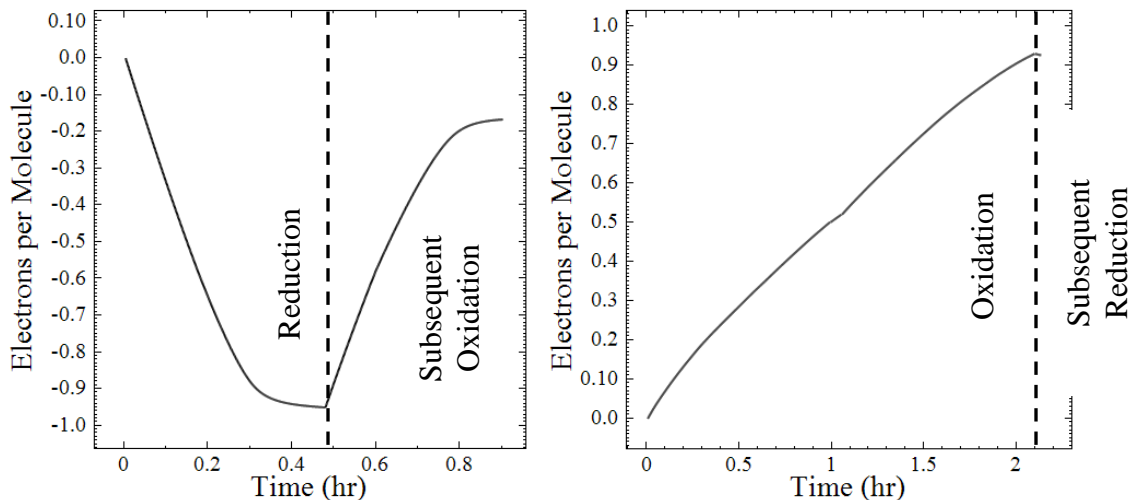
Figure 4.2.3-4 Electrons per molecule transferred during BE of the reduction reaction (left) and oxidation reaction (right) in Teflon XAS cell.

To ensure that the cell is air tight, CVs of air and water sensitive $V(acac)_3$ electrolytes were collected over time. $V(acac)_3$ has been shown to convert to $VO(acac)_2$ after exposure to air, and the conversion to $VO(acac)_2$ can be monitored using CV [36]. As seen in Figure 4.2.3-5, following air exposure to the Teflon cell for 12 hours, well in excess of the time required for the bulk electrolysis experiments, the CV signature of the $V(acac)_3$ electrolyte remains unchanged. This indicates that the cell is well sealed and any changes observed by XAS are not due to interactions with air or water.
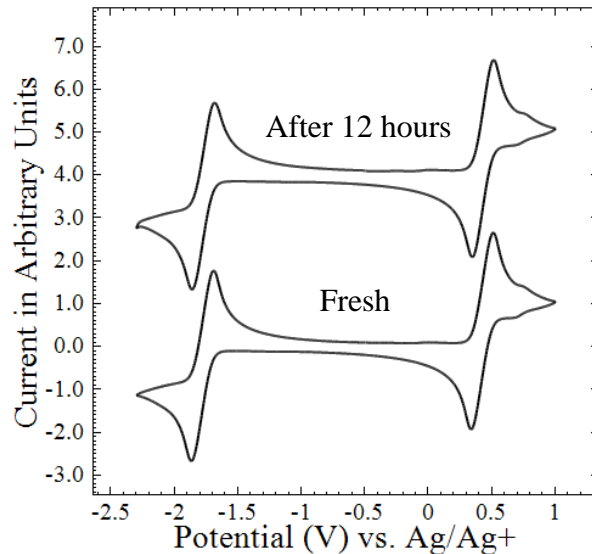
Figure 4.2.3-5 Cyclic voltammograms of 0.01M vanadium(III) acetylacetonate with 0.5M TBABF$_4$ in acetonitrile inside air-exposed Teflon XAS cell.

The XAS experiments were performed at beamline 10-BM (MR-CAT) of the Advanced Photon Source, Argonne National Laboratory. Beam size was set at 0.5 x 0.5mm and experiments were conducted in transmission mode with gas ionization chambers. XANES analysis consisted of observing changes in edge shift as well as transitions from one species to another as calculated by linear combination fitting (LCF) to known standards.

X-ray collection was taken from 200eV below the K edge of Ru metal (Ru K E$_0$ = 22117eV) to approximately 1200eV above the edge (~18Å^{-1}) with each measurement taken over the course of 30 minutes. EXAFS analysis was completed using the AUTOBK algorithm with a spline range from 0 to 18Å^{-1}, Rbkg=1.0 and a normalization order of 3. The EXAFS range was found to be excellent out to 18Å^{-1} and a Fourier transform was made using 3<k<16A^{-1}.

Sepctra for several Ru standards (Ru metal, Ru(acac)$_3$, tris(triphenylphosphine) ruthenium (II) dichloride (TTP-RuCl$_2$), RuO$_2$, and RuCl$_3$) were collected in polycarbonate cuvettes (liquid samples) or the material was ground to a fine powder and loaded into polyimide tape packets (solid samples).

The cell shown in Figure 4.2.3-3 was placed in the beamline such that a 1cm length of electrolyte could be measured in transmission mode (edge step ~0.7eV). The reduction and oxidation reactions were tested separately by conducting BE of the individual half-reactions charged from 0.0 electrons per molecule ("before electrolysis") to the maximum electrons per molecule in steps of 0.2, and subsequent discharge, with XAS measurement taken at each step. The BE experiment was conducted using the same method as described in Section 3.2.1 while using the Teflon cell. For the reduction reaction, the electrons per molecule were determined using the open circuit potential and the Nernst equation. For the oxidation reaction, the open circuit potential was not a reliable method of determining the electrons per molecule due to the side reaction changing the open circuit potential. Monitoring of current during each step demonstrated negligible changes in the oxidation state of the electrolyte while XAS was being collected.

4.3   Vanadium(III) Acetylacetonate

4.3.1   Background and Approach

Results in the literature, Chapter 2 and **Error! Reference source not found.** all ndicate that vanadium(III) acetylacetonate-based complexes form vanadyl(IV) acetylacetonate [VO(acac)$_2$] during oxidation, and shed the acac ligand during reduction [36], [40], [41]. The causes for these reactions are unknown, and understanding the cause

137

could allow for the design of more robust acetylacetonate-based complexes. Furthermore, active species concentrations determined from CVs of the cycled electrolytes are typically higher than expected based on capacity fade [36], [40], [41], indicating that other processes are occurring.

4.3.2   Results: Electrochemical Characterization
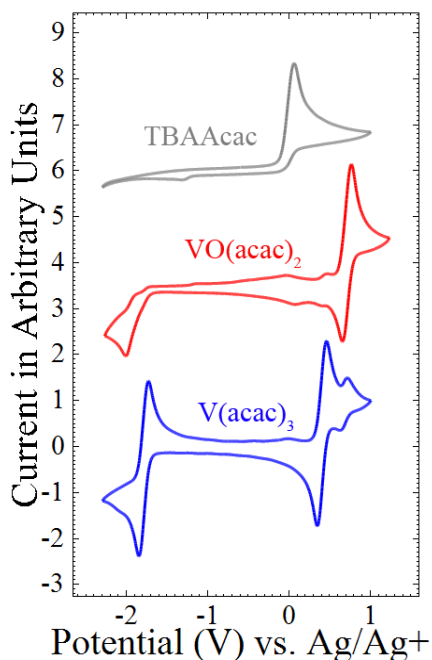
Figure 4.3.2-1 Cyclic voltammograms of TBAacac (gray), VO(acac)$_2$ (red) and V(acac)$_3$ (blue). Solutions comprised of 0.01M active species and 0.1M TBABF$_4$ in acetonitrile.

Cyclic voltammograms for a solution of V(acac)$_3$ in ACN with TBABF$_4$ (Figure 4.3.2-1) are consistent with Figure 2.3.2-1 and literature reports that the electrochemistry includes two quasi-reversible couples separated by ~2.2V, with minor couples at -2.1V, 0V, and 0.7 V [34]. The minor features are likely the consequence of VO(acac)$_2$ redox. Indeed, the CV for a solution of VO(acac)$_2$ in ACN includes couples at -2.1V and 0.68V, consistent with Figure 2.3.2-5 and reports in the literature [36], as well as a small oxidation peak at 0V. The irreversible oxidation of free acetylacetonate ligand has also

been reported to occur at 0 V [36], [41]. The CV for tetrabutylammonium acetylacetonate (TBAacac) in ACN (Figure 4.3.2-1) includes an oxidation peak at ~0V.

To characterize the cycle life of species at the negative electrode, the potential was held at -2.1V to completely reduce the electrolyte, then held at -1.4V to re-oxidize the electrolyte; this constituted a cycle. To characterize the reactions at the positive electrode, a cycle consisted of holding the potential at 0.5V to completely oxidize the electrolyte, then holding it at 0V to reduce the electrolyte. Variations in the measured capacity with cycle number are illustrated in Figure 4.3.2-2 along with the theoretical capacities estimated from CVs taken during the experiments; the CVs are illustrated in Figure 4.3.2-3.
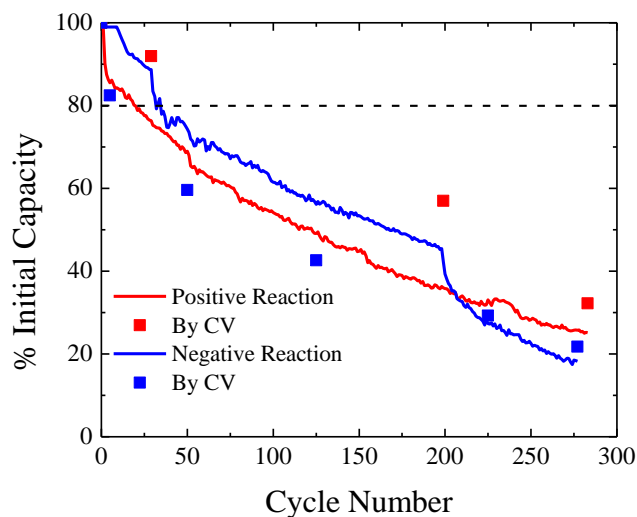
Figure 4.3.2-2 Capacity versus cycle number during cyclic BE of the reduction reaction (purple) and oxidation reaction (blue) of 0.01M V(acac)$_3$ with 0.5M TBABF$_4$ in acetonitrile. Theoretical capacity values were quantified using peak heights of cyclic voltammograms taken during experiment. Several of such cyclic voltammograms can be found in Figure 4.3.2-3.
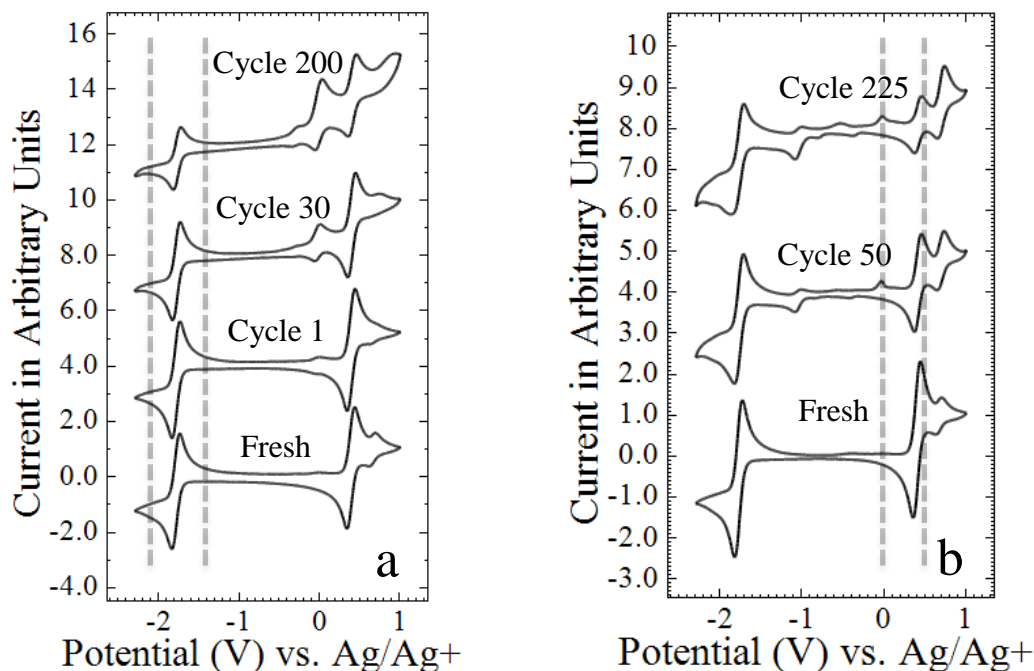
Figure 4.3.2-3 Cyclic voltammograms of V(acac)$_3$ during cyclic BE of the reduction reaction (a) and oxidation reaction (b). Solutions comprised of 0.01M active species and 0.5M TBABF$_4$ in acetonitrile. Dashed lines indicate holding potentials.

The initial BE cycles reached 97 and 100% of the theoretical capacity based on one equivalent per complex at the negative and positive electrodes, respectively. The capacities determined from the V(acac)$_3$ peak heights in CVs do not match the measured capacities. One can think of this as a species/charge balance – matching solution chemistry with charge-discharge capacities. For reactions at the negative electrode, the CV results typically underestimate the measured capacities while CV results overestimate the capacities for reactions at the positive electrode. This latter observation is consistent with reports in the literature that CVs of the catholyte after cycling contained more V(acac)$_3$ than could be accounted for based on the measured capacities [41].

The lower than anticipated concentration of V(acac)$_3$ at the negative electrode relative to the measured capacity could be a consequence of the presence of other, unaccounted for redox active species in the electrolyte. The CVs reveal an increase in the

intensity of a species at ~0V (Figure 4.3.2-3). This couple coincides with those for the free ligand and/or $VO(acac)_2$ (Figure 4.3.2-1), however, the redox couples at 0.68 and -2.1V, associated with $VO(acac)_2$, were not observed suggesting that the peak at ~0V is due to free ligand. The resulting metal complex does not appear to be electrochemically active in the stability window of the electrolyte. We believe redox of the free ligand could account for some if not all of the differences between the concentrations of $V(acac)_3$ and measured capacities at the negative electrode.

Behavior at the positive electrode was not as easy to explain. From CV, a significant amount of $VO(acac)_2$ was present in addition to $V(acac)_3$ with the couple associated with $V(acac)_3$ decreasing as the couple for $VO(acac)_2$ increased (Figure 4.3.2-3). The amounts of these two species do not account for capacities measured during charge-discharge experiments. The most likely explanation is that there is another species that contributes to the CV associated with $V(acac)_3$, and is not highly reversible. We hypothesize that this species is a product of reactions with $VO(acac)_2$. Consequently, BE was performed on a solution of $VO(acac)_2$ in ACN at -2.1V vs. Ag/Ag^+. Figure 4.3.2-4 compares CVs for solutions before and after BE, with those for the $V(acac)_3$ solutions. After BE, the CV of the $VO(acac)_2$ solution is very similar to that for the $V(acac)_3$ solution, with an irreversible oxidation peak at ~0V. It is unlikely that $VO(acac)_2$ converted back to $V(acac)_3$; in fact, this reaction is reported to be irreversible without a significant excess of acetylacetone [39]. The XAS results will provide important structural information regarding this new species.
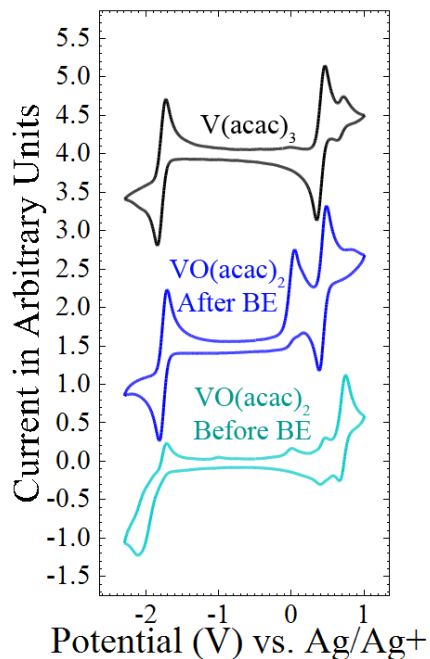
Figure 4.3.2-4 Cyclic voltammograms of VO(acac)$_2$ Before BE (teal), VO(acac)$_2$ After BE (blue) and V(acac)$_3$ (black). Solutions comprised of 0.005M (VO(acac)$_2$) or 0.01M (V(acac)$_3$) active species and 0.1M TBABF$_4$ in acetonitrile.

4.3.3 Results: Structural Characterization

X-ray absorption spectra at the V K-edge were collected for V(acac)$_3$ solutions as well as several standards, and the results are illustrated in Figure 4.3.3-1 for the first cycle at the negative electrode. Vanadium complexes that lack inversion symmetry, such as tetrahedral or distorted octahedral V-O geometries, produce a strong pre-edge feature at the V K-edge while inversion-symmetric structures such as octahedral V-O have a very weak pre-edge feature [136], [137]. V(acac)$_3$, which is octahedral, would have a very weak pre-edge while VO(acac)$_2$, which is square pyramidal, would have a very strong pre-edge feature.
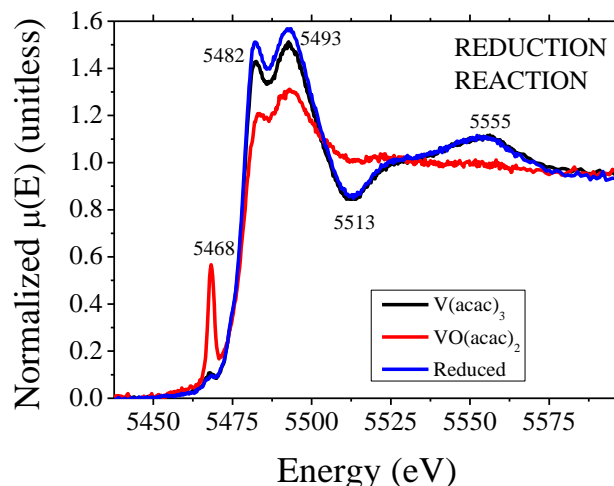
Figure 4.3.3-1 XANES of 0.01M V(acac)$_3$ with 0.5M TBABF$_4$ in acetonitrile after reduction.

After reduction of the V(acac)$_3$ solution, intensities of the peaks at 5482 and 5493 eV were reduced slightly, while the post-edge peaks at 5513 and 5555 eV were unaffected. This result is consistent with the CV which indicated little change after cycling at the negative electrode (Figure 4.3.2-3). The spectrum for VO(acac)$_2$ is also illustrated in Figure 4.3.3-1. Given the absence of VO(acac)$_2$ at the negative electrode, the cause of the peak observed in the CV at 0V was likely the free ligand that detached from V(acac)$_3$. DFT was used to optimize the structures for V(acac)$_3$ and [V(acac)$_3$]$^{-1}$, and the results can be seen in Table 4.3.3-1 and Figure 4.3.3-2.

Table 4.3.3-1 DFT optimized V-O bond lengths for [V(acac)$_3$]$^{-1}$ and V(acac)$_3$.

Species	V-O 1 Length (Å)	V-O 2 Length (Å)	V-O 3 Length (Å)	V-O 4 Length (Å)	V-O 5 Length (Å)	V-O 6 Length (Å)
[V(acac)$_3$]$^{-1}$	1.985	2.011	2.010	1.985	2.016	2.015
V(acac)$_3$	2.084	2.084	2.084	2.084	2.084	2.084
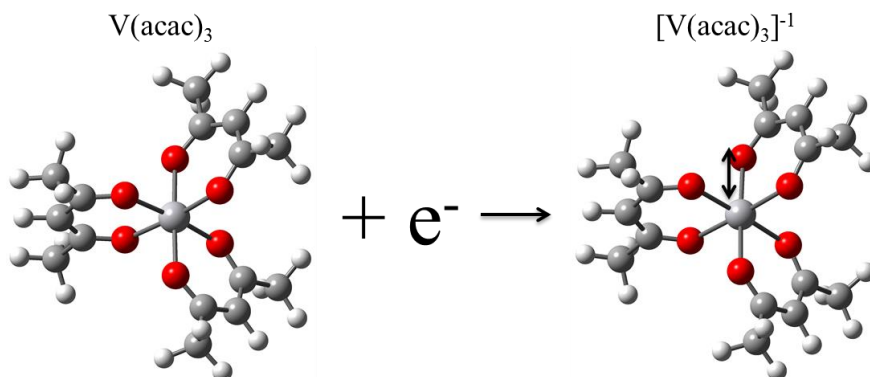
Figure 4.3.3-2 DFT optimized structures of V(acac)$_3$ and [V(acac)$_3$]$^{-1}$

The V-O bond lengths were predicted to increase by an average of 0.08Å after reduction with V-O bonds 1 and 4 increasing by 0.1Å (Table 3). This is very close to the limit where bond rupture would occur (0.1Å) according to results from previous studies [84]. Based on these findings, reactions at the negative electrode consist of the reversible reduction of V(acac)$_3$, and a minor amount of ligand shedding.
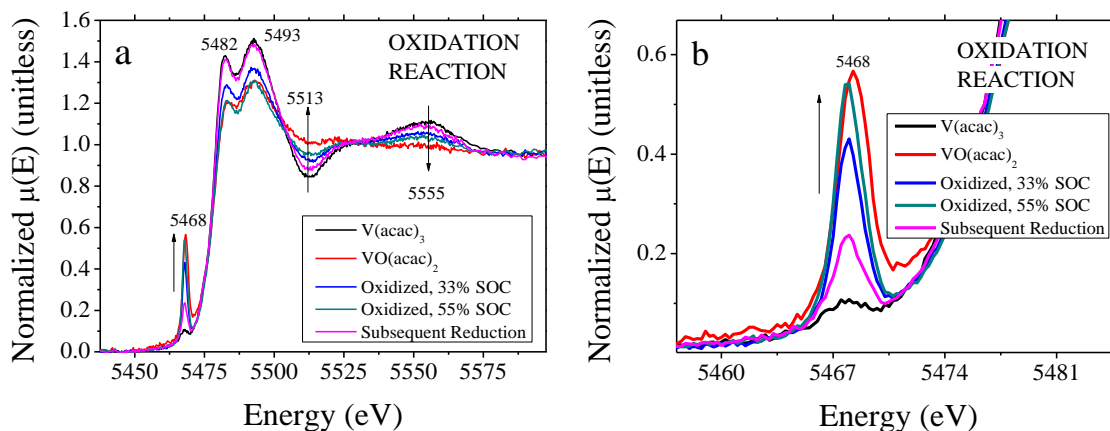
Figure 4.3.3-3 XANES of V(acac)$_3$ during oxidation reaction (a) and pre-edge during oxidation reaction (b) compared to fresh V(acac)$_3$ and VO(acac)$_2$.

X-ray absorption spectra at the V K-edge were also obtained during the first cycle of the oxidation reaction (Figure 4.3.3-3). After oxidation of the V(acac)$_3$ solution, peaks emerged at 5482, 5493, 5513 and 5555 eV in the XANES; these as well as the pre-edge feature at 5468 eV are consistent with the presence of VO(acac)$_2$. After oxidation, the

XANES is consistent with the sample consisting of only 23% $V(acac)_3$ and 77% $VO(acac)_2$, based on a linear combination fit of the XANES to $V(acac)_3$ and $VO(acac)_2$ standards (Table 4.3.3-2). This formation appears to be mostly reversed during subsequent reduction (Figure 4.3.3-3b), however, the reduction of $VO(acac)_2$ back to $V(acac)_3$ seems unlikely given the low concentrations of free ligand in solution. As we proposed earlier, it is likely a newly formed species; this species has a pre-edge feature similar to $VO(acac)_2$ and CV similar to $V(acac)_3$.

Table 4.3.3-2 XANES linear combination fitting of $V(acac)_3$ samples.

Reaction	SOC [%]	$V(acac)_3$ [%][a]	V charge[b]
Reduction	0	100±5	3.0±0.1
Reduction	100	100±5	3.0±0.1
Oxidation	0	100±5	3.0±0.1
Oxidation	33	43±5	3.6±0.1
Oxidation	55	23±5	3.8±0.1
Subsequent Reduction	6	75±5	3.2±0.1

[a] Percent of $V(acac)_3/(V(acac)_3+VO(acac)_2)$ determined. [b] Average formal V charge based on fraction of vanadyl.

Given the high concentration and mass action, it is possible that MeCN (ACN) coordinates to $VO(acac)_2$. Note that coordination with the support (TBABF$_4$) would result in a decrease in conductivity, and the resistance of the cell was stable throughout the experiments. DFT structure optimization calculations for both $VO(acac)_2$ and $VO(acac)_2ACN$, were conducted (Figure 4.3.3-4) and XYZ coordinates can be found in Appendix A.
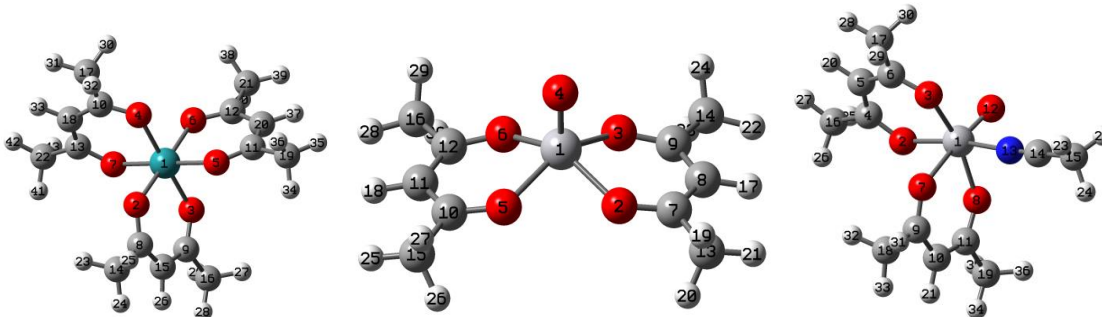
Figure 4.3.3-4 DFT optimized, proposed structures of V(acac)$_3$ (left), VO(acac)$_2$ (center), and VO(acac)$_2$MeCN (right).

VO(acac)$_2$ optimized to a square pyramidal structure, while VO(acac)$_2$MeCN optimized to an octahedral structure. The calculated positive couple for VO(acac)$_2$MeCN is 0.22V vs. Ag/Ag+; this is very close to the potential of V(acac)$_3$. It cannot be verified that the ACN ligand would increase the reversibility of the VO(acac)$_2$ oxidation couple based on structure optimization calculations, but a negative shift in the redox couple could explain why the CV at the positive electrode does not appear to change after cycling, while the XAS spectra do.

Table 4.3.3-3 List of EXAFS photoelectron paths for simulated V species.

V(acac)$_3$			VO(acac)$_2$			VO(acac)$_2$MeCN		
Path	Degen[a]	Distance [A]	Path	Degen[a]	Distance [A]	Path	Degen[a]	Distance [A]
V-O[b]	6	1.98	V-O[b]	1	1.56	V-O[b]	1	1.59
V-C	6	2.94	V-O[b]	4	1.97	V-O[b]	3	2
V-O-C	12	3.10	V-C	4	2.95	V-N	1	2.17
			V-O-C	8	3.10	V-O	1	2.19
						V-C	2	2.97

[a] Degeneracy. Synonymous with coordination number.
[b] Paths used in simulation. Additional parameters: σ^2=0.003 Å^2, ΔE^0=0 eV, S_0^2=0.8.

The same DFT-optimized structures were plotted as virtual paths overlaying our experimental EXAFS data (Table 4.3.3-3). In Figure 4.3.3-5, the V(acac)$_3$ and VO(acac)$_2$ EXAFS simulations correspond well with the experimental results. The simulation for

VO(acac)$_2$ACN appears at the range of the charged and discharged species, further supporting the coordination of VO(acac)$_2$ with ACN upon subsequent reduction.
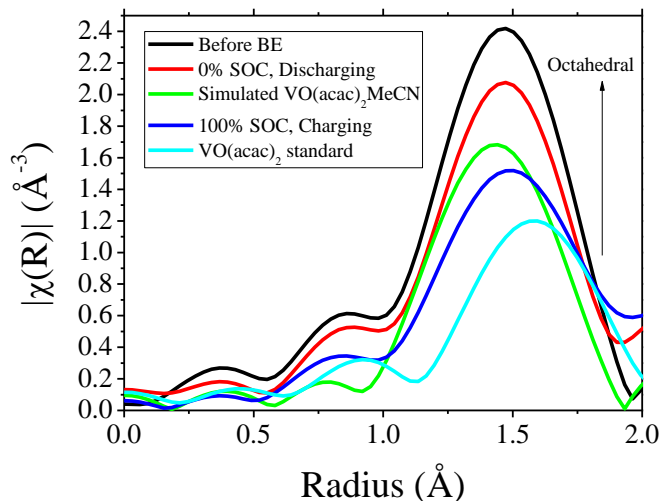
Figure 4.3.3-5 Oxidation reaction species compared with simulated EXAFS spectra.

Based on these results, we propose that the following reactions occurred at the positive electrode:

$$V(acac)_3 \leftrightarrow [V(acac)_3]^{+1} + e^- \qquad \text{Equation 4.3.3-1}$$

$$V(acac)_3 \rightarrow VO(acac)_2 + e^- + \text{ligand fragments} \qquad \text{Equation 4.3.3-2}$$

$$VO(acac)_2 + MeCN + e^- \leftrightarrow VO(acac)_2MeCN \qquad \text{Equation 4.3.3-3}$$
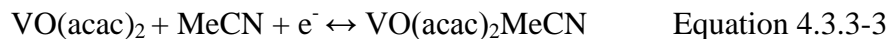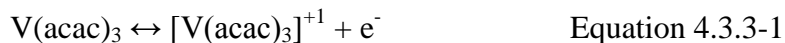
Equation 4.3.3-3 appears to be dominant, and as it is not completely reversible (Figure 4.3.3-3), it helps rationalize previous reports of the poor cyclability of V(acac)$_3$ based electrolytes.

4.3.4 Results: Charge Distribution Characterization

The DFT and XANES results allowed a determination of charge distributions within the products of V(acac)$_3$ oxidation and reduction. For metal(III) acetylacetonate complexes, redox is assumed to occur only at the metal center [33], that is the ligands are innocent. The oxidation state was experimentally determined by the edge shift in the XANES after reduction and oxidation versus known standards (Figure 4.3.4-1). VCl$_2$ and V$_2$O$_3$ were also tested as standards, but due to lack of linearity, the edge shift versus formal oxidation state correlation curve was constructed using vanadium metal, V(acac)$_3$, VO$_2$, and VO(acac)$_2$ standards.
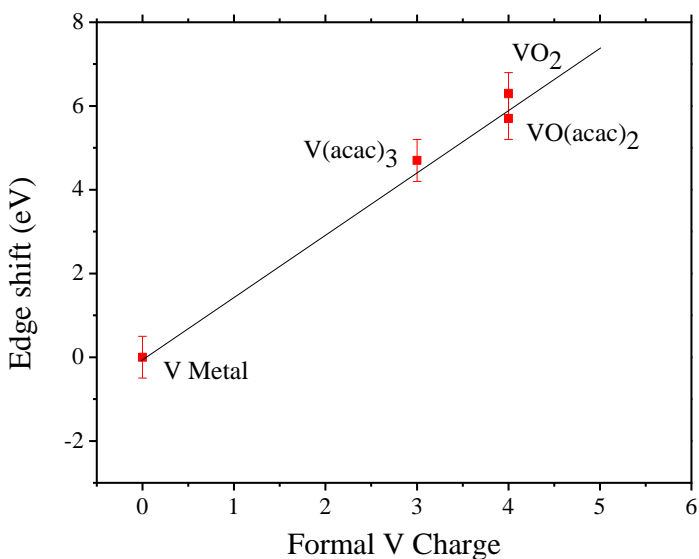
Figure 4.3.4-1 Correlation of formal charge on V to edge shift for standards.

The experimental and computational results (Table 4.3.4-1) for the reduction reaction are in good agreement because no side reactions are observed. Reduction has no significant effect on the XANES and indicates that very little charge is stored on V; the bulk of the charge is stored on the ligands. DFT predicts that there would be no change in the oxidation state of the vanadium atom after oxidation of V(acac)$_3$ to [V(acac)$_3$]$^{+1}$. The

XANES indicates a change of 0.8±0.1 which is consistent with the oxidation state of vanadium in VO(acac)$_2$. The non-innocence was not anticipated and is contrary to the presumed charge-storage mechanism for V(acac)$_3$, where vanadium is expected to be redox active, and the ligands are innocent [33]. If the ligand could be modified to be redox active, the reversibility of the complex might improve. This will be further explored in Section 4.4.

Table 4.3.4-1 Change of vanadium atom oxidation state in V(acac)$_3$ after complete reduction and oxidation, as determined by XANES and DFT. DFT calculation performed on $[V(acac)_3]^{+1}$ for oxidation reaction.

Method	Reduction Reaction	Oxidation Reaction
XANES	0.0±0.1	0.8±0.1
DFT	-0.19	0.0

4.3.5   Conclusions

Electrochemical, compositional and structural changes that occur to solutions of V(acac)$_3$ in ACN were systematically investigated to determine the cause of degradation observed during charge and discharge. The XAS results indicate only minor structural changes during reactions at the negative electrode, resulting in a relatively robust cycle life primarily limited by ligand detachment. Linear combination fitting revealed that reactions at the positive electrode resulted in the conversion of V(acac)$_3$ to VO(acac)$_2$ with subsequent conversion to a solvent stabilized complex that we believe is VO(acac)$_2$ACN. DFT and BE experiments were used to provide further evidence of the formation of VO(acac)$_2$ACN and a sequence of reactions at the positive electrode was proposed.

These results explain the discrepancy between the apparent cause of degradation observed during charge-discharge experiments, and the lingering CV features associated with V(acac)$_3$. Finally, contrary to the assumption that the ligands on V(acac)$_3$ are innocent, we found that the ligands participate in the electrochemistry and are non-innocent. The degree of ligand non-innocence appears to have a significant effect on stability and cyclability. This fundamental chemical information about the degradation of V(acac)$_3$ will inform the rational design of metallo-organic complexes that are resistant to degradation.

4.4 Ruthenium(III) Acetylacetonate

4.4.1 Background and Approach

While the cost and limited solubility of ruthenium(III) acetylacetonate [Ru(acac)$_3$] prevent it from being utilized as a commercial RFB active material, it does represent an interesting species for understanding how the structures and charge distributions are affected by electrochemical oxidation and reduction. Due to the weak x-ray absorption of ACN at the Ru K edge (22 keV), transmission measurements through a functioning cell can probe the Ru without excessive signal loss due to matrix absorption. Ru(acac)$_3$ also has properties that are similar to those of the other metal acetylacetonates. Chakrabarti and co-workers reported that while Ru(acac)$_3$ undergoes two quasi-reversible redox reactions over a 2V window in ACN, less than 12% state of charge (SOC) was achieved during charge-discharge experiments [28], and Section 3.5 demonstrated that Ru(acac)$_3$ has a relatively stable reduction reaction (43 cycles to 80% capacity) and an unstable oxidation reaction (0 cycles to 80% capacity) caused by an unknown side reaction. This suggests that products formed during CV were different from those formed during

150

charge-discharge experiments or that the initial products converted to other species. *In situ* XAS will allow us to characterize these species. The XAS was performed in specially designed electrochemical cells that allowed us to track changes in the structural and electronic properties of solvated $Ru(acac)_3$ while the material was being electrochemically oxidized or reduced, and isolated from air.

Our experimental protocol started with the use of bulk electrolysis (BE) to change oxidation states of the electrolytes. During BE, the electrolyte was held at a constant potential until a given degree of oxidation or reduction (i.e., SOC) was achieved or until the current decayed to essentially zero. When possible, the BE was carried out in steps of 0.2 electrons per molecule. The resulting materials were characterized using CV and XAS. In attempts to completely reduce $Ru(acac)_3$, the electrolyte was held at -1.5V; subsequently it was held at -0.7V to fully re-oxidize the electrolyte. In attempts to completely oxidize $Ru(acac)_3$, the electrolyte was held at 0.8V; subsequently it was held at 0.4V to reduce the electrolyte. The *in situ* XAS was performed in an air-tight teflon BE cell with windows to allow the X-ray beam to travel through the electrolyte. The experimental results were complemented by DFT structure optimization calculations using Gaussian 09 following the procedure outlined in Section 2.2.5, with Multiwfn for orbital density quantification following the procedure in Section 3.2.2 [83], [126], [138]. Together the results allowed us to define the structural and compositional properties of the electrolyte and determine the cause for degradation of the $Ru(acac)_3$ based electrolytes.

These results have been published and can be found in "Characterization of Structural and Electronic Transitions During Reduction and Oxidation of Ruthenium(III)

Acetylacetonate-Based Flow Battery Electrolytes Using X-Ray Absorption Spectroscopy" *ChemElectroChem*. **3**, 1-10 (2015) [139].

4.4.2   Results: Structural Changes During Oxidation and Reduction
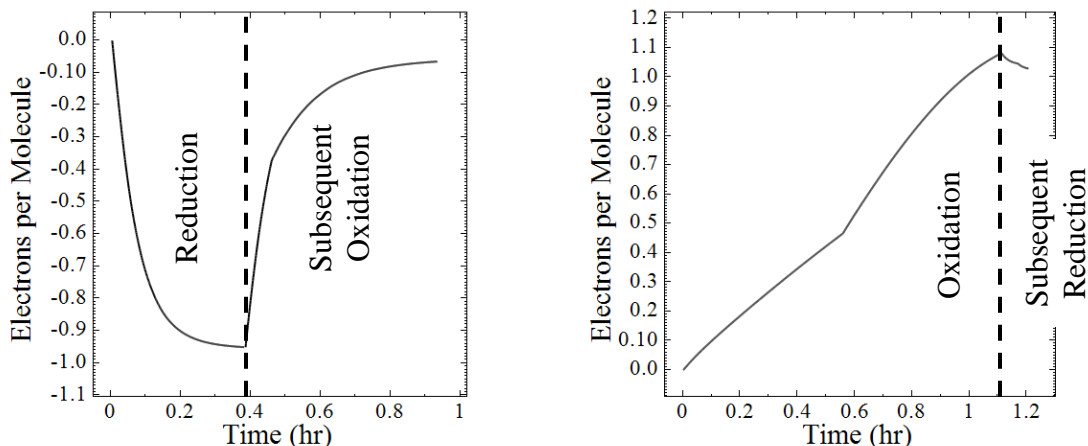
Figure 4.4.2-1 Electrons per molecule transferred during BE of the reduction reaction (left) and oxidation reaction (right).

During BE to reduce the Ru(acac)$_3$ solution, 0.95 electrons per molecule could be charged to the cell before the current decayed to zero, and 0.89 electrons per molecule could be extracted during the subsequent oxidation. The small difference in the number of electrons is likely due to cross-over, as CVs before and after BE were similar (Figure 4.4.2-2). Based on the literature [28], the reaction associated with the couple at   -1.1V is:

$$[Ru(acac)_3] + e^- \leftrightarrow [Ru(acac)_3]^- \qquad \text{Equation 4.4.2-1}$$
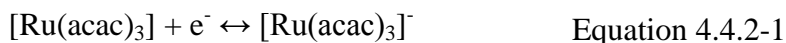
The results suggest that [Ru(acac)$_3$]$^-$ is not subject to further changes with time (i.e., it has a long shelf life). Also note that the couple at -0.2V remains a very minor feature in the CV and is inactive at the potentials used for BE.
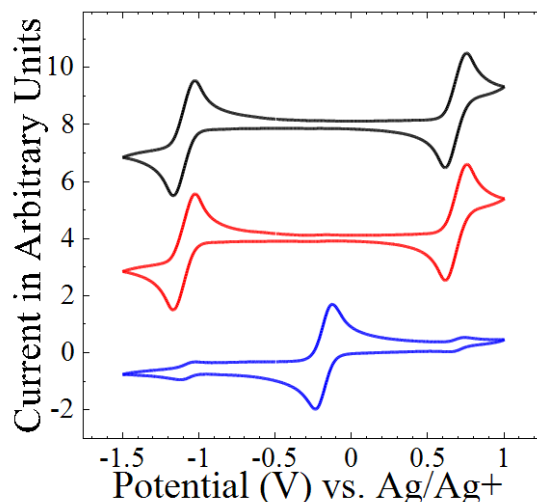
Figure 4.4.2-2 Cyclic voltammogram of Ru(acac)$_3$ electrolyte before (black), after reduction then oxidation (-1.5V then -0.7V) (red) and oxidation then reduction (0.8V then 0.4V) (blue).

During BE to oxidize the Ru(acac)$_3$ solution, 1.11 electrons per molecule could be extracted from the cell before the current decayed to zero, but only 0.08 electrons per molecule could be charged to the cell during the subsequent reduction. The resting potential shifted from 0.7V to -0.2V. In fact, the dominant couple in the CV after BE (Figure 4.4.2-2) is at -0.2V; consequently BE at 0.4 and 0.7V would have little effect on the electrolyte. The principal reaction associated with the couple at 0.7V has been reported to be [28]:

$$[Ru(acac)_3] \leftrightarrow [Ru(acac)_3]^+ + e^- \qquad \text{Equation 4.4.2-2}$$
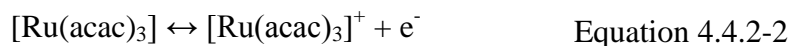
While the short-term product could be [Ru(acac)$_3$]$^+$ based on the CV, results from BE suggest a different product after electrochemical oxidation that yields a redox couple at -0.2V. This product is not free ligand, as the oxidation of acetylacetone is irreversible, occurring at ~0V vs Ag/Ag$^+$, as seen in Figure 4.3.2-1 and in the literature [43]. The peak height of the product suggests a diffusion coefficient that is comparable to that for Ru(acac)$_3$ in ACN and, based on the Stokes-Einstein equation [104], this species is

153

similar in size to Ru(acac)$_3$. The reversibility of the species giving rise to the couple at -0.2V was characterized by reducing the electrolyte at -0.5V, and subsequently oxidizing it at 0.4V. The BE of this species was very irreversible. The emergence of this species would explain the difficulties reported previously in attempts to completely discharge cells employing Ru(acac)$_3$ [28].
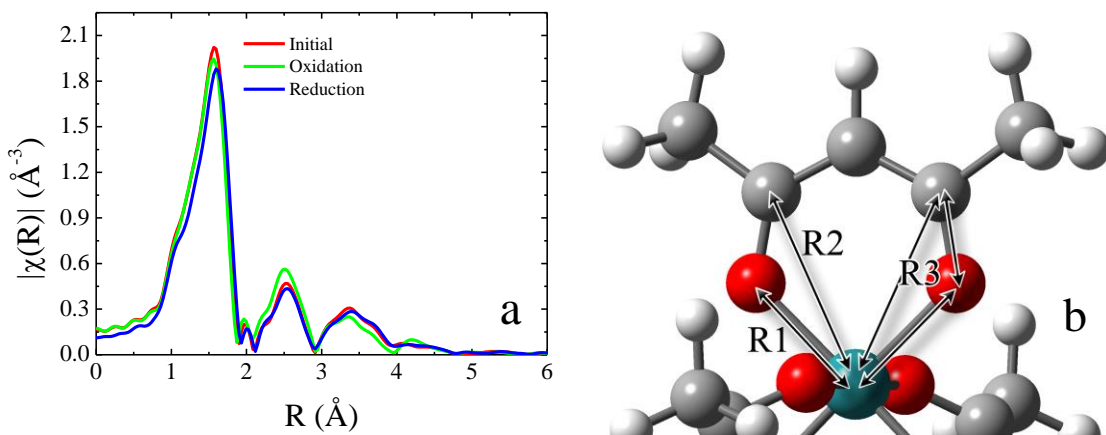
Figure 4.4.2-3 R-space EXAFS of Ru(acac)$_3$ before BE and following reduction and oxidation (k-weight=2) (a). Peaks at 1.6 and 2.5 are primarily formed from illustrated photoelectric paths (b). The peak at 3.3Å consists of a large number of photoelectric paths which could not be deconvoluted.

EXAFS spectra of the electrolytes before and after BE are shown in Figure 4.4.2-3, along with illustrations of the relevant photoelectron paths. Each peak represents a half-path: the distance a photoelectron travels from the Ru atom to one or more scattering electrons and then back to the same Ru atom, divided by two by convention. For single-scatterer paths, this is simply the distance from the Ru atom to the scattering atom, while for two-scatterer paths this is half the perimeter of the triangle formed by the scatterers and Ru. The peak at 1.6Å corresponds to the ~2Å path of a photoelectron to the 6-fold oxygen nearest neighbor (R1). The peak at 2.5 Å corresponds primarily to the path of a photoelectron to the ~3Å 6-fold carbon second-nearest-neighbor (R2), overlaid with

the triangular half-path from the Ru and around these same O and C atoms (R3, where the perimeter of this Ru-O-C triangle is 2R3). Using the Demeter software package [135], these three paths were generated from a DFT-optimized Ru(acac)$_3$ (Appendix A). A representative EXAFS fit can be found in Figure 4.4.2-4, and the full set of EXAFS data can be found in Table 4.4.2-1.
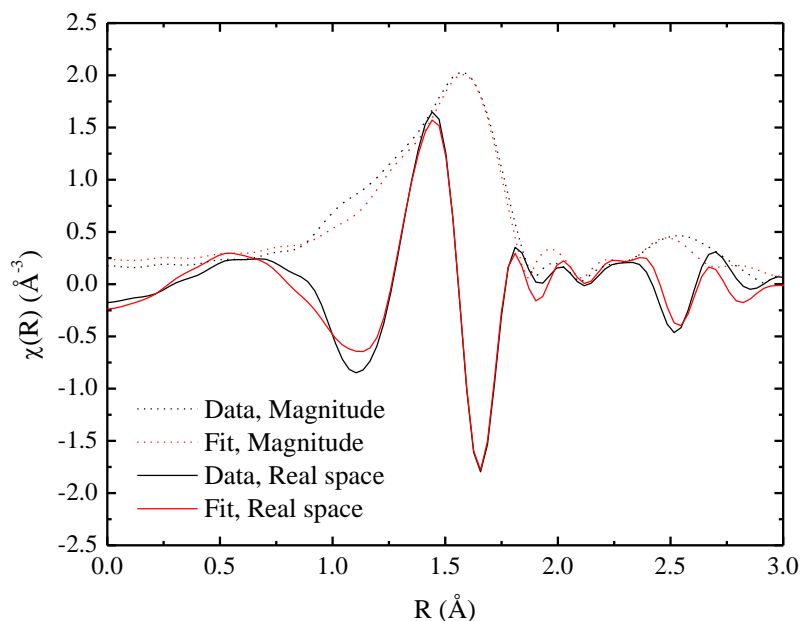
Figure 4.4.2-4 Example EXAFS fit of Ru(acac)$_3$ before BE expressed as the real portion (Re[$\chi(R)$]) and magnitude ($|\chi(R)|$) of the Fourier transform. Fitting range is 1.2<R<2.8Å.

Table 4.4.2-1 Full EXAFS regression parameters for Ru(acac)$_3$ during in situ reduction and oxidation reactions.

Reaction	SOC (%)	Amplitude	ΔE_0 (eV)	σ^2 (10^3 Å^2)	R1 (Å)	R2 (Å)	R3 (Å)	O-Ru-C Angle (°)
Reduction	0	1.0±0.1	1.6±1.7	3±1	2.019±0.009	2.94±0.02	3.08±0.05	14
Reduction	23	1.0±0.1	2.5±1.8	3±1	2.02±0.01	2.94±0.02	3.07±0.05	14
Reduction	34	1.0±0.1	3±2	3±1	2.03±0.01	2.94±0.02	3.08±0.06	14
Reduction	45	1.0±0.1	2.5±1.8	3±1	2.03±0.01	2.94±0.02	3.09±0.05	14
Reduction	55	1.0±0.1	2.7±1.7	3±1	2.04±0.01	2.95±0.02	3.09±0.05	14
Reduction	71	1.0±0.1	2.7±1.7	3±1	2.05±0.009	2.95±0.02	3.10±0.05	15
Reduction	77	1.0±0.1	2.9±1.8	3±1	2.05±0.01	2.95±0.02	3.10±0.05	15
Subsequent Oxidation	58	1.0±0.1	2.8±1.9	3±1	2.04±0.01	2.95±0.02	3.10±0.06	14
Subsequent Oxidation	45	1.0±0.1	2.3±1.8	3±1	2.04±0.01	2.94±0.02	3.09±0.05	15
Subsequent Oxidation	34	1.0±0.1	2.3±1.8	3±1	2.03±0.01	2.94±0.02	3.09±0.05	14
Subsequent Oxidation	21	1.0±0.1	2.8±1.7	3±1	2.021±0.009	2.94±0.02	3.08±0.05	14
Subsequent Oxidation	16	1.0±0.1	2.8±1.8	3±1	2.02±0.01	2.94±0.02	3.07±0.05	14
Oxidation	0	1.0±0.1	2.3±1.8	3±1	2.02±0.01	2.94±0.02	3.08±0.05	14
Oxidation	19	1.0±0.1	2.2±1.8	3±1	2.02±0.01	2.93±0.02	3.08±0.05	14
Oxidation	39	1.0±0.1	2.3±1.9	3±1	2.02±0.01	2.93±0.02	3.09±0.06	15
Oxidation	59	1.0±0.1	2.4±1.5	3±1	2.015±0.009	2.93±0.02	3.09±0.05	15
Oxidation	78	1.0±0.1	1.9±1.6	3±1	2.016±0.009	2.93±0.02	3.11±0.06	16
Oxidation	98	1.0±0.1	2±1.4	3±1	2.015±0.009	2.93±0.02	3.12±0.05	16
Oxidation	118	1.0±0.1	1.9±1.5	3±1	2.013±0.009	2.93±0.02	3.13±0.06	16

Before BE, the Ru-O bond distance (R1), the second-nearest-neighbor Ru-C distance (R2) and the Ru-O-C triangle (2R3) were found to be 2.02 ± 0.01Å, 2.94 ± 0.02Å, and 6.2 ± 0.1Å, respectively. These distances indicate an O-Ru-C angle of $14°$. The amplitude of this fit (where 1 represents $Ru(acac)_3$ and 0 represents a Ru atom with no local structure) was 1.0 ± 0.1 and the variance of these bond distances was found to be $\sigma^2 = 0.003\pm0.001$Å, which is the expected value at room temperature; these values held during the entire course of experiments.
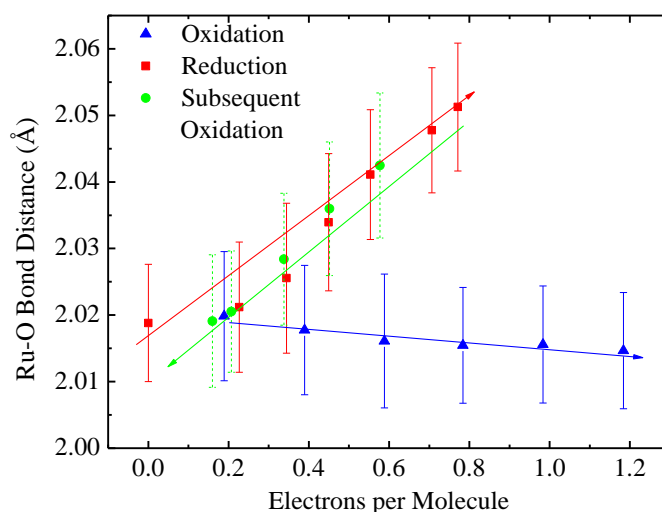
Figure 4.4.2-5 Changes in Ru-O bond length (Ru-O first shell) for $Ru(acac)_3$ during BE as determined using *in situ* EXAFS.

The electrochemical reduction of $Ru(acac)_3$ causes the Ru-O bond (R1) to lengthen from 2.02 to 2.05Å; subsequent oxidation causes the bond length to retract to its initial value (Figure 4.4.2-5). The average bond length varied linearly with the charge added or extracted per molecule. Although we expect these distances to represent two unique species - $Ru(acac)_3$ and $[Ru(acac)_3]^{-1}$ - the change in bond distances between them was too small to deconvolute into separate paths. Instead the bond length was taken as an

average for these species. Variations in the bond length determined using EXAFS were consistent with those calculated by DFT (Table 4.4.2-2). The optimized structures can be found in Appendix A. The acetylacetonate ligand is negatively charged, and as the complex is reduced, the Ru-O bond should lengthen due to repulsive forces; the opposite should occur with an increasing oxidation state. Interestingly, variations in R2 and R3 path distances were less than the estimated uncertainties, indicating minor changes in the corresponding bond lengths, if any. The uncertainties for R2 and R3 are 0.02 and 0.1Å, respectively, so the photoelectron path length is likely changing, but within error. Alternatively, the ligand is distorted to allow for a slight increase in R1, without changing R2 or R3. Recall that there were minimal changes in the electrochemistry observed from CVs collected before and after BE to reduce Ru(acac)$_3$ (Figure 4.4.2-2). The reversible Ru-O bond changes are consistent with those findings.

Table 4.4.2-2 Measured (EXAFS) and computed (DFT) bond length changes after reduction and oxidation of Ru(acac)$_3$.

Property	[Ru(acac)$_3$]$^{-1}$	[Ru(acac)$_3$]$^{+1}$
Experimental Average Ru-O Bond Length Change [Å]	0.03±0.01	-0.01±0.01
Computed Average Ru-O Bond Length Change [Å]	0.043	-0.042

When Ru(acac)$_3$ was electrochemically oxidized, the Ru-O bond length decreased by less than 0.01Å (Figure 4.4.2-5); the small change was linear with the charge extracted. As was found during the reduction of Ru(acac)$_3$, the amplitude of the EXAFS paths does not deviate from 1.0±0.1; therefore, ligand shedding, if any, was less than 10%. This result is apparently inconsistent with the CVs which indicated significant changes in the electrochemistry (Figure 4.4.2-2) and presumably the structure of

Ru(acac)$_3$ on oxidation. Based on the DFT calculations, a bond length change of 0.04Å should occur when Ru(acac)$_3$ is oxidized to [Ru(acac)$_3$]$^+$, providing further evidence for a species other than [Ru(acac)$_3$]$^+$. The EXAFS spectra allowed us to rule out the formation of RuO$_2$ (1.9Å Ru-O bond), a Ru acetylacetonate dimer (2.6Å Ru-Ru bond) or Ru metal (2.5Å Ru-Ru bond) as products [140]. As our EXAFS measurements in the 3-6Å range do not include enough data to deconvolute the large number of overlapping photoelectron paths generated by the acetylacetone ligand, we do not expect to observe any changes on the ligand 3Å from the Ru atoms. We have tentatively concluded that the structural and compositional changes occurred on the acetylacetone ligand, beyond the sampling range of EXAFS. The changes were irreversible and the resulting complex produces a couple at -0.2V vs Ag/Ag$^+$ (Figure 4.4.2-2). The Ru XANES will provide important information regarding relative contributions of the Ru and the ligand to the electrochemistry. Nevertheless, additional characterization will be required to provide a highly detailed description of the species.

4.4.3 Results: Reduction and Oxidation Charge Storage Mechanism
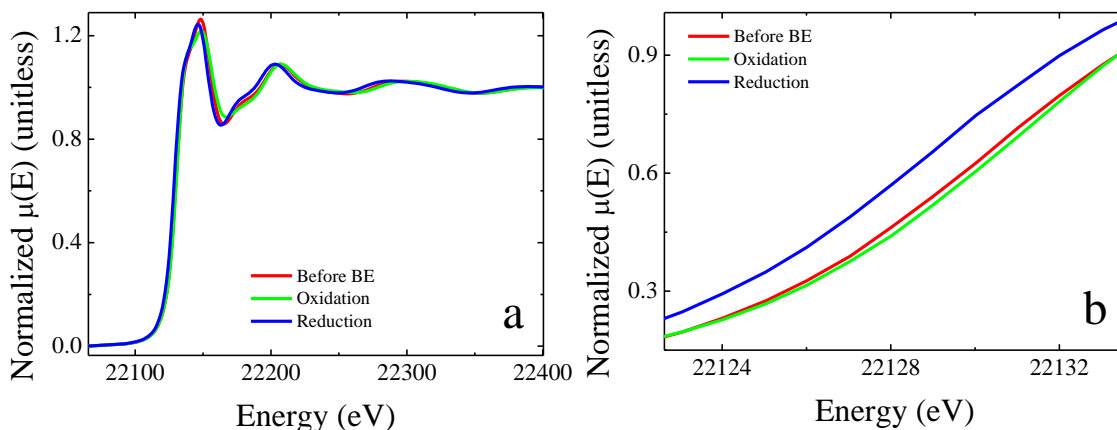
Figure 4.4.3-1 Full (a) and edge (b) XANES of Ru(acac)$_3$ solutions following reduction and oxidation via BE.

As previously discussed, the ligands for metal acetylacetonates are typically considered to be redox innocent, that is they do not contribute to the electrochemistry [33]. By tracking the oxidation state of Ru, we can determine the degree of innocence or non-innocence. One would expect the Ru oxidation states to change by ±1 if only the metal participated. The change in the charge on Ru following BE of Ru(acac)$_3$ was quantified by tracking edge shifts in the *in situ* XANES spectra (Figure 4.4.3-1). The Ru edge shifts to lower energy during reduction and to higher energy during oxidation, and these shifts were reversible. For both reactions, the post-edge features did not change significantly. A shift of +1.25eV corresponds to a +1 change in the oxidation state of Ru (Figure 4.4.3-2a) based on the correlation of edge shifts for known standards. Given this correlation, the oxidation state of Ru decreases from 2.2±0.2 to 1.0±0.2 during the reduction of Ru(acac)$_3$ (Figure 4.4.3-2b). In other words, most of the electrochemistry is due to Ru. Also note that XANES spectra after re-oxidizing the reduced Ru(acac)$_3$ (returning to zero electrons per molecule) were nearly identical to those for the fresh electrolyte.
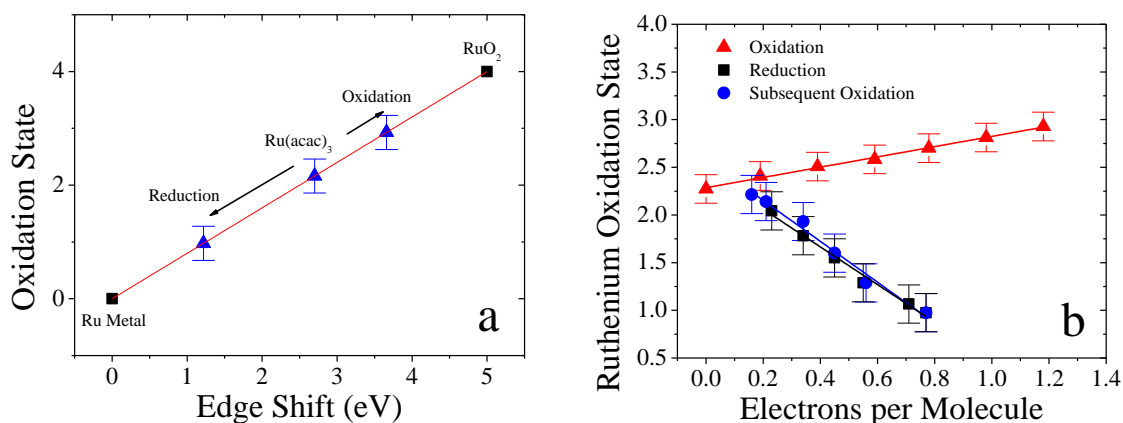
Figure 4.4.3-2 Edge shifts for standards and charged species associated with reduction and oxidation reactions (determined from standards) (a) and XANES-estimated oxidation states of samples during reduction (black/blue) and oxidation (red) (b).

Following electrochemical oxidation of Ru(acac)$_3$, the oxidation state of Ru increases from 2.2±0.2 to 2.9±0.2 for a net change of 0.7±0.2 (Figure 4.4.3-2b). The results indicate that while most of the electrochemistry can be attributed to the Ru, significant charge (~30±20%) is extracted from other constituents of the complex, namely the ligands. Given differences in products for the reduction and oxidation reactions, one might conclude that the stability of Ru(acac)$_3$ is correlated with the degree of charge that is stored on or extracted from Ru.

Table 4.4.3-1 Changes of oxidation state for Ru in Ru(acac)$_3$ during oxidation and reduction determined from XANES. The results are compared to the fraction of the orbital density as determined from DFT calculations.

Method	Reduction Reaction	Oxidation Reaction
XANES	-1.2±0.2	0.7±0.2
DFT	-0.67	0.53

Experimentally determined changes in the oxidation states were compared to the quantified HOMO and LUMO densities determined from the DFT calculations (Table 4.4.3-1). In all cases DFT calculations indicate less of the orbital density to be on the metal than determined from the XANES results; this is not unexpected as DFT is known to distribute charge throughout a complex [83]. Regardless, DFT predicts more of the orbital density to be on Ru during reduction of Ru(acac)$_3$ than during oxidation in agreement with the experimental results. The orbital densities for each atom type determined from the DFT calculations are shown in Figure 4.4.3-3. For the oxidized Ru(acac)$_3$ electrolyte, more of the orbital density is on the oxygen atoms than for the reduced Ru(acac)$_3$ electrolyte, and likewise for the carbon atoms, specifically those that are part of the conjugated ring portion of the acetylacetone ligands.

Both XANES and EXAFS of the oxidation reaction indicate the side reaction likely occurred on the conjugated portion of the ligands. K-edge XANES typically generate a pre-edge peak except when this is suppressed by inversion symmetry (e.g. octahedral) around the metal; this is a common method of quantifying transitions from octahedral (no pre-edge) to tetrahedral (strong pre-edge) in metals. In the case of Ru, a weak pre-edge shoulder is expected at 22,118 eV for non-inversion-symmetric species [141]. The lack of this feature in oxidized Ru(acac)$_3$ (Figure 4.4.3-1) indicates octahedral symmetry is maintained.
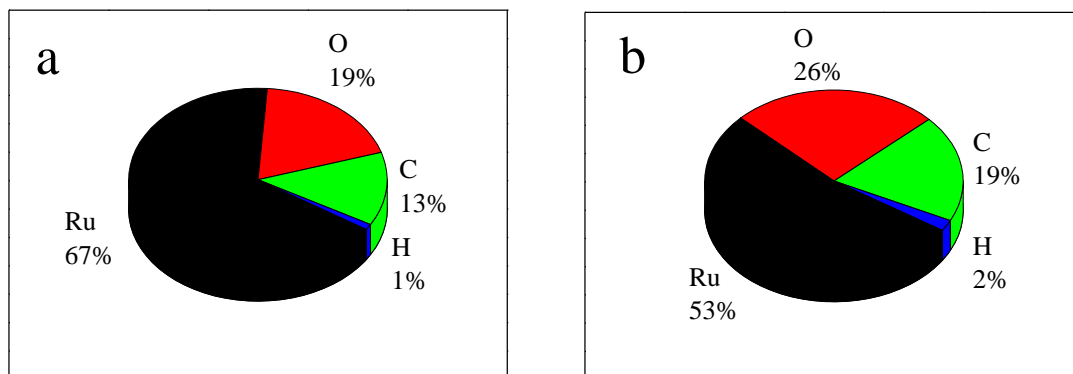
Figure 4.4.3-3 Neutral Ru(acac)$_3$ orbital density by atom type for LUMO (a) and HOMO (b).

4.4.4 Conclusions

The experimental and computational results presented in this chapter indicate the reversible reduction of Ru(acac)$_3$ to [Ru(acac)$_3$]$^-$ in ACN with essentially all of the charge localized to the metal center and the Ru-O bond length increasing on reduction and contracting during re-oxidation. The oxidation of Ru(acac)$_3$ in ACN appeared to initially produce [Ru(acac)$_3$]$^+$ which converted to another species via chemical or electrochemical processes. Approximately 70% of the charge was extracted from the Ru atom and ~30% from the acetylacetone ligands. Collectively, the results suggest that while the short-term

product of Ru(acac)$_3$ oxidation could be [Ru(acac)$_3$]$^+$, the long-term product has 6-fold Ru-O bonding with octahedral symmetry, has a structure that is identical to Ru(acac)$_3$ up to 3Å from Ru, has a Ru oxidation state of 2.9±0.2, and produced a couple at -0.2V vs Ag/Ag$^+$ which was found to be irreversible during BE. The results also indicate that stability and cyclability are functions of the degree of charge transfer with the metal center.

4.5 Discussion

The structural changes for both V(acac)$_3$ and Ru(acac)$_3$ follow similar trends, with M-O bond retractions during reduction, and elongations during oxidation. However, the extent of the bond change does not correlate to the experimental oxidation state of the metal, which agrees with the high M-O bond change p-value presented in **Error! eference source not found.** (Table 3.5.4-2). Furthermore, the stability of V(acac)$_3$ seems to increase with a decreasing percentage of charge stored on the metal, while the stability of Ru(acac)$_3$ was found to be greater with a high percentage of charge stored on the metal. The Ru(acac)$_3$ results agree with the correlation developed in **Error! Reference source not found.** (Equation 3.5.4-1) which indicated that the cycle life of the reaction for a given complex increased linearly with the DFT estimated percent of charge stored on the metal, but the V(acac)$_3$ results do not. Our hypothesis is that, while the DFT calculated values of percent metal storage can be used to estimate the cycle life of a given reaction, the actual oxidation state changes of the respective complexes differ. This hypothesis can be explored by obtaining the oxidation state changes via XAS of additional complexes, and will be further discussed in the recommended future work in Chapter 6.

V(acac)$_3$ was found to shed ligand during reduction, and undergo a VO(acac)$_2$ conversion coupled with a solvent stabilizing reaction during oxidation (Section 4.3.3). In contrast, no quantifiable ligand shedding occurred during the reduction of Ru(acac)$_3$. The reduction reaction of Ru(acac)$_3$ is more stable than the reduction of V(acac)$_3$ which is likely a result of increased charge stored on the metal for [Ru(acac)$_3$]$^{-1}$. Both oxidation reactions are complex and trends between the two are not obvious. Both undergo rapid side reactions; V(acac)$_3$ forms VO(acac)$_2$ and while Ru(acac)$_3$ converts to a different species, the structural changes occurred beyond 3Å away from the Ru atom. Therefore a RuO(acac)$_2$ complex does not form and the new species is not analogous to VO(acac)$_2$. Additional XAS experiments on other metals could help to establish more obvious trends. These results indicate that observed side reactions for a type of metal-acetylacetonate complex are not likely to translate to other metals, and each system should be evaluated independently. Furthermore, the synthetic steps to increase the stability of a given a metal-acetylacetonate will likely be specific to the chosen metal.

Overall, these experiments demonstrate a combination of electrochemical and spectroscopy techniques which allow for the characterization of RFB electrolytes in unparalleled detail. By understanding the charge distribution of these complexes, as well as accurately measuring structural changes during reduction and oxidation, one can begin to address the stability issues of MCCs in a rational way. We believe that this combination of techniques is the optimum path forward for RFB MCC active species research, and by studying additional metal-acetylacetonate complexes and other classes of MCCs, the design of complexes with commercially viable cycle lifes is possible.

Chapter 5

Salicylaldimine-Based Metal Coordination Complexes

5.1 Background

Salicylaldimine and salen-based MCCs (Figure 5.1-1) have been widely studied for catalytic applications, specifically for a variety of organic oxidation reactions (oxidation of hydrocarbons, olefins, alcohols, etc.) [142]–[153]. Their activity has been attributed to redox chemistry associated with the non-innocence of the ligands; in particular the ligands are able to donate an electron [154]–[157], and CVs of these complexes with various metals have shown peak height ratios indicative of reversible oxidation reactions [158], [159]. In both studies, the tested voltage windows were <2.0V, so it is unclear if multiple oxidation couples are available. However, DFT studies have shown that for salicylaldimine-based MCCs with a variety of metals (Ni, Pd, Pt, etc.), less than 15% of the oxidation occurs on the metal [154], [157], [160]–[162]. The results from Chapter 4 indicated that ligands capable of donating an electron could lead to increased stability of oxidation reactions. Therefore, it is likely that multiple oxidation reactions are possible. Furthermore, salicylaldimine-based MCCs can be readily modified to include different functional groups at various sites [144]. If structure-function relationships can be developed to allow for the design of salicylaldimine-based complexes with high solubility and stability, their tunability makes these complexes attractive as RFB active materials.
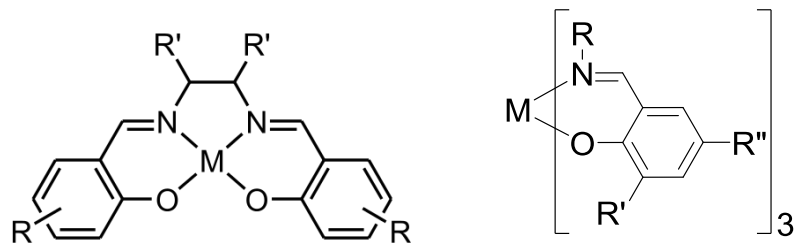
Figure 5.1-1 Metal-salen (left) and metal-salicylaldimine (right) generic structures. Metal-salicylaldimine complexes can also consist of two ligands rather than three.

For research described in this chapter, a number of salicylaldimine-based MCCs were synthesized and characterized to understand how functional groups impact the standard potentials, solubility, and ultimately the stability. A combination of electrochemical techniques and DFT structure optimization calculations were used establish trends which will allow for the rational design of future salicylaldimine-based complexes. The complexes were synthesized by Dr. James Suttil, Dr. Christo Sevov and Sharmila Samaroo of the Sanford group in the chemistry department at the University of Michigan. Details regarding the synthesis procedure and verification of the complex identities are available upon request, and will not be presented here. Dr. Krista Hawthorne (also from the Thompson group at the University of Michigan) assisted with the electrochemical characterization.

5.2 Experimental Techniques

The techniques used to collect results presented in this chapter have been previously described in detail. Briefly, CV was utilized to determine the standard potentials and estimate the reversibility of the electrochemical reactions of each complex, following the same procedure described in Section 2.2.2. The solubility of the complexes in ACN were quantified using the same method and instrument described in Section 2.2.1. To quantify the cyclability of complexes, cyclic BE was used, following the

procedure described in Section 3.2.1. For this chapter, the BE experiments were performed under constant current conditions to match conditions used during the flow cell experiments. All DFT structure optimization calculations followed the procedure described in Section 2.2.5, and subsequent HOMO density quantifications followed the procedure described in Section 3.2.2.

5.2.1 Flow Cell

General background regarding flow cells operations can be found in Section 2.2.4. For these experiments, a custom flow cell developed in the Savinell group at Case Western Reserve University (Figure 5.2.1-1) was used. The cell utilized a standard flow-through electrode configuration, with ~3.6cm^2 graphite felt SGL GFA 2.5 (2.5mm thickness, SGL group) electrodes. Daramic separators (250μm thickness, Daramic LLC) were used with no prior soaking. After cell assembly, the electrode compression was approximately 20%. The catholyte and anolyte each consisted of 15ml of a solution of 0.1M active species with 0.5M tetrabutylammonium tetrafluoroborate (99%, Aldrich) dissolved in anhydrous ACN (99.8%, Aldrich). The electrolyte was delivered to each cell compartment at 20ml/min by means of a peristaltic pump (Masterflex L/S, Cole-Parmer®) with two heads. Charge-discharge battery cycles were performed at a constant current density of 5mA/cm^2. Charging was limited by cut-offs of 80% SOC and a potential of 2.8V, while 1.9V was used as the discharge cut-off. EIS was carried out at frequencies ranging from 0.1Hz-250 kHz at the open circuit potential bias using an AC potential perturbation of 10mV. The ohmic resistance is reported as the intercept of the real part of the impedance at high frequency. A PGSTAT302N Autolab Potentiostat was

employed to conduct the battery cycle testing and EIS measurements. The flow cell was assembled and tested in an Ar-filled glovebox.
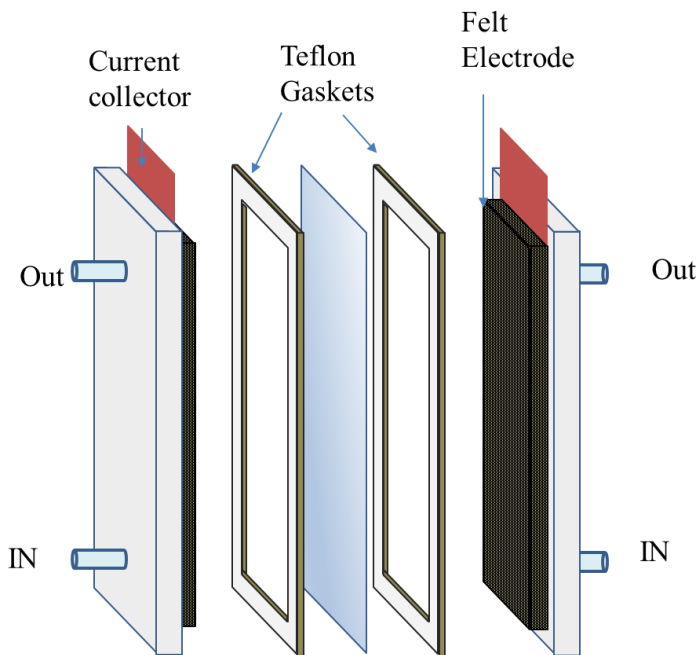
Figure 5.2.1-1 Flow Cell Schematic

5.3   Effect of Functional Group

5.3.1   Approach

A systematic study was conducted to determine the effect of ligand substituent location (R, R', and R") and type on the electrochemical stability and solubility for the salicylaldimine-based complexes seen in Figure 5.3.1-1. Similar to the initial studies conducted for acetylacetonate-based MCCs presented in Chapter 2, Cr was chosen as the metal due to ease of synthesis. Complexes **23-29** were used to investigate the effect of functionalizing the conjugated carbon ring portion of the ligand, and complexes **30-32** were used to investigate the effect of functionalizing the nitrogen. A combination of electrochemical, spectroscopic and theoretical techniques was used to determine how the

functional group type and location impact the electrochemistry, solubility and stability of the complexes. Finally, the most promising complex was characterized in a flow cell.
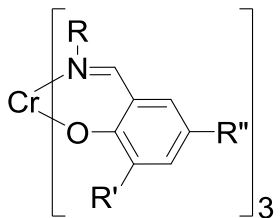
R = Ph, R' = H, R" = H (**23**)
R = CH$_2$CH$_2$OMe, R' = OMe, R" = H (**24**)
R = CH$_2$CH$_2$OMe, R' = H, R" = OMe (**25**)
R = CH$_2$CH$_2$OMe, R' = Me, R" = Me (**26**)
R = CH$_2$CH$_2$OMe, R' = OMe, R" = Br (**27**)
R = CH$_2$CH$_2$OMe, R' = OMe, R" = F (**28**)
R = CH$_2$CH$_2$OMe, R' = OMe, R" = OMe (**29**)
R = Ph, R' = t-Bu, R" = t-Bu (**30**)
R = CH$_2$CH$_2$OMe, R' = t-Bu, R" = t-Bu (**31**)
R = CH$_2$CH$_2$CN, R' = t-Bu, R" = t-Bu (**32**)

Figure 5.3.1-1 List of salicylaldimine complexes assessed herein.

5.3.2   Results: Standard Potentials

A widely-used time semi-derivative method was used to deconvolute the CVs, and the reversibility of each couple was estimated using the current peak height ratios (i_c/i_a or i_a/i_c) [105], [106]. The results can be found in Figure 5.3.2-1 and Table 5.3.2-1.
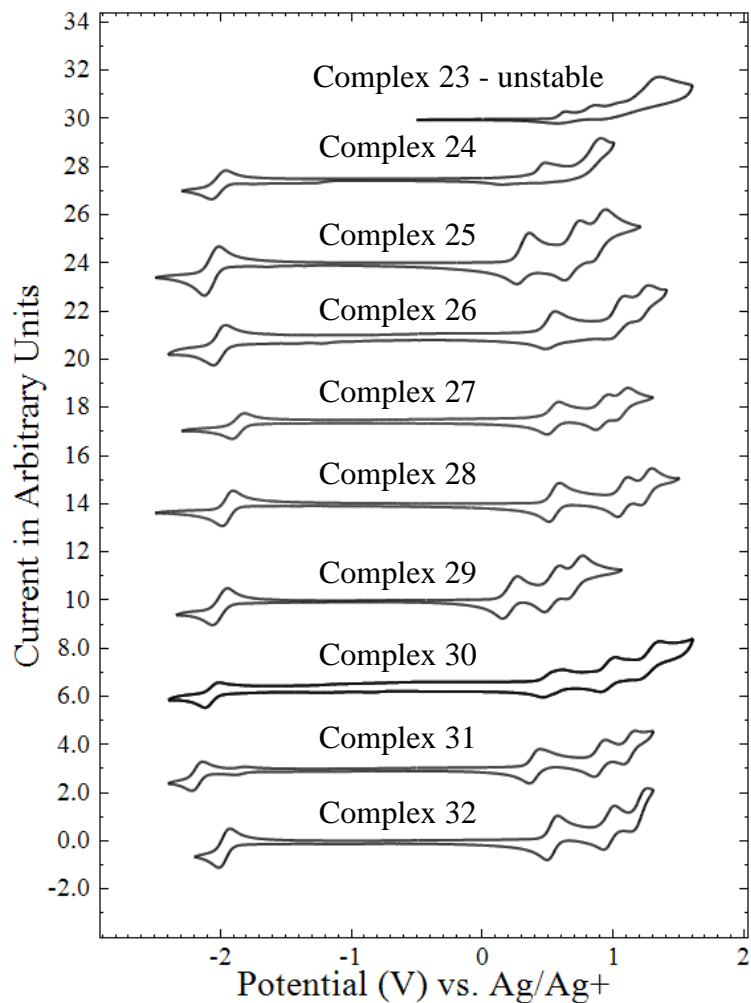
Figure 5.3.2-1 Cyclic voltammograms of each complex tested. Solutions comprised of 0.5M TBABF$_4$ in acetonitrile with varying concentrations of active species based on solubility and availability. Concentrations of active species are as follows: **23**-0.01M, **24**-0.005M, **25**-0.01M, **26**-0.005M, **27**-0.005M, **28**-0.005M, **29**-0.005M, **30**-0.001M, **31**-0.005M, and **32**-0.005 M.

Table 5.3.2-1 Standard potentials for salicylaldimine complexes. Values in parenthesis are peak height ratios of the respective couple. Peak height ratio is i_c/i_a or i_a/i_c (whichever results in a value less than 1).

Complex	E^1 [V vs. Ag/Ag$^+$]	E^2 [V vs. Ag/Ag$^+$]	E^3 [V vs. Ag/Ag$^+$]	E^4 [V vs. Ag/Ag$^+$]
23	-	-	-	-
24	-2.02 (0.97)	0.46 (0.02)	0.84 (0.40)	-
25	-2.06 (0.97)	0.30 (0.96)	0.68 (0.71)	0.89 (0.70)
26	-2.10 (1.00)	0.43 (0.39)	0.97 (0.71)	1.18 (0.68)
27	-1.87 (0.89)	0.53 (0.93)	0.91 (0.97)	1.07 (0.93)
28	-1.95 (0.97)	0.54 (0.89)	1.07 (0.95)	1.26 (0.89)
29	-2.07 (0.97)	0.14 (0.92)	0.46 (0.92)	0.65 (0.76)
30	-2.07 (0.83)	0.52 (0.84)	0.95 (0.83)	1.27 (0.53)
31	-2.16 (0.94)	0.41 (0.94)	0.92 (0.93)	1.15 (0.99)
32	-1.97 (0.99)	0.53 (0.90)	0.96 (0.88)	1.20 (0.97)

The CV of complex **23** shows that a salicylaldimine-based complex with an un-functionalized conjugated carbon ring is unstable, and a decreasing current indicates that the degraded complex adsorbs to the working electrode surface during oxidation. By functionalizing the ring with a OMe group at the ortho position (complex **24**), the oxidation couples are still relatively irreversible (peak height ratios <0.5), but the complex does not readily adsorb to the working electrode. However, by changing the location of the OMe group from the ortho to para position (complex **25**) the CV shows three oxidation couples with peak height ratios all greater than 0.7, and a reduction couple with a peak height ratio very close to unity. The CVs of all of the remaining complexes are very similar to that for complex **25** with slight shifting of the standard potentials and minor changes to the peak height ratios. This indicates that a functional group at the R" position leads to enhanced stability and additional functionalization does not have a major impact. With three oxidation couples all within 1V of each other, the deconvolution method is not able to completely isolate each couple, and the peak height

ratios likely have high associated errors. Bulk electrolysis is a much better method to determine the stability of the couples and is discussed in Section 5.3.4. The voltage separation between the reduction couple and the first oxidation couple for each complex is ~2.5V, approximately double the voltage achieved for aqueous RFBs.

Table 5.3.2-2 Calculated orbital energies from DFT optimized structures.

Complex	LUMO of MCC(sol) [Hartrees]	HOMO of MCC(sol) [Hartrees]	HOMO of MCC^{+1}(sol) [Hartrees]
23	-0.1962	-0.0707	NA
24	-0.1906	-0.0733	-0.2008
25	-0.1844	-0.0728	-0.1960
26	-0.1902	-0.0708	NA
27	-0.1945	-0.0795	NA
28	-0.1961	-0.0772	NA
29	-0.1775	-0.0719	-0.1840
30	-0.1924	-0.0783	NA
31	-0.1896	-0.0700	-0.2014
32	-0.1931	-0.0751	-0.2039

In Chapter 2 (Section 2.3.2) a correlation between LUMO and HOMO energies and standard potentials for a series of acetylacetonate-based complexes was presented, and it was hypothesized that the correlation would be applicable for other MCC classes. For this reason, LUMO and HOMO energies of each salicyladamine-based complex in Figure 5.3.1-1 were determined using DFT structure optimization calculations. The HOMO energies of the oxidized versions of a subset of complexes with the most attractive CV characteristics and solubilities (see Section 5.3.3) were also calculated to determine the accuracy of the correlation for multiple redox events. The optimized structures can be found in Appendix A. The energies were calculated following the same procedure described in Section 2.2.5, and were converted to theoretical standard

potentials following the correlation in Figure 2.3.2-7. The individual molecular orbital values can be seen in Table 5.3.2-2.
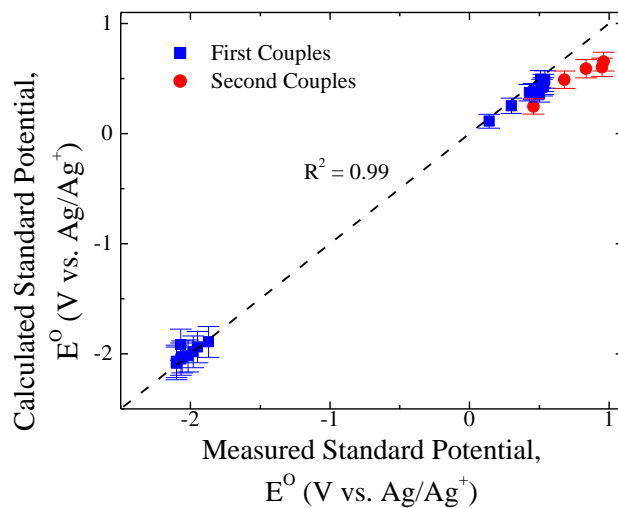
Figure 5.3.2-2 Standard potential prediction using acetylacetonate molecular orbital energy vs. standard potential correlation from Figure 2.3.2-7. Blue data points correspond first reduction and first oxidation reaction standard potentials (E^1 and E^2). Red data points correspond to second oxidation reaction standard potentials (E^3).

As seen in Figure 5.3.2-2, the theoretical standard potentials closely match the experimental values ($R^2=0.99$), even for complexes where multiple oxidations were considered. The strong R^2 value indicates that indeed the correlation developed for the acetylacetonate-based complexes is applicable to other MCC systems, which could dramatically decrease computational expense as not only are the oxidized and/or reduced structures not required, but a series of complexes with similar structures to establish a correlation curve is also not required.

5.3.3 Results: Solubilities
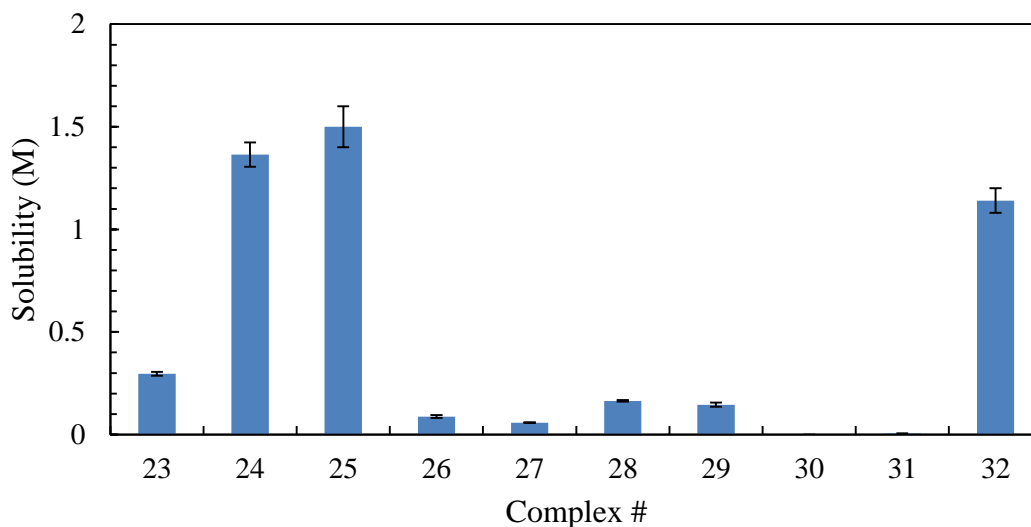
Figure 5.3.3-1 Solubilities of complexes from Figure 5.3.1-1, in acetonitrile.

While the CVs of the complexes did not vary significantly, the solubilities did (Figure 5.3.3-1). By changing the R group from a phenyl (Complex **23**) to CH_2CH_2OMe (Complexes **24** and **25**), the solubility significantly increases from ~0.3M to more than 1.3M. This is most likely a result of increasing the polarity of the R group, as similar results were presented for acetylacetonate-based complexes in Section 2.3.3. By utilizing R' and R" functionalities (complexes **26-31**), in an effort to produce a stable species, the solubility was adversely impacted, especially for large groups such as t-Bu (complexes **30** and **31**). To overcome this, a more polar R group (CH_2CH_2CN) was used to increase the solubilities of complexes **30** and **31**, and the resulting complex (**32**) was found to have a solubility of 1.14M.

While functional groups at all three locations R, R', R" clearly impact solubility, the nature of the R groups has the largest effect; specifically we were able to adjust the solubility from 0.00026M (complex **30**) to 1.5M (complex **25**). These solubilities are

very attractive, in particular for multiple electron transfer active materials, and are within the same range as the most promising acetylacetonate-based complexes (1.34M for functionalized V(acac)$_3$, Section 2.3.3).

5.3.4   Results: Stabilities

Table 5.3.4-1 Bulk electrolysis cycling parameters and quantified cycle lives. Solutions characterized using bulk electrolysis consisted of 0.005M active species with 0.5M TBABF$_4$ in acetonitrile.

Complex (Redox Couple)	Charging Potential Cutoff [V vs. Ag/Ag$^+$]	Discharging Potential Cutoff [V vs. Ag/Ag$^+$]	First Charge e$^-$/molecule	Average Coulombic Efficiency	Cycle Life [Cycles to 80% Capacity]
25 (E^2)	0.5	-0.1	1.00	1.9%	0
29 (E^2)	0.4	-0.2	1.00	81%	3
31 (E^2)	0.6	0.0	1.00	98%	73
32 (E^2)	0.7	0.2	1.00	99%	193
32 (E^2 + E^3)	1.0	0.2	2.00	2.0%	0
32 (E^1)	-2.2	-1.7	1.00	97%	20

The stabilities of the oxidation half-reactions for the complexes with the most attractive combination of reversibility (assessed by CV) and solubility (complexes **25, 29, 31,** and **32**) were assessed using cyclic BE, with the cycle life taken as the number of cycles to reach 80% initial charge capacity. As previously discussed in Section 3.2.1, cross-over is unavoidable during these experiments, and therefore the cycle life values are for comparative purposes, and could likely be increased through cell optimizations. The electrolytes consisted of 0.005M active material with 0.5M TBABF$_4$ in ACN, and the charge-discharge was carried out at a constant current of 2C (1.34mA). In situ CVs were taken at intervals throughout the BE experiments to monitor changes in the electrochemical properties over time. The cut-off potentials and the number of electrons

per molecule for the first charge can be found in Table 5.3.4-1. In all cases, the number of electrons per molecule matched the expected value.
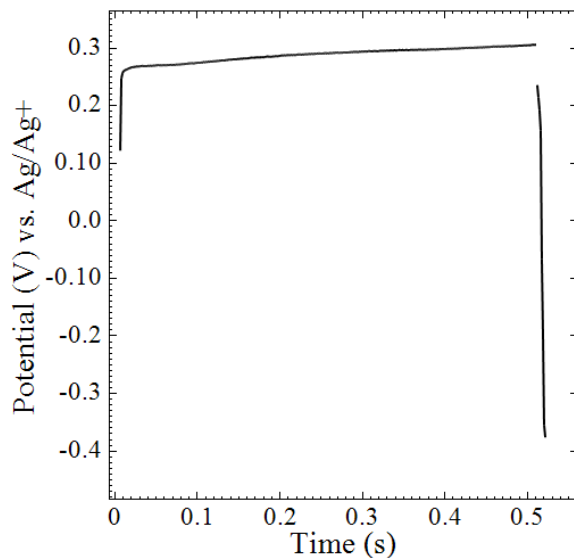
Figure 5.3.4-1 Charge-discharge curve during BE of the oxidation reaction (E^2) of 0.005M complex **25** with 0.5M TBABF$_4$.

Despite the CVs of each tested complex being very similar (Figure 5.3.2-1), the stabilities vary significantly. Complex **25** is able release a full one electron per molecule during oxidation, but the process is irreversible, and only a 1.93% coulombic efficiency is achieved for the full cycle. As seen in Figure 5.3.4-1 the complex oxidizes at approximately 0.3V which matches the standard potential assessed by CV, but a discharge plateau is not observed.
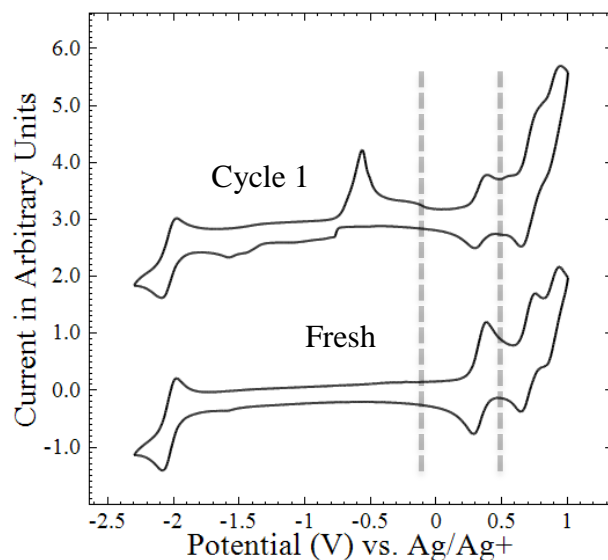
Figure 5.3.4-2 Cyclic voltammograms of complex **25** before and after cyclic BE of the oxidation reaction (E^2). Solution comprised of 0.005M active species with 0.5M TBABF$_4$ in acetonitrile. Dashed lines indicate cut-off potentials during BE experiments.

CVs of the electrolyte after the first cycle (Figure 5.3.4-2) show significant degradation of the electrolyte with an oxidation peak at -0.6V and several minor reduction peaks from -1.0V to -1.5V. There also appears to be a new couple between E^2 and E^3. These side reactions are likely due to ligand detachment which will be discussed later. These results demonstrate that the complex is electrochemically unstable; this could be due to the absence of both R' and R" functional groups. It is likely that, because of resonance delocalization between the ortho and para positions, substitution at these positions is required to inhibit decomposition pathways. To test this theory, R' and R" locations were functionalized with OMe groups (complex **29**). This resulted in a more stable complex.
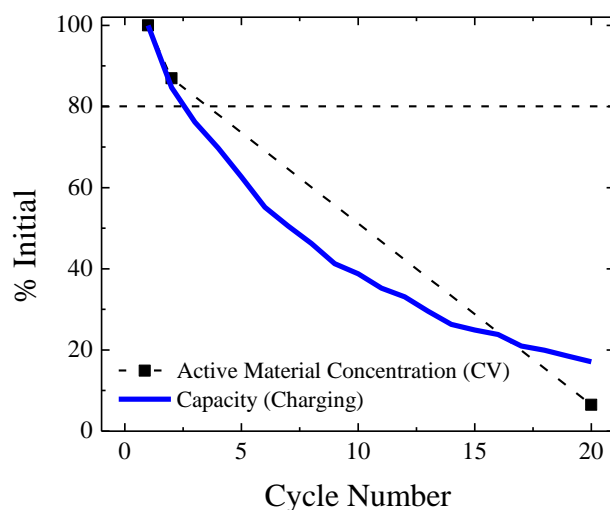
Figure 5.3.4-3 Capacity versus cycle number during cyclic BE of the oxidation reaction (E^2) of 0.005M complex **29** with 0.5M TBABF$_4$ in acetonitrile. Active material concentration determined from Figure 5.3.4-4.
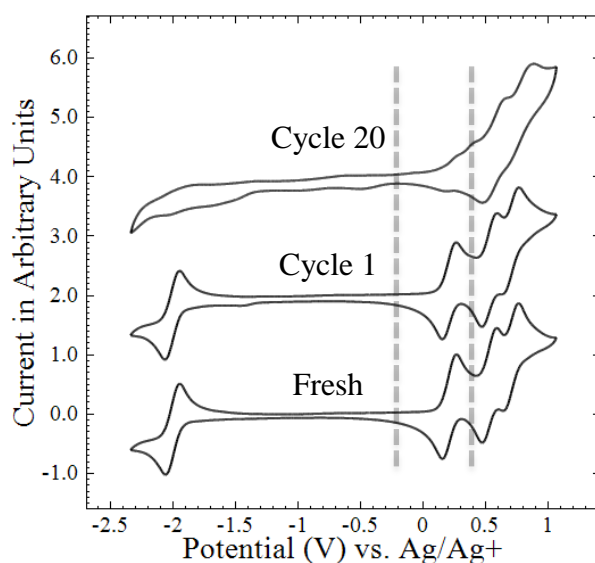
Figure 5.3.4-4 Cyclic voltammograms of complex **29** during cyclic BE of the oxidation reaction (E^2). Solution comprised of 0.005M active species with 0.5M TBABF$_4$ in acetonitrile. Dashed lines indicate cut-off potentials during BE experiments.

During cyclic BE of the oxidation reaction (E^2) of complex **29**, the complex is able to charge and discharge much more reversibly than complex **25**. However, significant capacity fade is still observed, and 20% of the initial capacity is lost within 3 cycles (Figure 5.3.4-3). CVs were taken during the BE experiment (Figure 5.3.4-4) which

178

show a continual decrease in the peak heights associated with E^2. The peak heights were quantified and used to determine the percent of the initial active material still available during cyclic BE; the amount closely correlates with the observed capacity fade (Figure 5.3.4-3). This indicates that regenerative reactions, such as those observed during cycling of V(acac)$_3$ (Chapter 4), do not occur for this system. The CV of the electrolyte after 20 cycles shows evidence of a new couple slightly more positive than E^2 and several minor peaks from -0.5V to -1.5V. These changes in the CV signature are similar to what was observed during cycling of complex **25** albeit at a slower rate.
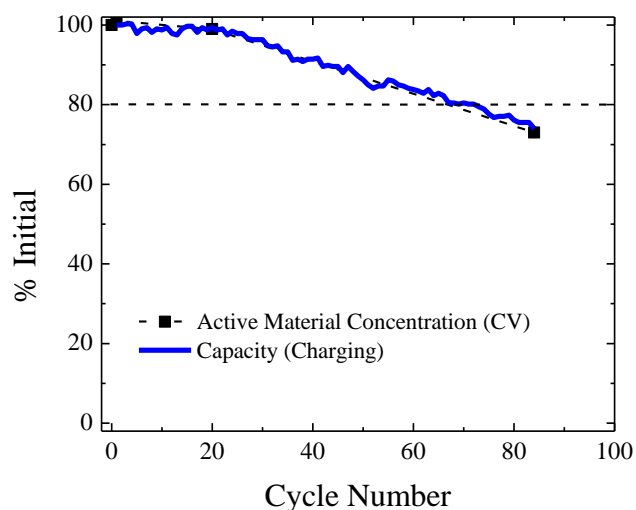
Figure 5.3.4-5 Capacity versus cycle number during cyclic BE of the oxidation reaction (E^2) of 0.005M complex **31** with 0.5M TBABF$_4$ in acetonitrile. Active material concentration determined from Figure 5.3.4-6.
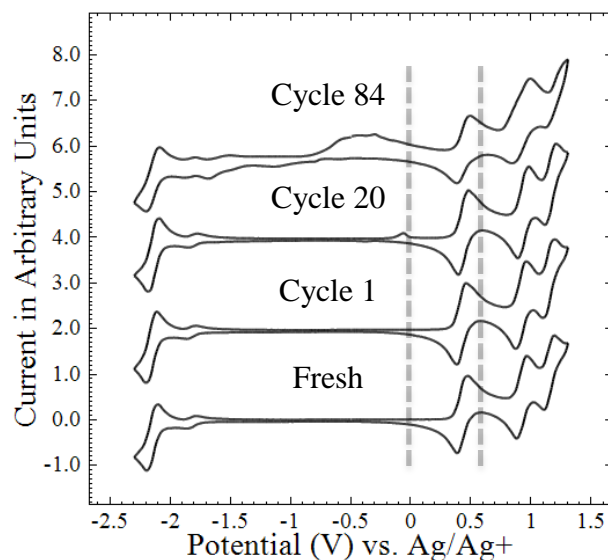
Figure 5.3.4-6 Cyclic voltammograms of complex **31** during cyclic BE of the oxidation reaction (E^2). Solution comprised of 0.005M active species with 0.5M TBABF$_4$ in acetonitrile. Dashed lines indicate cut-off potentials during BE experiments.

In an effort to increase the stability of complex **29**, t-Bu R' and R" groups were used to synthesize complex **31**. The degradation process during cyclic BE of E^2 for complex **31** is much slower than those for complexes **25** and **29**, indicating that t-Bu R' and R" functionalities stabilize the oxidized complex. This enhanced stability may result from the large steric bulk of the t-Bu, rendering it a better blocking group than a OMe group [163]. Figure 5.3.4-5 shows a cycle life of 73 cycles, meaning that E^2 for complex **31** is significantly more stable than any of the previously tested oxidation reactions for acetylacetonate-based MCCs (**Error! Reference source not found.**). Similar to the esults for complex **29**, the concentration of the active species via CVs closely match the observed capacity. The changes in the CV signature after cycling are also similar, with minor peaks at -0.5V, -1.1V, and -1.7V, and what appears to be a new couple slightly positive of E^2 (Figure 5.3.4-6). The presence of a new couple is difficult to verify as over 70% of the capacity is still available after 84 cycles, and long-term cycling would be required to increase the concentration of this side product.
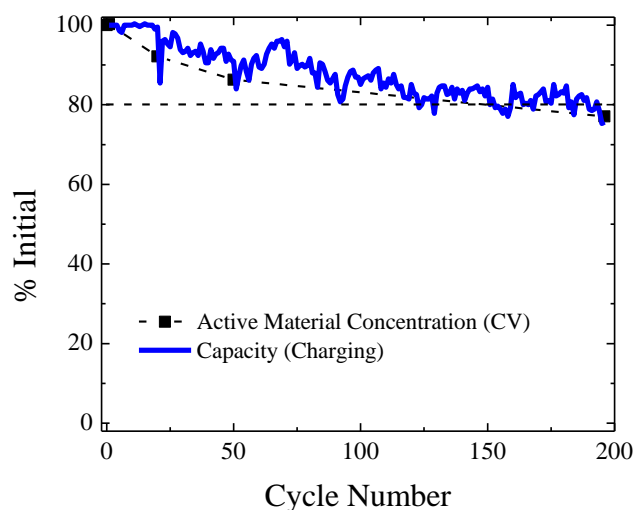
Figure 5.3.4-7 Capacity versus cycle number during cyclic BE of the oxidation reaction (E^2) of 0.005M complex **32** with 0.5M TBABF$_4$ in acetonitrile. Active material concentration determined from Figure 5.3.4-8.
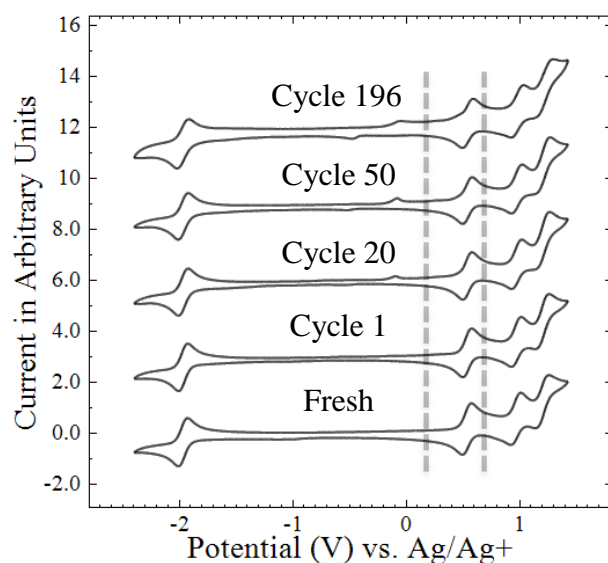
Figure 5.3.4-8 Cyclic voltammograms of complex **32** during cyclic BE of the oxidation reaction (E^2). Solution comprised of 0.005M active species with 0.5M TBABF$_4$ in acetonitrile. Dashed lines indicate cut-off potentials during BE experiments.

In an effort to improve solubility, the R group from complex **31** was changed from CH$_2$CH$_2$OMe to the more polar CH$_2$CH$_2$CN. As seen in Figure 5.3.4-7, the degradation process during cyclic BE of E^2 for the resulting complex **32** is further limited, and the electrolyte can be cyclically oxidized 193 times before reaching 80%

initial capacity. This is by far the most stable reaction we have tested. Like previous complexes, the concentration of the active species via CV closely matches the observed capacity. Figure 5.3.4-8 shows that as cyclic BE progresses, peaks due to side products begin to emerge at -0.1V and -0.5V. Due to the high cycle life, these side products are in low concentrations. Increased stability due to the CH_2CH_2CN functional group was not expected and the cause is not immediately apparent. This is further discussed in Section 5.4.
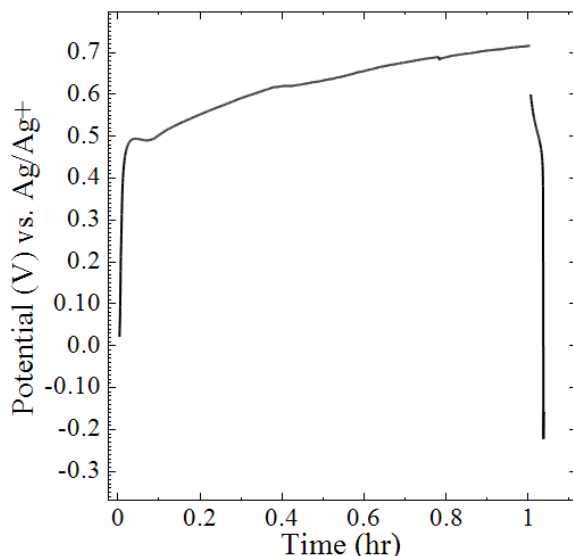
Figure 5.3.4-9 Charge-discharge curve during BE of the first two oxidation reactions (E^2 and E^3) of 0.005M complex **32** with 0.5M TBABF$_4$.

As E^2 of complex **32** was found to be the most stable half-reaction, BE was conducted on the first two oxidation reactions for complex **32** (E^2 and E^3). As seen in Figure 5.3.4-9 by withdrawing two electrons per molecule instead of just one, electrolytes containing complex **32** are not able to discharge at all. The charging curve follows the expected voltage profile, and does achieve 100% SOC based on 2e⁻, but has a minimal discharge resulting in a coulombic efficiency of 2.0% for the cycle. Therefore, the second oxidation reaction cycle life is much lower than the first. This instability could lead to the

cycle life differences for the first oxidation reactions of these complexes, and is further discussed in Section 5.4.3.
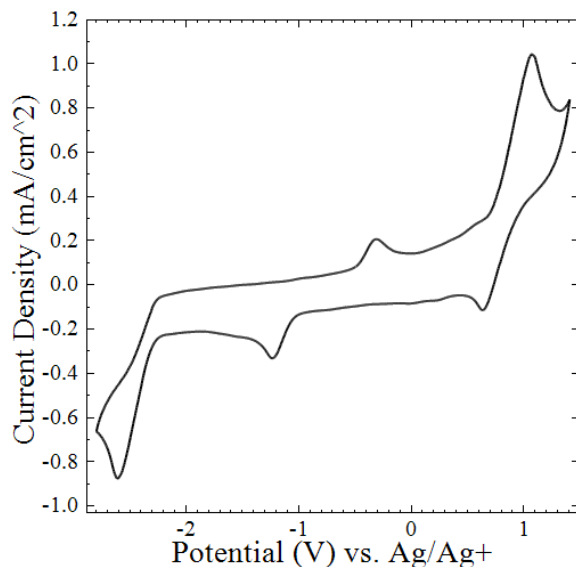
Figure 5.3.4-10 Cyclic voltammogram of complex **32** free ligand. Solution comprised of 0.005M active species with 0.1M TBABF$_4$ in acetonitrile.

To determine the primary side reactions, a CV was obtained for the free ligand of complex **32** which can be seen in Figure 5.3.4-10. The CV shows two large irreversible peaks at -2.1V and 0.9V with two resulting minor peaks at -1.2V and 0.2V. As previously presented, different functional groups will result in shifts of the standard potentials and this will translate to CVs of the ligands. Therefore, ligand shedding will result in minor peaks between E^1 and E^2 with larger irreversible couples negative of E^1 and positive of E^2. Similar features are seen after cycling complexes **31** and **32**, but they are more easily observed in the CVs of cycled electrolytes containing complexes **25** and **29** (Figure 5.3.4-2 and Figure 5.3.4-4) as significantly more active material degradation occurred. Ligand shedding is therefore the cause of the observed capacity loss during cycling of each complex. The rate of ligand shedding could be a result of the charge distribution or structural changes, which are discussed in Section 5.4.2.

183

Cyclic BE was also conducted on the reduction reaction of complex **32** (E^1), and the capacity fade results can be seen in Figure 5.3.4-11. The cycle life of the reduction reaction of complex **32** (E^1) was found to be 20 cycles, meaning it is less stable than the oxidation reaction (E^2). CVs during the BE experiment (Figure 5.3.4-12) show features consistent with ligand shedding: additional couples slightly more negative than the reduction couple and slightly more positive than the oxidation couple, as well as a minor oxidation peak at ~0.3V.
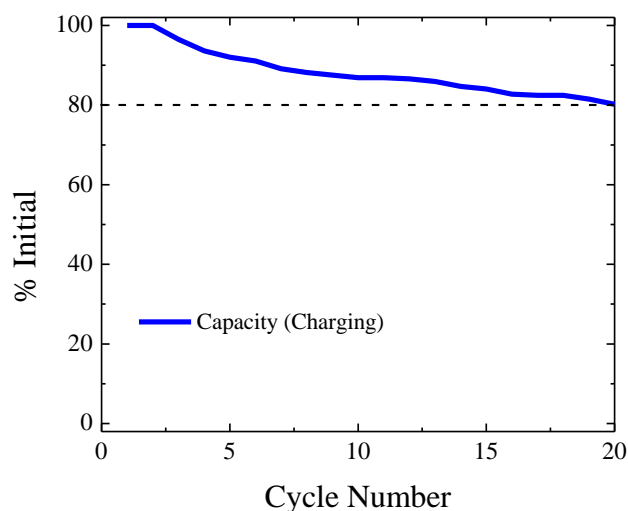
Figure 5.3.4-11 Capacity versus cycle number during cyclic BE of the reduction reaction (E^1) of 0.005M complex **32** with 0.5M TBABF$_4$ in acetonitrile. Converging CVs made concentration determinations inaccurate. Therefore they were not plotted.
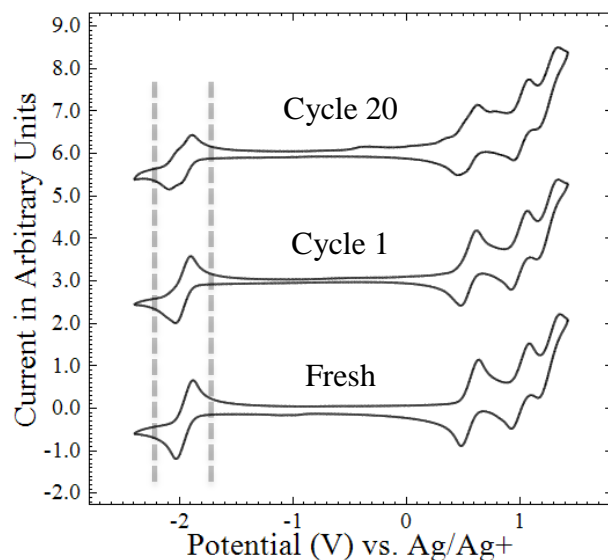
Figure 5.3.4-12 Cyclic voltammograms of complex **32** during cyclic BE of the reduction reaction (E^1). Solution comprised of 0.005M active species with 0.5M TBABF$_4$ in acetonitrile. Dashed lines indicate cut-off potentials during BE experiments.

The BE results demonstrate that R' and R'' functionalities lead to enhanced stability of the oxidation reaction, and t-Bu groups offer enhanced stability over OMe groups. While R groups were shown to be primarily responsible for modifying the solubility of these complexes, the CH$_2$CH$_2$CN R group led to an enhancement in stability over the CH$_2$CH$_2$OMe group. Ultimately, functional group modifications were used to alter the oxidation reaction cycle life of this class of complexes from completely irreversible, to almost 200 cycles.

5.3.5   Results: Flow Cell Performance

Complex **32** presented a stable oxidation reaction and was further characterized in a prototype flow cell to estimate how the complex would behave under more practical battery operation. The same complex was used as both the catholyte and anolyte to minimize the deleterious effects of cross-over.

A 0.1M solution of complex **32** with 0.5M tetraethylammonium tetrafluoroborate (TEABF$_4$) in ACN was evaluated in a laboratory-scale flow cell. The RFB cell resistance was 5.6Ω·cm^2 which resulted in an overpotential of 28mV when charging and discharging at a constant current of 5mA/cm^2. Charging was limited by cut-offs of 80% SOC and a potential of 2.8V, and 1.9V was used as the discharge cut-off. The electrolyte was pumped at a constant flow rate of 20ml/min, and Daramic was used as the separator. Daramic is a porous separator consisting of polypropylene and polyethylene and is reported to be compatible with ACN.
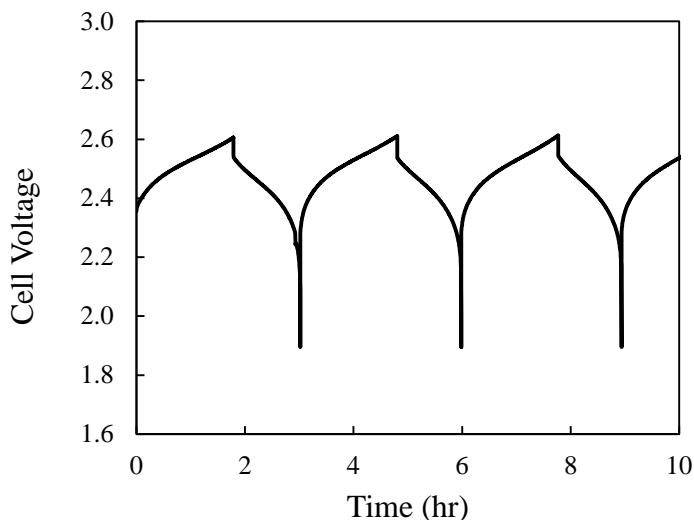
Figure 5.3.5-1 Flow battery charge-discharge cycles of 0.1M complex **32** with 0.5M TBABF$_4$ in acetonitrile at 5mA/cm^2 in a RFB cell with a Daramic membrane. Flow rate: 25ml/min. Room temperature.

Figure 5.3.5-1 shows that the electrolyte charges and discharges at the expected voltage of 2.5V, based on the standard potential values of -1.97V and 0.53V (Table 5.3.2-1). The charging potentials do not increase over time, indicating that the cell resistance is stable. This is in contrast to the flow cell studies described in Chapter 2 for acetylacetonate complexes; the resistance steadily increased during cycling as a result of

186

pore blocking for the acetylacetonate complexes. This indicates that the degradation product is soluble, further supporting our findings that ligand shedding is the primary degradation mechanism.
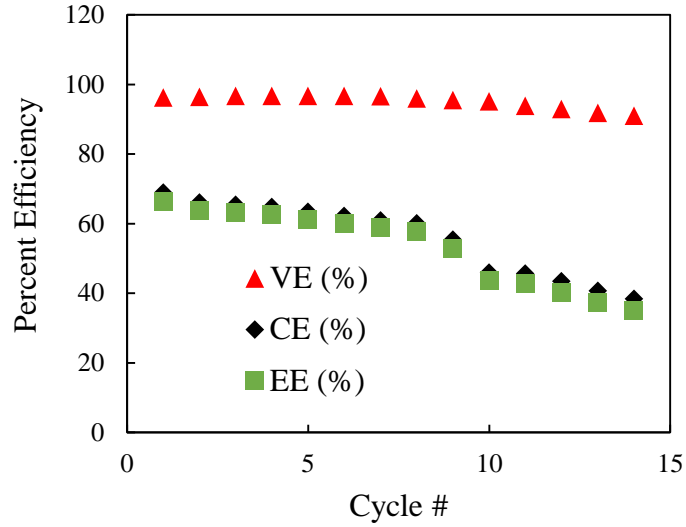
Figure 5.3.5-2 Voltaic efficiency (red), coulombic efficiency (black) and energy efficiency (green) versus cycle # for RFB cell.
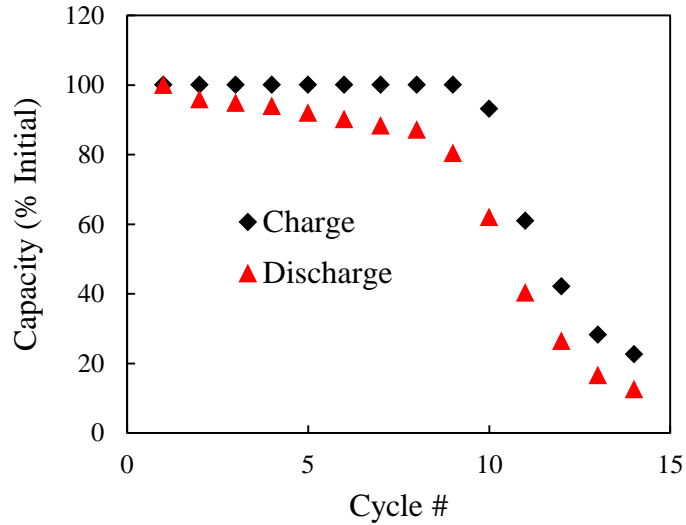
Figure 5.3.5-3 Charge (black) and discharge (red) capacity fade curves for RFB cell.

Figure 5.3.5-2 shows that the low resistance in the flow cell results in high voltaic efficiencies (>90%), but the coulombic efficiency of the cell is ~60% during the

first 10 cycles. The low coulombic efficiencies are likely due to high cross-over rates through the large pores of the separator (0.028μm) and degradation of the active material. Cross-over is not a significant issue and could be resolved through separator optimization, but the capacity fade observed in Figure 5.3.5-3 indicates an irreversible loss in active material over time. These results corroborate the cyclic BE results in the previous section, which demonstrated limited stability of the reduction reaction. If a more stable reduction reaction could be achieved, the cycle life of the cell would be improved. Similarly, pairing complex **32** in the catholyte with an acetylacetonate-based complex with a stable reduction reaction in the anolyte would also increase the cyclability of the cell. This would require new membranes.

5.4 Stability Trends

5.4.1 Approach

Error! Reference source not found. described a correlation between the stability nd theoretical molecular orbital densities for acetylacetonate-based MCCs, which demonstrated that the distribution of charge across the molecule could be used to understand the cause of degradation and identify complexes with increased stability. Similar DFT calculations were performed for the salicylaldimine-based MCCs.

5.4.2 Results: Charge Distribution and Structural Changes

The LUMO/HOMO densities of each complex previously tested using cyclic BE were quantified using the same procedure described in Section 3.2.2, and the results can be seen in Table 5.4.2-1. For each complex, DFT predicts that most of the charge is stored on the ligand during both reduction and oxidation which agrees with literature results for MCCs with similar ligand structures [154], [157], [160]–[162]. This is in

contrast to acetylacetonate complexes where DFT indicated that the charge storage was primarily metal-based (Section 3.5.4). For complex **32**, the oxidation reaction was found to be more stable than the reduction reaction, which could be a result of the ligand storing more charge during oxidation. This would need to be experimentally verified using XAS, and could lead to increased reduction stability by functionalizing the ligand to enhance reversible electron storage. The use of a different metal capable of reversibly accepting electrons could also lead to increased reversibility.

Table 5.4.2-1 DFT calculated bond length changes and LUMO/HOMO densities of complexes tested by BE.

Complex	LUMO Density on Metal [%]	HOMO Density on Metal [%]	Average M-O Bond Length Change (Second Oxidation) [Å]
25	11.7	5.6	-0.0094
29	15.3	4.5	-0.0112
31	16.8	6.0	0.0004
32	16.5	5.1	0.0060

Structural changes after the first and second oxidations were also determined using DFT structure optimization calculations following the procedure described in 2.2.5. The optimized structures can be found in Appendix A. A multi-term linear and non-linear regression analysis using Minitab [130] was performed to identify a relationship linking the experimentally determined cycle lifes to the DFT LUMO/HOMO densities and structural changes. All combination terms resulted in variance inflation factors (VIF) of greater than 5, indicating a high degree of correlation between the variables, and were therefore removed as possible terms. Minimal structural changes were predicted after the first oxidation, and no parameters yielded p-values of less than 0.05 from the regression

189

analysis. The bond length changes investigated included individual M-O, N-O, average M-O and N-O, individual M-ligand, conjugated carbons, functional groups, etc.

Similarly, limited structural changes were estimated for the complexes after the second oxidation, but in contrast to the structural changes after the first oxidation, a correlation between the cycle life and average M-O bond length changes was observed. The average M-O bond length changes from the neutral complex to the complex with a +2 charge can be seen in Table 5.4.2-1, and the regression analysis yielded a p-value of 0.046. The resulting correlation curve can be seen in Figure 5.4.2-1. It is important to mention that all of the bond length changes are small, and while the correlation does result in an R^2 value of 0.91, the fit is produced from four data points. The bond length changes are also counterintuitive. Ligand shedding was previously found to be the primary side reaction, and therefore M-O bond lengths were expected to increase for less stable complexes. However, the correlation demonstrates the opposite; extending the M-O bond lengths resulted in greater cycle lifes. It is likely that while the correlation factor is above 0.9, this is not the primary cause of instabilities, and XAS is needed to experimentally verify the charge distribution and structural changes.
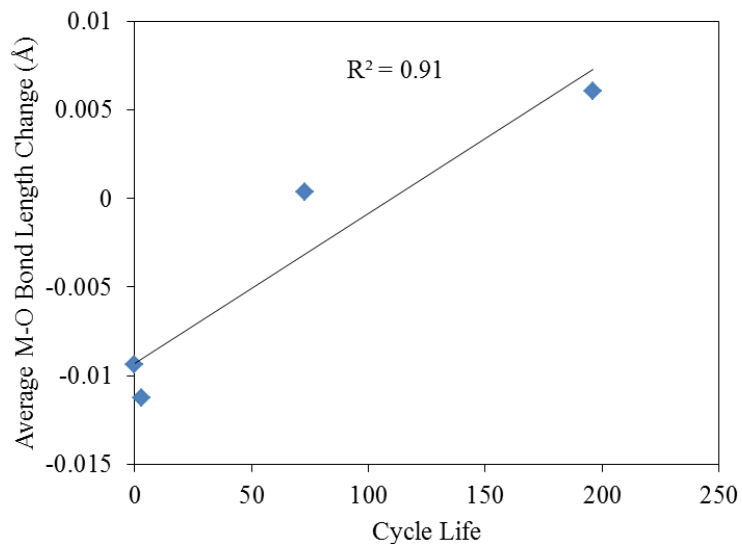
Figure 5.4.2-1 DFT calculated average M-O bond length changes during second oxidation reaction of complexes **25**, **29, 31** and **32** versus experimentally determined cycle lifes.

The lack of correlation between orbital densities and structural changes to experimentally determined cycle lifes was not expected based on the BE results, which showed significantly different E^2 cycle lifes for the tested complexes. Our hypothesis is that due to the close proximity standard potentials of E^2 and E^3, BE of E^2 unavoidably causes some of the E^3 reaction to take place. To test this possibility, the thermodynamics of coupled reactions were investigated.

5.4.3 Results: Coupled Redox Reactions – Nernstian Behavior

As alluded to in the last section, the apparent instabilities for the first oxidation reaction could be due to instabilities associated with the second or even third oxidation reactions. For uncoupled reactions with a potential separation of 180mV, only 0.1% of the second reaction will participate in the total reaction, when the overall SOC reaches 100% [20]. Assuming that the first reaction is ideally reversible, and the second reaction is completely irreversible, this will result in a cycle life of just 223 cycles. Coupled

191

reactions were not discussed. As seen in Table 5.3.2-1, E^2 and E^3 for each complex tested by BE are within 500mV from each other, and the BE results already demonstrated very poor stability for E^3 for complex **32**. For these reasons, the Nernstian response for two coupled reactions was calculated as follows:

$$E_2 = E^2 + \frac{RT}{F}\ln(\frac{C_{MCC+}}{C_{MCC}})$$

Equation 5.4.3-1

$$E_3 = E^3 + \frac{RT}{F}\ln(\frac{C_{MCC+2}}{C_{MCC+}})$$

Equation 5.4.3-2

Where E_2 is the potential of the first oxidation reaction, and E_3 is the potential of the second oxidation reaction. These equations can be presented in terms of SOC; when $SOC_2 = 1$, the complex (MCC) has completely oxidized, and when $SOC_3 = 1$, the oxidized complex (MCC+) has further oxidized to MCC+2. Therefore Equation 5.4.3-1 and Equation 5.4.3-2 can be converted to:

$$E_2 = E^2 + \frac{RT}{F}\ln(\frac{SOC_2}{1 - SOC_2})$$

Equation 5.4.3-3

$$E_3 = E^3 + \frac{RT}{F}\ln(\frac{SOC_2 SOC_3}{SOC_2(1 - SOC_3)})$$

Equation 5.4.3-4

Using these equations, the state of charge or extent of each reaction can be tracked at a given potential for a two-step reaction. An example of the results for two

reactions with a standard potential separation ($\Delta E^{2,3}$) of 0.1V can be seen in Figure
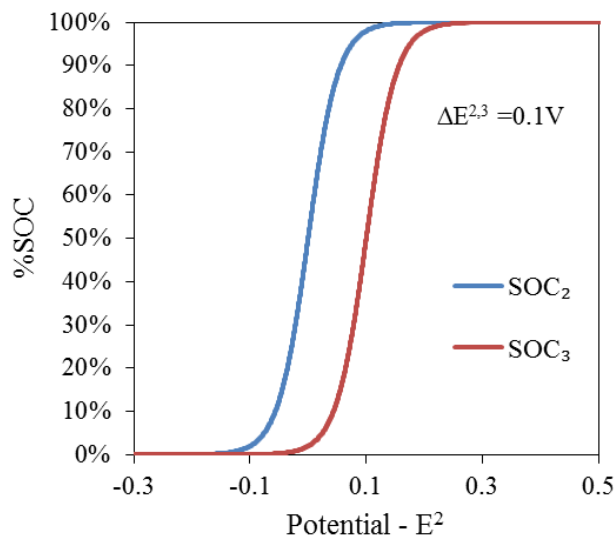
5.4.3-1.

Figure 5.4.3-1 Nernstian state of charge response for two coupled reactions with a standard potential separation of 0.1V.

For a standard potential separation of 0.1V, when 90% of the first reaction has completed (SOC_2=90%), ~5% of the second reaction has also taken place (SOC_3=5%). These overlapping reactions will contribute to the BE of each complex in Section 5.3.4 (Table 5.3.4-1). Therefore, these equations were used to determine what percentage of the observed SOC would result from coupled redox reactions, and the results can be seen in Figure 5.4.3-1.
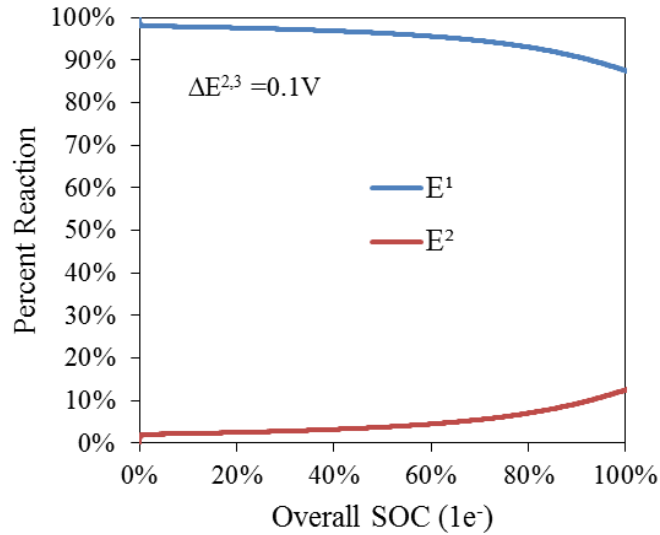
Figure 5.4.3-2 Nernstian plot of the percent of two reactions with a standard potential separation of 0.1V versus the overall SOC based on a one electron transfer.

For two reactions with a standard potential separation of 0.1V, at an overall 100% SOC, ~12.5% is the result of the second reaction (SOC_3). Assuming an irreversible second reaction, this would result in an overall cycle life of 1. This same procedure was used to determine the theoretical cycle life for reactions at varying standard potential differences assuming that the second reaction is completely irreversible. The results (Figure 5.4.3-3) show that even for two reactions with a standard potential difference of 0.3V, less than 100 cycles are expected. Furthermore, to achieve over 7000 cycles at 100% SOC, a standard potential separation of at least 0.55V is required.
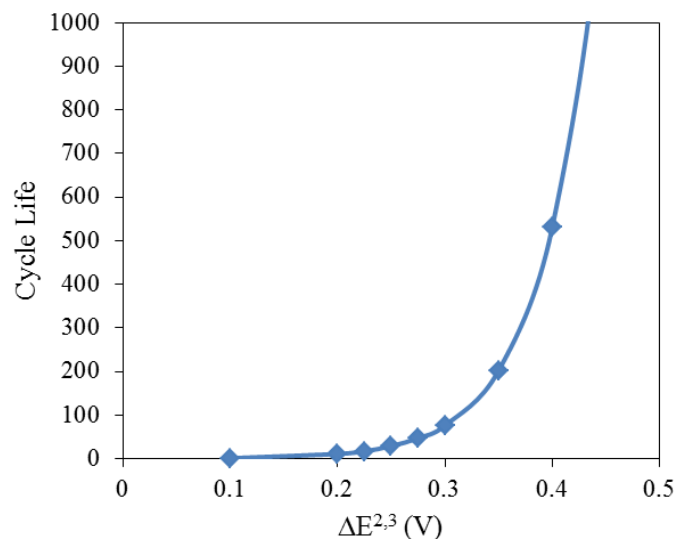
Figure 5.4.3-3 Theoretical Nernstian cycle life versus standard potential separation for a battery operating at 100% SOC.

The same procedure was also used to calculate the theoretical (Nernstian) cycle life of each complex tested using BE, using experimentally determined E^2 and E^3 values reported in Table 5.3.2-1. Again, the second oxidation reactions were assumed to be completely irreversible (therefore the calculated % SOC_3 is equal to the capacity loss per cycle), which is a reasonable assumption based on the poor stability of E^3 for complex **32**. As previously discussed, the instability of complex **25** is likely due to chemical reactions that occur to the oxidized complex at the un-functionalized R' location. Therefore, the Nernstian cycle life was not calculated for complex **25**.

Table 5.4.3-1 Calculated parameters and cycle lifes of complexes **25, 29, 31** and **32** from Equation 5.4.3-3 and Equation 5.4.3-4 for standard potentials obtained by CV.

Complex (Redox Couples)	$\Delta E^{2,3}$ [V]	Calculated % SOC_3	Nernstian Calculated Cycle Life	E^2 Estimated Irreversibility	Experimental Cycle Life
29 (E^2, E^3)	0.32	0.2%	113	5%	3
31 (E^2, E^3)	0.51	0.004%	4462	0.27%	73
32 (E^2, E^3)	0.43	0.022%	929	0.08%	193

In all cases, the calculated values are much higher than the experimentally determined values. To understand the significance of this difference, the percent irreversibility of the first oxidation reaction (E^2) was assumed, in order to match the Nernstian cycle life values to the experimental cycle lifes. By assuming a 0.27% irreversibility for E^2 of complex **31**, the calculated cycle life decreases from 4462 to 73, which demonstrates the impact that very minor side reactions can have over time for RFB chemistries. It also illustrates the minimal difference between an experimental cycle life of 73 and 193. While these values appear to be significantly different, they are the result of less than a 0.2% difference in reversibility - well within the error for CV experiments. Even for complex **7**, to match the calculated cycle life (113) to the experimental cycle life (3), only a 5% E^2 irreversibility was assumed.

Therefore, all E^3 reactions for complexes **29, 31** and **32** are likely unstable, and play a significant role in the varying experimental cycle life values. This is due to different standard potential separations leading to more of the second oxidation reaction (E^3) being accessed. Furthermore, very minor differences in the reversibility of E^2 were shown to have a major impact on the experimental cycle lifes. These minor reversibility differences could be the result of the theoretical structural changes discussed earlier, but must be verified experimentally.

5.5 Conclusions

These results demonstrate the ability to dramatically alter both the solubilities and stabilities of salicylaldimine-based MCCs by modifying the ligand with various functional groups at key locations. Substitutions at the nitrogen (R groups) were shown to primarily influence the solubility of the complex, while altering the functional groups at

the conjugated carbon ring (R' and R" groups) primarily impact the stability. Ultimately, these relationships allowed for the synthetic alteration of unstable complexes, to generate a complex with a solubility of 1.14M which can be reversibly oxidized for ~200 cycles.

The primary degradation mechanism for all of the complexes evaluated using BE, was ligand shedding which occurred during both reduction and oxidation reactions. For the complex with the most stable oxidation reaction, the degradation is more rapid during reduction, leading to flow cell operations with a cycle life of 10 cycles.

The standard potential and DFT molecular orbital energy correlation developed for acetylacetonate-based complexes in Chapter 2 was found to be highly accurate for salicylaldimine-based MCCs, and is likely to be applicable for a wide range of MCC classes. Additional DFT and Nernstian calculations demonstrated that the differences in the experimental cycle lifes are likely caused by a combination of the increased standard potential separations for complexes **31** and **32** and minor structural differences between each complex after multiple oxidations. Any attempts to correlate these effects to experimental cycle lifes is convoluted by minor irreversibilities playing a role in the cycle life values. To overcome this, more complexes with modest cycle lifes (20-50 cycles) are required.

Overall, salicylaldimine-based MCCs show promise as RFB active materials and should be further studied. Pairing complex **32** with a stable reduction reaction could yield a highly stable system, or the stability of the reduction reaction of complex **32** could be improved using different metal which are able to reversibly store electrons. Additional work to access all three oxidation reactions would have the largest impact. One method to

investigate this would be the use of different metals previously shown to reversibly oxidize (V, Fe, Mn).

Chapter 6

Conclusions and Future Work

6.1 Conclusions

Metal coordination complexes (MCCs) are being developed for use as active materials in non-aqueous RFBs. The design of these materials would benefit from a fundamental understanding of relationships between their structural and functional properties. In this dissertation, structure-function relationships are defined for metal acetylacetaonate and salicylaldimine complexes using a combination of experimental and computational techniques. The structures of the MCCs were modified using different functional groups and metals, and the standard potentials, solubilities, and stabilities were determined. Initial studies focused on identifying functional group types that could be used to increase the solubility, and a number of challenges involving the use of cyclic voltammetry (CV) to evaluate electrochemical reversibility were identified. Stability studies were conducted to quantify cycle lifes for individual half-cell reactions; changes in the structure and composition of the electrolytes were characterized using CV, X-ray Absorption Spectroscopy (XAS) and DFT structure optimization calculations. Finally, a second class of ligand was utilized to assess the validity of the relationships developed using acetylacetonate-based MCCs.

A series of metal(III) acetylacetonate complexes with varying metals and functional groups were used to determine how the electrochemistry and solubility could

be altered. The standard potentials were functions of the metal (Cr, V, Fe, Mn, Ru) primarily through influencing the free energy of the reduction or oxidation reaction. The metals types hade a minimal impact on the solubility. DFT calculations were shown to accurately calculate the free energy of these reactions, and theoretical molecular orbital energies were also shown to correlate to the standard potential values.

Chromium(III) acetylacetonate [$Cr(acac)_3$] modified to include functional groups of varying electronegativities demonstrated that, while functional groups with very low or high electronegativities led to increased solubilities of $Cr(acac)_3$ in ACN, the resulting complexes were very unstable. Ester functional groups of increasing chain lengths were found to increase the solubility of $Cr(acac)_3$ and $V(acac)_3$ in ACN to 1.8M and 1.34M, respectively. Regression analysis suggested that this result was primarily due to changes in the solvation energy and dipole moment of the complex. These solubilities represent 450% and 200% enhancements, respectively, compared to the corresponding $M(acac)_3$ parent complexes. Furthermore, the use of functional groups was shown to have a minimal impact on the standard potentials of the parent complexes. Finally, the stability of the most promising complex (an ester-modified $V(acac)_3$ complex) was assessed through charge-discharge cycling in a flow cell. Rapid capacity fade was observed despite minimal side reactions shown by CV. While CVs of the spent electrolyte provided evidence of ligand detachment, quantified concentrations did not match the observed capacities. Flow cell testing demonstrated limitations not only of CV to evaluate stability, but also of flow cell to fully understand the stability of both the reduction and oxidation reactions.

A detailed investigation of V(acac)$_3$ was conducted to identify the primary cause of capacity fade observed in flow cell experiments. Bulk electrolysis (BE), CV, and UV-Vis spectroscopy were used to determine the shelf life of neutral, oxidized and reduced complexes, which were all found to not cause the observed capacity fade. Likewise, the solubility of the neutral, oxidized and reduced versions were all found to be well above the concentrations used in flow cell experiments, and are therefore not the cause of capacity fade. By deduction, electrochemical degradation of acetylacetonate-based complexes is most likely the primary cause of capacity fade. The cycle lifes of 12 seemingly reversible redox couples (CV peak height ratios >0.8) were quantified using cyclic BE. The cycle lifes did not correlate with the CV peak height ratios, and in fact, the most stable redox couple had the lowest CV peak height ratio. This illustrates the importance of using electrochemical techniques that alter the bulk electrolyte concentrations, as the results could be dramatically different than with techniques employing small electrodes. A multi-term linear and non-linear regression analysis was performed, which resulted in the following equation:

$$CycleLife = 365.7 * MO_{Density} - 196.5$$

Equation 5.4.3-1

a cycle life predictive equation utilizing the lowest unoccupied or highest occupied molecular orbital metal density, with an R^2 value of 0.9. This equation suggests that the cycle life is primarily a function of the amount of charge stored on the metal, which can be theoretically calculated and used to predict the cycle life of a redox reaction for an acetylacetonate-based complex. While this correlation itself is a step forward for this class of MCCs, it was also shown to accurately calculate the cycle life of ferrocene, and could be applicable for other classes of MCCs where the metal stores most of the charge.

X-ray absorption spectroscopy was used to further characterize structural and electronic changes that occur to acetylacetonate complexes during reduction and oxidation. For V(acac)$_3$, minimal structural changes occurred during reduction, which led to a relatively high cycle life limited primarily by ligand detachment. Theoretical calculations indicated an increase in the V-O bond lengths during reduction; this is consistent with the experimental observation of ligand detachment. Oxidation resulted in the conversion of V(acac)$_3$ to VO(acac)$_2$ with subsequent conversion to a solvent stabilized complex which has been previously mistaken as native V(acac)$_3$. DFT and BE experiments were used to confirm the formation of VO(acac)$_2$ACN. Finally we proposed the following sequence of reactions to take place at the positive electrode:

$$V(acac)_3 \leftrightarrow [V(acac)_3]^{+1} + e^-$$
        Equation 4.3.3-1

$$V(acac)_3 \rightarrow VO(acac)_2 + e^- + \text{ligand fragments}$$
        Equation 4.3.3-2

$$VO(acac)_2 + MeCN + e^- \leftrightarrow VO(acac)_2MeCN$$
        Equation 4.3.3-3
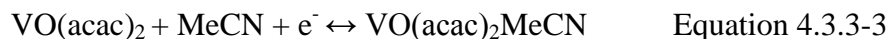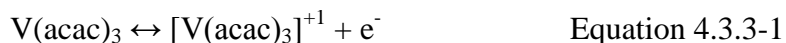
Similar experiments were performed for Ru(acac)$_3$ electrolytes, to determine if there were trends between different metals. Ru(acac)$_3$ reversibly converted to [Ru(acac)$_3$]$^-$ with the charge being stored entirely on the metal. This conversion results in elongation of the Ru-O bond which reversibly contracts during re-oxidation. These stretches are to a lesser extent than those calculated during the reduction of V(acac)$_3$, and the resulting cycle life for the reduction of Ru(acac)$_3$ is greater. The oxidation of Ru(acac)$_3$ in ACN appeared to initially produce [Ru(acac)$_3$]$^+$, as no structural changes were observed in the XAS spectra. However, the electrochemical signature dramatically changes, as Ru(acac)$_3$ converted to another species via chemical or electrochemical

processes, which is likely the result of ~30% of the charge coming from the acetylacetone ligands.

For the V(acac)$_3$ and Ru(acac)$_3$ experiments, significantly different degradation mechanisms were observed, which indicates that observed side reactions for a type of metal-acetylacetonate complex are not likely to translate to other metals, and each system should be evaluated independently. These studies demonstrate the need for detailed experiments concerning the electronic and structural changes of RFB active materials while in operation, instead of the typical post cycling CV, which has been shown to be misleading.

Results for the salicylaldimine complexes were significantly different from those for the acetylacetonate complexes. This was not unexpected given that the acetylacetonates are expected to be innocent ligands, while the salicylaldimines are non-innocent. Chromium(III) was used exclusively in this study to demonstrate that functional groups at different locations of the salicylaldimine ligand had a significant effect on both the solubility and stability. Solubility was found to be primarily influenced through substitution at the nitrogen, and similar to the acetylacetonate studies, electronegative groups were found to increase solubility. Altering the functional groups at the para and ortho positions of the conjugated carbon ring primarily impact the stability, and large sterically hindering functional groups such as t-Bu were found to make these complexes quite robust. The combination of electronegative functional groups on the nitrogen and t-Bu functional groups on the conjugated carbon ring led to a complex with a solubility of 1.14M in ACN that can be reversibly oxidized for ~200 cycles. While three oxidation couples are present in the CV, only the first was found to be stable, and evidence suggests

that capacity fade is primarily caused by unintentionally accessing the second oxidation reaction.

6.2 Future work

For the acetylacetonate and salicylaldimine complexes presented in this dissertation, the solubility could be manipulated significantly. For both complex classes, solubilities over 1.5M were achieved. Stability remains a significant challenge, and should be the focus of future research. The key next steps to improving stability are to modify the electrochemical cells used in bulk electrolysis (BE), identify additional mechanistic trends using X-ray absorption spectroscopy (XAS) and DFT transition state calculations, and synthetic modifications to the active materials.

Based on the fact that ferrocene was only able to achieve 100 cycles in the BE cell that was used, there are clearly limitations with regard to the cell and modifications are an obvious next step. Limiting cross-over from the working chamber to the counter chamber (and vice-versa) and working electrode surface treatments are key areas to examine. As described in Section 3.1.2, reticulated vitreous carbon (RVC) is analogous to glassy carbon, and is considered to be inert. Therefore, the cyclic voltammetry results should translate more accurately to the BE experiments, but RVC electrodes still have surface oxygen groups [118] which could react with MCCs. Two common methods to remove surface oxygen groups are high temperature treatments in inert gases and/or vacuum [164], and electrochemically cycling the electrode in a sacrificial electrolyte [165]. In the context of non-aqueous RFBs these treatments have not been widely studied, in part, because most studies are focused on finding an adequate active material. But if surface oxygen functional groups significantly influence the stability of an active material, then

an adequate active material may be disregarded due to electrode issues. While there has been significant interest in electrode pre-treatment effects for aqueous chemistries [166], this is an area of research that has yet to be explored for non-aqueous active materials and could significantly increase the observed cycle life values.

Cross-over between the working and counter chambers is also an issue in BE experiments, which convolutes the cycle life of an active species. To quantify the true electrochemical stability of an active material, new membranes with significantly lower cross-over and improved stability are required. A number of chemical compatibility issues have been raised with Neosepta membranes [55], which has been the primary membrane used in non-aqueous research [22]. Recent studies including those from out group have begun using porous separators to avoid chemical incompatibilities, but this dramatically increases cross-over, making concrete conclusions from extended cycle life experiments difficult to draw. Furthermore, new membranes with limited cross-over would also allow for more versatility in the selection of active species, such as different species being used in the anolyte and catholyte. Ligands such as bipyridines have shown the ability to generate MCCs with multiple reduction couples, while others such as salicylaldmines result in MCCs with multiple oxidation couples. Improved membranes would allow them to be used together, dramatically improving the possible energy density.

XAS has significantly increased the understanding of the charge distribution and side reactions that occur during the cycling of acetylacetonate-based MCCs, but only two MCCs were tested. Acetylacetonate-based complexes with different metals would be invaluable in verifying the DFT molecular orbital density results, and similar studies on

MCCs with different ligand could allow for more widely applicable structure-function relationships. We were also only able to conduct the XAS experiments for one charge-discharge cycle; testing in an actual flow cell would allow for extended cycling with in situ XAS. This could be accomplished by pumping the electrolyte through an in-line Kapton capillary, which would also allow for the use of in situ XAS for MCCs with metals with low energy photons.

All of the DFT calculations presented were for ground-state structures; in other words, transition states were neglected. The calculations were conducted in this fashion as transition state calculations can be computationally expensive and therefore any correlations developed would have limited applications. With that said, a possible reason for the lack of DFT calculated trends for salicylaldimine-based complexes could be that the degradation mechanism is kinetically, and not thermodynamically driven. Transition state theory would allow for the kinetics of a theoretical reaction to be evaluated and more exact mechanisms to be proposed. It is recommended that these types of calculations only be performed on complexes with highly desirable RFB properties (multiple redox couples, high solubility, high stability, etc.).

I would like to conclude by offering a recommendation regarding the screening process of future non-aqueous RFB active materials, including MCCs and organic active species. The Nernstian calculations described in Section 5.4.3 raise a number of issues for the future research of RFB active materials, primarily the required standard potential separation. If an electrolyte undergoes a reversible and irreversible reaction, to fully access the reversible reaction, the standard potentials must be separated by more than 0.55V (Figure 6.2-1). It is important to mention that this does not necessarily have to be a

reaction of the active material; it could be the irreversible degradation of the solvent or supporting electrolyte. For the supporting electrolyte used for these studies (TBABF$_4$), irreversible reactions were found to occur at 1.4V versus Ag/Ag$^+$, and therefore, if a SOC of 100% is desired, the standard potential of the catholyte reaction must be a maximum of 0.95V to achieve a cycle life of at least 7,000 cycles. One method to overcome this is to decrease the maximum state of charge (SOC) of the battery (Figure 6.2-1), but this would further decrease the energy density in a class of batteries that already suffer from low energy densities. Even for a SOC of 50%, a standard potential separation of at least 0.275V is required to reach 7,000 cycles. Therefore, active material CVs should be conducted in potential windows well beyond the standard potential of the redox couple of interest. This will greatly assist in understanding the causes of capacity fade. As such, this is a concern that must be addressed in future studies.
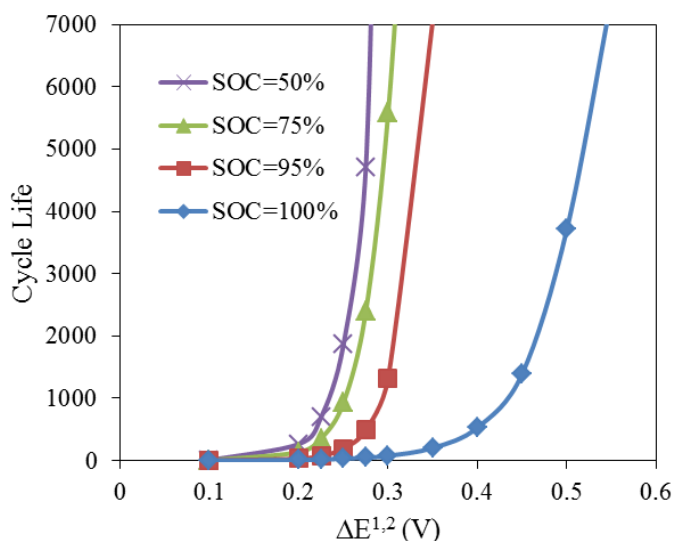
Figure 6.2-1 Theoretical Nernstian cycle life versus standard potential separation for a battery operating at varying SOCs.

Appendix A

Supporting Information

A.a. DFT Optimized Structures - Acetylacetonates

A.a.i. Complex 1

Table A-1 Optimized structures of Complex **1**

Atom	Complex **1**			[Complex **1**]$^{+1}$			[Complex **1**]$^{-1}$		
	X	Y	Z	X	Y	Z	X	Y	Z
V	0.000	0.048	0.000	0.000	-0.001	0.000	0.000	0.000	0.000
O	-1.526	0.162	-1.262	0.348	1.534	1.108	-0.892	1.472	-1.174
O	1.526	0.162	1.262	1.554	0.235	-1.111	-1.718	-0.116	1.174
O	0.863	-1.387	-1.089	-0.576	-1.464	-1.109	0.959	-1.431	1.174
O	-0.863	-1.387	1.089	-1.500	-0.468	1.111	1.722	0.037	-1.174
O	0.963	1.468	-1.083	-0.983	1.228	-1.110	-0.829	-1.510	-1.174
O	-0.963	1.468	1.083	1.156	-1.067	1.110	0.758	1.546	1.175
C	-2.675	0.720	-1.134	0.027	2.783	1.038	-0.835	2.731	-1.030
C	2.676	0.720	1.134	2.778	-0.174	-1.041	-2.716	-0.886	1.030
C	-3.652	0.443	-2.253	0.552	3.652	2.143	-1.587	3.545	-2.077
C	-3.038	1.549	-0.066	-0.760	3.297	0.001	-0.151	3.417	-0.001
C	0.762	-2.658	-0.981	-1.540	-2.320	-1.037	2.125	-1.909	1.030
C	-0.762	-2.658	0.981	-2.424	-1.367	1.040	2.783	-0.642	-1.030
C	2.154	1.900	-0.979	-1.241	2.491	-1.039	-1.948	-2.089	-1.030
C	-2.154	1.900	0.979	2.398	-1.414	1.039	0.590	2.795	1.030
C	3.652	0.443	2.253	3.681	0.286	-2.148	-3.814	-0.738	2.076
C	3.038	1.549	0.066	3.236	-0.993	-0.001	-2.884	-1.839	0.000
C	1.538	-3.458	-2.001	-1.591	-3.335	-2.142	2.548	-2.932	2.077
C	0.000	-3.318	0.000	-2.479	-2.306	0.002	3.035	-1.577	0.000
C	-1.539	-3.458	2.001	-3.440	-1.345	2.145	3.864	-0.398	-2.076
C	2.602	2.866	-2.053	-2.090	3.044	-2.146	-2.277	-3.147	-2.076
C	-2.602	2.866	2.053	2.891	-2.297	2.148	1.266	3.672	2.077
H	-3.805	-0.639	-2.344	1.645	3.572	2.186	-1.190	3.311	-3.073
H	-3.223	0.788	-3.202	0.167	3.291	3.104	-2.645	3.252	-2.075
H	-4.617	0.932	-2.096	0.271	4.699	2.012	-1.514	4.625	-1.908
H	-4.031	1.984	-0.067	-1.004	4.353	0.001	-0.198	4.502	-0.001
H	3.805	-0.639	2.344	3.681	1.382	-2.190	-3.395	-0.929	3.072
H	3.223	0.788	3.202	3.290	-0.071	-3.108	-4.182	0.296	2.074
H	4.617	0.932	2.096	4.704	-0.071	-2.019	-4.657	-1.418	1.907
H	4.031	1.984	0.067	4.272	-1.310	-0.002	-3.800	-2.423	-0.001
H	2.600	-3.190	-1.944	-0.645	-3.889	-2.176	1.833	-3.765	2.083
H	1.194	-3.192	-3.008	-1.697	-2.821	-3.104	2.511	-2.470	3.072
H	1.431	-4.537	-1.859	-2.417	-4.039	-2.015	3.555	-3.327	1.904
H	0.000	-4.402	0.000	-3.272	-3.043	0.002	3.999	-2.078	0.000
H	-2.600	-3.190	1.944	-3.924	-0.362	2.177	4.138	0.665	-2.077
H	-1.194	-3.192	3.008	-2.935	-1.485	3.107	3.464	-0.628	-3.072
H	-1.431	-4.537	1.859	-4.201	-2.118	2.020	4.764	-0.999	-1.906
H	1.924	3.728	-2.070	-3.033	2.488	-2.200	-2.273	-2.687	-3.073
H	2.527	2.379	-3.032	-1.577	2.898	-3.104	-1.495	-3.917	-2.074
H	3.626	3.216	-1.902	-2.303	4.106	-2.010	-3.249	-3.625	-1.908
H	-1.924	3.728	2.069	2.270	-3.198	2.205	2.346	3.473	2.078
H	-2.527	2.379	3.032	2.782	-1.772	3.105	0.889	3.407	3.072
H	-3.626	3.216	1.902	3.935	-2.584	2.012	1.100	4.742	1.906

A.a.ii.   Complex **2**

Table A-2 Optimized structures of Complex **2**

Atom	Complex **2**			[Complex **2**]$^{+1}$			[Complex **2**]$^{+2}$			[Complex **2**]$^{-1}$			[Complex **2**]$^{-2}$		
	X	Y	Z	X	Y	Z	X	Y	Z	X	Y	Z	X	Y	Z
Cr	0.000	0.000	0.000	0.000	-0.139	0.000	-0.081	0.000	0.000	-0.004	0.000	0.000	0.001	-0.003	0.000
O	-1.612	0.060	1.141	-0.921	1.216	-1.001	-1.550	-0.487	-1.273	-1.395	0.836	1.142	-1.609	-0.203	1.141
O	-0.863	-1.363	-1.142	0.921	1.217	1.000	-1.550	0.482	1.273	-1.393	-0.839	-1.142	-0.570	-1.524	-1.138
O	-0.750	1.428	-1.141	-1.376	-0.190	1.311	-0.088	-1.779	0.728	-0.035	1.626	-1.137	-1.033	1.249	-1.140
O	0.858	1.366	1.141	-0.975	-1.502	-0.982	1.249	-0.537	-1.251	1.418	0.780	1.142	0.630	1.495	1.139
O	1.611	-0.065	-1.142	0.976	-1.501	0.982	1.248	0.540	1.249	1.420	-0.778	-1.142	1.602	0.268	-1.141
O	0.754	-1.426	1.141	1.377	-0.190	-1.311	-0.094	1.777	-0.728	-0.032	-1.626	1.136	0.985	-1.295	1.138
C	-2.688	-0.617	1.021	-0.820	2.496	-0.933	-2.803	-0.439	-1.216	-2.665	0.701	1.030	-2.525	-1.093	1.029
C	-2.944	-1.551	0.002	-0.001	3.159	0.000	-3.484	-0.004	0.001	-3.319	-0.003	0.000	-2.604	-2.052	0.000
C	-2.030	-1.869	-1.019	0.818	2.497	0.933	-2.803	0.432	1.217	-2.663	-0.706	-1.030	-1.651	-2.203	-1.027
C	-3.735	-0.351	2.080	-1.648	3.265	-1.924	-3.619	-0.833	-2.402	-3.481	1.403	2.099	-3.603	-1.038	2.097
C	-2.403	-2.883	-2.077	1.646	3.267	1.923	-3.620	0.824	2.404	-3.479	-1.410	-2.099	-1.852	-3.267	-2.091
C	-0.605	2.692	-1.019	-2.602	-0.589	1.202	0.857	-2.648	0.705	0.720	2.657	-1.024	-1.088	2.525	-1.028
C	0.129	3.324	-0.001	-3.072	-1.313	0.102	1.963	-2.528	-0.180	1.660	2.867	0.004	-0.485	3.276	0.001
C	0.811	2.636	1.019	-2.221	-1.787	-0.923	2.067	-1.530	-1.181	1.941	1.946	1.031	0.311	2.731	1.027
C	1.566	3.410	2.077	-2.733	-2.717	-1.987	3.105	-1.615	-2.256	2.962	2.294	2.098	0.896	3.642	2.092
C	-1.298	3.521	-2.077	-3.488	-0.266	2.372	0.721	-3.821	1.624	0.519	3.717	-2.091	-1.909	3.227	-2.094
C	2.633	-0.823	-1.021	2.222	-1.785	0.924	2.063	1.536	1.180	1.945	-1.942	-1.031	2.734	-0.322	-1.029
C	2.815	-1.773	-0.001	3.073	-1.311	-0.101	1.956	2.533	0.179	1.665	-2.864	-0.004	3.085	-1.220	-0.002
C	1.879	-2.019	1.019	2.602	-0.588	-1.202	0.849	2.649	-0.705	0.725	-2.655	1.024	2.216	-1.637	1.026
C	2.174	-3.057	2.079	3.489	-0.266	-2.372	0.707	3.824	-1.622	0.527	-3.716	2.091	2.713	-2.595	2.093
C	3.696	-0.639	-2.080	2.734	-2.714	1.988	3.102	1.623	2.254	2.967	-2.289	-2.098	3.753	0.042	-2.094
H	-3.903	-2.056	0.002	-0.002	4.242	0.000	-4.571	-0.004	0.001	-4.405	-0.005	0.000	-3.459	-2.723	-0.001
H	-4.640	-0.945	1.932	-1.539	4.345	-1.806	-4.303	-1.651	-2.137	-4.560	1.304	1.933	-4.384	-1.793	1.943
H	-3.313	-0.573	3.067	-1.352	2.981	-2.940	-4.250	0.009	-2.721	-3.237	0.989	3.087	-3.155	-1.190	3.088
H	-3.996	0.714	2.073	-2.704	2.993	-1.809	-2.976	-1.141	-3.227	-3.219	2.469	2.125	-4.067	-0.041	2.105
H	-3.404	-3.295	-1.927	1.536	4.346	1.805	-4.304	1.642	2.139	-4.558	-1.315	-1.932	-2.768	-3.849	-1.932
H	-1.672	-3.699	-2.073	2.702	2.994	1.810	-2.977	1.132	3.229	-3.214	-2.476	-2.126	-0.991	-3.951	-2.098
H	-2.352	-2.409	-3.065	1.350	2.983	2.940	-4.250	-0.018	2.721	-3.236	-0.995	-3.087	-1.896	-2.800	-3.084
H	0.172	4.407	-0.001	-4.106	-1.637	0.101	2.699	-3.324	-0.181	2.207	3.806	0.003	-0.645	4.351	0.001
H	1.506	4.491	1.926	-3.800	-2.922	-1.879	3.896	-2.325	-2.007	3.412	3.281	1.941	0.629	4.694	1.937
H	1.161	3.160	3.064	-2.544	-2.278	-2.974	2.627	-1.944	-3.189	2.488	2.277	3.089	0.545	3.330	3.085
H	2.618	3.102	2.072	-2.176	-3.660	-1.943	3.534	-0.626	-2.448	3.758	1.537	2.112	1.992	3.549	2.097
H	-1.153	4.594	-1.929	-4.513	-0.612	2.218	1.429	-4.618	1.388	1.153	4.597	-1.930	-1.958	4.311	-1.937
H	-2.371	3.296	-2.070	-3.493	0.816	2.545	-0.302	-4.209	1.588	-0.533	4.033	-2.108	-2.930	2.820	-2.104
H	-0.915	3.238	-3.065	-3.081	-0.735	3.275	0.901	-3.485	2.655	0.743	3.297	-3.081	-1.478	3.032	-3.086
H	3.733	-2.350	0.000	4.107	-1.634	-0.100	2.689	3.331	0.180	2.215	-3.802	-0.003	4.096	-1.618	-0.001
H	3.138	-3.549	1.925	4.513	-0.611	-2.218	1.443	4.603	-1.418	1.162	-4.595	1.930	3.757	-2.891	1.935
H	2.168	-2.578	3.065	3.082	-0.735	-3.275	0.830	3.482	-2.659	0.751	-3.295	3.081	2.623	-2.131	3.084

H	1.379	-3.811	2.082	3.493	0.817	-2.546	-0.304	4.239	-1.542	-0.524	-4.033	2.109	2.084	-3.497	2.104
H	4.557	-1.295	-1.926	3.802	-2.917	1.882	3.890	2.336	2.005	3.419	-3.274	-1.940	4.714	-0.465	-1.945
H	4.032	0.404	-2.082	2.180	-3.659	1.943	3.534	0.636	2.445	3.761	-1.530	-2.112	3.919	1.129	-2.093
H	3.261	-0.840	-3.066	2.543	-2.276	2.975	2.623	1.951	3.188	2.492	-2.272	-3.089	3.365	-0.220	-3.088

A.a.iii.   Complex 3

Table A-3 Optimized structures of Complex **3**

Atom	Complex **3**			[Complex **3**]$^{+1}$			[Complex **3**]$^{-1}$		
	X	Y	Z	X	Y	Z	X	Y	Z
Mn	0.002	0.057	0.000	-0.003	0.000	-0.001	-0.001	-0.001	0.001
O	0.869	1.342	1.176	1.271	0.856	1.112	0.447	-1.766	1.221
O	-0.554	1.511	-1.169	-0.132	1.533	-1.108	1.630	-0.802	-1.221
C	0.942	2.614	1.059	1.750	2.051	1.020	1.310	-2.674	1.061
C	0.388	3.353	0.002	1.416	2.953	0.004	2.238	-2.763	-0.003
C	-0.328	2.765	-1.052	0.503	2.654	-1.014	2.338	-1.836	-1.066
C	1.692	3.312	2.168	2.720	2.419	2.107	1.334	-3.761	2.134
C	-0.899	3.619	-2.158	0.183	3.645	-2.097	3.400	-2.078	-2.137
O	1.844	-0.203	-1.120	1.387	-0.650	-1.115	-1.513	-1.013	-1.223
O	0.600	-1.372	1.151	0.107	-1.536	1.105	-1.750	0.497	1.222
C	2.719	-1.088	-0.912	2.049	-1.755	-1.021	-2.762	-1.101	-1.068
C	2.669	-2.037	0.146	1.862	-2.696	-0.002	-3.512	-0.552	-0.001
C	1.651	-2.118	1.096	0.912	-2.542	1.014	-2.968	0.202	1.065
C	3.897	-1.117	-1.867	3.065	-1.968	-2.108	-3.512	-1.886	-2.143
C	1.721	-3.155	2.196	0.752	-3.568	2.100	-3.919	0.719	2.144
O	-0.897	-1.198	-1.159	-1.265	-0.872	-1.116	-0.118	1.813	-1.222
O	-1.854	0.204	1.114	-1.383	0.667	1.113	1.303	1.266	1.225
C	-2.080	-1.706	-1.100	-2.552	-0.888	-1.019	0.426	2.941	-1.066
C	-3.055	-1.413	-0.147	-3.270	-0.256	0.002	1.278	3.316	0.000
C	-2.899	-0.474	0.909	-2.657	0.481	1.022	1.655	2.468	1.069
C	-2.370	-2.704	-2.200	-3.249	-1.656	-2.108	0.116	3.980	-2.142
C	-4.055	-0.247	1.866	-3.462	1.130	2.112	2.580	3.032	2.146
H	0.515	4.429	0.002	1.885	3.929	0.005	2.923	-3.607	-0.004
H	2.710	2.910	2.228	3.550	1.703	2.118	0.349	-4.241	2.180
H	1.738	4.394	2.023	3.114	3.429	1.977	2.098	-4.525	1.953
H	1.202	3.096	3.125	2.219	2.348	3.080	1.513	-3.297	3.112
H	-0.686	4.682	-2.015	0.729	4.581	-1.969	3.988	-2.986	-1.962
H	-0.484	3.292	-3.118	0.433	3.209	-3.072	2.911	-2.148	-3.116
H	-1.984	3.470	-2.208	-0.894	3.849	-2.102	4.076	-1.214	-2.175
H	3.487	-2.744	0.230	2.479	-3.585	0.000	-4.586	-0.720	-0.003
H	3.528	-1.278	-2.887	2.558	-1.982	-3.080	-3.342	-1.412	-3.118
H	4.396	-0.140	-1.855	3.768	-1.128	-2.123	-3.099	-2.901	-2.201
H	4.625	-1.896	-1.621	3.616	-2.901	-1.974	-4.590	-1.947	-1.955
H	2.619	-3.774	2.125	1.437	-4.409	1.972	-4.965	0.451	1.958
H	1.705	-2.652	3.170	0.933	-3.097	3.073	-3.612	0.314	3.116
H	0.834	-3.797	2.150	-0.280	-3.938	2.108	-3.832	1.811	2.206
H	-4.004	-1.931	-0.228	-4.349	-0.342	0.004	1.667	4.330	0.001
H	-1.638	-3.519	-2.156	-2.876	-2.686	-2.128	-0.970	4.127	-2.197
H	-3.379	-3.121	-2.128	-4.332	-1.665	-1.972	0.600	4.947	-1.960
H	-2.251	-2.216	-3.174	-3.008	-1.207	-3.079	0.439	3.595	-3.117
H	-4.932	-0.854	1.626	-4.534	0.969	1.980	2.863	4.076	1.966
H	-3.726	-0.478	2.886	-3.151	0.725	3.082	2.083	2.957	3.122
H	-4.334	0.813	1.850	-3.255	2.206	2.131	3.488	2.419	2.198

211

A.a.iv.   Complex 4

Table A-4 Optimized structures of Complex **4**

Atom	Complex **4**			[Complex **4**]$^{+1}$			[Complex **4**]$^{-1}$		
	X	Y	Z	X	Y	Z	X	Y	Z
Fe	0.003	-0.005	-0.004	0.004	-0.002	0.000	0.000	-0.001	-0.001
O	-0.978	1.318	-1.171	0.217	1.495	1.109	-0.834	1.565	-1.166
O	0.470	1.576	1.160	-1.206	0.897	-1.117	0.819	1.571	1.165
C	-1.128	2.580	-1.053	-0.346	2.648	1.008	-0.738	2.816	-1.019
C	-0.605	3.349	0.002	-1.253	2.994	-0.001	-0.018	3.478	0.001
C	0.161	2.810	1.051	-1.638	2.106	-1.014	0.709	2.822	1.021
C	-1.932	3.245	-2.148	0.046	3.630	2.079	-1.480	3.662	-2.051
C	0.683	3.711	2.148	-2.609	2.515	-2.088	1.442	3.674	2.054
O	-1.590	-0.390	1.175	1.389	0.589	-1.118	-1.769	-0.081	1.169
O	-0.667	-1.511	-1.167	1.192	-0.927	1.116	-0.941	-1.503	-1.167
C	-2.515	-1.262	1.064	2.651	0.355	-1.016	-2.799	-0.798	1.022
C	-2.616	-2.188	0.010	3.226	-0.419	0.000	-3.007	-1.753	0.001
C	-1.693	-2.261	-1.049	2.472	-1.023	1.014	-2.074	-2.044	-1.021
C	-3.551	-1.255	2.167	3.492	0.984	-2.094	-3.904	-0.588	2.055
C	-1.882	-3.284	-2.147	3.124	-1.846	2.091	-2.435	-3.109	-2.053
O	1.144	-1.191	1.163	-0.180	-1.501	-1.109	0.954	-1.496	1.164
O	1.635	0.176	-1.179	-1.394	-0.559	1.118	1.771	-0.063	-1.170
C	2.367	-1.539	1.053	-1.022	-2.470	-1.008	2.093	-2.025	1.020
C	3.213	-1.155	-0.003	-1.985	-2.571	0.003	3.025	-1.722	0.001
C	2.803	-0.324	-1.062	-2.125	-1.614	1.017	2.809	-0.769	-1.021
C	2.893	-2.428	2.158	-0.898	-3.518	-2.081	2.464	-3.086	2.052
C	3.778	0.035	-2.162	-3.166	-1.759	2.093	3.913	-0.546	-2.051
H	-0.801	4.415	0.006	-1.672	3.992	0.000	-0.024	4.565	0.003
H	-2.927	2.788	-2.197	1.134	3.760	2.078	-2.545	3.396	-2.037
H	-2.038	4.323	-1.996	-0.436	4.600	1.939	-1.376	4.739	-1.875
H	-1.446	3.062	-3.114	-0.231	3.226	3.060	-1.101	3.424	-3.053
H	0.403	4.758	2.000	-2.984	3.529	-1.931	1.324	4.750	1.882
H	0.294	3.366	3.113	-2.114	2.460	-3.065	1.068	3.428	3.055
H	1.775	3.632	2.194	-3.450	1.814	-2.111	2.510	3.422	2.037
H	-3.450	-2.880	0.012	4.299	-0.557	-0.001	-3.945	-2.300	0.000
H	-3.053	-1.415	3.131	3.195	0.577	-3.068	-3.504	-0.788	3.057
H	-4.027	-0.268	2.210	3.307	2.063	-2.124	-4.219	0.463	2.037
H	-4.320	-2.020	2.027	4.557	0.801	-1.938	-4.777	-1.227	1.884
H	-2.767	-3.906	-1.991	4.201	-1.940	1.937	-3.423	-3.552	-1.883
H	-1.968	-2.767	-3.110	2.937	-1.381	3.067	-2.409	-2.663	-3.056
H	-0.994	-3.925	-2.203	2.671	-2.844	2.116	-1.678	-3.903	-2.033
H	4.234	-1.517	-0.001	-2.648	-3.426	0.003	3.970	-2.258	0.002
H	2.272	-3.328	2.228	0.117	-3.931	-2.076	1.715	-3.888	2.030
H	3.935	-2.720	2.002	-1.618	-4.327	-1.945	3.457	-3.519	1.883
H	2.806	-1.901	3.116	-1.054	-3.054	-3.062	2.432	-2.642	3.055
H	4.763	-0.415	-2.012	-3.785	-2.646	1.943	4.792	-1.177	-1.880
H	3.372	-0.295	-3.125	-2.672	-1.824	3.070	3.517	-0.747	-3.055
H	3.883	1.125	-2.212	-3.803	-0.868	2.111	4.218	0.508	-2.030

212

A.a.v.   Complex 7

Table A-5 Optimized structures of Complex **7**

Atom	Complex **7**			[Complex **7**]$^{+1}$			[Complex **7**]$^{-1}$		
	X	Y	Z	X	Y	Z	X	Y	Z
Ru	0.000	0.095	0.000	0.002	0.000	0.000	0.000	-0.001	0.000
O	-0.982	-1.308	1.109	0.136	1.624	1.166	-0.747	1.521	-1.222
O	0.982	-1.308	-1.109	1.341	-0.925	1.173	0.694	-1.547	1.222
O	-0.975	1.543	1.100	-1.298	0.978	-1.171	0.994	1.372	1.224
O	1.509	0.089	1.365	1.500	0.632	-1.174	1.689	-0.117	-1.225
O	0.975	1.543	-1.100	-1.471	-0.692	1.173	-0.948	-1.406	-1.224
O	-1.509	0.089	-1.365	-0.199	-1.618	-1.168	-1.685	0.173	1.225
C	-0.825	-2.569	0.954	-0.472	2.752	1.034	-0.501	2.752	-1.032
C	0.825	-2.568	-0.954	-1.741	2.180	-1.038	1.797	-2.146	1.032
C	-2.199	1.857	0.953	-0.148	3.764	2.098	-1.146	3.689	-2.046
C	2.667	0.614	1.176	-1.373	3.055	-0.002	0.286	3.315	-0.001
C	2.198	1.857	-0.953	-1.026	-2.597	-1.034	0.963	2.626	1.032
C	-2.667	0.614	-1.176	2.621	-0.965	1.038	2.634	-0.942	-1.034
C	-1.632	-3.418	1.913	2.763	0.411	-1.040	-2.136	-1.809	-1.032
C	0.000	-3.196	0.000	-2.148	-1.780	1.040	-2.756	-0.481	1.034
C	1.632	-3.418	-1.913	-2.715	2.608	-2.102	2.107	-3.237	2.050
C	-2.738	2.814	1.995	-0.918	-3.654	-2.100	2.732	-1.903	-0.001
C	-3.046	1.414	-0.090	-1.967	-2.709	0.002	1.757	3.439	2.047
C	3.662	0.322	2.278	3.336	-1.750	2.104	3.766	-0.854	-2.051
C	3.045	1.415	0.090	3.334	-0.343	0.000	-2.628	-2.832	-2.049
C	2.738	2.814	-1.995	3.622	1.034	-2.106	-3.016	-1.411	0.002
C	-3.662	0.322	-2.278	-3.187	-2.002	2.106	-3.857	-0.202	2.052
H	-2.697	-3.185	1.801	0.935	3.929	2.130	-0.813	3.418	-3.056
H	-1.480	-4.489	1.752	-0.443	3.369	3.077	-2.235	3.562	-2.020
H	-1.353	-3.166	2.943	-0.654	4.716	1.927	-0.905	4.742	-1.863
H	0.000	-4.280	0.000	-1.818	4.042	-0.001	0.380	4.398	-0.002
H	2.697	-3.185	-1.801	-3.555	1.905	-2.134	2.125	-2.801	3.057
H	1.480	-4.488	-1.752	-2.223	2.568	-3.081	1.308	-3.989	2.037
H	1.353	-3.166	-2.943	-3.094	3.617	-1.931	3.066	-3.732	1.859
H	-2.115	3.715	2.019	0.109	-4.035	-2.137	3.623	-2.524	-0.001
H	-3.776	3.098	1.804	-1.132	-3.207	-3.078	2.805	3.114	2.038
H	-2.670	2.347	2.985	-1.605	-4.484	-1.926	1.367	3.246	3.055
H	-4.063	1.787	-0.086	-2.606	-3.584	0.001	1.717	4.516	1.851
H	3.776	-0.762	2.389	2.930	-2.768	2.145	3.365	-1.016	-3.060
H	4.641	0.769	2.083	3.149	-1.289	3.081	4.197	0.155	-2.033
H	3.274	0.706	3.229	4.412	-1.797	1.929	4.562	-1.583	-1.863
H	4.063	1.788	0.086	4.411	-0.452	0.000	-2.570	-2.401	-3.057
H	2.115	3.716	-2.019	3.430	2.112	-2.149	-1.970	-3.710	-2.034
H	3.776	3.098	-1.804	3.347	0.618	-3.083	-3.657	-3.155	-1.859
H	2.670	2.347	-2.984	4.685	0.862	-1.929	-4.000	-1.871	0.002
H	-3.776	-0.763	-2.389	-3.861	-1.139	2.148	-3.492	-0.440	3.059
H	-4.641	0.769	-2.083	-2.694	-2.075	3.083	-4.103	0.868	2.042
H	-3.275	0.706	-3.229	-3.769	-2.908	1.929	-4.768	-0.778	1.857

A.a.vi. Complexes 8, 10 and 15

Table A-6 Optimized structures of Complexes **8, 10** and **15**

Atom	Complex **8**			Atom	Complex **10**			Atom	Complex **15**		
	X	Y	Z		X	Y	Z		X	Y	Z
Cr	-0.004	0.000	0.000	Cr	0.003	-0.001	0.080	Cr	-0.304	-0.400	0.185
O	-1.393	-0.815	-1.125	O	-0.065	-1.615	-1.039	O	-0.952	1.294	-0.571
O	-1.424	0.758	1.126	O	-1.401	-0.800	1.201	O	0.841	0.659	1.381
O	0.046	-1.613	1.120	O	-1.363	0.860	-1.041	O	1.138	-0.480	-1.149
O	1.400	-0.790	-1.124	O	0.011	1.617	1.197	O	0.399	-2.075	0.935
O	-0.019	1.613	-1.120	O	1.432	0.744	-1.043	O	-1.758	-0.382	1.505
O	1.368	0.845	1.124	O	1.399	-0.813	1.201	O	-1.492	-1.419	-1.001
C	-2.665	-0.761	-1.033	C	-0.732	-2.692	-0.891	C	-0.615	2.498	-0.306
C	-3.333	-0.066	0.000	C	-1.626	-2.946	0.179	C	0.335	2.891	0.670
C	-2.693	0.655	1.034	C	-1.928	-1.961	1.151	C	0.993	1.925	1.471
C	-3.421	-1.500	-2.111	C	-0.502	-3.725	-1.976	C	-1.361	3.535	-1.127
H	-2.701	-1.944	-2.801	H	0.095	-3.273	-2.769	H	-1.929	3.022	-1.905
H	-4.051	-2.285	-1.679	H	-1.445	-4.091	-2.398	H	-0.689	4.262	-1.595
H	-4.087	-0.823	-2.657	H	0.047	-4.591	-1.582	H	-2.061	4.098	-0.496
C	-3.478	1.363	2.111	C	-2.952	-2.232	2.236	C	1.957	2.347	2.565
H	-2.776	1.836	2.801	H	-3.131	-1.308	2.788	H	2.449	1.457	2.961
H	-4.117	0.661	2.657	H	-3.900	-2.595	1.822	H	2.718	3.049	2.206
H	-4.139	2.123	1.679	H	-2.584	-2.989	2.941	H	1.418	2.841	3.383
Br	-5.258	-0.104	0.000	C	-2.324	-4.300	0.256	C	0.642	4.369	0.870
C	0.772	-2.660	1.026	H	-1.697	-5.090	-0.170	H	-0.244	4.978	0.669
C	1.723	-2.846	-0.002	H	-2.495	-4.596	1.297	H	0.884	4.574	1.917
C	1.994	-1.916	-1.031	C	-3.626	-4.342	-0.436	C	1.799	4.878	-0.009
C	3.020	-2.194	-2.103	N	-4.652	-4.355	-0.983	H	1.585	4.723	-1.075
H	3.051	-1.342	-2.785	C	-1.965	1.974	-0.894	H	2.718	4.309	0.181
H	2.771	-3.104	-2.658	C	-1.743	2.876	0.177	C	2.112	6.348	0.198
H	4.012	-2.352	-1.664	C	-0.739	2.650	1.149	O	1.564	7.082	0.996
C	0.546	-3.699	2.097	C	-2.974	2.289	-1.981	O	3.101	6.756	-0.630
H	-0.223	-3.335	2.781	H	-2.875	1.548	-2.776	C	3.504	8.145	-0.526
H	0.229	-4.652	1.658	H	-2.824	3.290	-2.401	H	2.631	8.776	-0.719
H	1.470	-3.897	2.652	H	-3.999	2.240	-1.589	H	3.835	8.335	0.500
Br	2.725	-4.491	-0.001	C	-0.471	3.670	2.237	C	4.613	8.378	-1.535
C	0.666	2.688	-1.027	H	0.418	3.366	2.793	H	4.266	8.176	-2.555
C	1.608	2.912	0.002	H	-0.314	4.674	1.827	H	5.474	7.733	-1.330
C	1.916	1.994	1.031	H	-1.314	3.724	2.939	H	4.944	9.421	-1.485
C	0.398	3.717	-2.098	C	-2.571	4.155	0.253	C	1.385	-2.796	0.561
H	-0.356	3.322	-2.782	H	-3.567	4.004	-0.176	C	2.237	-2.520	-0.537
H	0.043	4.656	-1.659	H	-2.746	4.449	1.293	C	2.042	-1.365	-1.334
H	1.313	3.952	-2.653	C	-1.959	5.306	-0.437	C	1.574	-4.050	1.398
C	2.930	2.313	2.103	N	-1.460	6.203	-0.982	H	0.945	-3.975	2.287
H	2.995	1.464	2.786	C	2.698	0.710	-0.896	H	2.615	-4.198	1.702
H	3.915	2.511	1.664	C	3.367	0.069	0.176	H	1.269	-4.938	0.829
H	2.644	3.213	2.658	C	2.668	-0.684	1.150	C	2.926	-1.093	-2.538
Br	2.543	4.596	0.001	C	3.475	1.424	-1.985	H	2.713	-0.089	-2.910
				H	2.785	1.697	-2.785	H	3.992	-1.172	-2.302
				H	4.275	0.798	-2.395	H	2.715	-1.813	-3.339
				H	3.933	2.343	-1.597	C	3.370	-3.482	-0.872
				C	3.417	-1.426	2.240	H	3.084	-4.509	-0.624
				H	2.709	-2.047	2.792	H	3.554	-3.500	-1.949
				H	4.212	-2.061	1.831	C	4.694	-3.153	-0.156
				H	3.882	-0.722	2.943	H	5.013	-2.127	-0.389
				C	4.889	0.147	0.253	H	4.582	-3.178	0.934
				H	5.256	1.084	-0.176	C	5.831	-4.077	-0.549
				H	5.230	0.152	1.294	O	5.842	-4.807	-1.521
				C	5.581	-0.960	-0.435	O	6.865	-3.979	0.317
				N	6.109	-1.841	-0.979	C	8.035	-4.784	0.026
								H	7.732	-5.835	-0.014
								H	8.412	-4.505	-0.964
								C	9.055	-4.524	1.119
								H	9.341	-3.467	1.148
								H	8.658	-4.802	2.101
								H	9.956	-5.120	0.931

							C	-2.940	-0.864	1.437
							C	-3.486	-1.549	0.323
							C	-2.706	-1.787	-0.836
							C	-3.273	-2.563	-2.011
							H	-2.574	-2.493	-2.847
							H	-4.252	-2.188	-2.327
							H	-3.399	-3.622	-1.749
							C	-3.755	-0.666	2.703
							H	-3.207	0.001	3.371
							H	-4.744	-0.242	2.501
							H	-3.908	-1.624	3.216
							C	-4.925	-2.047	0.375
							H	-5.035	-2.969	-0.203
							H	-5.196	-2.329	1.397
							C	-5.950	-1.020	-0.141
							H	-5.722	-0.725	-1.174
							H	-5.908	-0.088	0.436
							C	-7.378	-1.531	-0.115
							O	-7.718	-2.666	0.156
							O	-8.252	-0.553	-0.445
							C	-9.654	-0.919	-0.482
							H	-9.941	-1.299	0.504
							H	-9.783	-1.730	-1.205
							C	-10.442	0.320	-0.867
							H	-10.136	0.691	-1.851
							H	-10.297	1.122	-0.135
							H	-11.511	0.079	-0.907

A.a.vii.   Complexes 16, 17 and 19

Table A-7 Optimized structures of Complexes **16, 17** and **19**

Atom	Complex **16**			Atom	Complex **17**			Atom	Complex **19**		
	X	Y	Z		X	Y	Z		X	Y	Z
Cr	-0.498	-0.294	0.287	Cr	0.572	-0.666	0.222	Cr	-0.959	-0.385	0.468
O	-1.734	-1.362	-0.795	O	-0.503	0.635	-0.785	O	-0.541	-2.060	1.405
O	-2.022	0.103	1.460	O	1.074	0.799	1.431	O	0.178	-1.012	-1.005
O	-0.887	1.303	-0.787	O	2.140	-0.291	-0.902	O	0.578	0.508	1.306
O	0.688	0.839	1.373	O	1.691	-1.927	1.232	O	-1.320	1.295	-0.486
O	1.002	-0.770	-0.881	O	0.017	-2.113	-0.986	O	-2.128	0.190	1.939
O	-0.044	-1.876	1.358	O	-0.981	-1.107	1.341	O	-2.533	-1.225	-0.354
C	-3.007	-1.479	-0.736	C	-0.694	1.882	-0.582	C	0.192	-3.044	1.049
C	-3.840	-0.887	0.250	C	-0.143	2.633	0.487	C	0.894	-3.145	-0.178
C	-3.266	-0.158	1.326	C	0.722	2.027	1.432	C	0.823	-2.108	-1.141
C	-3.567	-2.339	-1.853	C	-1.574	2.544	-1.627	C	0.240	-4.169	2.067
H	-4.531	-2.798	-1.627	H	-2.012	1.768	-2.257	H	-0.229	-3.825	2.991
H	-2.836	-3.116	-2.088	H	-2.373	3.147	-1.185	H	1.263	-4.497	2.282
H	-3.691	-1.726	-2.756	H	-0.978	3.212	-2.263	H	-0.311	-5.044	1.700
C	-4.116	0.368	2.470	C	1.348	2.842	2.550	C	1.525	-2.240	-2.481
H	-3.461	0.880	3.178	H	1.828	2.159	3.254	H	1.450	-1.288	-3.010
H	-4.881	1.070	2.121	H	0.617	3.458	3.084	H	2.580	-2.512	-2.377
H	-4.632	-0.447	2.991	H	2.111	3.521	2.148	H	1.046	-3.016	-3.092
C	-5.349	-1.074	0.179	C	-0.479	4.110	0.617	C	1.724	-4.388	-0.469
H	-5.809	-0.823	1.138	H	-0.637	4.553	-0.372	H	1.285	-5.267	0.009
H	-5.592	-2.131	0.010	H	0.361	4.659	1.053	H	1.706	-4.618	-1.539
C	-6.060	-0.230	-0.925	C	-1.739	4.386	1.485	C	3.193	-4.269	-0.019
H	-5.605	-0.469	-1.891	H	-1.586	3.987	2.493	H	3.251	-4.051	1.057
C	-7.504	-0.691	-1.056	H	-2.614	3.894	1.050	H	3.700	-3.431	-0.510
O	-7.938	-1.357	-1.977	C	-1.990	5.872	1.610	C	3.995	-5.532	-0.266
O	-8.263	-0.305	-0.004	O	-1.369	6.622	2.341	O	3.533	-6.625	-0.524
C	-9.652	-0.720	-0.018	O	-2.965	6.292	0.772	O	5.325	-5.300	-0.146
H	-9.688	-1.813	-0.064	C	-3.227	7.711	0.755	C	6.194	-6.440	-0.322
H	-10.121	-0.330	-0.927	H	-2.308	8.248	0.500	H	6.034	-6.876	-1.312
C	-10.306	-0.178	1.239	H	-3.549	8.025	1.754	H	5.964	-7.198	0.432
H	-9.822	-0.573	2.139	C	-4.309	7.989	-0.266	C	7.616	-5.923	-0.171
H	-10.255	0.916	1.271	H	-5.154	7.302	-0.095	H	7.757	-5.477	0.827
H	-11.362	-0.473	1.261	O	-3.798	7.777	-1.583	H	7.819	-5.144	-0.923
C	-5.952	1.285	-0.689	C	-4.681	8.468	-2.466	O	8.479	-7.031	-0.352
H	-6.444	1.579	0.244	H	-4.163	8.591	-3.420	C	9.855	-6.699	-0.243
H	-4.899	1.582	-0.640	H	-5.589	7.864	-2.632	H	10.132	-5.943	-0.995
H	-6.421	1.843	-1.508	C	-5.019	9.792	-1.752	H	10.078	-6.288	0.754
C	1.844	-1.733	-0.812	H	-4.339	10.587	-2.073	C	10.656	-7.973	-0.470
C	1.885	-2.716	0.209	H	-6.041	10.123	-1.967	H	10.377	-8.730	0.282
C	0.899	-2.728	1.234	C	-4.803	9.457	-0.251	H	10.431	-8.385	-1.467
C	2.836	-1.721	-1.959	H	-5.718	9.561	0.342	O	12.028	-7.639	-0.362
H	3.306	-2.685	-2.156	H	-4.047	10.116	0.191	C	12.886	-8.749	-0.554
H	2.318	-1.375	-2.858	C	3.323	-0.773	-0.856	H	13.910	-8.384	-0.449
H	3.632	-0.995	-1.745	C	3.787	-1.720	0.091	H	12.757	-9.185	-1.557
C	0.868	-3.817	2.292	C	2.921	-2.240	1.086	H	12.702	-9.532	0.199
H	0.054	-3.598	2.987	C	4.238	-0.255	-1.951	C	-3.386	0.039	2.102
H	1.808	-3.876	2.850	H	3.739	0.571	-2.462	C	-4.256	-0.625	1.199
H	0.692	-4.801	1.841	H	5.202	0.088	-1.564	C	-3.756	-1.229	0.019
C	2.966	-3.789	0.187	H	4.442	-1.045	-2.686	C	-3.911	0.623	3.401
H	2.692	-4.617	0.846	C	3.411	-3.280	2.078	H	-3.114	1.203	3.871
H	3.038	-4.231	-0.815	H	2.655	-3.405	2.856	H	-4.786	1.263	3.251
C	4.391	-3.308	0.610	H	4.364	-3.005	2.540	H	-4.211	-0.178	4.090
H	4.698	-2.499	-0.060	H	3.559	-4.246	1.579	C	-4.679	-1.989	-0.917
C	5.353	-4.467	0.399	C	5.232	-2.192	0.036	H	-4.124	-2.249	-1.820
O	5.483	-5.412	1.153	H	5.588	-2.202	-1.000	H	-5.564	-1.408	-1.193
O	6.034	-4.351	-0.766	H	5.312	-3.226	0.382	H	-5.029	-2.916	-0.444
C	6.943	-5.432	-1.096	C	6.205	-1.324	0.882	C	-5.743	-0.696	1.511
H	6.371	-6.364	-1.147	H	5.883	-1.328	1.929	H	-5.910	-0.718	2.591
H	7.672	-5.530	-0.286	H	6.200	-0.290	0.527	H	-6.167	-1.631	1.132
C	7.601	-5.091	-2.420	C	7.609	-1.885	0.831	C	-6.556	0.489	0.924
H	8.161	-4.152	-2.351	O	7.991	-2.856	1.454	H	-6.146	1.433	1.303

H	6.857	-4.993	-3.217	O	8.396	-1.203	-0.036	H	-6.484	0.509	-0.167
H	8.300	-5.888	-2.698	C	9.743	-1.700	-0.215	C	-8.007	0.423	1.349
C	4.454	-2.817	2.062	H	9.707	-2.725	-0.594	O	-8.397	0.519	2.496
H	4.257	-3.637	2.760	H	10.261	-1.706	0.750	O	-8.839	0.219	0.300
H	3.718	-2.023	2.227	C	10.431	-0.780	-1.218	C	-10.247	0.122	0.607
H	5.446	-2.412	2.296	H	9.800	-0.700	-2.113	H	-10.416	-0.703	1.305
C	-0.302	2.440	-0.816	O	11.670	-1.419	-1.575	H	-10.585	1.049	1.079
C	0.732	2.849	0.065	C	12.745	-0.477	-1.478	C	-10.959	-0.117	-0.716
C	1.107	2.027	1.161	H	13.653	-1.040	-1.240	H	-10.758	0.713	-1.412
C	2.033	2.550	2.245	H	12.888	0.030	-2.445	H	-10.596	-1.047	-1.182
H	2.258	1.736	2.936	C	12.310	0.510	-0.394	O	-12.343	-0.206	-0.430
H	2.968	2.953	1.845	H	12.502	0.087	0.599	C	-13.144	-0.429	-1.582
H	1.545	3.359	2.805	H	12.827	1.473	-0.459	H	-12.861	-1.373	-2.074
C	-0.856	3.379	-1.873	C	10.798	0.618	-0.666	H	-13.013	0.388	-2.308
H	-1.633	2.852	-2.431	H	10.600	1.387	-1.422	C	-14.595	-0.494	-1.128
H	-0.083	3.713	-2.571	H	10.215	0.874	0.224	H	-14.877	0.450	-0.635
H	-1.294	4.275	-1.416	C	-1.861	-2.024	1.208	H	-14.724	-1.310	-0.399
C	1.391	4.210	-0.100	C	-1.929	-2.947	0.135	O	-15.391	-0.718	-2.279
H	0.756	4.881	-0.683	C	-0.966	-2.926	-0.905	C	-16.774	-0.799	-1.989
H	1.503	4.691	0.880	C	-2.865	-2.077	2.346	H	-17.290	-0.969	-2.937
C	2.798	4.178	-0.784	H	-2.729	-1.193	2.973	H	-17.144	0.136	-1.538
H	3.451	3.519	-0.203	H	-3.900	-2.112	1.991	H	-16.991	-1.633	-1.303
C	3.382	5.581	-0.713	H	-2.698	-2.969	2.963	C	-0.697	2.411	-0.458
O	3.079	6.501	-1.448	C	-1.020	-3.935	-2.037	C	0.449	2.691	0.328
O	4.263	5.708	0.307	H	-0.316	-3.628	-2.813	C	1.006	1.705	1.179
C	4.840	7.024	0.504	H	-2.020	-4.030	-2.472	C	-1.315	3.478	-1.343
H	5.362	7.314	-0.414	H	-0.729	-4.930	-1.676	H	-2.063	3.009	-1.986
H	4.028	7.740	0.667	C	-3.046	-3.979	0.098	H	-0.575	3.992	-1.965
C	5.779	6.942	1.693	H	-2.706	-4.899	-0.386	H	-1.810	4.244	-0.732
H	6.581	6.217	1.513	H	-3.324	-4.274	1.116	C	2.198	2.025	2.065
H	5.242	6.646	2.600	C	-4.321	-3.494	-0.640	H	2.548	1.100	2.528
H	6.236	7.923	1.870	H	-4.056	-3.184	-1.658	H	3.022	2.485	1.510
C	2.760	3.687	-2.237	H	-4.761	-2.627	-0.140	H	1.908	2.724	2.861
H	2.287	2.702	-2.291	C	-5.350	-4.599	-0.761	C	1.080	4.074	0.259
H	2.206	4.387	-2.872	O	-5.141	-5.682	-1.272	H	0.322	4.834	0.053
H	3.773	3.598	-2.646	O	-6.543	-4.250	-0.225	H	1.506	4.345	1.231
C	-7.594	-5.241	-0.286	C	-7.594	-5.241	-0.286	C	2.190	4.201	-0.818
H	-7.275	-6.146	0.238	H	-7.275	-6.146	0.238	H	1.778	3.929	-1.797
H	-7.790	-5.500	-1.332	H	-7.790	-5.500	-1.332	H	3.020	3.521	-0.610
C	-8.824	-4.637	0.383	C	-8.824	-4.637	0.383	C	2.697	5.624	-0.922
H	-8.543	-4.284	1.385	H	-8.543	-4.284	1.385	O	2.005	6.587	-1.183
O	-9.783	-5.702	0.516	O	-9.783	-5.702	0.516	O	4.026	5.714	-0.672
C	-11.050	-5.282	-0.005	C	-11.050	-5.282	-0.005	C	4.602	7.037	-0.738
H	-11.560	-6.172	-0.386	H	-11.560	-6.172	-0.386	H	4.467	7.447	-1.743
H	-11.660	-4.846	0.802	H	-11.660	-4.846	0.802	H	4.095	7.694	-0.025
C	-10.717	-4.239	-1.072	C	-10.717	-4.239	-1.072	C	6.075	6.882	-0.396
H	-11.554	-3.566	-1.289	H	-11.554	-3.566	-1.289	H	6.565	6.207	-1.115
H	-10.427	-4.733	-2.006	H	-10.427	-4.733	-2.006	H	6.189	6.447	0.610
C	-9.516	-3.519	-0.432	C	-9.516	-3.519	-0.432	O	6.650	8.175	-0.450
H	-8.839	-3.066	-1.163	H	-8.839	-3.066	-1.163	C	8.037	8.190	-0.146
H	-9.860	-2.721	0.237	H	-9.860	-2.721	0.237	H	8.215	7.806	0.870
								H	8.596	7.558	-0.854
								C	8.514	9.632	-0.247
								H	8.335	10.016	-1.265
								H	7.952	10.263	0.459
								O	9.897	9.645	0.059
								C	10.465	10.940	0.007
								H	11.523	10.836	0.257
								H	9.986	11.616	0.734
								H	10.372	11.379	-0.999

A.a.viii. Complex 18

Table A-8 Optimized structures of Complex **18**

Atom	Complex **18**			[Complex **18**]$^{+1}$			[Complex **18**]$^{+2}$			[Complex **18**]$^{-1}$			[Complex **18**]$^{-2}$		
	X	Y	Z	X	Y	Z	X	Y	Z	X	Y	Z	X	Y	Z
Cr	-0.508	-0.513	0.144	0.235	-0.312	0.211	-0.006	-0.091	0.195	0.245	-0.568	-0.457	-0.375	-0.381	-0.037
O	-0.029	-2.042	1.281	1.478	-1.309	1.265	0.796	-1.505	1.220	0.968	-1.898	0.896	-0.013	-1.818	1.264
O	1.080	-0.918	-0.941	1.700	0.005	-1.017	1.542	-0.195	-0.963	2.115	-0.590	-1.237	1.291	-0.861	-0.974
O	-0.926	1.035	-0.993	-0.935	0.755	-0.852	-0.722	1.384	-0.841	-0.369	0.845	-1.804	-0.755	1.047	-1.342
O	0.548	0.699	1.274	0.644	1.307	1.194	0.835	1.275	1.310	0.706	1.447	0.705	0.658	0.920	1.027
O	-1.608	-1.687	-0.983	-0.260	-1.888	-0.770	-0.923	-1.377	-0.900	-0.714	-2.327	-1.715	-1.398	-1.693	-1.095
O	-2.113	-0.169	1.223	-1.177	-0.714	1.452	-1.544	-0.084	1.351	-1.623	-0.685	0.369	-2.039	0.109	0.899
C	0.941	-2.869	1.190	2.582	-1.885	0.932	1.681	-2.372	0.896	2.133	-2.373	1.057	0.964	-2.647	1.307
C	1.942	-2.850	0.185	3.249	-1.665	-0.297	2.429	-2.318	-0.323	3.265	-2.083	0.243	2.020	-2.721	0.360
C	1.935	-1.862	-0.831	2.769	-0.672	-1.202	2.335	-1.171	-1.180	3.162	-1.206	-0.875	2.106	-1.823	-0.737
C	0.933	-3.942	2.263	3.125	-2.828	1.978	1.884	-3.476	1.899	2.256	-3.354	2.221	0.875	-3.641	2.458
H	0.217	-3.658	3.036	2.591	-2.669	2.917	1.415	-3.195	2.844	1.327	-3.315	2.796	0.105	-3.292	3.150
H	1.917	-4.095	2.717	4.198	-2.701	2.143	2.939	-3.707	2.067	3.098	-3.127	2.884	1.818	-3.757	3.007
H	0.620	-4.904	1.836	2.967	-3.868	1.661	1.408	-4.397	1.537	2.395	-4.380	1.856	0.585	-4.641	2.100
C	2.981	-1.869	-1.931	3.515	-0.330	-2.467	3.198	-1.033	-2.407	4.373	-0.964	-1.774	3.224	-1.946	-1.765
H	2.897	-0.940	-2.499	3.106	0.590	-2.888	3.128	-0.012	-2.784	4.121	-0.162	-2.471	3.213	-1.046	-2.386
H	4.000	-1.966	-1.543	4.590	-0.214	-2.305	4.244	-1.283	-2.215	5.273	-0.684	-1.214	4.219	-2.054	-1.315
H	2.809	-2.710	-2.616	3.380	-1.136	-3.201	2.836	-1.715	-3.188	4.616	-1.865	-2.354	3.070	-2.814	-2.422
C	3.035	-3.907	0.199	4.533	-2.414	-0.602	3.388	-3.438	-0.656	4.604	-2.722	0.569	3.082	-3.797	0.520
H	2.657	-4.844	0.618	4.495	-3.416	-0.168	2.998	-4.388	-0.279	4.464	-3.707	1.027	2.657	-4.695	0.983
H	3.341	-4.148	-0.825	4.618	-2.579	-1.681	3.449	-3.562	-1.742	5.180	-2.900	-0.345	3.456	-4.117	-0.459
C	4.295	-3.491	1.007	5.816	-1.717	-0.105	4.821	-3.265	-0.098	5.485	-1.867	1.535	4.306	-3.352	1.381
H	4.747	-2.592	0.579	5.974	-0.748	-0.591	5.377	-2.476	-0.615	5.664	-0.884	1.088	4.782	-2.484	0.914
H	4.007	-3.266	2.040	5.756	-1.499	0.970	4.803	-2.976	0.961	4.959	-1.724	2.483	3.964	-3.064	2.379
C	5.308	-4.614	1.050	7.047	-2.584	-0.326	5.595	-4.576	-0.194	6.800	-2.541	1.830	5.312	-4.464	1.541
O	5.171	-5.646	1.676	7.016	-3.767	-0.593	5.076	-5.667	-0.287	7.029	-3.289	2.762	5.319	-5.296	2.430
O	6.386	-4.358	0.270	8.175	-1.871	-0.167	6.921	-4.368	-0.134	7.734	-2.260	0.878	6.219	-4.475	0.527
C	7.394	-5.391	0.208	9.427	-2.594	-0.307	7.756	-5.556	-0.157	9.007	-2.914	1.017	7.190	-5.539	0.541
H	6.948	-6.320	-0.161	9.482	-3.031	-1.307	7.588	-6.099	-1.091	8.870	-3.999	1.028	6.679	-6.507	0.504
H	7.794	-5.574	1.210	9.464	-3.400	0.431	7.487	-6.205	0.680	9.478	-2.618	1.959	7.775	-5.495	1.465
C	8.473	-4.883	-0.734	10.540	-1.583	-0.081	9.195	-5.074	-0.049	9.841	-2.475	-0.176	8.076	-5.336	-0.678
H	8.896	-3.938	-0.354	10.455	-1.140	0.925	9.357	-4.527	0.894	9.947	-1.379	-0.184	8.550	-4.341	-0.642
H	8.046	-4.686	-1.731	10.469	-0.766	-0.819	9.443	-4.394	-0.880	9.348	-2.775	-1.115	7.475	-5.385	-1.601
O	9.469	-5.886	-0.805	11.755	-2.288	-0.223	10.008	-6.228	-0.095	11.111	-3.098	-0.060	9.057	-6.357	-0.664
C	10.548	-5.539	-1.654	12.902	-1.474	-0.032	11.405	-5.973	-0.050	11.982	-2.775	-1.125	9.957	-6.268	-1.757
H	11.249	-6.377	-1.637	13.773	-2.120	-0.164	11.902	-6.943	-0.092	12.922	-3.303	-0.943	10.673	-7.092	-1.667
H	11.059	-4.630	-1.300	12.919	-1.042	0.980	11.675	-5.455	0.882	12.179	-1.691	-1.169	10.510	-5.314	-1.748
H	10.205	-5.374	-2.688	12.939	-0.659	-0.771	11.716	-5.356	-0.905	11.568	-3.097	-2.094	9.431	-6.358	-2.722

218

C	-2.853	-1.967	-0.916	-1.193	-2.747	-0.580	-2.012	-2.028	-0.712	-1.770	-2.963	-1.492	-2.650	-1.966	-1.057
C	-3.754	-1.471	0.061	-2.080	-2.728	0.533	-2.841	-1.874	0.441	-2.765	-2.610	-0.514	-3.590	-1.388	-0.162
C	-3.308	-0.601	1.086	-1.993	-1.701	1.515	-2.545	-0.881	1.425	-2.607	-1.487	0.339	-3.213	-0.392	0.779
C	-3.322	-2.936	-1.986	-1.266	-3.831	-1.627	-2.354	-3.009	-1.803	-1.967	-4.231	-2.336	-3.071	-3.054	-2.037
H	-2.526	-3.055	-2.724	-0.628	-3.559	-2.470	-1.720	-2.820	-2.670	-1.183	-4.251	-3.096	-2.241	-3.231	-2.725
H	-4.234	-2.600	-2.488	-2.287	-3.996	-1.983	-3.405	-2.952	-2.100	-2.945	-4.275	-2.830	-3.964	-2.793	-2.619
H	-3.538	-3.918	-1.545	-0.910	-4.784	-1.213	-2.176	-4.035	-1.456	-1.875	-5.135	-1.717	-3.290	-3.999	-1.516
C	-4.261	-0.116	2.165	-2.870	-1.709	2.743	-3.414	-0.693	2.640	-3.687	-1.164	1.378	-4.229	0.181	1.760
H	-3.756	0.649	2.759	-2.733	-0.773	3.288	-3.118	0.219	3.161	-3.478	-0.171	1.782	-3.775	1.048	2.248
H	-5.185	0.300	1.750	-3.928	-1.832	2.493	-4.477	-0.639	2.385	-4.704	-1.179	0.969	-5.166	0.493	1.283
H	-4.543	-0.943	2.830	-2.592	-2.541	3.402	-3.286	-1.541	3.326	-3.655	-1.885	2.207	-4.490	-0.550	2.539
C	-5.215	-1.889	0.009	-3.118	-3.824	0.678	-4.064	-2.753	0.596	-4.015	-3.465	-0.388	-5.038	-1.848	-0.213
H	-5.316	-2.897	-0.404	-2.750	-4.760	0.252	-3.886	-3.731	0.143	-3.798	-4.510	-0.630	-5.101	-2.898	-0.520
H	-5.629	-1.949	1.022	-3.290	-4.045	1.736	-4.244	-2.956	1.657	-4.382	-3.471	0.644	-5.493	-1.802	0.783
C	-6.107	-0.936	-0.831	-4.471	-3.489	0.017	-5.357	-2.174	-0.024	-5.191	-3.002	-1.310	-5.926	-1.013	-1.189
H	-6.103	0.074	-0.413	-4.957	-2.627	0.488	-5.740	-1.316	0.537	-5.447	-1.964	-1.075	-5.927	0.034	-0.874
H	-5.711	-0.874	-1.851	-4.336	-3.212	-1.037	-5.176	-1.812	-1.045	-4.878	-3.054	-2.356	-5.509	-1.072	-2.198
C	-7.527	-1.452	-0.928	-5.423	-4.677	0.056	-6.439	-3.245	-0.117	-6.406	-3.877	-1.144	-7.341	-1.534	-1.244
O	-7.842	-2.518	-1.420	-5.084	-5.820	0.286	-6.216	-4.436	-0.157	-6.677	-4.864	-1.801	-7.750	-2.404	-1.992
O	-8.422	-0.594	-0.382	-6.683	-4.298	-0.216	-7.666	-2.700	-0.179	-7.182	-3.465	-0.100	-8.135	-0.947	-0.308
C	-9.807	-1.004	-0.415	-7.683	-5.350	-0.258	-8.771	-3.629	-0.333	-8.329	-4.276	0.203	-9.494	-1.417	-0.229
H	-10.120	-1.160	-1.451	-7.407	-6.081	-1.023	-8.640	-4.201	-1.255	-9.007	-4.302	-0.656	-9.990	-1.280	-1.195
H	-9.924	-1.947	0.127	-7.719	-5.854	0.711	-8.784	-4.322	0.512	-8.016	-5.302	0.422	-9.503	-2.485	0.012
C	-10.601	0.115	0.241	-9.008	-4.679	-0.585	-10.037	-2.785	-0.378	-8.996	-3.635	1.409	-10.175	-0.601	0.858
H	-10.454	1.058	-0.309	-8.944	-4.160	-1.555	-10.008	-2.079	-1.224	-9.281	-2.596	1.179	-10.124	0.474	0.615
H	-10.256	0.269	1.277	-9.255	-3.929	0.185	-10.148	-2.197	0.547	-8.299	-3.614	2.262	-9.666	-0.748	1.825
O	-11.961	-0.274	0.218	-9.977	-5.705	-0.621	-11.116	-3.684	-0.524	-10.145	-4.407	1.722	-11.522	-1.033	0.930
C	-12.823	0.686	0.803	-11.283	-5.234	-0.916	-12.398	-3.072	-0.572	-10.850	-3.916	2.844	-12.272	-0.333	1.911
H	-13.838	0.289	0.730	-11.940	-6.106	-0.915	-13.125	-3.876	-0.687	-11.709	-4.575	2.997	-13.292	-0.731	1.897
H	-12.771	1.648	0.268	-11.318	-4.753	-1.905	-12.465	-2.381	-1.425	-11.209	-2.888	2.675	-12.309	0.748	1.696
H	-12.574	0.855	1.862	-11.628	-4.517	-0.155	-12.597	-2.516	0.355	-10.222	-3.925	3.749	-11.850	-0.475	2.919
C	-0.549	2.252	-0.903	-1.496	1.889	-0.603	-0.791	2.639	-0.625	-0.726	2.062	-1.757	-0.362	2.267	-1.348
C	0.284	2.780	0.116	-1.145	2.722	0.485	-0.181	3.282	0.505	-0.537	2.958	-0.672	0.416	2.886	-0.333
C	0.770	1.952	1.158	-0.037	2.382	1.316	0.636	2.527	1.419	0.157	2.559	0.522	0.861	2.167	0.809
C	-1.102	3.148	-1.997	-2.574	2.272	-1.587	-1.580	3.420	-1.642	-1.457	2.536	-3.017	-0.866	3.068	-2.543
H	-1.573	2.521	-2.757	-2.494	1.638	-2.472	-1.762	2.791	-2.516	-1.305	1.784	-3.796	-1.301	2.368	-3.261
H	-0.330	3.765	-2.466	-2.522	3.323	-1.884	-1.075	3.509	-1.951	-1.112	3.509	-3.385	-0.077	3.643	-3.044
H	-1.859	3.831	-1.589	-3.562	2.113	-1.135	-2.549	3.713	-1.216	-2.537	2.620	-2.830	-1.647	3.783	-2.245
C	1.613	2.529	2.282	0.433	3.298	2.419	1.321	3.189	2.584	0.243	3.542	1.701	1.649	2.863	1.912
H	1.998	1.707	2.888	1.409	2.963	2.773	2.030	2.490	3.031	0.910	3.107	2.450	2.032	2.095	2.590
H	2.452	3.128	1.912	0.495	4.342	2.102	1.843	4.105	2.294	0.623	4.530	1.414	2.493	3.455	1.536
H	1.005	3.179	2.925	-0.273	3.251	3.260	0.578	3.464	3.345	-0.744	3.693	2.159	1.011	3.543	2.494
C	0.651	4.256	0.093	-1.890	4.026	0.704	-0.374	4.764	0.708	-1.087	4.371	-0.771	0.778	4.355	-0.472
H	-0.148	4.848	-0.359	-2.934	3.917	0.399	-1.356	5.073	0.341	-1.982	4.402	-1.401	-0.006	4.898	-1.012
H	0.751	4.638	1.115	-1.929	4.256	1.773	-0.375	4.999	1.777	-1.408	4.730	0.213	0.845	4.831	0.513
C	1.964	4.559	-0.675	-1.299	5.241	-0.044	0.687	5.653	0.012	-0.066	5.406	-1.348	2.127	4.597	-1.219

H	2.817	4.054	-0.216	-0.318	5.531	0.346	1.674	5.561	0.474	0.836	5.408	-0.728	2.940	4.118	-0.665
H	1.878	4.184	-1.703	-1.141	5.004	-1.105	0.817	5.366	-1.040	0.212	5.116	-2.365	2.075	4.150	-2.215
C	2.229	6.047	-0.760	-2.236	6.438	0.009	0.251	7.115	0.031	-0.651	6.793	-1.403	2.419	6.067	-1.387
O	1.448	6.865	-1.204	-3.438	6.361	0.164	-0.896	7.482	0.171	-1.264	7.278	-2.335	2.076	6.757	-2.331
O	3.448	6.378	-0.270	-1.568	7.591	-0.167	1.296	7.939	-0.154	-0.464	7.465	-0.230	3.088	6.578	-0.319
C	3.797	7.779	-0.307	-2.363	8.805	-0.203	0.991	9.358	-0.219	-1.055	8.771	-0.139	3.358	7.992	-0.344
H	3.782	8.135	-1.342	-3.078	8.745	-1.029	0.272	9.538	-1.022	-0.644	9.424	-0.916	3.953	8.241	-1.228
H	3.068	8.357	0.268	-2.918	8.903	0.734	0.548	9.677	0.728	-2.138	8.703	-0.287	2.416	8.548	-0.397
C	5.189	7.890	0.296	-1.390	9.957	-0.396	2.311	10.069	-0.479	-0.721	9.292	1.250	4.116	8.315	0.935
H	5.906	7.292	-0.290	-0.821	9.824	-1.331	2.748	9.748	-1.438	0.372	9.330	1.388	5.043	7.721	0.988
H	5.187	7.502	1.328	-0.669	9.991	0.438	3.040	9.841	0.316	-1.136	8.619	2.017	3.506	8.061	1.817
O	5.542	9.260	0.276	-2.167	11.135	-0.440	2.023	11.451	-0.506	-1.283	10.589	1.367	4.410	9.700	0.912
C	6.831	9.509	0.806	-1.395	12.312	-0.620	3.158	12.293	-0.649	-1.046	11.179	2.630	5.127	10.129	2.059
H	6.998	10.587	0.744	-2.096	13.149	-0.640	2.789	13.319	-0.659	-1.519	12.164	2.618	5.305	11.205	1.958
H	6.900	9.192	1.859	-0.684	12.452	0.209	3.854	12.153	0.192	-1.485	10.577	3.443	4.553	9.949	2.984
H	7.610	8.988	0.227	-0.838	12.280	-1.569	3.686	12.075	-1.590	0.032	11.297	2.822	6.098	9.614	2.145

A.a.ix. Complex 20

Table A-9 Optimized structures of Complex **20**

Atom	Complex **20**			[Complex **20**]$^{+1}$			[Complex **20**]$^{-1}$		
	X	Y	Z	X	Y	Z	X	Y	Z
V	-0.363	-0.743	0.121	-0.265	-0.435	0.385	0.403	-0.366	0.167
O	-1.766	-1.086	1.470	-1.722	-0.427	1.634	1.980	-0.266	-1.160
O	-1.600	-1.750	-1.120	-1.500	-1.399	-0.728	1.708	-1.441	1.349
O	0.999	-0.687	-1.301	1.138	-0.740	-0.887	-1.151	-0.602	1.505
O	0.553	-2.460	0.658	0.461	-1.996	1.241	-0.296	-2.120	-0.666
C	-2.980	-1.494	1.377	-2.925	-0.896	1.645	3.156	-0.738	-1.091
C	-3.574	-1.996	0.200	-3.483	-1.619	0.568	3.698	-1.466	0.009
C	-2.808	-2.123	-0.995	-2.705	-1.841	-0.589	2.921	-1.768	1.166
C	2.089	-1.343	-1.490	2.075	-1.618	-1.029	-2.038	-1.505	1.600
C	2.493	-2.463	-0.734	2.268	-2.695	-0.138	-2.181	-2.626	0.730
C	1.657	-2.977	0.299	1.412	-2.828	0.978	-1.282	-2.854	-0.353
C	-3.750	-1.436	2.684	-3.685	-0.635	2.919	4.005	-0.491	-2.338
C	-3.400	-2.778	-2.229	-3.215	-2.643	-1.760	3.531	-2.581	2.307
C	2.917	-0.838	-2.656	2.935	-1.417	-2.250	-2.987	-1.330	2.786
C	2.027	-4.253	1.034	1.526	-3.976	1.948	-1.446	-4.093	-1.235
O	-1.144	0.996	-0.440	-0.728	1.210	-0.475	0.973	1.427	1.012
O	0.724	0.315	1.397	0.756	0.706	1.545	-0.801	0.798	-1.038
C	-0.861	2.198	-0.107	-0.474	2.463	-0.273	0.591	2.615	0.781
C	0.097	2.565	0.874	0.365	2.921	0.764	-0.360	3.006	-0.207
C	0.819	1.578	1.588	0.962	1.976	1.632	-0.982	2.054	-1.068
C	-1.674	3.253	-0.835	-1.139	3.375	-1.270	1.272	3.673	1.649
C	1.780	1.965	2.699	1.887	2.381	2.752	-1.941	2.523	-2.162
C	3.804	-3.159	-1.059	3.371	-3.711	-0.382	-3.323	-3.601	0.961
C	5.010	-2.608	-0.246	4.709	-3.349	0.291	-4.630	-3.222	0.192
C	6.294	-3.296	-0.652	5.748	-4.446	0.121	-5.738	-4.206	0.459
O	6.943	-3.021	-1.642	5.505	-5.567	-0.275	-6.554	-4.138	1.359
O	6.615	-4.302	0.201	6.967	-4.010	0.493	-5.697	-5.256	-0.416
C	7.777	-5.101	-0.117	8.063	-4.962	0.470	-6.642	-6.322	-0.216
C	9.034	-4.472	0.474	8.750	-4.953	-0.891	-7.945	-6.019	-0.948
O	10.090	-5.392	0.265	9.882	-5.788	-0.772	-8.767	-7.172	-0.846
C	11.344	-4.914	0.721	10.619	-5.913	-1.979	-10.035	-6.999	-1.447
C	-5.023	-2.454	0.216	-4.898	-2.164	0.661	5.143	-1.930	-0.054
C	-6.028	-1.331	-0.155	-5.972	-1.186	0.149	6.160	-0.885	0.511
C	-7.445	-1.859	-0.228	-7.374	-1.762	0.274	7.577	-1.388	0.426
O	-7.812	-2.742	-0.977	-7.624	-2.890	0.645	8.160	-2.031	1.278
O	-8.262	-1.243	0.664	-8.298	-0.847	-0.078	8.144	-1.081	-0.779
C	-9.637	-1.684	0.722	-9.697	-1.224	0.021	9.466	-1.587	-1.037
C	-10.487	-0.908	-0.279	-10.178	-1.844	-1.286	10.518	-0.616	-0.513
O	-11.833	-1.287	-0.056	-11.570	-2.040	-1.144	11.786	-1.092	-0.941
C	-12.741	-0.672	-0.953	-12.170	-2.651	-2.276	12.859	-0.303	-0.467
C	0.334	4.038	1.173	0.652	4.402	0.951	-0.725	4.474	-0.344
C	1.464	4.661	0.324	1.764	4.935	0.028	-1.937	4.898	0.548
C	1.610	6.153	0.549	2.133	6.375	0.349	-2.264	6.359	0.384
O	0.696	6.912	0.803	1.808	6.959	1.363	-1.810	7.273	1.046
O	2.900	6.549	0.414	2.891	6.903	-0.631	-3.117	6.566	-0.664
C	3.189	7.956	0.580	3.406	8.248	-0.440	-3.441	7.928	-0.996
C	3.060	8.686	-0.752	2.424	9.278	-0.986	-4.642	8.400	-0.183
O	3.500	10.014	-0.537	3.072	10.530	-0.899	-5.006	9.683	-0.669
C	3.392	10.830	-1.690	2.266	11.613	-1.339	-6.084	10.257	0.044
H	-3.165	-0.868	3.411	-3.766	-1.561	3.504	3.458	0.198	-2.987
H	-4.734	-0.970	2.570	-3.148	0.103	3.518	4.989	-0.064	-2.113
H	-3.909	-2.446	3.083	-4.702	-0.282	2.729	4.175	-1.425	-2.892
H	-2.700	-2.659	-3.059	-2.524	-2.539	-2.599	2.828	-2.568	3.143
H	-3.564	-3.850	-2.059	-3.283	-3.705	-1.491	3.690	-3.627	2.006
H	-4.367	-2.345	-2.507	-4.214	-2.323	-2.071	4.497	-2.191	2.647
H	2.850	-1.531	-3.504	2.665	-2.150	-3.022	-2.808	-2.097	3.552
H	2.523	0.130	-2.973	2.764	-0.418	-2.654	-2.795	-0.350	3.229
H	3.978	-0.733	-2.406	3.999	-1.548	-2.034	-4.045	-1.393	2.505
H	1.960	-5.120	0.364	1.210	-4.911	1.468	-1.189	-5.008	-0.683
H	3.048	-4.225	1.429	2.556	-4.122	2.289	-2.465	-4.219	-1.618
H	1.327	-4.396	1.860	0.883	-3.789	2.809	-0.758	-3.997	-2.079

221

H	-2.391	3.729	-0.154	-2.115	2.962	-1.540	1.955	4.296	1.053
H	-1.051	4.049	-1.255	-1.260	4.398	-0.911	0.564	4.350	2.142
H	-2.229	2.769	-1.642	-0.535	3.404	-2.187	1.857	3.155	2.413
H	2.320	1.072	3.020	2.352	1.489	3.176	-2.395	1.638	-2.614
H	2.500	2.726	2.383	2.664	3.073	2.412	-2.737	3.178	-1.787
H	1.233	2.369	3.561	1.324	2.890	3.544	-1.407	3.077	-2.946
H	3.722	-4.234	-0.873	3.060	-4.698	-0.032	-3.036	-4.614	0.660
H	4.039	-3.062	-2.124	3.536	-3.835	-1.457	-3.570	-3.667	2.026
H	5.127	-1.539	-0.445	5.120	-2.410	-0.097	-4.970	-2.235	0.519
H	4.835	-2.742	0.825	4.577	-3.186	1.369	-4.420	-3.180	-0.880
H	7.590	-6.074	0.341	8.750	-4.621	1.246	-6.171	-7.213	-0.637
H	7.869	-5.207	-1.200	7.689	-5.959	0.712	-6.825	-6.465	0.852
H	9.249	-3.513	-0.022	8.064	-5.328	-1.667	-8.440	-5.148	-0.492
H	8.890	-4.283	1.551	9.046	-3.924	-1.157	-7.736	-5.788	-2.005
H	12.077	-5.697	0.514	11.463	-6.572	-1.767	-10.583	-7.936	-1.315
H	11.636	-3.993	0.193	10.003	-6.356	-2.776	-10.597	-6.181	-0.970
H	11.325	-4.713	1.804	10.996	-4.936	-2.317	-9.944	-6.783	-2.524
H	-5.289	-2.845	1.204	-5.130	-2.434	1.694	5.433	-2.158	-1.086
H	-5.176	-3.286	-0.477	-4.980	-3.101	0.104	5.280	-2.862	0.504
H	-5.775	-0.932	-1.145	-5.806	-0.924	-0.904	5.933	-0.689	1.563
H	-5.972	-0.504	0.559	-5.943	-0.233	0.692	6.064	0.051	-0.046
H	-9.964	-1.471	1.742	-10.228	-0.291	0.219	9.539	-1.674	-2.123
H	-9.692	-2.757	0.526	-9.832	-1.916	0.854	9.588	-2.570	-0.575
H	-10.179	-1.151	-1.308	-9.663	-2.800	-1.469	10.474	-0.567	0.585
H	-10.357	0.175	-0.123	-9.961	-1.165	-2.128	10.331	0.393	-0.916
H	-13.739	-1.031	-0.692	-13.235	-2.751	-2.053	13.780	-0.752	-0.850
H	-12.714	0.425	-0.859	-12.044	-2.031	-3.176	12.785	0.735	-0.830
H	-12.518	-0.946	-1.996	-11.743	-3.648	-2.462	12.893	-0.291	0.634
H	0.577	4.178	2.231	0.933	4.605	1.986	-0.971	4.718	-1.383
H	-0.576	4.620	1.012	-0.257	4.990	0.792	0.123	5.115	-0.081
H	1.250	4.518	-0.745	1.485	4.869	-1.029	-1.695	4.723	1.599
H	2.425	4.171	0.506	2.678	4.333	0.131	-2.808	4.291	0.285
H	4.220	7.997	0.937	4.339	8.275	-1.005	-3.685	7.919	-2.061
H	2.517	8.387	1.325	3.603	8.418	0.619	-2.578	8.573	-0.816
H	2.014	8.672	-1.094	1.496	9.274	-0.392	-4.379	8.450	0.884
H	3.682	8.189	-1.516	2.169	9.039	-2.032	-5.478	7.692	-0.304
H	3.754	11.823	-1.412	2.866	12.518	-1.228	-6.283	11.233	-0.406
H	4.006	10.438	-2.516	1.981	11.492	-2.396	-6.990	9.634	-0.029
H	2.347	10.907	-2.029	1.355	11.703	-0.729	-5.834	10.393	1.108

A.a.x. Complexes 21 and 22

Table A-10 Optimized structures of Complexes **21** and **22**

Atom	Complex **21**			[Complex **21**]$^{+1}$			Atom	Complex **22**			[Complex **22**]$^{+1}$		
	X	Y	Z	X	Y	Z		X	Y	Z	X	Y	Z
V	0.000	0.000	-0.555	0.017	0.000	-0.496	Fe	0.000	0.000	0.000	0.000	0.000	-0.001
O	1.331	1.360	0.037	1.235	1.286	0.175	C	-1.675	0.841	0.878	-1.697	-0.534	1.093
O	1.332	-1.360	0.038	1.236	-1.286	0.174	H	-1.650	1.590	1.659	-1.671	-1.009	2.066
O	-0.001	-0.001	-2.131	0.296	0.000	-2.026	C	-1.675	-0.575	1.071	-1.698	-1.205	-0.170
O	-1.331	1.360	0.038	-1.345	1.275	-0.179	H	-1.651	-1.086	2.025	-1.673	-2.276	-0.321
O	-1.331	-1.360	0.039	-1.344	-1.275	-0.178	C	-1.676	-1.196	-0.215	-1.698	-0.210	-1.198
C	2.587	1.233	0.263	2.531	1.223	0.275	H	-1.652	-2.262	-0.407	-1.674	-0.397	-2.264
C	3.253	0.000	0.353	3.212	0.000	0.264	C	-1.676	-0.165	-1.204	-1.697	1.075	-0.570
C	2.587	-1.232	0.263	2.532	-1.222	0.274	H	-1.653	-0.311	-2.277	-1.672	2.031	-1.078
C	-2.587	1.233	0.263	-2.575	1.221	0.235	C	-1.675	1.095	-0.529	-1.696	0.875	0.846
C	-3.253	0.000	0.353	-3.214	0.000	0.471	H	-1.651	2.069	-1.000	-1.670	1.653	1.599
C	-2.587	-1.233	0.263	-2.575	-1.221	0.236	C	1.675	0.818	0.899	1.697	-0.559	1.081
C	3.338	2.527	0.456	3.225	2.536	0.453	H	1.650	1.546	1.700	1.671	-1.056	2.043
C	3.340	-2.526	0.456	3.226	-2.535	0.452	C	1.675	-0.602	1.056	1.698	-1.200	-0.197
C	-3.339	2.527	0.456	-3.255	2.542	0.409	H	1.651	-1.139	1.996	1.673	-2.269	-0.373
C	-3.339	-2.526	0.457	-3.254	-2.542	0.411	C	1.676	-1.190	-0.247	1.698	-0.183	-1.202
H	4.318	0.001	0.554	4.288	0.001	0.381	H	1.652	-2.250	-0.467	1.674	-0.346	-2.273
H	-4.318	0.000	0.554	-4.250	0.000	0.788	C	1.676	-0.133	-1.208	1.697	1.088	-0.546
H	3.240	3.140	-0.447	3.040	3.165	-0.426	H	1.652	-0.251	-2.284	1.672	2.055	-1.031
H	2.883	3.091	1.278	2.801	3.060	1.318	C	1.675	1.108	-0.500	1.696	0.855	0.866
H	4.398	2.367	0.670	4.301	2.414	0.590	H	1.651	2.095	-0.945	1.670	1.616	1.636
H	4.400	-2.365	0.669	4.302	-2.413	0.590							
H	2.885	-3.091	1.278	2.802	-3.060	1.315							
H	3.241	-3.139	-0.448	3.041	-3.164	-0.428							
H	-4.399	2.366	0.669	-4.284	2.428	0.753							
H	-2.884	3.092	1.277	-2.693	3.151	1.128							
H	-3.240	3.139	-0.449	-3.245	3.084	-0.545							
H	-4.399	-2.366	0.671	-4.283	-2.429	0.755							
H	-3.241	-3.138	-0.448	-3.245	-3.085	-0.543							
H	-2.883	-3.092	1.277	-2.692	-3.151	1.130							

A.a.xi.   V(acac)₂ACN

Table A-11 Optimized structures of V(acac)₂ACN

Atom	Complex **1**		
	X	Y	Z
V	-0.042	0.302	-0.772
O	-1.352	-1.197	-0.700
O	-1.405	1.461	0.145
C	-2.579	-1.172	-0.341
C	-3.240	-0.053	0.191
C	-2.620	1.189	0.421
O	0.452	-0.172	1.313
O	1.415	-1.034	-1.124
C	1.227	-1.055	1.787
C	2.051	-1.894	1.003
C	2.096	-1.836	-0.397
O	-0.239	0.831	-2.254
N	1.445	1.835	-0.377
C	2.211	2.682	-0.219
C	3.175	3.759	-0.027
C	-3.323	-2.476	-0.518
C	-3.407	2.318	1.049
C	1.248	-1.192	3.298
C	3.008	-2.771	-1.163
H	-4.283	-0.160	0.466
H	2.679	-2.620	1.506
H	3.247	4.360	-0.938
H	2.857	4.402	0.800
H	4.161	3.343	0.204
H	-3.303	-2.762	-1.576
H	-2.806	-3.267	0.038
H	-4.361	-2.416	-0.180
H	-4.447	2.045	1.248
H	-2.926	2.614	1.989
H	-3.384	3.190	0.384
H	1.509	-0.226	3.748
H	0.242	-1.448	3.652
H	1.953	-1.953	3.645
H	3.602	-3.410	-0.503
H	2.404	-3.402	-1.826
H	3.679	-2.186	-1.803

A.b. DFT Optimized Structures – Salicylaldimines

A.b.i.   Complexes 23 and 24

Table A-12 Optimized structures of Complexes **23** and **24**

Atom	Complex **1** X	Y	Z	Atom	Complex **2** X	Y	Z	[Complex **2**]⁺¹ X	Y	Z
Cr	0.160	0.130	-0.242	Cr	-0.118	-0.197	0.067	-0.205	-0.172	0.067
C	-1.028	-2.446	0.892	C	1.318	-2.816	-0.565	0.813	-2.928	-0.642
C	-2.174	-1.770	1.437	C	2.599	-2.180	-0.719	2.181	-2.501	-0.720
C	-2.353	-0.351	1.335	C	2.776	-0.771	-0.541	2.560	-1.141	-0.503
O	-1.486	0.438	0.771	O	1.803	0.040	-0.243	1.698	-0.204	-0.196
C	-3.156	-2.555	2.092	C	3.701	-3.002	-1.072	3.158	-3.467	-1.072
C	-4.476	-0.594	2.527	C	5.149	-1.081	-1.072	4.865	-1.771	-1.018
C	2.665	0.709	1.307	C	4.099	-0.248	-0.721	3.937	-0.802	-0.665
C	3.469	0.689	0.111	C	-1.835	0.438	-2.305	-1.688	0.978	-2.248
C	2.973	0.204	-1.142	C	-3.032	0.454	-1.504	-2.857	1.205	-1.428
O	1.753	-0.238	-1.301	C	-3.049	-0.044	-0.171	-3.014	0.571	-0.155
C	4.815	1.114	0.211	O	-1.995	-0.511	0.435	-2.089	-0.155	0.392
C	5.184	0.602	-2.108	C	-4.227	0.924	-2.111	-3.910	1.970	-1.963
C	-1.474	1.059	-2.593	C	-5.459	0.409	-0.100	-5.285	1.496	-0.019
C	-1.374	2.433	-2.182	C	-4.311	-0.069	0.515	-4.274	0.713	0.533
C	-0.461	2.860	-1.165	O	4.334	1.105	-0.643	4.340	0.507	-0.559
O	0.315	2.041	-0.513	C	4.152	1.709	0.645	4.461	1.014	0.777
C	-2.147	3.394	-2.878	O	-4.259	-0.585	1.779	-4.350	0.055	1.707
C	-1.162	5.165	-1.586	C	-5.464	-0.655	2.522	-5.568	0.113	2.454
H	-1.018	-3.530	1.064	O	-0.422	4.279	-0.378	0.456	4.254	-0.171
H	-2.998	-3.631	2.162	C	-0.536	5.649	-0.721	0.685	5.629	-0.494
H	-5.369	-0.135	2.946	C	0.312	0.768	2.901	0.450	0.506	2.930
H	3.212	0.975	2.221	C	0.271	2.152	2.514	0.782	1.871	2.585
H	5.174	1.475	1.174	C	-0.049	2.552	1.185	0.486	2.416	1.295
H	5.844	0.570	-2.972	O	-0.311	1.723	0.223	-0.061	1.735	0.346
H	-2.043	0.900	-3.518	C	0.511	3.126	3.522	1.335	2.692	3.582
H	-2.823	3.049	-3.659	C	0.144	4.889	1.915	1.344	4.590	2.069
H	-1.076	6.224	-1.352	C	-0.107	3.964	0.913	0.776	3.814	1.060
N	-0.034	-1.941	0.224	H	1.333	-3.902	-0.718	0.656	-3.994	-0.837
N	-0.956	0.014	-2.026	H	3.534	-4.069	-1.205	2.844	-4.495	-1.237
N	1.405	0.434	1.424	H	6.127	-0.630	-1.216	5.899	-1.463	-1.149
C	0.835	0.533	2.780	H	-1.987	0.720	-3.354	-1.770	1.347	-3.276
C	0.284	1.933	3.086	H	-4.185	1.300	-3.131	-3.788	2.436	-2.937
H	1.607	0.267	3.518	H	-6.406	0.400	0.429	-6.228	1.619	0.501
H	0.035	-0.208	2.864	H	4.834	1.255	1.377	5.206	0.436	1.339
C	-0.353	2.014	4.480	H	3.117	1.615	0.983	3.497	0.989	1.295
H	1.106	2.660	3.010	H	4.407	2.764	0.519	4.800	2.047	0.678
H	-0.449	2.200	2.318	H	-6.209	-1.287	2.020	-6.402	-0.298	1.874
C	-0.874	3.417	4.814	H	-5.889	0.344	2.693	-5.791	1.143	2.758
H	-1.181	1.294	4.542	H	-5.196	-1.103	3.481	-5.397	-0.502	3.338
H	0.381	1.708	5.242	H	0.415	6.182	-0.578	1.752	5.873	-0.431
H	-1.332	3.446	5.810	H	-1.322	6.146	-0.135	0.108	6.286	0.166
H	-0.062	4.156	4.799	H	-0.806	5.670	-1.779	0.342	5.747	-1.522
H	-1.630	3.741	4.088	H	0.434	0.607	3.979	0.530	0.276	3.998
C	-1.159	-1.264	-2.736	H	0.740	2.791	4.531	1.539	2.274	4.564
C	-2.536	-1.890	-2.468	H	0.100	5.952	1.700	1.569	5.636	1.895
H	-0.366	-1.949	-2.244	N	0.175	-2.275	-0.263	-0.244	-2.213	-0.376
H	-1.033	-1.101	-3.816	N	0.209	-0.288	2.153	0.056	-0.438	2.139
C	-2.713	-3.242	-3.173	N	-0.632	0.110	-1.947	-0.601	0.362	-1.914
H	-2.680	-2.009	-1.388	C	0.398	0.175	-2.994	0.419	0.210	-2.967
H	-3.316	-1.193	-2.807	C	1.109	1.531	-3.012	1.399	1.389	-2.998
C	-4.096	-3.861	-2.938	H	-0.053	-0.004	-3.979	-0.066	0.124	-3.947
H	-2.547	-3.117	-4.253	H	1.135	-0.613	-2.818	0.975	-0.713	-2.790
H	-1.936	-3.939	-2.824	H	0.375	2.341	-3.161	0.850	2.328	-3.186
H	-4.191	-4.828	-3.447	H	1.622	1.704	-2.060	1.920	1.482	-2.037
H	-4.281	-4.024	-1.869	C	2.908	2.607	-4.105	3.365	2.064	-4.126
H	-4.892	-3.206	-3.315	H	3.572	2.480	-4.964	4.000	1.756	-4.961
C	1.013	-2.905	-0.180	H	2.352	3.552	-4.218	2.981	3.077	-4.321
C	2.092	-3.098	0.894	H	3.507	2.652	-3.184	3.956	2.070	-3.199

H	1.475	-2.530	-1.095	C	0.256	-1.573	2.869	-0.277	-1.721	2.789
H	0.543	-3.874	-0.404	C	1.694	-2.065	3.043	0.970	-2.581	3.026
C	3.182	-4.088	0.457	H	-0.316	-2.315	2.311	-0.978	-2.266	2.156
H	2.546	-2.128	1.124	H	-0.213	-1.477	3.856	-0.778	-1.537	3.746
H	1.619	-3.454	1.822	H	2.210	-2.116	2.074	1.553	-2.692	2.099
C	4.266	-4.286	1.523	H	2.257	-1.364	3.684	1.623	-2.099	3.773
H	2.722	-5.059	0.218	C	2.921	-3.894	3.903	1.572	-4.709	3.872
H	3.645	-3.728	-0.472	H	2.764	-4.876	4.357	1.105	-5.638	4.205
H	5.030	-4.997	1.186	H	3.500	-4.011	2.974	2.240	-4.920	3.023
H	4.771	-3.339	1.753	H	3.495	-3.262	4.600	2.163	-4.283	4.696
H	3.840	-4.673	2.458	C	-0.966	-3.211	-0.189	-1.529	-2.948	-0.426
C	-4.295	-1.990	2.635	C	-1.677	-3.352	-1.537	-2.124	-2.971	-1.837
H	-5.038	-2.606	3.133	H	-1.680	-2.837	0.545	-2.238	-2.466	0.248
C	-3.536	0.204	1.898	H	-0.618	-4.202	0.130	-1.379	-3.980	-0.088
H	-3.673	1.279	1.813	H	-2.116	-2.393	-1.844	-2.287	-1.947	-2.207
C	-2.062	4.744	-2.587	H	-0.961	-3.667	-2.317	-1.430	-3.473	-2.535
H	-2.669	5.467	-3.125	C	-3.495	-4.492	-2.527	-4.001	-3.815	-3.005
C	3.875	0.168	-2.238	H	-4.233	-5.265	-2.294	-4.921	-4.373	-2.818
H	3.496	-0.202	-3.187	H	-4.017	-3.557	-2.781	-4.251	-2.833	-3.435
C	-0.377	4.254	-0.899	H	-2.897	-4.814	-3.395	-3.378	-4.372	-3.721
H	0.325	4.577	-0.136	O	1.640	-3.346	3.648	0.518	-3.833	3.492
C	5.671	1.085	-0.876	O	2.032	1.494	-4.092	2.305	1.121	-4.049
H	6.698	1.424	-0.783	O	-2.687	-4.333	-1.375	-3.343	-3.675	-1.754
				C	4.961	-2.466	-1.253	4.485	-3.112	-1.221
				H	5.800	-3.098	-1.531	5.229	-3.851	-1.499
				C	-5.420	0.913	-1.420	-5.100	2.126	-1.261
				H	-6.332	1.282	-1.879	-5.903	2.727	-1.677
				C	0.457	4.471	3.230	1.624	4.030	3.324
				H	0.645	5.215	3.998	2.061	4.652	4.099

A.b.ii.   Complex 25

Table A-13 Optimized structures of Complex **25**

Atom	Complex **3**			[Complex **3**]^{+1}			[Complex **3**]^{+2}		
	X	Y	Z	X	Y	Z	X	Y	Z
Cr	0.226	-0.081	-0.197	0.300	-0.118	-0.190	0.145	-0.115	-0.177
C	-1.614	-2.527	-0.347	-1.523	-2.540	-0.264	-2.180	-2.025	-0.623
C	-2.713	-1.830	0.268	-2.639	-1.806	0.273	-3.119	-1.165	0.065
C	-2.616	-0.470	0.704	-2.518	-0.449	0.712	-2.728	0.094	0.643
O	-1.522	0.238	0.616	-1.389	0.215	0.660	-1.505	0.523	0.619
C	-3.929	-2.540	0.421	-3.873	-2.475	0.389	-4.447	-1.583	0.159
C	-5.049	-1.946	0.980	-4.995	-1.838	0.914	-5.417	-0.794	0.809
C	-4.965	-0.602	1.402	-4.880	-0.498	1.346	-5.039	0.454	1.371
C	2.396	-0.742	1.776	2.533	-0.501	1.758	2.021	-1.395	1.767
C	3.423	-0.542	0.786	3.509	-0.220	0.730	3.124	-1.266	0.838
C	3.130	-0.408	-0.608	3.174	-0.235	-0.663	2.921	-0.962	-0.553
O	1.912	-0.441	-1.090	1.951	-0.427	-1.093	1.746	-0.694	-1.047
C	4.765	-0.538	1.231	4.845	-0.038	1.122	4.410	-1.565	1.294
C	5.821	-0.397	0.345	5.859	0.149	0.180	5.514	-1.561	0.422
C	5.542	-0.271	-1.031	5.534	0.118	-1.195	5.312	-1.282	-0.955
O	-6.178	-2.728	1.078	-6.135	-2.576	0.972	-6.651	-1.304	0.839
C	-7.339	-2.162	1.665	-7.315	-1.991	1.523	-7.726	-0.598	1.490
O	-1.113	6.674	-1.177	-1.793	6.352	-1.161	1.264	6.707	-0.824
C	8.194	-0.251	0.016	8.201	0.508	-0.227	7.891	-1.902	0.177
O	7.087	-0.397	0.890	7.107	0.336	0.675	6.696	-1.845	0.979
C	-0.854	7.817	-0.380	-1.675	7.552	-0.392	1.821	7.746	0.010
C	-0.666	2.012	-2.175	-0.797	1.803	-2.209	0.022	2.282	-2.045
C	-0.433	3.069	-1.225	-0.681	2.891	-1.260	0.570	3.168	-1.031
C	0.295	2.855	-0.013	0.131	2.787	-0.080	1.058	2.690	0.241
O	0.772	1.692	0.347	0.764	1.698	0.252	1.026	1.449	0.584
C	-0.869	4.368	-1.572	-1.286	4.113	-1.582	0.674	4.520	-1.333
C	-0.628	5.457	-0.749	-1.142	5.236	-0.759	1.232	5.442	-0.414
C	0.093	5.258	0.446	-0.339	5.143	0.401	1.712	4.978	0.841
H	-1.832	-3.566	-0.623	-1.735	-3.588	-0.504	-2.612	-2.946	-1.024
H	-3.996	-3.574	0.092	-3.967	-3.510	0.068	-4.763	-2.532	-0.265
H	-5.825	-0.106	1.840	-5.736	0.022	1.762	-5.772	1.076	1.873
H	2.767	-0.958	2.786	2.946	-0.663	2.760	2.282	-1.824	2.740
H	4.984	-0.644	2.291	5.113	-0.040	2.175	4.585	-1.819	2.336
H	6.346	-0.164	-1.752	6.304	0.245	-1.948	6.146	-1.294	-1.648
H	-7.704	-1.301	1.088	-7.637	-1.122	0.936	-7.900	0.366	1.001
H	-7.157	-1.854	2.704	-7.160	-1.700	2.570	-7.503	-0.462	2.553
H	-8.094	-2.950	1.650	-8.078	-2.768	1.471	-8.598	-1.239	1.371
H	8.248	-1.075	-0.709	8.328	-0.375	-0.865	7.803	-2.682	-0.586
H	9.081	-0.274	0.653	9.081	0.633	0.404	8.689	-2.153	0.874
H	8.160	0.706	-0.523	8.064	1.403	-0.846	8.089	-0.929	-0.284
H	0.224	8.000	-0.274	-0.632	7.887	-0.345	2.876	7.541	0.217
H	-1.307	7.725	0.618	-2.071	7.410	0.621	1.249	7.832	0.940
H	-1.312	8.657	-0.906	-2.274	8.294	-0.918	1.724	8.659	-0.574
H	-1.026	2.347	-3.155	-1.174	2.088	-3.197	-0.161	2.758	-3.013
H	-1.409	4.528	-2.502	-1.883	4.211	-2.485	0.330	4.907	-2.288
H	0.310	6.091	1.107	-0.198	6.004	1.045	2.147	5.669	1.554
N	-0.430	-2.070	-0.628	-0.319	-2.105	-0.497	-0.915	-1.817	-0.821
N	-0.471	0.740	-2.011	-0.467	0.568	-2.018	-0.239	1.023	-1.929
N	1.111	-0.715	1.605	1.252	-0.613	1.605	0.779	-1.099	1.551
C	0.291	-0.947	2.803	0.473	-0.954	2.809	-0.166	-1.380	2.650
C	-0.056	0.366	3.508	0.064	0.296	3.595	-0.307	-0.186	3.603
H	0.825	-1.598	3.508	1.061	-1.610	3.464	0.166	-2.258	3.215
H	-0.633	-1.453	2.511	-0.424	-1.498	2.508	-1.143	-1.613	2.225
H	0.869	0.904	3.775	0.964	0.852	3.910	0.640	-0.030	4.146
H	-0.650	1.007	2.846	-0.548	0.958	2.968	-0.533	0.733	3.041
C	-1.234	1.164	5.395	-1.100	0.896	5.565	-1.499	0.412	5.563
H	-1.781	0.798	6.268	-1.642	0.434	6.393	-2.327	0.051	6.176
H	-0.390	1.787	5.733	-0.248	1.468	5.964	-0.587	0.456	6.175
H	-1.905	1.784	4.780	-1.772	1.583	5.028	-1.732	1.419	5.188
C	-0.721	-0.102	-3.192	-0.569	-0.324	-3.190	-0.742	0.360	-3.152
C	-2.207	-0.435	-3.344	-2.012	-0.767	-3.453	-2.259	0.523	-3.316
H	-0.149	-1.025	-3.095	0.054	-1.201	-3.016	-0.501	-0.701	-3.099
H	-0.371	0.403	-4.101	-0.177	0.182	-4.080	-0.233	0.767	-4.032

H	-2.602	-0.880	-2.420	-2.464	-1.186	-2.541	-2.783	0.301	-2.372
H	-2.783	0.486	-3.542	-2.626	0.098	-3.758	-2.498	1.565	-3.588
C	-3.680	-1.693	-4.697	-3.243	-2.164	-4.916	-3.986	-0.190	-4.780
H	-3.664	-2.392	-5.537	-3.076	-2.905	-5.701	-4.158	-0.936	-5.557
H	-4.146	-2.181	-3.827	-3.808	-2.626	-4.092	-4.702	-0.344	-3.959
H	-4.281	-0.812	-4.971	-3.828	-1.326	-5.326	-4.129	0.815	-5.201
C	0.479	-3.041	-1.269	0.624	-3.119	-1.022	-0.212	-2.894	-1.563
C	1.301	-3.823	-0.242	1.309	-3.909	0.098	0.241	-4.034	-0.641
H	1.163	-2.500	-1.924	1.383	-2.613	-1.617	0.663	-2.466	-2.051
H	-0.096	-3.755	-1.872	0.087	-3.823	-1.669	-0.873	-3.302	-2.335
H	1.967	-3.148	0.313	1.887	-3.238	0.751	0.875	-3.649	0.174
H	0.635	-4.320	0.484	0.553	-4.419	0.722	-0.636	-4.521	-0.180
C	2.944	-5.520	-0.135	2.851	-5.679	0.390	1.349	-6.125	-0.779
H	3.467	-6.228	-0.783	3.464	-6.360	-0.204	1.879	-6.736	-1.512
H	3.679	-4.858	0.347	3.502	-5.084	1.048	2.021	-5.898	0.062
H	2.402	-6.079	0.646	2.153	-6.263	1.008	0.476	-6.679	-0.407
O	-2.336	-1.336	-4.430	-1.961	-1.730	-4.483	-2.644	-0.369	-4.332
O	-0.783	0.029	4.681	-0.660	-0.157	4.721	-1.350	-0.514	4.491
O	2.053	-4.788	-0.957	2.153	-4.849	-0.528	0.951	-4.934	-1.453
C	4.230	-0.281	-1.489	4.224	-0.083	-1.600	4.045	-1.004	-1.426
H	4.019	-0.185	-2.550	3.972	-0.116	-2.656	3.876	-0.801	-2.479
C	-3.781	0.110	1.265	-3.670	0.173	1.250	-3.730	0.882	1.284
H	-3.721	1.145	1.589	-3.581	1.201	1.587	-3.426	1.831	1.714
C	0.544	3.991	0.795	0.285	3.950	0.721	1.628	3.640	1.149
H	1.111	3.844	1.710	0.915	3.874	1.602	1.994	3.263	2.099

A.b.iii.   Complexes 26, 27 and 28

Table A-14 Optimized structures of Complexes **26, 27** and **28**

Atom	Complex **4**			Atom	Complex **5**			Atom	Complex **6**		
	X	Y	Z		X	Y	Z		X	Y	Z
Cr	0.085	-0.096	-0.169	Cr	0.095	-0.383	0.300	Cr	0.102	-0.099	-0.169
C	-2.110	-2.208	-0.370	C	2.519	-2.148	0.861	C	-2.049	-2.263	-0.293
C	-3.093	-1.374	0.260	C	3.424	-1.276	0.158	C	-3.050	-1.422	0.305
C	-2.806	-0.041	0.687	C	2.990	-0.057	-0.449	C	-2.787	-0.072	0.694
O	-1.624	0.501	0.586	O	1.756	0.354	-0.430	O	-1.612	0.483	0.579
C	-4.401	-1.905	0.422	C	4.781	-1.684	0.078	C	-4.349	-1.976	0.472
C	-5.128	0.159	1.378	C	5.299	0.307	-1.191	C	-5.117	0.136	1.377
C	2.028	-1.169	1.861	C	3.982	0.730	-1.123	C	2.084	-1.052	1.882
C	3.119	-1.125	0.926	C	-1.581	-1.862	-1.692	C	3.168	-0.998	0.938
C	2.920	-0.904	-0.470	C	-2.725	-1.848	-0.814	C	2.955	-0.833	-0.465
O	1.738	-0.707	-0.996	C	-2.614	-1.492	0.558	O	1.762	-0.701	-0.987
C	4.425	-1.370	1.425	O	-1.500	-1.117	1.117	C	4.482	-1.178	1.444
C	5.314	-1.171	-0.784	C	-3.964	-2.285	-1.354	C	5.358	-1.018	-0.809
C	-0.132	2.087	-2.247	C	-4.997	-2.018	0.824	C	-0.213	2.013	-2.306
C	0.448	3.072	-1.380	C	-3.793	-1.602	1.372	C	0.321	3.046	-1.462
C	0.953	2.754	-0.085	O	3.635	1.870	-1.800	C	0.866	2.780	-0.170
O	0.912	1.556	0.427	C	3.148	2.967	-1.010	O	0.896	1.589	0.361
C	0.550	4.400	-1.875	O	-3.615	-1.266	2.679	C	0.342	4.365	-1.989
C	1.622	5.082	0.146	C	-4.734	-1.346	3.552	C	1.428	5.144	0.030
H	-2.479	-3.198	-0.665	O	-2.081	2.561	-2.334	H	-2.400	-3.269	-0.553
H	-4.587	-2.927	0.091	C	-2.769	3.336	-3.305	H	-4.555	-3.002	0.181
H	-5.927	0.762	1.810	C	-0.114	2.053	2.081	H	-5.944	0.712	1.784
H	2.309	-1.481	2.875	C	-0.729	2.843	1.047	H	2.379	-1.330	2.901
H	4.546	-1.539	2.494	C	-1.095	2.286	-0.210	H	4.653	-1.309	2.509
H	6.174	-1.185	-1.454	O	-0.897	1.049	-0.541	H	6.232	-1.028	-1.456
H	-0.381	2.460	-3.249	C	-1.003	4.205	1.348	H	-0.478	2.348	-3.317
H	0.161	4.610	-2.871	C	-1.995	4.482	-0.848	H	-0.063	4.574	-2.975
H	2.086	5.867	0.744	C	-1.748	3.154	-1.155	H	1.852	5.980	0.580
N	-0.870	-1.929	-0.654	H	2.993	-3.038	1.291	N	-0.815	-1.971	-0.579
N	-0.377	0.834	-2.007	H	5.087	-2.618	0.540	N	-0.397	0.758	-2.032
N	0.774	-0.909	1.646	H	6.015	0.923	-1.725	N	0.823	-0.835	1.665
C	-0.119	-1.041	2.807	H	-1.771	-2.295	-2.681	C	-0.064	-0.969	2.831
C	-0.211	0.270	3.590	H	-4.025	-2.559	-2.402	C	-0.189	0.354	3.591
H	0.244	-1.831	3.478	H	-5.890	-2.090	1.432	H	0.320	-1.737	3.515
H	-1.115	-1.325	2.463	H	3.909	3.272	-0.279	H	-1.053	-1.284	2.494
H	0.791	0.565	3.947	H	2.217	2.704	-0.502	H	0.804	0.675	3.950
H	-0.591	1.070	2.942	H	2.973	3.783	-1.713	H	-0.581	1.135	2.927
C	-1.248	1.189	5.505	H	-5.121	-2.372	3.612	C	-1.246	1.274	5.495
H	-1.932	0.910	6.311	H	-5.537	-0.668	3.234	H	-1.933	0.992	6.297
H	-0.291	1.516	5.941	H	-4.366	-1.038	4.532	H	-0.295	1.613	5.935
H	-1.681	2.026	4.937	H	-2.161	4.186	-3.644	H	-1.685	2.104	4.919
C	-0.958	0.083	-3.132	H	-3.728	3.705	-2.914	C	-0.934	-0.055	-3.136
H	-0.678	-0.967	-3.047	H	-2.954	2.665	-4.145	C	-2.462	0.000	-3.183
H	-0.555	0.452	-4.084	H	-0.001	2.573	3.039	H	-0.615	-1.090	-3.007
C	-0.124	-3.007	-1.332	H	-0.728	4.607	2.319	H	-0.531	0.293	-4.096
C	0.579	-3.939	-0.343	H	-2.482	5.138	-1.559	H	-2.890	-0.273	-2.208
H	0.629	-2.556	-1.981	N	1.242	-2.003	1.052	H	-2.796	1.025	-3.419
H	-0.805	-3.605	-1.951	N	0.300	0.825	2.020	C	-4.298	-0.915	-4.360
H	1.342	-3.393	0.227	N	-0.376	-1.458	-1.439	H	-4.517	-1.647	-5.141
H	-0.151	-4.358	0.372	C	0.606	-1.619	-2.522	H	-4.812	-1.208	-3.431
C	1.948	-5.865	-0.312	C	0.712	-0.363	-3.392	H	-4.670	0.072	-4.674
H	2.359	-6.619	-0.989	H	0.330	-2.471	-3.158	C	-0.041	-3.061	-1.208
H	2.774	-5.338	0.189	H	1.583	-1.834	-2.085	C	0.643	-3.956	-0.172
H	1.330	-6.365	0.452	H	-0.268	-0.129	-3.840	H	0.723	-2.621	-1.849
O	-1.078	0.044	4.691	H	1.026	0.495	-2.786	H	-0.702	-3.683	-1.826
O	1.174	-4.979	-1.100	C	2.004	0.482	-5.183	H	1.378	-3.384	0.410
C	-5.428	-1.168	0.978	H	2.739	0.151	-5.922	H	-0.104	-4.368	0.531
C	-3.873	0.732	1.249	H	1.122	0.882	-5.708	C	2.022	-5.871	-0.045
C	-3.595	2.149	1.680	H	2.443	1.275	-4.561	H	2.464	-6.635	-0.690
H	-2.852	2.181	2.487	C	0.870	0.287	3.266	H	2.826	-5.330	0.477
H	-3.179	2.741	0.857	C	2.370	0.573	3.359	H	1.376	-6.358	0.702
H	-4.509	2.636	2.036	H	0.705	-0.790	3.298	O	-2.890	-0.903	-4.188
C	-6.819	-1.730	1.162	H	0.362	0.721	4.136	O	-1.059	0.126	4.687

H	-6.884	-2.757	0.786	H	2.886	0.232	2.450	O	1.278	-5.004	-0.882
H	-7.111	-1.745	2.220	H	2.542	1.659	3.452	C	5.540	-1.176	0.571
H	-7.571	-1.133	0.629	C	4.251	0.115	4.715	C	-5.343	-1.196	1.001
C	1.561	3.804	0.678	H	4.529	-0.458	5.603	C	0.880	5.378	-1.238
C	1.121	5.418	-1.135	H	4.850	-0.229	3.858	F	6.811	-1.338	1.045
C	2.123	3.479	2.037	H	4.463	1.181	4.892	F	0.898	6.653	-1.730
H	1.347	3.091	2.708	C	0.590	-3.088	1.815	F	-6.596	-1.712	1.167
H	2.892	2.699	1.971	C	0.068	-4.197	0.899	C	1.435	3.867	0.572
H	2.568	4.367	2.500	H	-0.249	-2.670	2.373	C	4.087	-0.853	-1.341
C	1.221	6.834	-1.655	H	1.301	-3.526	2.527	C	-3.862	0.710	1.232
H	0.819	6.913	-2.671	H	-0.707	-3.808	0.224	C	3.866	-0.686	-2.822
H	0.662	7.538	-1.023	H	0.889	-4.599	0.280	H	3.230	-1.485	-3.221
H	2.261	7.183	-1.682	C	-1.065	-6.268	1.007	H	3.354	0.260	-3.039
C	4.061	-0.940	-1.331	H	-1.436	-6.987	1.741	H	4.817	-0.699	-3.364
C	5.533	-1.389	0.599	H	-1.907	-5.906	0.397	C	-3.598	2.140	1.624
C	3.864	-0.717	-2.808	H	-0.337	-6.767	0.348	H	-2.854	2.200	2.427
H	3.205	-1.479	-3.243	O	2.867	-0.105	4.499	H	-3.188	2.711	0.782
H	3.390	0.252	-3.002	O	1.666	-0.652	-4.402	H	-4.515	2.629	1.967
H	4.822	-0.749	-3.340	O	-0.463	-5.210	1.732	C	2.035	3.588	1.925
C	6.929	-1.630	1.128	C	-5.069	-2.355	-0.542	H	1.289	3.167	2.610
H	7.586	-0.770	0.942	C	5.695	-0.900	-0.590	H	2.842	2.848	1.852
H	6.917	-1.810	2.209	C	-1.618	4.997	0.410	H	2.440	4.502	2.371
H	7.397	-2.502	0.652	Br	-1.999	6.830	0.797				
C	-2.483	0.198	-3.156	Br	-6.747	-2.932	-1.253				
H	-2.779	1.246	-3.335	Br	7.523	-1.440	-0.704				
H	-2.911	-0.110	-2.193								
O	-2.960	-0.633	-4.202								
C	-4.370	-0.598	-4.338								
H	-4.722	0.417	-4.585								
H	-4.629	-1.275	-5.156								
H	-4.870	-0.931	-3.416								

A.b.iv.   Complex 29

Table A-15 Optimized structures of Complex **29**

Atom	Complex **7**			[Complex **7**]$^{+1}$			[Complex **7**]$^{+2}$		
	X	Y	Z	X	Y	Z	X	Y	Z
Cr	-0.045	-0.366	0.180	-0.076	-0.396	0.184	0.165	-0.232	0.190
C	2.071	-2.569	0.366	2.052	-2.546	0.347	2.600	-2.000	0.740
C	3.135	-1.705	-0.079	3.105	-1.659	-0.067	3.536	-1.034	0.189
C	2.911	-0.332	-0.405	2.855	-0.289	-0.380	3.110	0.266	-0.268
O	1.743	0.248	-0.336	1.665	0.261	-0.305	1.873	0.616	-0.295
C	4.422	-2.285	-0.206	4.402	-2.207	-0.193	4.871	-1.400	0.117
C	5.498	-1.536	-0.649	5.464	-1.429	-0.632	5.844	-0.508	-0.411
C	5.301	-0.178	-0.965	5.232	-0.074	-0.946	5.466	0.773	-0.829
C	4.048	0.412	-0.845	3.965	0.485	-0.823	4.134	1.186	-0.744
C	-1.827	-1.054	-2.130	-1.842	-0.929	-2.163	-1.250	-1.562	-2.094
C	-2.998	-1.065	-1.289	-3.020	-0.900	-1.322	-2.473	-1.675	-1.329
C	-2.899	-1.067	0.129	-2.926	-1.008	0.100	-2.498	-1.445	0.080
O	-1.764	-1.031	0.778	-1.800	-1.034	0.743	-1.465	-1.038	0.756
C	-4.260	-1.140	-1.932	-4.273	-0.888	-1.952	-3.620	-2.130	-1.990
C	-5.422	-1.207	-1.190	-5.449	-0.969	-1.201	-4.811	-2.362	-1.282
C	-5.352	-1.222	0.220	-5.387	-1.104	0.202	-4.855	-2.165	0.114
C	-4.121	-1.162	0.867	-4.153	-1.141	0.845	-3.722	-1.726	0.794
O	6.709	-2.184	-0.743	6.677	-2.045	-0.727	7.086	-0.991	-0.445
C	7.820	-1.464	-1.254	7.789	-1.305	-1.224	8.166	-0.194	-0.973
O	3.924	1.719	-1.258	3.795	1.787	-1.227	3.896	2.425	-1.176
C	3.518	2.669	-0.262	3.511	2.737	-0.191	2.714	3.197	-0.872
O	-0.532	6.337	2.113	-0.382	6.241	2.190	-3.531	5.418	1.734
C	-7.825	-1.326	-1.176	-7.856	-1.030	-1.226	-7.108	-3.088	-1.401
O	-3.968	-1.184	2.223	-3.986	-1.282	2.176	-3.652	-1.517	2.118
C	-5.126	-1.281	3.034	-5.135	-1.458	3.006	-4.792	-1.814	2.938
O	-6.606	-1.264	-1.896	-6.605	-0.923	-1.907	-5.850	-2.782	-2.022
C	-0.960	7.495	1.418	-0.696	7.463	1.520	-4.312	6.360	0.982
O	-1.453	3.462	-1.736	-1.407	3.472	-1.673	-2.093	2.876	-2.140
C	-1.893	4.558	-2.518	-1.785	4.587	-2.482	-2.817	3.691	-3.073
C	0.092	1.603	2.474	0.066	1.508	2.526	-0.598	1.729	2.348
C	-0.261	2.714	1.628	-0.243	2.648	1.686	-1.388	2.518	1.423
C	-0.676	2.523	0.282	-0.667	2.492	0.329	-1.392	2.268	0.015
O	-0.762	1.362	-0.301	-0.796	1.348	-0.257	-0.747	1.294	-0.542
C	-0.237	4.008	2.211	-0.176	3.920	2.269	-2.121	3.585	1.950
C	-0.600	5.117	1.475	-0.498	5.064	1.531	-2.868	4.432	1.111
C	-1.014	4.959	0.132	-0.917	4.945	0.190	-2.877	4.220	-0.283
C	-1.057	3.696	-0.450	-1.008	3.689	-0.404	-2.152	3.165	-0.831
H	2.387	-3.596	0.584	2.375	-3.571	0.557	3.070	-2.913	1.119
H	4.572	-3.333	0.037	4.580	-3.254	0.041	5.206	-2.377	0.454
H	6.111	0.450	-1.320	6.027	0.570	-1.305	6.185	1.485	-1.216
H	-2.031	-1.203	-3.198	-2.044	-1.049	-3.232	-1.318	-1.930	-3.123
H	-4.321	-1.137	-3.017	-4.350	-0.822	-3.033	-3.609	-2.325	-3.058
H	-6.261	-1.281	0.806	-6.298	-1.184	0.779	-5.768	-2.362	0.659
H	8.080	-0.613	-0.610	8.028	-0.457	-0.570	8.301	0.709	-0.370
H	7.632	-1.104	-2.275	7.604	-0.947	-2.245	7.971	0.061	-2.019
H	8.651	-2.172	-1.268	8.627	-2.004	-1.231	9.048	-0.829	-0.900
H	4.248	2.690	0.560	4.331	2.761	0.538	2.500	3.165	0.199
H	2.523	2.438	0.122	2.567	2.502	0.310	1.856	2.834	-1.437
H	3.510	3.640	-0.763	3.438	3.707	-0.687	2.976	4.211	-1.174
H	-7.884	-2.230	-0.554	-7.940	-1.992	-0.705	-6.994	-3.905	-0.679
H	-8.614	-1.358	-1.930	-8.617	-0.970	-2.004	-7.760	-3.404	-2.214
H	-7.967	-0.438	-0.544	-7.991	-0.204	-0.517	-7.526	-2.200	-0.915
H	-5.680	-2.209	2.836	-5.692	-2.357	2.719	-5.063	-2.872	2.855
H	-5.793	-0.419	2.887	-5.790	-0.579	2.962	-5.642	-1.178	2.666
H	-4.768	-1.287	4.065	-4.748	-1.575	4.019	-4.479	-1.593	3.958
H	-2.015	7.422	1.120	-1.746	7.479	1.202	-5.123	5.851	0.448
H	-0.343	7.686	0.529	-0.038	7.618	0.656	-3.678	6.915	0.282
H	-0.842	8.324	2.119	-0.526	8.250	2.255	-4.729	7.042	1.722
H	-1.091	5.295	-2.667	-0.942	5.276	-2.621	-2.458	4.726	-3.044
H	-2.763	5.052	-2.065	-2.637	5.119	-2.043	-3.892	3.655	-2.867
H	-2.179	4.138	-3.484	-2.074	4.165	-3.445	-2.615	3.259	-4.053
H	0.227	1.865	3.531	0.185	1.748	3.588	-0.660	2.062	3.389
H	0.070	4.135	3.245	0.129	4.041	3.304	-2.123	3.789	3.017

H	-1.304	5.825	-0.448	-1.171	5.830	-0.378	-3.447	4.877	-0.926
N	0.816	-2.281	0.545	0.786	-2.281	0.497	1.315	-1.892	0.844
N	0.249	0.358	2.145	0.197	0.273	2.168	0.162	0.716	2.087
N	-0.589	-0.917	-1.773	-0.607	-0.871	-1.784	-0.101	-1.127	-1.686
C	0.409	-0.959	-2.853	0.411	-0.977	-2.844	1.000	-1.182	-2.666
C	0.729	0.440	-3.386	0.785	0.393	-3.420	1.098	0.107	-3.491
H	0.044	-1.581	-3.682	0.042	-1.617	-3.655	0.866	-2.037	-3.337
H	1.326	-1.414	-2.472	1.305	-1.446	-2.429	1.942	-1.331	-2.135
H	-0.192	0.928	-3.747	-0.111	0.881	-3.841	0.255	0.163	-4.199
H	1.156	1.060	-2.590	1.193	1.041	-2.634	1.044	0.991	-2.838
C	2.198	1.497	-4.907	2.295	1.340	-4.974	2.493	1.075	-5.148
H	2.889	1.257	-5.719	3.018	1.035	-5.734	3.468	0.918	-5.611
H	1.412	2.168	-5.291	1.517	1.960	-5.447	1.711	1.016	-5.918
H	2.745	2.008	-4.101	2.805	1.928	-4.198	2.467	2.071	-4.681
C	0.574	-0.552	3.254	0.476	-0.681	3.258	0.879	0.148	3.248
C	2.083	-0.616	3.499	1.975	-0.772	3.558	2.254	0.795	3.452
H	0.200	-1.549	3.018	0.103	-1.665	2.971	1.012	-0.922	3.096
H	0.074	-0.227	4.175	-0.059	-0.382	4.167	0.281	0.277	4.156
H	2.617	-0.883	2.576	2.548	-0.959	2.637	2.817	0.832	2.504
H	2.453	0.372	3.825	2.332	0.183	3.982	2.132	1.834	3.804
C	3.684	-1.716	4.846	3.488	-1.972	4.927	4.141	0.590	4.876
H	3.750	-2.488	5.617	3.499	-2.812	5.624	4.559	-0.106	5.604
H	4.284	-2.021	3.974	4.165	-2.186	4.086	4.857	0.731	4.052
H	4.091	-0.773	5.243	3.836	-1.065	5.445	3.954	1.558	5.363
C	-0.027	-3.405	0.997	-0.053	-3.434	0.898	0.634	-3.049	1.478
C	-0.636	-4.168	-0.182	-0.519	-4.249	-0.311	0.322	-4.161	0.468
H	-0.837	-3.011	1.612	-0.927	-3.063	1.433	-0.298	-2.699	1.923
H	0.567	-4.104	1.598	0.513	-4.089	1.571	1.266	-3.460	2.273
H	-1.315	-3.519	-0.750	-1.088	-3.617	-1.011	-0.281	-3.775	-0.368
H	0.159	-4.516	-0.865	0.351	-4.654	-0.857	1.260	-4.563	0.046
C	-2.044	-6.012	-0.629	-1.798	-6.171	-0.828	-0.639	-6.326	0.414
H	-2.548	-6.834	-0.113	-2.401	-6.934	-0.331	-1.172	-7.014	1.071
H	-2.796	-5.387	-1.135	-2.421	-5.634	-1.558	-1.265	-6.096	-0.461
H	-1.360	-6.428	-1.386	-0.964	-6.657	-1.357	0.296	-6.796	0.077
O	2.314	-1.584	4.509	2.146	-1.824	4.483	2.926	0.011	4.407
O	1.651	0.271	-4.454	1.743	0.149	-4.432	2.330	0.047	-4.175
O	-1.340	-5.276	0.354	-1.324	-5.297	0.186	-0.375	-5.153	1.179

232

Table A-16 Optimized structures of Complexes **30** and **31**

Atom	Complex **8**			Atom	Complex **9**			[Complex **9**]$^{+1}$			[Complex **9**]$^{+2}$		
	X	Y	Z		X	Y	Z	X	Y	Z	X	Y	Z
Cr	0.094	-0.381	0.062	Cr	0.105	-0.440	0.333	-0.017	-0.518	-0.304	-0.026	-0.472	-0.275
C	2.484	-2.170	0.671	C	2.391	-2.345	0.961	-2.239	-2.482	-0.825	-2.078	-2.547	-0.870
C	3.424	-1.209	0.186	C	3.377	-1.545	0.289	-3.246	-1.658	-0.223	-3.144	-1.802	-0.269
C	3.042	-0.026	-0.522	C	3.074	-0.271	-0.289	-2.955	-0.388	0.368	-2.944	-0.529	0.359
O	1.785	0.247	-0.740	O	1.849	0.176	-0.340	-1.718	0.051	0.424	-1.733	-0.012	0.432
C	4.793	-1.530	0.391	C	4.698	-2.063	0.264	-4.565	-2.174	-0.231	-4.426	-2.395	-0.308
C	5.808	-0.719	-0.068	C	5.746	-1.358	-0.293	-5.622	-1.470	0.315	-5.533	-1.770	0.249
C	5.407	0.458	-0.753	C	5.435	-0.068	-0.799	-5.314	-0.199	0.863	-5.306	-0.502	0.843
C	4.094	0.844	-0.997	C	4.171	0.509	-0.808	-4.047	0.377	0.911	-4.078	0.151	0.921
C	-1.792	-2.048	-1.602	C	-1.533	-2.067	-1.589	1.778	-1.852	1.664	1.844	-1.824	1.664
C	-2.892	-1.816	-0.711	C	-2.731	-1.905	-0.810	2.936	-1.615	0.841	3.014	-1.560	0.850
C	-2.759	-1.171	0.561	C	-2.719	-1.394	0.528	2.832	-1.246	-0.543	2.925	-1.061	-0.508
O	-1.583	-0.787	0.998	O	-1.597	-1.027	1.097	1.655	-1.040	-1.084	1.774	-0.789	-1.018
C	-4.146	-2.298	-1.153	C	-3.932	-2.359	-1.401	4.190	-1.887	1.415	4.249	-1.912	1.381
C	-5.299	-2.153	-0.403	C	-5.145	-2.309	-0.736	5.372	-1.777	0.688	5.448	-1.764	0.649
C	-5.151	-1.489	0.835	C	-5.112	-1.795	0.581	5.242	-1.412	-0.672	5.339	-1.268	-0.671
C	-3.951	-0.993	1.347	C	-3.967	-1.346	1.240	4.035	-1.159	-1.325	4.143	-0.920	-1.293
C	0.266	2.138	1.710	C	0.059	2.016	2.069	-0.258	1.830	-2.155	-0.374	1.869	-2.145
C	-0.499	2.897	0.764	C	-0.507	2.842	1.038	0.197	2.761	-1.148	0.010	2.839	-1.134
C	-1.003	2.362	-0.466	C	-0.937	2.328	-0.228	0.761	2.343	0.112	0.617	2.463	0.135
O	-0.802	1.115	-0.799	O	-0.770	1.070	-0.546	0.802	1.087	0.436	0.711	1.234	0.471
C	-0.726	4.252	1.108	C	-0.679	4.207	1.365	0.141	4.118	-1.484	-0.129	4.176	-1.465
C	-1.431	5.115	0.290	C	-1.259	5.108	0.491	0.606	5.117	-0.622	0.283	5.217	-0.596
C	-1.916	4.565	-0.920	C	-1.705	4.577	-0.741	1.192	4.685	0.588	0.922	4.835	0.607
C	-1.739	3.245	-1.331	C	-1.587	3.242	-1.131	1.316	3.355	0.986	1.142	3.521	1.003
H	2.948	-3.077	1.066	H	2.790	-3.269	1.397	-2.615	-3.428	-1.227	-2.386	-3.502	-1.307
H	5.013	-2.448	0.927	H	4.859	-3.044	0.702	-4.722	-3.151	-0.678	-4.524	-3.365	-0.786
H	6.196	1.107	-1.113	H	6.256	0.510	-1.207	-6.137	0.368	1.277	-6.166	-0.004	1.271
H	-2.049	-2.655	-2.475	H	-1.672	-2.658	-2.504	1.990	-2.377	2.602	2.055	-2.397	2.573
H	-4.180	-2.792	-2.122	H	-3.877	-2.749	-2.416	4.216	-2.189	2.460	4.284	-2.316	2.389
H	-6.041	-1.350	1.433	H	-6.048	-1.749	1.120	6.150	-1.331	-1.251	6.252	-1.160	-1.236
H	0.610	2.718	2.572	H	0.225	2.543	3.016	-0.472	2.294	-3.124	-0.606	2.316	-3.117
H	-0.319	4.603	2.055	H	-0.334	4.535	2.344	-0.282	4.388	-2.448	-0.570	4.428	-2.425
H	-2.469	5.221	-1.578	H	-2.182	5.256	-1.433	1.586	5.444	1.247	1.275	5.625	1.253
N	1.173	-2.127	0.709	N	1.125	-2.107	1.148	-0.964	-2.252	-0.968	-0.814	-2.239	-0.971
N	0.604	0.877	1.693	N	0.366	0.755	2.040	-0.408	0.548	-2.065	-0.431	0.584	-2.051
N	-0.557	-1.632	-1.529	N	-0.331	-1.646	-1.336	0.539	-1.566	1.409	0.610	-1.512	1.429
C	-6.650	-2.688	-0.918	C	0.705	-2.092	-2.286	-0.452	-2.084	2.377	-0.372	-2.043	2.406
C	-7.005	-2.001	-2.259	C	0.771	-1.220	-3.539	-0.500	-1.280	3.680	-0.379	-1.274	3.733
C	-6.553	-4.217	-1.141	H	0.509	-3.127	-2.595	-0.219	-3.127	2.619	-0.148	-3.095	2.612
C	-7.804	-2.425	0.070	H	1.675	-2.076	-1.789	-1.439	-2.064	1.916	-1.367	-1.995	1.967
H	-7.087	-0.915	-2.133	H	-0.217	-1.176	-4.028	0.494	-1.261	4.159	0.617	-1.315	4.207
H	-6.245	-2.189	-3.025	H	1.067	-0.195	-3.280	-0.799	-0.242	3.483	-0.630	-0.216	3.568
H	-7.964	-2.374	-2.642	C	0.409	-3.138	1.927	-0.209	-3.342	-1.628	0.031	-3.260	-1.638
H	-6.312	-4.734	-0.205	C	-0.112	-4.279	1.051	0.142	-4.485	-0.670	0.347	-4.461	-0.736
H	-7.507	-4.613	-1.514	H	-0.437	-2.671	2.432	0.711	-2.930	-2.041	0.967	-2.796	-1.947
H	-5.778	-4.472	-1.872	H	1.076	-3.562	2.688	-0.803	-3.752	-2.454	-0.476	-3.620	-2.540
H	-8.738	-2.826	-0.342	H	-0.888	-3.916	0.364	0.793	-4.127	0.142	0.795	-4.131	0.216
H	-7.636	-2.912	1.038	H	0.710	-4.703	0.447	-0.775	-4.895	-0.211	-0.578	-5.011	-0.494
H	-7.958	-1.354	0.247	C	0.882	0.208	3.306	-0.813	-0.131	-3.312	-0.769	-0.126	-3.306
C	-3.932	-0.255	2.706	C	2.394	0.404	3.437	-2.322	-0.031	-3.557	-2.277	-0.128	-3.590
C	-3.038	-1.004	3.721	H	0.653	-0.857	3.356	-0.527	-1.180	-3.252	-0.423	-1.156	-3.233
C	-3.404	1.186	2.512	H	0.385	0.688	4.157	-0.279	0.305	-4.164	-0.241	0.338	-4.146
C	-5.335	-0.144	3.341	H	2.921	-0.034	2.579	-2.885	-0.383	-2.681	-2.844	-0.441	-2.700
H	-3.393	-2.030	3.875	H	2.634	1.481	3.463	-2.607	1.020	-3.736	-2.614	0.889	-3.856
H	-2.004	-1.040	3.375	C	-6.439	-2.799	-1.416	6.729	-2.070	1.350	6.784	-2.153	1.283
H	-3.054	-0.490	4.691	C	-6.693	-1.979	-2.705	6.925	-1.129	2.565	6.993	-1.319	2.576
H	-4.060	1.754	1.842	C	-6.298	-4.295	-1.789	6.752	-3.542	1.835	6.743	-3.663	1.649
H	-3.373	1.709	3.478	C	-7.676	-2.650	-0.508	7.914	-1.862	0.387	7.983	-1.909	0.347
H	-2.401	1.187	2.087	H	-6.804	-0.913	-2.475	6.917	-0.078	2.255	7.026	-0.246	2.355
H	-5.253	0.401	4.289	H	-5.871	-2.081	-3.422	6.143	-1.264	3.321	6.206	-1.493	3.319
H	-6.036	0.412	2.707	H	-7.612	-2.319	-3.201	7.888	-1.333	3.048	7.946	-1.598	3.038
H	-5.773	-1.124	3.566	H	-6.124	-4.906	-0.895	6.617	-4.235	0.997	6.594	-4.284	0.759

C	7.304	-1.025	0.122	H	-7.211	-4.658	-2.278	7.715	-3.768	2.310	7.696	-3.951	2.106
C	7.975	0.115	0.926	H	-5.462	-4.466	-2.477	5.966	-3.744	2.570	5.951	-3.897	2.368
C	7.534	-2.344	0.885	H	-8.566	-3.009	-1.039	8.852	-2.074	0.912	8.905	-2.201	0.859
C	7.992	-1.145	-1.260	H	-7.583	-3.239	0.412	7.866	-2.534	-0.478	7.921	-2.506	-0.570
H	7.884	1.082	0.418	H	-7.858	-1.606	-0.230	7.971	-0.830	0.021	8.086	-0.853	0.072
H	7.518	0.214	1.918	C	-4.049	-0.794	2.681	4.010	-0.777	-2.821	4.119	-0.402	-2.741
H	9.045	-0.089	1.061	C	-3.163	-1.632	3.634	3.177	-1.804	-3.626	3.275	-1.352	-3.632
H	7.113	-3.204	0.350	C	-3.589	0.684	2.703	3.411	0.641	-2.991	3.526	1.031	-2.778
H	8.610	-2.522	0.999	C	-5.485	-0.834	3.247	5.424	-0.754	-3.442	5.534	-0.332	-3.355
H	7.095	-2.316	1.890	H	-3.469	-2.686	3.630	3.580	-2.817	-3.507	3.668	-2.374	-3.602
H	9.061	-1.363	-1.139	H	-2.112	-1.578	3.348	2.132	-1.811	-3.313	2.227	-1.374	-3.329
H	7.543	-1.953	-1.851	H	-3.259	-1.257	4.662	3.210	-1.553	-4.693	3.321	-1.008	-4.671
H	7.905	-0.220	-1.841	H	-4.250	1.306	2.087	4.019	1.388	-2.467	4.133	1.722	-2.179
C	3.791	2.184	-1.709	H	-3.623	1.072	3.730	3.393	0.909	-4.055	3.528	1.397	-3.811
C	2.912	1.969	-2.962	H	-2.572	0.790	2.327	2.392	0.693	-2.605	2.500	1.054	-2.406
C	3.057	3.133	-0.731	H	-5.477	-0.426	4.265	5.343	-0.479	-4.499	5.457	0.047	-4.379
C	5.073	2.907	-2.174	H	-6.182	-0.226	2.658	6.079	-0.016	-2.965	6.195	0.351	-2.809
H	3.380	1.255	-3.652	H	-5.881	-1.855	3.308	5.914	-1.734	-3.399	6.014	-1.315	-3.412
H	1.924	1.600	-2.689	C	7.189	-1.886	-0.370	-7.069	-1.990	0.347	-6.943	-2.378	0.244
H	2.785	2.920	-3.496	C	8.135	-0.950	0.423	-7.986	-1.020	-0.438	-7.912	-1.422	-0.497
H	3.688	3.357	0.139	C	7.320	-3.305	0.216	-7.196	-3.390	-0.285	-6.982	-3.749	-0.458
H	2.824	4.083	-1.230	C	7.646	-1.936	-1.849	-7.552	-2.077	1.816	-7.422	-2.564	1.707
H	2.120	2.697	-0.385	H	8.119	0.073	0.032	-7.976	-0.010	-0.014	-7.978	-0.441	-0.015
H	4.792	3.843	-2.670	H	7.847	-0.908	1.480	-7.677	-0.948	-1.488	-7.600	-1.269	-1.537
H	5.734	3.170	-1.339	H	9.169	-1.312	0.365	-9.023	-1.377	-0.414	-8.921	-1.850	-0.507
H	5.647	2.313	-2.897	H	6.694	-4.027	-0.320	-6.592	-4.136	0.246	-6.343	-4.487	0.041
C	-2.333	2.750	-2.668	H	8.360	-3.644	0.134	-8.239	-3.721	-0.237	-8.004	-4.140	-0.437
C	-1.218	2.187	-3.582	H	7.049	-3.336	1.279	-6.901	-3.393	-1.341	-6.683	-3.682	-1.511
C	-3.390	1.652	-2.394	H	8.676	-2.306	-1.920	-8.584	-2.446	1.852	-8.428	-2.998	1.715
C	-3.037	3.875	-3.456	H	7.002	-2.603	-2.434	-6.926	-2.764	2.397	-6.758	-3.240	2.258
H	-0.469	2.957	-3.802	H	7.615	-0.947	-2.320	-7.533	-1.102	2.314	-7.468	-1.615	2.251
H	-0.716	1.340	-3.114	C	3.955	1.950	-1.323	-3.848	1.793	1.496	-3.968	1.549	1.567
H	-1.648	1.852	-4.535	C	2.955	1.970	-2.503	-2.827	1.767	2.658	-2.967	1.525	2.747
H	-4.223	2.056	-1.805	C	3.413	2.831	-0.170	-3.350	2.741	0.378	-3.508	2.573	0.501
H	-3.798	1.278	-3.342	C	5.264	2.598	-1.820	-5.157	2.388	2.054	-5.319	2.045	2.127
H	-2.962	0.811	-1.847	H	3.323	1.353	-3.333	-3.167	1.095	3.456	-3.274	0.793	3.503
H	-3.427	3.462	-4.394	H	1.976	1.602	-2.196	-1.844	1.439	2.319	-1.958	1.280	2.415
H	-3.888	4.300	-2.909	H	2.837	2.997	-2.874	-2.727	2.772	3.086	-2.942	2.511	3.228
H	-2.352	4.691	-3.718	H	4.129	2.865	0.661	-4.091	2.815	-0.427	-4.237	2.639	-0.316
C	-1.663	6.583	0.701	H	3.258	3.859	-0.523	-3.193	3.749	0.784	-3.422	3.568	0.953
C	-2.459	6.630	2.028	H	2.459	2.454	0.204	-2.406	2.397	-0.048	-2.538	2.304	0.078
C	-0.301	7.291	0.902	H	5.050	3.617	-2.161	-4.950	3.387	2.455	-5.177	3.036	2.570
C	-2.457	7.374	-0.357	H	6.021	2.672	-1.029	-5.928	2.504	1.284	-6.084	2.147	1.349
H	-3.436	6.143	1.916	H	5.702	2.055	-2.667	-5.571	1.788	2.874	-5.709	1.391	2.916
H	-1.926	6.122	2.840	C	-2.161	2.766	-2.482	2.056	2.989	2.287	1.912	3.199	2.292
H	-2.630	7.669	2.340	C	-1.038	2.170	-3.362	1.136	2.183	3.234	1.012	2.406	3.272
H	0.285	7.282	-0.024	C	-3.256	1.700	-2.234	3.315	2.156	1.934	3.177	2.369	1.940
H	-0.452	8.337	1.200	C	-2.811	3.910	-3.290	2.532	4.235	3.064	2.386	4.474	3.022
H	0.298	6.807	1.681	H	-0.273	2.926	-3.582	0.255	2.770	3.518	0.121	2.984	3.543
H	-2.593	8.408	-0.016	H	-0.557	1.329	-2.864	0.800	1.257	2.769	0.694	1.455	2.847
H	-1.934	7.411	-1.320	H	-1.453	1.823	-4.318	1.683	1.934	4.152	1.572	2.206	4.193
H	-3.455	6.950	-0.525	H	-4.088	2.127	-1.660	4.000	2.736	1.304	3.836	2.927	1.264
C	1.477	0.468	2.756	H	-3.657	1.343	-3.193	3.851	1.890	2.854	3.738	2.164	2.858
C	1.096	-0.551	3.637	H	-2.865	0.844	-1.684	3.062	1.233	1.410	2.924	1.415	1.473
C	2.719	1.096	2.929	H	-3.197	3.505	-4.232	3.042	3.908	3.977	2.935	4.180	3.922
C	1.942	-0.930	4.680	H	-3.656	4.367	-2.761	3.248	4.838	2.494	3.066	5.079	2.413
H	0.132	-1.026	3.515	H	-2.093	4.700	-3.544	1.700	4.879	3.371	1.550	5.104	3.349
C	3.563	0.714	3.975	C	-1.412	6.594	0.872	0.496	6.597	-1.018	0.061	6.674	-0.994
H	3.030	1.865	2.227	C	-2.278	6.720	2.149	1.303	6.838	-2.320	0.833	6.956	-2.314
C	3.179	-0.301	4.854	C	-0.016	7.206	1.145	-0.993	6.950	-1.267	-1.457	6.905	-1.229
H	1.628	-1.716	5.363	C	-2.083	7.423	-0.241	1.039	7.544	0.069	0.547	7.668	0.078
H	4.525	1.206	4.093	H	-3.278	6.301	1.986	2.363	6.600	-2.177	1.910	6.801	-2.185
H	3.837	-0.601	5.666	H	-1.830	6.191	2.998	0.931	6.234	-3.155	0.492	6.327	-3.143
C	0.554	-3.379	1.042	H	-2.392	7.774	2.436	1.229	7.891	-2.615	0.675	7.999	-2.607
C	-0.520	-3.448	1.940	H	0.622	7.138	0.256	-1.591	6.798	-0.361	-2.034	6.717	-0.316
C	1.025	-4.574	0.466	H	-0.106	8.265	1.421	-1.083	8.003	-1.560	-1.622	7.947	-1.524
C	-1.085	-4.679	2.275	H	0.500	6.692	1.964	-1.433	6.346	-2.068	-1.860	6.271	-2.026
H	-0.918	-2.537	2.361	H	-2.165	8.469	0.079	0.920	8.581	-0.261	0.346	8.689	-0.259
C	0.457	-5.804	0.805	H	-1.501	7.408	-1.171	0.498	7.438	1.016	0.025	7.534	1.033
H	1.819	-4.536	-0.274	H	-3.096	7.068	-0.465	2.107	7.385	0.260	1.626	7.595	0.254

C	-0.599	-5.865	1.717	O	1.722	-1.812	-4.409	-1.438	-1.928	4.514	-1.343	-1.906	4.539
H	-1.914	-4.707	2.978	O	2.801	-0.219	4.644	-2.602	-0.823	-4.691	-2.470	-1.021	-4.660
H	0.837	-6.712	0.344	O	-0.640	-5.266	1.920	0.797	-5.470	-1.438	1.241	-5.271	-1.459
H	-1.046	-6.820	1.978	C	1.897	-1.087	-5.614	-1.578	-1.312	5.786	-1.441	-1.355	5.850
C	0.316	-2.149	-2.543	H	2.249	-0.063	-5.419	-1.922	-0.271	5.690	-1.728	-0.295	5.814
C	1.092	-1.279	-3.318	H	2.648	-1.621	-6.201	-2.323	-1.889	6.336	-2.213	-1.924	6.370
C	0.377	-3.530	-2.792	H	0.959	-1.035	-6.189	-0.627	-1.325	6.340	-0.489	-1.455	6.391
C	1.907	-1.783	-4.333	C	-1.242	-6.347	1.231	1.187	-6.608	-0.683	1.516	-6.522	-0.833
H	1.046	-0.217	-3.125	H	-1.611	-7.043	1.989	1.676	-7.295	-1.376	2.209	-7.054	-1.487
C	1.198	-4.028	-3.807	H	-2.085	-6.007	0.610	1.894	-6.333	0.115	1.981	-6.378	0.154
C	-0.201	-4.211	-2.174	H	-0.514	-6.867	0.587	0.315	-7.106	-0.233	0.598	-7.115	-0.717
C	1.965	-3.157	-4.583	C	4.186	-0.077	4.901	-3.960	-0.754	-5.106	-3.796	-1.012	-5.185
H	2.495	-1.094	-4.933	H	4.393	-0.598	5.839	-4.057	-1.406	-5.977	-3.815	-1.743	-5.994
H	1.237	-5.101	-3.985	H	4.791	-0.522	4.096	-4.637	-1.102	-4.312	-4.528	-1.296	-4.416
H	2.604	-3.544	-5.373	H	4.466	0.984	5.007	-4.236	0.273	-5.388	-4.054	-0.021	-5.583

A.b.vi.   Complex 32

Table A-17 Optimized structures of Complex **32**

Atom	Complex **10**			[Complex **10**]$^{+1}$			[Complex **10**]$^{+2}$		
	X	Y	Z	X	Y	Z	X	Y	Z
Cr	-0.164	-0.468	-0.283	-0.091	-0.556	-0.268	0.040	-0.521	0.394
C	-2.494	-2.327	-0.924	-2.352	-2.487	-0.801	2.182	-2.502	1.037
C	-3.467	-1.492	-0.285	-3.347	-1.640	-0.221	3.208	-1.733	0.408
C	-3.143	-0.213	0.275	-3.047	-0.347	0.317	2.969	-0.454	-0.193
O	-1.904	0.197	0.353	-1.800	0.071	0.386	1.738	0.031	-0.252
C	-4.805	-1.973	-0.280	-4.676	-2.141	-0.221	4.509	-2.299	0.419
C	-5.842	-1.228	0.237	-5.728	-1.397	0.277	5.589	-1.642	-0.143
C	-5.507	0.066	0.718	-5.409	-0.098	0.749	5.325	-0.360	-0.689
C	-4.229	0.613	0.741	-4.136	0.469	0.780	4.082	0.273	-0.729
C	1.389	-2.112	1.702	1.589	-1.919	1.790	-1.675	-1.952	-1.626
C	2.598	-2.020	0.934	2.778	-1.757	0.999	-2.895	-1.724	-0.872
C	2.625	-1.535	-0.415	2.737	-1.412	-0.397	-2.893	-1.246	0.500
O	1.523	-1.133	-1.006	1.589	-1.157	-0.979	-1.785	-0.935	1.070
C	3.771	-2.519	1.548	3.999	-2.084	1.618	-4.082	-2.123	-1.460
C	4.991	-2.537	0.895	5.205	-2.055	0.926	-5.325	-2.044	-0.781
C	4.994	-2.044	-0.430	5.136	-1.709	-0.443	-5.305	-1.559	0.548
C	3.879	-1.555	-1.112	3.967	-1.403	-1.141	-4.158	-1.166	1.230
C	0.016	1.953	-2.064	-0.143	1.784	-2.165	0.231	1.905	2.201
C	0.623	2.764	-1.051	0.363	2.700	-1.170	-0.147	2.819	1.140
C	0.995	2.261	0.238	0.839	2.277	0.126	-0.711	2.372	-0.125
O	0.739	1.025	0.587	0.761	1.034	0.483	-0.767	1.125	-0.407
C	0.894	4.105	-1.415	0.431	4.045	-1.546	-0.045	4.173	1.415
C	1.520	4.991	-0.558	0.942	5.031	-0.692	-0.456	5.164	0.489
C	1.900	4.468	0.700	1.437	4.593	0.555	-1.059	4.713	-0.708
C	1.682	3.159	1.129	1.434	3.271	0.998	-1.243	3.377	-1.049
H	-2.911	-3.248	-1.350	-2.739	-3.437	-1.185	2.543	-3.427	1.494
H	-4.984	-2.957	-0.704	-4.842	-3.134	-0.627	4.635	-3.273	0.882
H	-6.321	0.676	1.089	-6.232	0.504	1.112	6.168	0.172	-1.109
H	1.495	-2.676	2.637	1.750	-2.418	2.752	-1.822	-2.537	-2.537
H	3.688	-2.890	2.567	3.978	-2.369	2.667	-4.051	-2.528	-2.467
H	5.937	-2.052	-0.959	6.065	-1.690	-0.994	-6.249	-1.501	1.068
H	-0.120	2.470	-3.022	-0.317	2.246	-3.143	0.427	2.399	3.159
H	0.590	4.426	-2.410	0.069	4.320	-2.532	0.365	4.479	2.373
H	2.407	5.136	1.382	1.860	5.340	1.210	-1.414	5.464	-1.398
N	-1.216	-2.123	-1.098	-1.072	-2.269	-0.955	0.902	-2.243	1.161
N	-0.367	0.711	-2.011	-0.388	0.518	-2.053	0.326	0.618	2.158
N	0.204	-1.657	1.417	0.367	-1.599	1.482	-0.470	-1.599	-1.323
C	-0.865	-2.035	2.354	-0.677	-2.048	2.422	0.586	-2.121	-2.224
C	-1.058	-0.985	3.469	-0.927	-1.032	3.557	0.785	-1.237	-3.474
H	-0.637	-3.007	2.810	-0.393	-3.014	2.856	0.325	-3.141	-2.525
H	-1.797	-2.143	1.798	-1.602	-2.197	1.866	1.519	-2.169	-1.666
H	-0.123	-0.844	4.023	-0.019	-0.893	4.156	-0.113	-1.245	-4.103
H	-1.327	-0.022	3.027	-1.197	-0.061	3.134	0.976	-0.201	-3.180
C	-0.516	-3.176	-1.855	-0.328	-3.361	-1.620	0.140	-3.251	1.949
C	0.012	-4.301	-0.934	0.129	-4.450	-0.622	0.080	-4.678	1.350
H	0.330	-2.728	-2.375	0.550	-2.936	-2.103	-0.875	-2.878	2.083
H	-1.191	-3.610	-2.603	-0.957	-3.821	-2.391	0.600	-3.342	2.939
H	0.749	-3.897	-0.235	0.732	-4.001	0.172	1.083	-5.084	1.178
H	-0.810	-4.725	-0.344	-0.739	-4.927	-0.149	-0.393	-5.335	2.091
C	-0.916	0.173	-3.262	-0.855	-0.145	-3.285	0.650	-0.047	3.436
C	-2.443	0.407	-3.361	-2.388	-0.016	-3.448	2.186	-0.225	3.630
H	-0.707	-0.896	-3.311	-0.574	-1.196	-3.241	0.154	-1.016	3.441
H	-0.424	0.639	-4.124	-0.356	0.290	-4.158	0.237	0.529	4.270
H	-2.950	0.006	-2.478	-2.898	-0.316	-2.527	2.700	-0.181	2.664
H	-2.656	1.482	-3.392	-2.663	1.028	-3.640	2.595	0.584	4.245
C	-3.006	-0.224	-4.558	-2.872	-0.853	-4.548	2.491	-1.517	4.245
N	-3.426	-0.741	-5.510	-3.225	-1.543	-5.412	2.671	-2.583	4.670
C	-2.106	-1.394	4.408	-2.010	-1.487	4.431	1.927	-1.717	-4.257
N	-2.934	-1.744	5.143	-2.877	-1.871	5.102	2.850	-2.110	-4.841
C	0.635	-5.379	-1.708	0.930	-5.477	-1.293	-0.683	-4.761	0.104
N	1.118	-6.227	-2.338	1.574	-6.269	-1.847	-1.300	-4.788	-0.879
C	6.251	-3.084	1.594	6.522	-2.417	1.633	-6.601	-2.501	-1.480
C	6.523	-2.277	2.887	6.731	-1.478	2.848	-6.787	-1.676	-2.784

236

C	6.033	-4.573	1.961	6.445	-3.884	2.128	-6.454	-4.007	-1.843
C	7.507	-2.992	0.704	7.746	-2.283	0.707	-7.858	-2.327	-0.607
H	6.690	-1.218	2.661	6.791	-0.430	2.532	-6.892	-0.607	-2.568
H	5.687	-2.341	3.592	5.921	-1.564	3.581	-5.958	-1.807	-3.487
H	7.416	-2.662	3.397	7.666	-1.731	3.361	-7.699	-2.009	-3.291
H	5.845	-5.175	1.065	6.299	-4.576	1.291	-6.314	-4.621	-0.947
H	6.921	-4.977	2.464	7.377	-4.158	2.636	-7.367	-4.343	-2.345
H	5.181	-4.705	2.637	5.625	-4.036	2.838	-5.616	-4.196	-2.522
H	8.372	-3.386	1.250	8.654	-2.538	1.264	-8.735	-2.665	-1.167
H	7.404	-3.581	-0.215	7.692	-2.963	-0.152	-7.813	-2.926	0.310
H	7.737	-1.957	0.426	7.870	-1.260	0.333	-8.033	-1.279	-0.334
C	4.008	-1.033	-2.561	4.015	-1.045	-2.642	-4.227	-0.660	2.680
C	3.091	-1.838	-3.515	3.150	-2.033	-3.464	-3.392	-1.584	3.606
C	3.627	0.467	-2.612	3.505	0.403	-2.852	-3.693	0.795	2.756
C	5.446	-1.159	-3.108	5.447	-1.113	-3.214	-5.672	-0.650	3.223
H	3.333	-2.908	-3.484	3.472	-3.069	-3.305	-3.753	-2.618	3.560
H	2.040	-1.712	-3.252	2.093	-1.955	-3.205	-2.331	-1.571	3.349
H	3.229	-1.492	-4.547	3.252	-1.812	-4.533	-3.494	-1.244	4.642
H	4.313	1.063	-1.997	4.135	1.121	-2.312	-4.297	1.467	2.133
H	3.693	0.836	-3.644	3.545	0.659	-3.918	-3.763	1.151	3.790
H	2.612	0.633	-2.249	2.476	0.520	-2.508	-2.652	0.866	2.437
H	5.472	-0.768	-4.132	5.417	-0.850	-4.277	-5.660	-0.276	4.252
H	6.168	-0.579	-2.521	6.128	-0.406	-2.726	-6.330	0.012	2.648
H	5.787	-2.201	-3.149	5.877	-2.119	-3.143	-6.116	-1.651	3.251
C	-7.302	-1.712	0.291	-7.181	-1.896	0.321	7.011	-2.218	-0.183
C	-8.196	-0.770	-0.551	-8.073	-0.966	-0.539	7.965	-1.284	0.604
C	-7.458	-3.142	-0.261	-7.316	-3.331	-0.222	7.082	-3.624	0.443
C	-7.794	-1.708	1.759	-7.684	-1.882	1.786	7.481	-2.314	-1.656
H	-8.164	0.262	-0.185	-8.058	0.068	-0.179	7.997	-0.274	0.181
H	-7.880	-0.764	-1.601	-7.749	-0.965	-1.587	7.665	-1.204	1.655
H	-9.242	-1.102	-0.513	-9.114	-1.310	-0.508	8.985	-1.683	0.574
H	-6.865	-3.867	0.310	-6.726	-4.048	0.362	6.449	-4.344	-0.088
H	-8.507	-3.451	-0.194	-8.362	-3.649	-0.163	8.110	-3.997	0.387
H	-7.165	-3.209	-1.316	-7.013	-3.406	-1.274	6.798	-3.621	1.503
H	-8.837	-2.047	1.812	-8.721	-2.234	1.830	8.495	-2.727	-1.696
H	-7.187	-2.377	2.380	-7.076	-2.537	2.419	6.826	-2.969	-2.242
H	-7.750	-0.708	2.205	-7.660	-0.877	2.222	7.507	-1.336	-2.148
C	-3.994	2.070	1.203	-3.936	1.929	1.245	3.949	1.706	-1.292
C	-3.017	2.133	2.400	-2.942	2.011	2.428	2.930	1.757	-2.454
C	-3.413	2.891	0.024	-3.403	2.769	0.058	3.499	2.653	-0.152
C	-5.302	2.760	1.644	-5.254	2.581	1.714	5.287	2.248	-1.840
H	-3.387	1.532	3.240	-3.289	1.405	3.273	3.228	1.082	-3.264
H	-2.024	1.784	2.117	-1.946	1.680	2.133	1.926	1.491	-2.119
H	-2.924	3.170	2.749	-2.866	3.049	2.775	2.894	2.772	-2.868
H	-4.111	2.900	-0.823	-4.120	2.768	-0.772	4.245	2.678	0.652
H	-3.249	3.930	0.335	-3.255	3.810	0.371	3.391	3.675	-0.536
H	-2.456	2.484	-0.310	-2.446	2.386	-0.305	2.541	2.344	0.272
H	-5.077	3.790	1.945	-5.049	3.611	2.026	5.130	3.262	-2.222
H	-6.041	2.813	0.836	-6.005	2.630	0.918	6.062	2.313	-1.068
H	-5.765	2.263	2.506	-5.691	2.062	2.575	5.670	1.646	-2.672
C	2.190	2.694	2.511	2.084	2.893	2.342	-1.990	2.983	-2.332
C	1.007	2.203	3.376	1.065	2.185	3.266	-1.074	2.148	-3.261
C	3.222	1.555	2.328	3.294	1.962	2.071	-3.251	2.161	-1.951
C	2.891	3.821	3.300	2.613	4.125	3.108	-2.465	4.214	-3.133
H	0.293	3.016	3.559	0.211	2.837	3.482	-0.182	2.716	-3.550
H	0.480	1.387	2.883	0.694	1.265	2.815	-0.758	1.221	-2.782
H	1.372	1.851	4.351	1.546	1.937	4.220	-1.621	1.899	-4.177
H	4.094	1.911	1.766	4.048	2.472	1.460	-3.927	2.750	-1.319
H	3.575	1.205	3.308	3.766	1.685	3.021	-3.796	1.897	-2.865
H	2.795	0.707	1.792	2.997	1.045	1.558	-2.996	1.238	-1.427
H	3.223	3.424	4.266	3.057	3.790	4.051	-2.996	3.870	-4.026
H	3.780	4.202	2.783	3.395	4.659	2.557	-3.163	4.840	-2.566
H	2.222	4.665	3.507	1.815	4.834	3.360	-1.632	4.837	-3.477
C	1.784	6.450	-0.980	0.966	6.501	-1.134	-0.271	6.643	0.822
C	2.653	6.474	-2.260	1.814	6.631	-2.426	-1.072	6.970	2.114
C	0.437	7.157	-1.268	-0.484	6.967	-1.424	1.238	6.915	1.072
C	2.520	7.254	0.110	1.568	7.432	-0.064	-0.757	7.575	-0.304
H	3.619	5.986	-2.088	2.848	6.309	-2.256	-2.143	6.782	1.977
H	2.163	5.961	-3.096	1.406	6.037	-3.252	-0.729	6.392	2.979
H	2.845	7.509	-2.574	1.834	7.677	-2.753	-0.944	8.030	2.357

H	-0.201	7.165	-0.376	-1.110	6.893	-0.527	1.834	6.701	0.178
H	0.606	8.197	-1.575	-0.480	8.013	-1.749	1.377	7.971	1.325
H	-0.119	6.660	-2.071	-0.958	6.377	-2.217	1.639	6.324	1.903
H	2.683	8.281	-0.240	1.553	8.464	-0.432	-0.579	8.615	-0.012
H	1.943	7.313	1.040	0.995	7.412	0.870	-0.216	7.407	-1.243
H	3.503	6.827	0.342	2.612	7.184	0.161	-1.832	7.474	-0.493

References

[1]   Energy Information Administration, "Annual Energy Outlook 2015," pp. 1–13, www.eia.gov, 2015.

[2]   P. Denholm, E. Ela, B. Kirby, and M. Milligan, "The Role of Energy Storage with Renewable Electricity Generation - NREL-TP-6A2-471," 2010.

[3]   L. Jorrissen and H. Frey, "Energy Storage," *Encyclopedia of Electrochemical Power Sources*. Elsevier, pp. 215–231, 2009.

[4]   L. Li, S. Kim, W. Wang, M. Vijayakumar, Z. Nie, B. Chen, J. Zhang, G. Xia, J. Hu, G. Graff, J. Liu, and Z. Yang, "A stable vanadium redox-flow battery with high energy density for large-scale energy storage," *Adv. Energy Mater.*, vol. 1, no. 3, pp. 394–400, 2011.

[5]   Z. Yang, J. Zhang, M. C. W. Kintner-Meyer, X. Lu, D. Choi, J. P. Lemmon, and J. Liu, "Electrochemical energy storage for green grid," *Chem. Rev.*, vol. 111, pp. 3577–3613, 2011.

[6]   A. Z. Weber, M. M. Mench, J. P. Meyers, P. N. Ross, J. T. Gostick, and Q. Liu, "Redox flow batteries: A review," *Journal of Applied Electrochemistry*, vol. 41. pp. 1137–1164, 2011.

[7]   W. Wang, Q. Luo, B. Li, X. Wei, L. Li, and Z. Yang, "Recent progress in redox flow battery research and development," *Adv. Funct. Mater.*, vol. 23, pp. 970–986, 2013.

[8]   C. Ponce de León, A. Frías-Ferrer, J. González-García, D. A. Szánto, and F. C. Walsh, "Redox flow cells for energy conversion," *J. Power Sources*, vol. 160, pp. 716–732, 2006.

[9]   A. M. Posner, "Redox fuel cell," *Fuel*, vol. 34, pp. 330–338, 1955.

[10]   G. L. Soloveichik, "Flow Batteries: Current Status and Trends," *Chem. Rev.*, vol. 115, no. 20, pp. 11533–11558, 2015.

[11]   L. H. Thaller, "Electrically rechargeable redox flow cell," US Patent: 3996064, 1976.

[12]   E. Sum and M. Skyllas-Kazacos, "A study of the V(II)/V(III) redox couple for redox flow cell applications," *J. Power Sources*, vol. 15, pp. 179–190, 1985.

[13]   E. Sum, M. Rychcik, and M. Skyllas-Kazacos, "Investigation of the V(V)/V(IV) system for use in the positive half-cell of a redox battery," *J. Power Sources*, vol. 16, pp. 85–95, 1985.

[14]   P. Alotto, M. Guarnieri, and F. Moro, "Redox flow batteries for the storage of renewable energy: A review," *Renew. Sustain. Energy Rev.*, vol. 29, pp. 325–335, 2014.

[15]   M. Kazacos, M. Skyllas-Kazacos, and N. Kazacos, "Vanadium halide redox flow battery," US Patent: 7976974, 2011.

[16]   M. Skyllas-Kazacos, G. Kazacos, G. Poon, and H. Verseema, "Recent advances with UNSW vanadium-based redox flow batteries," *Int. J. Energy Res.*, vol. 34,

no. 2, pp. 182–189, 2010.

[17] B. Huskinson, M. P. Marshak, C. Suh, S. Er, M. R. Gerhardt, C. J. Galvin, X. Chen, A. Aspuru-Guzik, R. G. Gordon, and M. J. Aziz, "A metal-free organic-inorganic aqueous flow battery.," *Nature*, vol. 505, pp. 195–8, 2014.

[18] B. Yang, L. Hoober-Burkhardt, F. Wang, G. K. Surya Prakash, and S. R. Narayanan, "An Inexpensive Aqueous Flow Battery for Large-Scale Electrical Energy Storage Based on Water-Soluble Organic Redox Couples," *J. Electrochem. Soc.*, vol. 161, no. 9, pp. A1371–A1380, 2014.

[19] R. M. Darling, K. G. Gallagher, and F. R. Brushett, "Environmental Science Pathways to low-cost electrochemical energy storage : a comparison of aqueous and nonaqueous fl ow batteries †," *Energy Environemntal Sci.*, vol. 7, pp. 3459–3477, 2014.

[20] A. J. Bard and L. R. Faulkner, *Electrochemical Methods: Fundamentals and Applications*, 2nd ed. New York, NY: John Wiley & Sons, Inc, 2001.

[21] C. M. Hansen, *Hansen Solubility Parameters A User's Handbook*, 2nd ed. Boca Raton, FL: CRC Press, 2007.

[22] Y. Huang, S. Gu, Y. Yan, and S. F. Y. Li, "Nonaqueous redox-flow batteries: features, challenges, and prospects," *Curr. Opin. Chem. Eng.*, vol. 8, pp. 105–113, 2015.

[23] J. Huang, L. Su, J. a. Kowalski, J. L. Barton, M. Ferrandon, A. K. Burrell, F. R. Brushett, and L. Zhang, "A subtractive approach to molecular engineering of dimethoxybenzene-based redox materials for non-aqueous flow batteries," *J. Mater. Chem. A*, vol. 3, pp. 14971–14976, 2015.

[24] G. Nagarjuna, J. Hui, K. J. Cheng, T. Lichtenstein, M. Shen, J. S. Moore, and J. Rodriguez-Lopez, "Impact of Redox-Active Polymer Molecular Weight on the Electrochemical Properties and Transport Across Porous Separators in Nonaqueous Solvents," *J. Am. Chem. Soc.*, vol. 136, no. 46, pp. 16309–16316, 2014.

[25] J. Winsberg, T. Hagemann, S. Muench, C. Friebe, B. Häupler, T. Janoschka, S. Morgenstern, M. D. Hager, and U. S. Schubert, "Poly(boron-dipyrromethene)—A Redox-Active Polymer Class for Polymer Redox-Flow Batteries," *Chem. Mater.*, vol. 28, pp. 3401–3405, 2016.

[26] Y. Matsuda, K. Tanaka, M. Okada, Y. Takasu, M. Morita, and T. Matsumura-Inoue, "A rechargeable redox battery utilizing ruthenium complexes with non-aqueous organic electrolyte," *J. Appl. Electrochem.*, vol. 18, pp. 909–914, 1988.

[27] P. J. Cabrera, X. Yang, J. A. Suttil, K. L. Hawthorne, R. E. M. Brooner, M. S. Sanford, and L. T. Thompson, "Complexes Containing Redox Noninnocent Ligands for Symmetric, Multielectron Transfer Nonaqueous Redox Flow Batteries," *J. Phys. Chem. C*, vol. 119, no. 28, pp. 15882–15889, 2015.

[28] M. H. Chakrabarti, R. A. W. Dryfe, and E. P. L. Roberts, "Evaluation of electrolytes for redox flow battery applications," *Electrochim. Acta*, vol. 52, pp. 2189–2195, 2007.

[29] J. Mun, M.-J. Lee, J.-W. Park, D.-J. Oh, D.-Y. Lee, and S.-G. Doo, "Non-Aqueous Redox Flow Batteries with Nickel and Iron Tris(2,2′-bipyridine) Complex Electrolyte," *Electrochem. Solid-State Lett.*, vol. 15, no. 6, p. A80, 2012.

[30] C. K. Jørgensen, "Differences between the four halide ligands, and discussion

remarks on trigonal-bipyramidal complexes, on oxidation states, and on diagonal elements of one-electron energy," *Coodination Chem. Rev.*, vol. 1, no. 1–2, pp. 164–178, 1966.

[31] B. Butschke, K. L. Fillman, T. Bendikov, L. J. W. Shimon, Y. Diskin-Posner, G. Leitus, S. I. Gorelsky, M. L. Neidig, and D. Milstein, "How Innocent are Potentially Redox Non-Innocent Ligands? Electronic Structure and Metal Oxidation States in Iron-PNN Complexes as a Representative Case Study," *Inorg. Chem.*, vol. 54, no. 10, pp. 4909–4926, 2015.

[32] P. J. Cappillino, H. D. Pratt, N. S. Hudak, N. C. Tomson, T. M. Anderson, and M. R. Anstey, "Application of Redox Non-Innocent Ligands to Non-Aqueous Flow Battery Electrolytes," *Adv. Energy Mater.*, vol. 4, 2014.

[33] Z. Zhang and S. S. Zhang, Eds., *Rechargeable Batteries: Materials, Technologies and New Trends*, 1st ed. Switzerland: Springer International Publishing, 2015.

[34] Q. Liu, A. E. S. Sleightholme, A. a. Shinkle, Y. Li, and L. T. Thompson, "Non-aqueous vanadium acetylacetonate electrolyte for redox flow batteries," *Electrochem. Commun.*, vol. 11, pp. 2312–2315, 2009.

[35] A. A. Shinkle, T. J. Pomaville, A. E. S. Sleightholme, L. T. Thompson, and C. W. Monroe, "Solvents and supporting electrolytes for vanadium acetylacetonate flow batteries," *J. Power Sources*, vol. 248, pp. 1299–1305, 2014.

[36] A. A. Shinkle, A. E. S. Sleightholme, L. D. Griffith, L. T. Thompson, and C. W. Monroe, "Degradation mechanisms in the non-aqueous vanadium acetylacetonate redox flow battery," *J. Power Sources*, vol. 206, pp. 490–496, 2012.

[37] A. E. S. Sleightholme, A. A. Shinkle, Q. Liu, Y. Li, C. W. Monroe, and L. T. Thompson, "Non-aqueous manganese acetylacetonate electrolyte for redox flow batteries," *J. Power Sources*, vol. 196, no. 13, pp. 5742–5745, 2011.

[38] Q. Liu, A. A. Shinkle, Y. Li, C. W. Monroe, L. T. Thompson, and A. E. S. Sleightholme, "Non-aqueous chromium acetylacetonate electrolyte for redox flow batteries," *Electrochem. Commun.*, vol. 12, pp. 1634–1637, 2010.

[39] A. A. Shinkle, A. E. S. Sleightholme, L. T. Thompson, and C. W. Monroe, "Electrode kinetics in non-aqueous vanadium acetylacetonate redox flow batteries," *J. Appl. Electrochem.*, vol. 41, pp. 1191–1199, 2011.

[40] J. D. Saraidaridis, B. M. Bartlett, and C. W. Monroe, "Spectroelectrochemistry of Vanadium Acetylacetonate and Chromium Acetylacetonate for Symmetric Nonaqueous Flow Batteries," *J. Electrochem. Soc.*, vol. 163, no. 7, pp. A1239–A1246, 2016.

[41] I. L. Escalante-Garcia, J. S. Wainright, L. T. Thompson, and R. F. Savinell, "Performance of a Non-Aqueous Vanadium Acetylacetonate Prototype Redox Flow Battery: Examination of Separators and Capacity Decay," *J. Electrochem. Soc.*, vol. 162, no. 3, pp. A363–A372, 2014.

[42] T. Herr, J. Noack, P. Fischer, and J. Tübke, "1,3-Dioxolane, tetrahydrofuran, acetylacetone and dimethyl sulfoxide as solvents for non-aqueous vanadium acetylacetonate redox-flow-batteries," *Electrochim. Acta*, vol. 113, pp. 127–133, 2013.

[43] M. A. Nawi and T. L. Riechel, "Electrochemical studies of vanadium(III) and vanadium(IV) acetylacetonate complexes in dimethylsulfoxide," *Inorg. Chem.*, vol. 20, no. 6, pp. 1974–1978, 1981.

[44] G. L. Geoffroy, "Organometallic photochemistry," *J. Chem. Educ.*, vol. 60, no. 10, p. 861, 1983.

[45] I. J. S. Fairlamb and J. M. Lynam, Eds., *Organometallic Chemistry, Volume 37*. Cambridge, UK: The Royal Society of Chemistry, 2011.

[46] X. Wei, L. Cosimbescu, W. Xu, J. Z. Hu, M. Vijayakumar, J. Feng, M. Y. Hu, X. Deng, J. Xiao, J. Liu, V. Sprenkle, and W. Wang, "Towards high-performance nonaqueous redox flow electrolyte via ionic modification of active species," *Adv. Energy Mater.*, pp. 1–7, 2014.

[47] L. Cosimbescu, X. Wei, M. Vijayakumar, W. Xu, M. L. Helm, S. D. Burton, C. M. Sorensen, J. Liu, V. Sprenkle, and W. Wang, "Anion-Tunable Properties and Electrochemical Performance of Functionalized Ferrocene Compounds.," *Sci. Rep.*, vol. 5, p. 14117, 2015.

[48] Y. Wang, E. I. Rogers, and R. G. Compton, "The measurement of the diffusion coefficients of ferrocene and ferrocenium and their temperature dependence in acetonitrile using double potential step microdisk electrode chronoamperometry," *J. Electroanal. Chem.*, vol. 648, no. 1, pp. 15–19, 2010.

[49] N. G. Tsierkezos, "Cyclic voltammetric studies of ferrocene in nonaqueous solvents in the temperature range from 248.15 to 298.15 K," *J. Solution Chem.*, vol. 36, no. 3, pp. 289–302, 2007.

[50] Y. I. Moharram, "Extraction of electrode kinetics and transport parameters of ferrocene at a platinum electrode from semiintegral electroanalysis," *J. Electroanal. Chem.*, vol. 587, no. 1, pp. 115–126, 2006.

[51] F. A. Abeed, T. A. K. Al-Allaf, and S. T. Sulaiman, "Electroanalytical studies of ferrocene and substituted ferrocene in non-aqueous solvents by rotating disc voltammetry," *Analyst*, vol. 113, no. February, p. 333, 1988.

[52] C. O. Laoire, E. Plichta, M. Hendrickson, S. Mukerjee, and K. M. Abraham, "Electrochemical studies of ferrocene in a lithium ion conducting organic carbonate electrolyte," *Electrochim. Acta*, vol. 54, no. 26, pp. 6560–6564, 2009.

[53] T. Yamamura, Y. Shiokawa, H. Yamana, and H. Moriyama, "Electrochemical investigation of uranium beta-diketonates for all-uranium redox flow battery," *Electrochim. Acta*, vol. 48, pp. 43–50, 2002.

[54] D. Zhang, H. Lan, and Y. Li, "The application of a non-aqueous bis(acetylacetone)ethylenediamine cobalt electrolyte in redox flow battery," *J. Power Sources*, vol. 217, pp. 199–203, 2012.

[55] A. A. Shinkle, "Non-Aqueous Single-Metal Redox Flow Batteries," PhD Dissertation - University of Michigan, 2013.

[56] S.-H. Shin, S.-H. Yun, and S.-H. Moon, "A review of current developments in non-aqueous redox flow batteries: characterization of their membranes for design perspective," *RSC Adv.*, vol. 3, p. 9095, 2013.

[57] T. Herr, P. Fischer, J. Tübke, K. Pinkwart, and P. Elsner, "Increasing the energy density of the non-aqueous vanadium redox flow battery with the acetonitrile-1,3-dioxolane-dimethyl sulfoxide solvent mixture," *J. Power Sources*, vol. 265, pp. 317–324, 2014.

[58] R. Freitag, "Computational, Structural and Electrochemical Properties of Metal(III) Tris-betadiketonato Complexes," Masters Thesis - University of the Free State, 2013.

[59] University of Cambridge, "Linear Sweep and Cyclic Voltametry: The Principles." [Online]. Available: http://www.ceb.cam.ac.uk/research/.

[60] Bioanalytical Systems Inc., "Cyclic Voltammetry - Data Analysis." [Online]. Available: www.BASinc.com.

[61] R. G. Compton and C. E. Banks, *Understanding Voltammetry*, 2nd ed. Singapore: Imperial College Press, 2011.

[62] R. Guidelli, R. G. Compton, J. M. Feliu, E. Gileadi, J. Lipkowski, W. Schmickler, and S. Trasatti, "Defining the transfer coefficient in electrochemistry: An assessment (IUPAC Technical Report)," in *Pure and Applied Chemistry*, 2014, vol. 86, no. 2, pp. 245–258.

[63] R. S. Nicholson and I. Shain, "Theory of Stationary Electrode Polarography: Single Scan and Cyclic Methods Applied to Reversible, Irreversible, and Kinetic Systems," *Anal. Chem.*, vol. 36, no. 4, pp. 706–723, 1964.

[64] R. Atanasoski and J.-P. Dodelet, "Fuel Cells – Proton-Exchange Membrane Fuel Cells | Catalysts: Non Platinum," in *Encyclopedia of Electrochemical Power Sources*, 1st ed., Elsevier Science, 2009, pp. 639–649.

[65] D. A. Shores and G. A. Deluga, *Handbook of Fuel Cells*, vol. 3. 2003.

[66] Y. Sone, P. Ekdunge, and D. Simonsson, "Proton Conductivily of Nafion 117 as Measured by a Four Electrode AC Impedance Method," *J. Electrochem. Soc.*, vol. 143, no. 4, pp. 1254–1259, 1996.

[67] N. H. Jalani and R. Datta, "The effect of equivalent weight, temperature, cationic forms, sorbates, and nanoinorganic additives on the sorption behavior of Nafion®," *J. Memb. Sci.*, vol. 264, no. 1–2, pp. 167–175, 2005.

[68] F. Jensen, *Introduction to Computational Chemistry*, 2nd ed. Wiley, 2007.

[69] E. Schrodinger, *Statistical Thermodynamics*. New York: Dover Publications, Inc., 1989.

[70] E. K. U. Gross and R. M. Dreizler, Eds., *Density Functional Theory*, Series B: . New York and London: Plenum Publishing Corporation, 1995.

[71] M. Born and J. R. Oppenheimer, "On the Quantum Theory of Molecules," *Ann. Phys.*, vol. 84, p. 457, 1927.

[72] D. R. Hartree, "The Wave Mechanics of an Atom with a Non-Coulomb Central Field. Part I. Theory and Methods," *Math. Proc. Cambridge Philos. Soc.*, vol. 24, no. 01, pp. 89–110, 1928.

[73] P. H. and W. Kohn, "Inhomogenous Electron Gas," *Phys. Rev.*, vol. 136, no. 3 B, pp. 864–871, 1964.

[74] W. Kohn and L. J. Sham, "Self-consistent equations including exchange and correlation effects," *Phys. Rev.*, vol. 140, no. 4A, 1965.

[75] M. Urban, V. Kello, and P. Carsky, "Polarization functions for gaussian basis sets for the first row atoms," *Theor. Chim. Acta*, vol. 45, no. 3, pp. 205–213, 1977.

[76] J. Yarwood, R. Douthwaite, and S. Duckett, *Spectroscopic Properties of Inorganic and Organometallic Compounds*, vol. 43, no. 1. 2012.

[77] T. H. Dunning Jr. and P. J. Hay, "Modern Theoretical Chemistry," in *Modern Theoretical Chemistry*, H. F. Schaefer, Ed. New York: Plenum, 1977, pp. 1–28.

[78] P. J. Hay and W. R. Wadt, "Ab initio effective core potentials for molecular calculations. Potentials for the transition metal atoms Sc to Hg," *J. Chem. Phys.*, vol. 82, no. 1, p. 270, 1985.

[79]   W. R. Wadt and P. J. Hay, "Ab initio effective core potentials for molecular calculations. Potentials for main group elements Na to Bi," *J. Chem. Phys.*, vol. 82, no. 1, pp. 284–298, 1985.

[80]   P. J. Hay and W. R. Wadt, "Ab initio effective core potentials for molecular calculations. Potentials for K to Au including the outermost core orbitals," *J. Chem. Phys.*, vol. 82, no. 1, pp. 299–310, 1985.

[81]   N. Emel'yanova, N. Sanina, A. Krivenko, R. Manzhos, K. Bozhenko, and S. Aldoshin, "Comparison of pure and hybrid DFT functionals for geometry optimization and calculation of redox potentials for iron nitrosyl complexes with 'µ-SCN' bridging ligands," *Theor. Chem. Acc.*, no. 132, p. 1316, 2013.

[82]   A. D. Becke, "Density-functional thermochemistry. III. The role of exact exchange," *J. Chem. Phys.*, vol. 98, no. 7, p. 5648, 1993.

[83]   Gaussian 09 Rev E.01, M. J. Frisch, G. W. Trucks, H. B. Schlegel, G. E. Scuseria, M. A. Robb, J. R. Cheeseman, G. Scalmani, V. Barone, B. Mennucci, G. A. Petersson, H. Nakatsuji, M. Caricato, X. Li, H. P. Hratchian, A. F. Izmaylov, J. Bloino, G. Zheng, J. L. Sonnenberg, M. Hada, M. Ehara, K. Toyota, R. Fukuda, J. Hasegawa, M. Ishida, T. Nakajima, Y. Honda, O. Kitao, H. Nakai, T. Vreven, J. Montgomery, J. A., J. E. Peralta, F. Ogliaro, M. Bearpark, J. J. Heyd, E. Brothers, K. N. Kudin, V. N. Staroverov, R. Kobayashi, J. Normand, K. Raghavachari, A. Rendell, J. C. Burant, S. S. Iyengar, J. Tomasi, M. Cossi, N. Rega, J. M. Millam, M. Klene, J. E. Knox, J. B. Cross, V. Bakken, C. Adamo, J. Jaramillo, R. Gomperts, R. E. Stratmann, O. Yazyev, A. J. Austin, R. Cammi, C. Pomelli, J. W. Ochterski, R. L. Martin, K. Morokuma, V. G. Zakrzewski, G. A. Voth, P. Salvador, J. J. Dannenberg, S. Dapprich, A. D. Daniels, Ö. Farkas, J. B. Foresman, J. V. Ortiz, J. Cioslowski, and D. J. Fox, "Gaussian 09 Rev E.01." Gaussian Inc., Wallingford CT, 2009.

[84]   L. Cheng, R. S. Assary, X. Qu, A. Jain, S. P. Ong, N. N. Rajput, K. Persson, and L. A. Curtiss, "Accelerating Electrolyte Discovery for Energy Storage with High Throughput Screening," *J. Phys. Chem. Lett.*, vol. 6, no. 2, pp. 283–291, 2015.

[85]   N. Shao, X. G. Sun, S. Dai, and D. E. Jiang, "Electrochemical windows of sulfone-based electrolytes for high-voltage Li-ion batteries," *J. Phys. Chem. B*, vol. 115, pp. 12120–12125, 2011.

[86]   N. Shao, X. Sun, S. Dai, and D. Jiang, "Supporting Information for: Electrochemical Windows of Sulfone-Based Electrolytes for High- Voltage Li-Ion Batteries," *J. Phys. Chem. B*, pp. 12120–12125, 2011.

[87]   M. Ue, A. Murakami, and S. Nakamura, "Anodic Stability of Several Anions Examined by Ab Initio Molecular Orbital and Density Functional Theories," *J. Electrochem. Soc.*, vol. 149, no. 12, p. A1572, 2002.

[88]   R. I. Zubatyuk, L. Gorb, O. V Shishkin, M. O. Qasim, and J. Leszczynski, "Exploration of density functional methods for one-electron reduction potential of nitrobenzenes," *J. Comput. Chem.*, vol. 31, no. 1, pp. 144–150, 2010.

[89]   X. Zhang, J. K. Pugh, and P. N. Ross, "Computation of Thermodynamic Oxidation Potentials of Organic Solvents Using Density Functional Theory," *J. Electrochem. Soc.*, vol. 148, no. 5, p. E183, 2001.

[90]   Y. K. Han, J. Jung, J. J. Cho, and H. J. Kim, "Determination of the oxidation potentials of organic benzene derivatives: Theory and experiment," *Chemical*

Physics Letters, vol. 368, no. 5–6. pp. 601–608, 2003.

[91] D. S. Palmer, A. Llinàs, I. Morao, G. M. Day, J. M. Goodman, R. C. Glen, and J. B. O. Mitchell, "Predicting intrinsic aqueous solubility by a thermodynamic cycle," *Mol. Pharm.*, vol. 5, no. 2, pp. 266–279, 2008.

[92] G. B. Kauffman, "Inorganic Chemistry, 2nd Edition (Miessler, Gary L.; Tarr, Donald A.)," *J. Chem. Educ.*, vol. 77, p. 165, 2000.

[93] C. C. Vequi-Suplicy, K. Coutinho, and M. T. Lamy, "Electric dipole moments of the fluorescent probes Prodan and Laurdan: Experimental and theoretical evaluations," *Biophys. Rev.*, vol. 6, no. 1, pp. 63–74, 2014.

[94] R. E. Trifonov, A. V. Gaenko, S. N. Vergizov, M. B. Shcherbinin, and V. A. Ostrovskii, "A Theoretical and Experimental Study of Dipole Moments of 3-Aminofurazans," *Croat. Chem. ACTA*, vol. 76, no. 2, pp. 177–182, 2003.

[95] H. G. Kjaergaard, K. J. Bezar, and K. A. Brooking, "Calculation of dipole moment functions with density functional theory: application to vibrational band intensities," *Mol. Phys.*, vol. 96, no. 7, pp. 1125–1138, 1999.

[96] C. J. Cramer and D. G. Truhlar, "Implicit Solvation Models: Equilibria, Structure, Spectra, and Dynamics.," *Chem. Rev.*, vol. 99, no. 8, pp. 2161–2200, 1999.

[97] J. Tomasi, B. Mennucci, and R. Cammi, "Quantum mechanical continuum solvation models," *Chem. Rev.*, vol. 105, no. 8, pp. 2999–3093, 2005.

[98] C. J. Cramer and D. G. Truhlar, "A Universal Approach to Solvation Modeling," *Acc. Chem. Res.*, vol. 41, no. 6, pp. 760–768, 2008.

[99] S. Miertus, E. Scrocco, and J. Tomasi, "Electrostatic interaction of a solute with a continuum. A direct utilizaion of AB initio molecular potentials for the prevision of solvent effects," *Chem. Phys.*, vol. 55, no. 1, pp. 117–129, 1981.

[100] L. Hu and G. W. Wei, "Nonlinear poisson equation for heterogeneous media," *Biophys. J.*, vol. 103, no. 4, pp. 758–766, 2012.

[101] H. Thomas, "Molecular Field Theory, the Onsager Reaction Field, and the Spherical Model," *J. Appl. Phys.*, vol. 39, no. 2, p. 624, 1968.

[102] O. Hammerich and B. Speiser, Eds., *Organic Electrochemistry: Revised and Expanded*, 5th ed. Boca Raton: CBC Press, 2016.

[103] C. F. Matta, Ed., *Quantum Biochemistry*. Weinheim: Wiley-VHC, 2010.

[104] H. Ikeuchi, K. Naganuma, M. Ichikawa, H. Ozawa, T. Ino, M. Sato, H. Yonezawa, S. Mukaida, A. Yamamoto, and T. Hashimoto, "Diffusion Coefficients of Tris(β-diketonato)ruthenium Complexes of Different Charge Numbers in Acetonitrile Solutions, Measured by Chronoamperometry," *J. Solution Chem.*, vol. 36, no. 10, pp. 1243–1259, Sep. 2007.

[105] M. I. Pilo, G. Sanna, and R. Seeber, "Analysis of cyclic voltammetric responses by Fourier transform-based deconvolution and convolution procedures," *J. Electroanal. Chem.*, vol. 323, no. 1–2, pp. 103–115, 1992.

[106] X. Zhang, S. Wang, and Q. Shen, "The electrochemical behavior of p-aminophenol at a w-mercaptopropionic acid self-assembled gold electrode," *Microchim. Acta*, vol. 149, no. 1–2, pp. 37–42, 2005.

[107] T. Paczesniak, P. Boniarz, K. Rydel, and A. Sobkowiak, "Electrochemical catalytic processes with hydrogen peroxide showing oxidative and reductive properties (acting as oxidant or reductant)," *Electroanalysis*, vol. 19, no. 9, pp. 945–951, 2007.

[108] C. W. Anderson, K. R. Lung, and T. A. Nile, "Electrochemistry of homogeneous catalysts: correlation of the electrochemistry and the Ziegler-Natta catalytic activity of metal acetylacetonate complexes," *Inorganica Chim. Acta*, vol. 85, no. 1, pp. 33–36, 1984.

[109] C. Tsiamis, C. C. Hadjikostas, S. Karageorgiou, and G. Manoussakis, "Ligand field, electronic and solvent effects in the non-aqueous electrochemistry of tris(??-dionato)chromium(III) chelates," *Inorganica Chim. Acta*, vol. 143, no. 1, pp. 17–23, 1988.

[110] K. B. Takvorian and R. B. Barker, "Tris(3-cyanomethyl-2,4-pentanedionato) chromium(III)," *Inorg. Synth.*, vol. 12, pp. 85–88, 1970.

[111] K. M. De Fina, C. Ezell, and J. Acree, William E., "Solubility of ferrocene in organic nonelectrolyte solvents. Comparison of observed versus predicted values based upon mobile order theory," *Phys. Chem. Liq.*, vol. 39, no. 6, pp. 699–710, 2001.

[112] M. Rychcik and M. Skyllas-Kazacos, "Evaluation of electrode materials for vanadium redox cell," *J. Power Sources*, vol. 19, no. 1, pp. 45–54, 1987.

[113] B. Sun and M. Skyllas-Kazacos, "Modification of graphite electrode materials for vanadium redox flow battery application—I. Thermal treatment," *Electrochim. Acta*, vol. 37, no. 7, pp. 1253–1260, 1992.

[114] Entegris, "Properties and Characteristics of Graphite: For the semiconductor industry," 2013.

[115] R. L. McCreery, "Advanced carbon electrode materials for molecular electrochemistry," *Chemical Reviews*, vol. 108, no. 7. pp. 2646–2687, 2008.

[116] J. N. Noack and J. Tübke, "A Comparison of Materials and Treatment of Materials for Vanadium Redox Flow Battery," *ECS Trans.*, vol. 25, no. 35, pp. 235–245, 2010.

[117] J. Wang, "Reticulated vitreous carbon—a new versatile electrode material," *Electrochim. Acta*, vol. 26, no. 12, pp. 1721–1726, 1981.

[118] J. M. Friedrich, C. Ponce-de-León, G. W. Reade, and F. C. Walsh, "Reticulated vitreous carbon as an electrode material," *J. Electroanal. Chem.*, vol. 561, no. SUPPL. 1, pp. 203–217, 2004.

[119] Astom Corporation, "Ion exchange membrane [Neosepta]." [Online]. Available: http://www.astom-corp.jp/en/.

[120] BASI, "Bulk Electrolysis Cell." [Online]. Available: www.basinc.com.

[121] R. S. Mulliken, "Electronic Population Analysis on LCAO-MO Molecular Wave Functions. I," *J. Chem. Phys.*, vol. 23, no. 10, pp. 1833–1840, 1955.

[122] J. P. Foster and F. Weinhold, "Natural Hybrid Orbitals," *J. Am. Chem. Soc.*, vol. 102, no. 22, pp. 7211–7218, 1980.

[123] R. F. W. Bader, *Atoms in Molecules: A Quantum Theory, International Series of Monographs on Chemistry*, 1st ed., vol. 22. Clarendon Press, 1994.

[124] F. L. Hirshfeld, "Bonded-atom fragments for describing molecular charge densities," *Theor. Chim. Acta*, vol. 44, no. 2, pp. 129–138, 1977.

[125] T. Lu, "Multiwfn: A Multifunctional Wavefunction Analyzer - Software Manual," Beijing, 2015.

[126] T. Lu and F. Chen, "Multiwfn: A multifunctional wavefunction analyzer," *J. Comput. Chem.*, vol. 33, no. 5, pp. 580–592, 2012.

[127] J. F. Kucharyson, J. R. Gaudet, B. M. Wyvratt, and L. T. Thompson, "Understanding the Stability and Cyclability of Vanadium(III) Acetylacetonate-Based Redox Flow Battery Electrolytes," *J. Mater. Chem. A*, vol. Submitted, 2016.

[128] H. Brunner and T. Tsuno, "Ligand Dissociation: Planar or Pyrimidal Imtermediates?," *Acc. Chem. Res.*, vol. 42, no. 10, pp. 1501–1510, 2009.

[129] X. Wang, "Spectroscopy and Structures of Cu-Organonitrogen Complexes," PhD Dissertation - University of Kentucky, 2007.

[130] Minitab 17 Statistical Software, "Minitab 17 Statistical Software." Minitab Inc., State College, PA, 2010.

[131] C. Jia, Q. Liu, C. Sun, F. Yang, Y. Ren, S. M. Heald, Y. Liu, Z. Li, W. Lu, and J. Xie, "In Situ X-ray Near-Edge Absorption Spectroscopy Investigation of the State of Charge of All-Vanadium Redox Flow Batteries," *ACS Appl Mater Interfaces*, vol. 6, pp. 17920–17925, 2014.

[132] C. A. Apblett, D. M. Stewart, R. T. Fryer, J. C. Sell, H. D. I. Pratt, T. M. Anderson, and R. W. Meulenberg, "In situ XANES and EXAFS Analysis of Redox Active Fe Center Ionic Liquids," *Electrochim. Acta*, vol. 185, pp. 156–161, 2015.

[133] J. E. Penner-Hahn, "X-ray Absorption Spectroscopy," *Compr. Coord. Chem. II*, pp. 159–186, 2003.

[134] K. Z. Bencze, K. C. Kondapalli, and T. L. Stemmler, "X-Ray Absorption Spectroscopy," *Encyclopedia of Inorganic Chemistry*. John Wiley & Sons, Ltd, 2008.

[135] B. Ravel and M. Newville, "ATHENA, ARTEMIS, HEPHAESTUS: Data analysis for X-ray absorption spectroscopy using IFEFFIT," in *Journal of Synchrotron Radiation*, 2005, vol. 12, no. 4, pp. 537–541.

[136] J. Wong, F. W. Lytle, R. P. Messmer, and D. H. Maylotte, "K-edge absorption spectra of selected vanadium compounds," *Phys. Rev. B*, vol. 30, no. 10, pp. 5596–5610, 1984.

[137] G. Silversmit, J. A. Van Bokhoven, H. Poelman, a. M. J. Van Der Eerden, G. B. Marin, M. F. Reyniers, and R. De Gryse, "The structure of supported and unsupported vanadium oxide under calcination, reduction and oxidation determined with XAS," *Appl. Catal. A Gen.*, vol. 285, pp. 151–162, 2005.

[138] N. M. O'Boyle, A. L. Tenderholt, and K. M. Langner, "Cclib: A library for package-independent computational chemistry algorithms," *J. Comput. Chem.*, vol. 29, pp. 839–845, 2008.

[139] J. F. Kucharyson, J. R. Gaudet, B. M. Wyvratt, and L. T. Thompson, "Characterization of Structural and Electronic Transitions During Reduction and Oxidation of Ruthenium(III) Acetylacetonate-Based Flow Battery Electrolytes Using XRay Absorption Spectroscopy," *ChemElectroChem*, vol. 3, pp. 1875–1883, 2016.

[140] S. Kar, N. Chanda, S. M. Mobin, A. Datta, F. A. Urbanos, V. G. Puranik, R. Jimenez-aparicio, and G. K. Lahiri, "Diruthenium complexes [((acac)₂,Ru^{III})₂(mu-OC₂H₅)₂], [((acac)₂Ru^{III})₂(mu-L)](ClO₄)₂, and [((bpy)₂Ru^{II})₂," *Inorg. Chem.*, vol. 43, pp. 4911–4920, 2004.

[141] K. Getty, M. U. Delgado-Jaime, and P. Kennepohl, "Assignment of pre-edge features in the Ru K-edge X-ray absorption spectra of organometallic ruthenium

complexes," *Inorganica Chim. Acta*, vol. 361, no. 4, pp. 1059–1065, 2008.

[142] A. Böttcher, M. W. Grinstaff, J. A. Labinger, and H. B. Gray, "Aerobic oxidation of hydrocarbons catalyzed by electronegative iron salen complexes," *J. Mol. Catal. A Chem.*, vol. 113, no. 1–2, pp. 191–200, 1996.

[143] K. Noda, N. Hosoya, R. Irie, Y. Ito, and T. Katsuki, "Asymmetric Aziridination By Using Optically-Active (Salen)Manganese(III) Complexes," *Synlett*, no. 7, pp. 469–471, 1993.

[144] P. G. Cozzi, "Metal-Salen Schiff base complexes in catalysis: practical aspects.," *Chem. Soc. Rev.*, vol. 33, no. 7, pp. 410–421, 2004.

[145] A. S. Abu-Surrah, H. M. Abdel-Halim, and F. M. Al-Qaisi, "Trans- and cis-Cobalt(III), Iron(III), and Chromium(III) Complexes Based on α- and γ-Diimine Schiff Base Ligands: Synthesis and Evaluation of the Complexes as Catalysts for Oxidation of L-Cysteine," *Z. Anorg. Allg. Chem.*, vol. 634, no. 5, pp. 956–961, 2008.

[146] J. A. Castro-Osma, K. J. Lamb, and M. North, "Cr(salophen) Complex Catalyzed Cyclic Carbonate Synthesis at Ambient Temperature and Pressure," *ACS Catal.*, vol. 6, no. 8, pp. 5012–5025, 2016.

[147] H. Chen, Z. Sun, X. Liu, A. Han, and P. Du, "Cobalt-Salen Complexes as Catalyst Precursors for Electrocatalytic Water Oxidation at Low Overpotential," *J. Phys. Chem. C*, vol. 119, no. 17, pp. 8998–9004, 2015.

[148] R. Irie and T. Katsuki, "Selective aerobic oxidation of hydroxy compounds catalyzed by photoactivated ruthenium-salen complexes (selective catalytic aerobic oxidation)," *Chem. Rec.*, vol. 4, no. 2, pp. 96–109, 2004.

[149] H. Shimizu, S. Onitsuka, H. Egami, and T. Katsuki, "Ruthenium(salen)-catalyzed aerobic oxidative desymmetrization of meso-diols and its kinetics.," *J. Am. Chem. Soc.*, vol. 127, no. 3, pp. 5396–5413, 2005.

[150] B. Fan, H. Li, W. Fan, C. Jin, and R. Li, "Oxidation of cyclohexane over iron and copper salen complexes simultaneously encapsulated in zeolite Y," *Appl. Catal. A Gen.*, vol. 340, no. 1, pp. 67–75, 2008.

[151] G. C. Salomão, M. H. N. Olsen, V. Drago, C. Fernandes, L. Cardozo Filho, and O. A. C. Antunes, "Oxidation of cyclohexane promoted by [Fe(III)(Salen)Cl] and [Mn(III)(Salen)Cl]," *Catal. Commun.*, vol. 8, no. 1, pp. 69–72, 2007.

[152] N. H. Lee, C. S. Lee, and D. S. Jung, "Selective oxidation of benzylic hydrocarbons to carbonyl compounds catalyzed by Mn(III) salen complexes," *Tetrahedron Lett.*, vol. 39, no. 11, pp. 1385–1388, 1998.

[153] M. Bandini, P. G. Cozzi, and A. Umani-Ronchi, "[Cr(Salen)] as a 'bridge' between asymmetric catalysis, Lewis acids and redox processes.," *Chem. Commun.*, no. 9, pp. 919–927, 2002.

[154] O. Rotthaus, O. Jarjayes, C. Perez Del Valle, C. Philouze, and F. Thomas, "A versatile electronic hole in one-electron oxidized NiIIbis-salicylidene phenylenediamine complexes.," *Chem. Commun.*, vol. 1, no. 43, pp. 4462–4, 2007.

[155] T. Storr, P. Verma, R. C. Pratt, E. C. Wasinger, Y. Shimazaki, and T. D. P. Stack, "Defining the electronic and geometric structure of one-electron oxidized copper-bis-phenoxide complexes," *J. Am. Chem. Soc.*, vol. 130, no. 46, pp. 15448–15459, 2008.

[156] T. J. Dunn, C. F. Ramogida, C. Simmonds, A. Paterson, E. W. Y. Wong, L.

Chiang, Y. Shimazaki, and T. Storr, "Non-innocent ligand behavior of a bimetallic Ni schiff-base complex containing a bridging catecholate," *Inorg. Chem.*, vol. 50, no. 14, pp. 6745–6755, 2011.

[157] K. Asami, K. Tsukidate, S. Iwatsuki, F. Tani, S. Karasawa, L. Chiang, T. Storr, F. Thomas, and Y. Shimazaki, "New insights into the electronic structure and reactivity of one-electron oxidized copper(II)-(Disalicylidene)diamine Complexes," *Inorg. Chem.*, vol. 51, no. 22, pp. 12450–12461, 2012.

[158] R. N. Bose, B. Fonkeng, G. Barr-David, R. P. Farrell, R. J. Judd, P. A. Lay, and D. F. Sangster, "Redox Potentials of Chromium(V)/(IV), -(V)/(III), and -(IV)/(III) Complexes with 2-Ethyl-2-hydroxybutanoato(2-/1-) Ligands," *J. Am. Chem. Soc.*, no. 118, pp. 7139–7144, 1996.

[159] F. Miomandre, P. Audebert, M. Maumy, and L. Uhl, "Electrochemical behaviour of iron(III) salen and poly(iron-salen). Application to the electrocatalytic reduction of hydrogen peroxide and oxygen," *J. Electroanal. Chem.*, vol. 516, no. 1–2, pp. 66–72, 2001.

[160] Y. Shimazaki, T. D. Stack, and T. Storr, "Detailed evaluation of the geometric and electronic structures of one-electron oxidized group 10 (Ni, Pd, and Pt) metal(II)-(disalicylidene)diamine complexes," *Inorg Chem*, vol. 48, no. 17, pp. 8383–8392, 2009.

[161] O. Rotthaus, O. Jarjayes, F. Thomas, C. Philouze, C. P. Del Valle, E. Saint-Aman, and J. L. Pierre, "Fine tuning of the oxidation locus, and electron transfer, in nickel complexes of pro-radical ligands," *Chem. - A Eur. J.*, vol. 12, no. 8, pp. 2293–2302, 2006.

[162] O. Rotthaus, O. Jarjayes, C. Philouze, C. P. Del Valle, and F. Thomas, "One-electron oxidized nickel(II) complexes of bis and tetra(salicylidene) phenylenediamine Schiff bases: from monoradical to interacting Ni(III) ions.," *Dalt. Trans.*, no. 10, pp. 1792–1800, 2009.

[163] P. G. M. Wuts, *Greene's Protective Groups in Organic Synthesis*, 5th ed. Wiley, 2014.

[164] D. T. Fagan, I. Hu, and T. Kuwana, "Vacuum heat treatment for activation of glassy carbon electrodes," *Anal. Chem.*, vol. 57, pp. 2759–2763, 1985.

[165] R. C. Engstrom, "Electrochemical Pretreatment of Glassy Carbon Electrodes," *Anal. Chem.*, vol. 54, no. 8, pp. 2310–2314, 1982.

[166] A. M. Pezeshki, J. T. Clement, G. M. Veith, T. A. Zawodzinski, and M. M. Mench, "High performance electrodes in vanadium redox flow batteries through oxygen-enriched thermal activation," *J. Power Sources*, vol. 294, pp. 333–338, 2015.